# A Bottom-Up Method to Calibrate Building Energy Models Using Building Automation System (BAS) Trend Data

Nicholas Zibin

A Thesis
in
The Department
of
Building, Civil, and Environmental Engineering

Presented in Partial Fulfilment of the Requirements
for the Degree of Master of Applied Science (Building Engineering) at
Concordia University
Montreal, Quebec, Canada

December 2014

**CONCORDIA UNIVERSITY**

**School of Graduate Studies**

This is to certify that the thesis prepared

By: Nicholas Zibin

Entitled: A Bottom-Up Method to Calibrate Building Energy Models Using Building Automation System (BAS) Trend Data

and submitted in partial fulfilment of the requirements for the degree of

**Master of Applied Science (Building Engineering)**

complies with the regulations of the University and meets the accepted standards with respect to originality and quality.

Signed by the final Examining Committee:

_____ Chair

*Dr. A. Athienitis*

_____ Examiner

*Dr. L. Lopes*

_____ Examiner

*Dr. Z. Zhu*

_____ Co-Supervisor

*Dr. R. Zmeureanu*

_____ Co-Supervisor

*Dr. J. Love*

Approved by _____

Chair of Department of Graduate Program Director

December 2014 _____

Dean of Faculty

## Abstract

A Bottom-Up Method to Calibrate Building Energy Models Using
Building Automation System (BAS) Trend Data

Nicholas Zibin

Ongoing commissioning based on calibrated building energy models is one of the most promising means to improve the energy performance of existing buildings. Many calibration methods in the literature relied on whole-building utility data to calibrate building energy models. Recent studies revealed that only using this data could result in offsetting errors occurring at sub-utility levels. To reduce offsetting errors, a new bottom-up calibration method was developed where the zone, system, plant, and whole-building models are sequentially calibrated.

The number of candidate measurement points required for bottom-up calibration is large. Fortunately, building automation systems (BASs), common in many commercial/institutional buildings, can provide some of the required data. To reduce the time for BAS trend data analysis, a new proof-of-concept prototype, called the Automatic Assisted Calibration Tool (AACT) was developed and tested to couple trend data with calibrated simulation by automatically generating inputs to update an eQUEST input file.

This thesis documents the use of the AACT and bottom-up method to calibrate an eQUEST energy model of a case study building focusing on the zone and system level models. Using inputs generated from trend data and calibrating the zone level first often yielded a calibrated system level model. Limitations representing measured physical performance in eQUEST were encountered causing unintended offsetting errors occurring at the sub-utility levels. Overall, the use of BAS trend data with a bottom-up method can reduce offsetting errors during calibrated simulation.

**Acknowledgments**

I first wish to express my sincere gratitude to my supervisors. I thank Dr. Radu Zmeureanu for his guidance, leadership, and many inspiring discussions. His incredible problem solving skills have greatly influenced me and shall have a lasting effect on my career. His support and kindness will not be forgotten. I also thank Dr. Jim Love for his guidance and detailed constructive comments that improved this work. His contributions were thought provoking and added new perspective to the research. I also thank him for taking the time to improve my professional writing.

The rapid support from the team at Concordia Facilities Management was crucial to performing this research. I thank them for volunteering their time to promptly answer questions and for helping with data collection.

I would also like to thank all my friends at Concordia and especially the students in EV-16.411. Thank you for creating a great environment through the brainstorming sessions, engaging conversations, and good times.

Finally, I am deeply grateful to my family for their encouragement and support. I would also like to thank Sarah for her loving support.

I also sincerely thank the Natural Sciences and Engineering Research Council of Canada (NSERC) Smart Net-Zero Energy Buildings Strategic Research Network, NSERC, the American Society of Heating, Refrigeration, and Air-Conditioning Engineers (ASHRAE), and the Faculty of Engineering and Computer Science at Concordia University for their generous financial support.

## Table of Contents

## List of Figures

## List of Tables

## List of Equations

## Nomenclature

| | |
|---|---|
| AACT | Automated Assisted Calibration Tool |
| ACH | Air changes per hour |
| AHU | Air-handling unit |
| AMY | Actual Meteorological Year |
| ASHRAE | American Society of Heating Refrigeration Air Conditioning Engineers |
| BAS | Building automation system |
| CV(RMSE) | Coefficient of variation of the root-mean-squared error |
| DOE-2.2 | Whole-building energy modelling program |
| EEM | Energy efficiency measure |
| eQUEST | Graphical user interface for DOE-2.2 |
| FDD | Fault detection and diagnosis |
| GE | Genome Building |
| GLC | Glycol |
| GUI | Graphical user interface |
| HVAC | Heating ventilation and air conditioning |
| Input(s) | Information entered into building simulation software |
| MBE | Mean Bias Error |
| Output(s) | Information extracted from building simulation software |
| RMSE | Root-mean-squared error |
| VAV | Variable Air Volume |
| VFD | Variable Frequency Drive |
| WD | Weekday |
| WEH | Weekend/holiday |

## List of Symbols

| | | Units |
|---|---|---|
| $b$ | Equation y-intercept from linear regression used in mixing air damper and heat recovery analysis | °C |
| $C$ | Ratio of minimum to maximum heat capacity rate | W/K |
| $C_{air}$ | Zone air capacity | W/K |
| $c_p$ | Specific heat capacity | J/(kg·K) |
| $CP$ | Change Point | °C |
| $EIR$ | Electric input ratio | - |
| $FHP_{hr}$ | Heat recovery fan heating penalty | °C |
| $HV$ | Humidification damper position | % |
| $n$ | Number | - |
| $NTU$ | Number of thermal units | - |
| $p$ | Equation slope from linear regression used in mixing air damper and heat recovery analysis | - |
| $PLR$ | Part load ratio | - |
| $pf$ | Power factor | - |
| $\dot{Q}_{fuel}$ | Whole-building fuel demand | W |
| $\dot{Q}_{hc}$ | Heating coils heat flow rate | W |
| $\dot{Q}_{hr}$ | Heat recovery heat flow rate | W |
| $\dot{Q}_{hw}$ | Heat exchanger hot water heat flow rate | W |
| $\dot{Q}_{plant}$ | Plant level heating load | W |
| $\dot{Q}_{zheat}$ | Zone reheat heat flow rate | W |
| $\dot{Q}_{zload}$ | Sum of all zone loads at a given hour including thermal capacity effects | W |
| $\dot{Q}_{zsys}$ | Zone heating/cooling system response | W |
| $R^2$ | Coefficient of determination | - |
| $t$ | Time | s |
| $T_i$ | Heat exchanger hot water inlet temperature | °C |
| $T_o$ | Heat exchanger hot water outlet temperature | °C |
| $T_{hcr}$ | Heating coils return glycol temperature | °C |
| $T_{hca}$ | Heating coils supply glycol temperature | °C |
| $T_{hd}$ | Air temperature exiting heating coils | °C |
| $T_{hr}$ | Air temperature exiting outdoor air heat recovery coils | °C |
| $T_{hre}$ | Heat recovery glycol temperature exiting coils in contact with exhaust air | °C |
| $T_{hra}$ | Heat recovery glycol temperature entering coils in contact with exhaust air | °C |
| $T_{GER}$ | Whole-building hot water return temperature | °C |

| | | |
|---|---|---|
| $T_{GES}$ | Whole-building hot water supply temperature | °C |
| $T_m$ | Mixed air temperature | °C |
| $T_{oa}$ | Outdoor air temperature | °C |
| $T_{erv}$ | Simulated air temperature exiting heating coils before mixing with the bypassed air | °C |
| $T_s$ | Supply air temperature | °C |
| $T_z$ | Zone indoor air temperature | °C |
| $T_{zs}$ | Zone supply air temperature | °C |
| $UA$ | Overall heat transfer value | W/K |
| $UA_{design}$ | Overall design heat recovery outdoor air heat transfer value | W/K |
| $V_e$ | Exhaust air flow rate | L/s |
| $V_{GE}$ | Whole-building hot water flow rate | L/s |
| $V_{hc}$ | Heating coils glycol flow rate | L/s |
| $V_{hr}$ | Total heat recovery glycol flow rate | L/s |
| $V_{hw}$ | Hot water flow rate passing through heat exchanger | L/s |
| $V_{LL}$ | Line-to-line voltage | V |
| $V_{oa}$ | Outdoor air flow rate | L/s |
| $V_r$ | Return air flow rate | L/s |
| $V_s$ | Supply air flow rate | L/s |
| $V_{zs}$ | Zone supply air flow rate | L/s |
| $V_{zr}$ | Zone return air flow rate | L/s |
| $\dot{W}_{sfan}$ | Supply air fan power | W |
| $x$ | Sampled data | - |
| $\hat{x}$ | Simulated data | - |
| $\bar{x}$ | Mean of the sampled data | - |
| $n$ | Sample size | - |
| | | |
| $\alpha$ | Outdoor air flow ratio | - |
| $\alpha_{hr}$ | Ratio of heat recovery glycol flow rate passing through the outdoor-side to the exhaust-side | - |
| $\beta$ | Simulated bypassed to total outside air flow ratio | - |
| $\Delta T_{fan}$ | Temperature rise across the supply air fan | °C |
| $\Delta T_H$ | Temperature rise due to steam humidification | °C |
| $\Delta T_{hc}$ | Temperature difference across the heating coils | °C |
| $\Delta T_{sm}$ | Supply and mixed air temperature difference | °C |
| $\varepsilon_{hr}$ | Heat recovery effectiveness | - |
| $\eta$ | Efficiency | - |
| $\rho$ | Density | $kg/m^3$ |

# 1 Introduction

## *1.1 Building Energy Consumption*

Buildings use between 20 to 40% of total energy use in developed countries (Lombard et al. 2008). The predominant role of fossil fuels in energy production makes buildings substantial contributors to anthropogenic climate change. The commercial/institutional building sector in Canada consumed 1,057 PJ which represents 12% of secondary energy use and 11% of greenhouse gas emissions in 2010 (NRCan 2014). Continuous evaluation of building energy performance is a process that helps reduce energy use, demand, and associated negative environmental effects in old and new buildings.

## *1.2 Building Commissioning*

Building systems are often poorly maintained and improperly controlled, resulting in an estimated 15 to 30% waste of energy (Katipamula and Brambley 2005). Commissioning helps reduce this energy waste by assuring that the energy and environmental control performance of a building meets or exceeds the design intent, after construction is complete. As a building operates, equipment degrades, faults occur, requirements change and operators change control settings for a variety of reasons, which may improve or impair energy and/or environmental control performance. Achieving good long-term performance is important because the lifespan of commercial/institutional buildings ranges over multiple decades.

The term commissioning originates from shipbuilding where a ship is ready for service once its systems and construction/materials have been tested and verified to be operating correctly. Generally, there are two types of commissioning: process and technical. Process commissioning relates to project management by ensuring the designers and contractors followed the owner's requirements and code specifications. However, measurements are not used to prove code compliance or if the systems are functioning correctly. This thesis focuses on technical commissioning (Figure 1.1) which ensures that all building systems function properly based on inspections and physical testing. Technical commissioning can be classified into four types (AECOM 2010):

- *Initial commissioning* is applied after a building is finished construction;
- *Ongoing commissioning* is realized after initial commissioning to continuously monitor and optimize performance;
- *Retro*-commissioning is implemented in an existing building in which the commissioning process was not applied or when documentation is missing;
- *Re-commissioning* is performed sometime after initial commissioning or retro-commissioning to verify and improve performance.

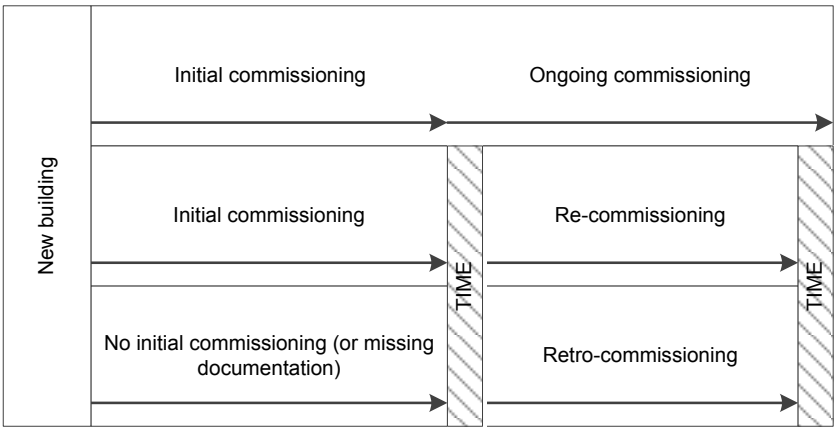


Figure 1.1 Technical commissioning (Based on AECOM 2010)

Commissioning is a general term that involves many different procedures. For example, buildings can be benchmarked using metrics to measure performance relative to other metrics and buildings. It can involve fault detection and diagnosis (FDD) to determine if and where a fault has occurred in a system. It also utilizes techniques such as demand response aiming to reduce or shift a building's load during peak electricity production. Optimizing the control systems and set points can also be used to maintain top performance. In addition, simple or complex models can be used to identify energy efficiency measures (EEMs).

Commissioning is proven to be effective at improving energy performance. The Texas LoanSTAR program provides low interest rate loans for energy related cost-reduction retrofits in public institutional buildings (Turner et al. 1998). The program began in 1988 and has resulted with a total of $395 million in loans and cumulative

energy savings of $419 million (SECO 2014). The loans are repaid using energy cost savings realized from commissioning. In Canada, BC Hydro's Continuous Optimization Program applied re-commissioning to 296 buildings resulting in an average energy cost savings of 8.9% and a simple payback of 1.6 years (BC Hydro 2014).

Applying the commissioning process to an existing building consists of three levels (Thumann and Younger 2008) that increase with complexity, time, and cost:

- *Level 1−Walkthrough Audit:* visually inspect the energy systems and evaluate whole-building electricity and/or fuel use;
- *Level 2−Standard Audit:* quantify energy losses through short-term measurements and simplified engineering calculations with utility bills;
- *Level 3−Building Simulation:* create a detailed building energy model to perform commissioning.

Building performance simulation software is one of the most promising and powerful tools to assist in the commissioning process. A computer simulation model of a building often has the capacity to provide guidance when applying all of the commissioning services mentioned earlier.

### *1.3 Building Simulation*

The first building simulation tools were developed in the 1960s (IBPSA-USA 2014). They have since evolved into detailed whole-building energy simulation tools that model the complex non-linear, dynamic, and interactive phenomena that occur in buildings. Oh (2013) provides a comprehensive history of the evolution of models used to simulate buildings. Current software can model a building's heating and cooling loads (e.g., solar gains, thermal response, envelope thermal resistance, lighting, equipment, and occupants), systems (e.g., air handling units (AHUs), heating and cooling coils, heat recovery, fans, heat pumps), and plant (e.g., boilers, chillers, cooling towers).

Some examples of commonly used detailed hourly/sub-hourly whole building energy simulation programs are DOE-2, EnergyPlus, Esp-r, and TRNSYS. eQUEST (the quick energy simulation tool) is a popular program in Canada and the USA that is based

on DOE-2. Crawley et al. (2008) provide a comparison of many building energy programs developed over the last 50 years.

In general, there are two methods used to model the performance of buildings:

(1) *Black-box*: also known as inverse or data driven modelling, is completely empirical and uses mathematical and statistical (e.g., multi-variable regression, artificial neural networks, etc.) to relate measured inputs to outputs;

(2) *White-box:* also known as forward, based on first principles (e.g., heat and mass transfer).

Black-box models are easy to create given measured input and output data. Black-box models have the capacity to identify simple EEMs whereas white-box models offer much more flexibility when evaluating EEMs. White-box model flexibility is the main reason they are used in building energy simulation programs. White-box models are difficult to create because they require a large number of inputs which are not often available and/or are very difficult to measure. Inputs refer herein to information entered into a model and outputs to information extracted from simulation results. White-box models of existing buildings are typically underdetermined (i.e., there are many more uncertain than certain inputs) (Sun and Reddy 2006). Thus, modelling an existing building using the white-box method requires the model to be calibrated. Calibrating a model refers to tuning inputs until simulated and measured energy use or other variables (e.g., fluid temperatures or flow rates) match with acceptable accuracy.

### *1.3.1 Calibrated simulation*

A calibrated building energy model is a powerful tool that can create benchmarks for operation, perform fault detection and diagnostics (Bynum et al. 2012; O'Neill et al. 2014), and identify EEMs such as optimal control of building energy use and demand response (Lavigne et al. 2014).

The tuning processes in many calibration methods are heuristic, relying heavily on analyst experience (Reddy 2006). There are no standard methods for calibrating building energy models (Reddy 2006; Coakley et al. 2014) which may result in modellers

using different combinations of inputs to achieve a calibrated model. This is another property of underdetermined models Inputs tuning is heuristic because the most commonly available energy use data is whole-building utility bills resulting in many uncertain inputs related to a building's loads and HVAC systems. Models created using only whole-building data are highly susceptible to offsetting errors occurring at sub-utility levels in the model (Gestwick and Love 2014).

Throughout the three decades of research into calibrated simulation, the basic issues with underdetermined models remain. One approach to overcome this issue is to increase the amount of measured data used in the model creation. Building automation systems (BASs), which are common in many commercial/institutional buildings, record trend data that can increase the number of available inputs used in models. Trend data herein refer to measurements recorded in a BAS.

### *1.4 BASs*

A BAS, building management system (BMS), or building automation and control system (BACS) are computerized systems used to monitor and control building services such as room air temperature and humidity, HVAC systems, security, and lighting, etc. Their names may be different but they perform the same task. Buildings may also have automated energy management systems, referred to as energy management control systems (EMCSs), building energy management systems (BEMSs), or energy information systems (EISs), which focus on monitoring energy use. In some cases an EIS monitors only whole-building electricity use (Motegi et al. 2003). These are normally considered to be part of a BAS (Wang 2010). BAS is used herein to describe these systems.

BASs were first introduced into buildings in the 1960s and have since greatly advanced. Today they contain microprocessors, graphical user interfaces (GUI), wireless communication, and are highly flexible in creating custom control functions with high-level-language programming (e.g., C, Fortan, etc.) and proportional-integral-derivative control functions (Wang 2010). Their system architecture typically consists of management, automation, and field levels (Figure 1.2), as described in Wang (2010). The connections between levels can be web-based, wireless, or hard-wired. Field control

stations provide the interaction between sensors and actuators, often controlling room conditions. For example, a field control station regulates the supply air flow rate passing into a room to keep the room's air temperature at set point. The field network allows communication between multiple field control stations. For example, this is used to control the plenum return/exhaust air flow rate based on the sum of supply air flow rates required in many rooms.

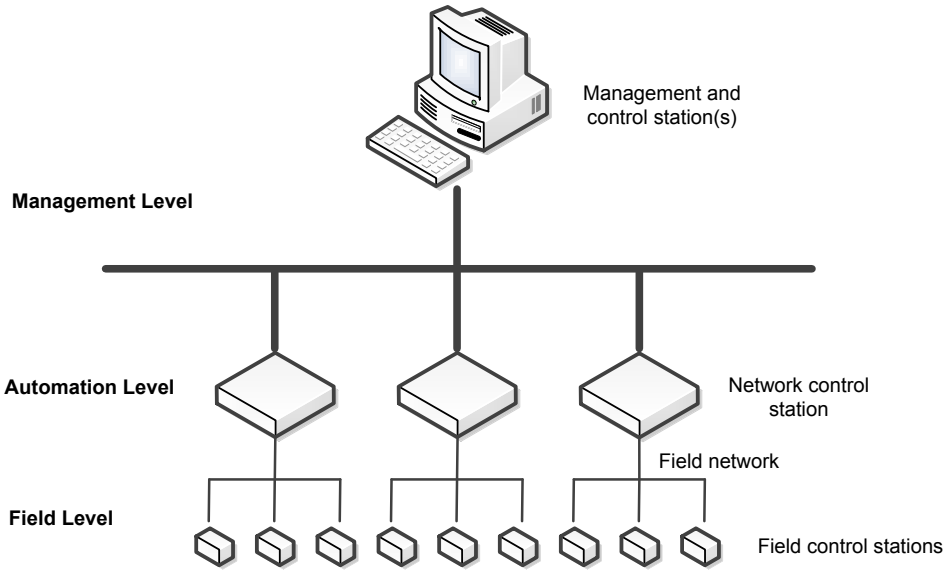


Figure 1.2 Typical BAS architecture

The network control stations at the automation level have higher storage capacity and processing speed than the field controllers. For example, they are used to control the AHUs, which need to communicate with all field controllers to determine supply/return air flow rates. The network control stations integrate the field control networks at the management level.

The management level includes computers to provide data storage, central management, and GUIs for operators. They have the capacity to generate reports, format data, create trend data graphics, and store trend data. The management level can also be remotely monitored and controlled.

Typical trend data include temperature, humidity, valve and damper positions, on/off control signals, and air flow rates; rarely are thermofluid flow rates and sub-hourly electric demand available. Data logging is a common feature of BASs at no additional

hardware cost (Friedman and Piette 2001). The number of BAS sensors in buildings is very large and manual commissioning demands intensive labour (i.e., cost) and, therefore, automatic tools using trend data to aid in the commissioning process are preferred (Xiao and Wang 2009). The computing power and wireless capacity of technology has made BASs economical and feasible for widespread adoption in buildings but trend data they record are rarely used effectively to maintain optimal energy performance. Currently, BASs perform poorly when diagnosing HVAC faults (Djuric and Novakovic 2009) yet are essential to provide data for commissioning.

### *1.5 Problem Statements*

Chapter 2 provides a literature review summarizing the existing methods and use of trend data in calibrated simulation. Two problem statements were identified:

*(1) Current calibrated simulation methods are highly susceptible to offsetting errors occurring at sub-utility levels when using only whole-building utility data (Gestwick and Love 2014);*

*(2) Trend data are rarely used effectively in calibrated simulation.*

### *1.6 Research Questions*

Research questions addressing the problem statements are listed below:

*(1) How can a bottom-up calibration method, where the zone, system, plant, and whole-building level models are sequentially calibrated, reduce offsetting errors at sub-utility levels?*

*(2) How can calibrated simulation be improved using an automatic tool coupling trend data with detailed building simulation software?*

### *1.7 Thesis Structure*

The following chapters are structured as follows:

- Chapter 2 reviews calibration methods in the literature;
- Chapter 3 defines the bottom-up calibration method and describes a case study university research center to which it is applied;

- Chapter 4 describes a tool used to automatically couple trend data with ongoing-commissioning and calibrated simulation;
- Chapter 5 describes the initial building energy model and performs trial application of the bottom-up method to a shoulder season;
- Chapter 6 applies the bottom-up method to calibrate heating seasons;
- Chapter 7 concludes the thesis and discusses future work.

# 2 Literature Review

The earliest studies on calibrating building energy models began in the early 1980s (Diamond and Hunn 1981). Over the past three decades there have been many advances in computing, building energy simulation programs, and calibration methods to generate increasingly detailed and accurate calibrated models. Reddy (2006) and Coakley et al. (2014) recently created comprehensive literature reviews. This chapter reviews, compares, and analyses current calibration methods and summarizes how trend data is currently used in the literature.

## *2.1 First Calibration Methods*

The first calibration studies (Diamond and Hunn 1981; Haberl and Claridge 1985; Heidell & Taylor 1985; Jamieson & Harding 1989; Carrabott 1989; Carroll et al. 1989; Kaplan et al. 1990, Norford et al. 1994; Zmeureanu et al. 1995) all used similar calibration methods. They consisted of approximately three iterative steps: (1) entering inputs, as detailed as warranted, into a building energy model, (2) comparing the measured data to the simulated data, and (3) using experience and occasionally additional information to modify the uncertain inputs until the simulated and measured end-use matched.

One of the first new methods to appear was the primary and secondary terms analysis and renormalization (PSTAR) (Subbarao 1988). The method used short-term measurements and renormalization with linear equations to estimate the heat flow through the envelope allowing the model to estimate annual energy performance of single family dwellings. Short-term, computer-controlled, intrusive measurements were implemented to control the heating system in order to keep the room temperature constant and therefore to estimate the heating load. A blower door or trace gas test was also used to estimate envelope air infiltration.

In addition to a method resembling that in the earliest studies, Kaplan et al. (1990) applied measured on-site weather data when calibrating a building energy model. They also recommended tuning during periods that occur during a hot, cold, shoulder seasons

with two daytypes and suggested a tuning strategy during calibration similar to the bottom-up method:

(1) Correct obvious simulation errors;
(2) Tune the internal end-uses that are likely to contribute the most to HVAC loads on a zonal basis;
(3) Adjust inputs affecting HVAC energy use;
(4) Tune on a whole-building end-use basis;
(5) Compare the measured and simulated annual end-use performance.

A procedure to calibrate whole-building non-weather-dependant energy use was developed by Bronson et al. (1992) using a graphical procedure and day-typing. Three-dimensional figures were plotted using the hour, day, and non-weather-dependent electricity load to aid in the calibration process. The plots also displayed hourly differences in the model over the measured data period to identify when large differences occurred to help identify where further tuning was required.

Carroll and Hitchcock (1993) describe a method to systematically tune inputs using an optimization approach where selected inputs were tuned until the differences between simulated and measured outputs were minimized. They questioned the existence and uniqueness of calibrated models because it was likely that different combinations of tuned inputs could produce a calibrated model (i.e., underdetermination). The inputs chosen to be varied were heuristically selected.

Clarke et al. (1993) proposed a classification system consisting of four general calibration methods: (1) informative graphical methods, (2) special tests, (3) manual, iterative, and heuristic methods, and (4) analytical methods of calibration. The same classification system was adopted in Reddy's (2006) literature review. Coakley et al. (2014) extended the classification to consider methods be either manual and automated or only automated. The following review discusses the calibration methods using the classification described by Clarke et al. (1993).

### *2.1.1 Comparative graphical methods*

Expanding the method of Bronson et al. (1992), Bou-Saada & Haberl (1995) introduced the use of box-whisker-mean (BWM) plots which display the $10^{th}$, $25^{th}$, $75^{th}$, $90^{th}$ percentile points, maximum, minimum, mean, and median for data bins. BWM plots helped statistically characterize scatter plots and allowed clear comparison when superimposing measured and simulated data bins. Scatter and BWM graphs were plotted for 24-hour temperature day-type bin analysis. They also developed 52-week binned box-whisker mean plots. These plots were superimposed for comparison to aid in the calibration process.

### *2.1.2 Special tests*

Subbarao's (1988) method gave rise to the special tests and analytical procedures. Katipamula & Claridge (1993) used the simplified energy analysis procedure (Knebel, 1983) and developed a calibration method where simulated daily cooling loads and residuals were plotted against outdoor dry-bulb temperature. This allowed them to identify weather-dependant parameters that required further measurement or adjustment in order to minimize residuals.

Soebarto (1997) developed a calibration method using two to four weeks of hourly monitored data along with monthly utility records. On-off tests were used to measure the power density of the weather-independent loads. This was used to determine the lighting and receptacle gains without having to measure each fixture. The result of the study showed that short-term measured data were sufficient to calibrate models to monthly utility records. Liu & Claridge (1998) expanded the method developed by Katipamula & Claridge (1993) and applied it to a two-zone (interior and exterior) model. Their process also helped identify parameters to optimize HVAC systems and identify HVAC faults.

Wei et al. (1998) analysed the heating and cooling loads associated with typical AHUs through the use of characteristic signatures and calibration signatures. A characteristic signature, which was similar to sensitivity analysis, was a plot defined by the ratio of the changes in energy consumption to the maximum baseline energy

consumption when one parameter was changed in a baseline model (eq. 2.1) (Wei et al. 1998).

$$characteristic\ signature = \frac{\Delta\ energy\ consumption}{maximum\ energy\ consumption} \times 100\% \qquad \text{eq. 2.1}$$

A calibration signature was defined as the difference between measured and simulated energy consumption divided by the maximum measured energy consumption (eq. 2.2) and was normally plotted against the outdoor air temperature (Liu et al. 2003). Calibration and characteristic signatures offered a visual technique to aid analysts in making quick and appropriate decisions when choosing which weather-dependant inputs to tune during calibration. For example, if the calibration and characteristic signature shapes match for a certain variable, then the analyst has identified which variable may be causing the residual and should be tuned or measured.

$$calibration\ signature = \frac{measured - simulated}{maximum\ measured} \times 100\% \qquad \text{eq. 2.2}$$

Liu, G & Liu, M (2011) expanded the method developed by Wei et al. (1998) to calibrate an HVAC system using a two-zone model with two weeks of hourly heating and cooling data. Kandil & Love (2013) applied the signature analysis calibration method (Liu et al. 2003) with short-term data (hourly for electricity and weekly for natural gas). They first modified weather independent errors, used the calibration signature method to modify weather-independent parameters, and then adjusted the weather-independent factors affecting electric demand using hourly data. This was one of the first calibration studies to use field data from a building with combustion-based heating, which introduces further complexities in modelling the energy conversion process (e.g. most boiler models are based on steady state lab conditions).

### *2.1.3 Manual procedures*

Pedrini et al. (2002), Carling et al. (2003), Tamburrini et al. (2003) and Hubler (2010) used similar three step methods based on earlier iterative methods (Section 2.1). Expanding earlier iterative methods, Yoon et al. (2003) estimated a building's base electricity consumption by plotting it against outdoor temperatures. The base load was

considered when cooling loads were minimal to verify the internal gains. Their model took 17 person-days to calibrate. Westphal and Lamberts (2005) used sensitivity analysis to identify influential inputs affecting heat gains and losses which were iteratively tuned to produce a calibrated model.

Monfet et al. (2009) calibrated AHU supply airflow rates and estimated cooling coil loads using measured data for the cooling season and the shoulder season when there was minimal cooling. This was one of the first calibration studies that focused on calibration at the sub-utility level.

Raftery et al. (2011) developed a method that utilized version control software to record the inputs tuning procedure. Their aim was to add rigor and transparency to previous heuristic tuning procedures because Reddy et al. (2006) noted that many studies failed to report the inputs tuned and the information/sources used. A data source hierarchy was introduced where data sources were ranked in terms of their accuracy and reliability. For example, measured data were ranked more reliable than information found in design documents. This focused the analysis on tuning inputs using data ranked most reliable from evidence.

Monfet and Zmeureanu (2013) showed that it was possible to calibrate a central plant model using measurements and manufacturers' data without tuning by trial-and-error and using stochastic methods. They also pointed out differences between quasi-steady state models of chillers and the measured transient performance.

Mihai (2014) calibrated a research center model using a bottom-up method with trend data for a cooling season. She calibrated the zone level first using the zone supply air flow rates before sequentially calibrating the AHU air flow rate, supply air temperature, and cooling coil load.

### *2.1.4 Analytical procedures*

Liu & Henze (2005) expanded the optimization approach (Carroll & Hitchcock 1993) using system identification to select initial inputs affecting the cooling load. These inputs were optimized to minimize the residuals for measured and simulated energy use. The optimization process continued by varying inputs related to the capacities, efficiencies, and part load performance of the building energy system.

Sun & Reddy (2006) developed a methods with four steps: (1) the analyst heuristically determined a set of influential inputs and estimated their range of variation; (2) a Monte Carlo coarse grid search determined the most influential inputs; (3) a finer grid search was used with the selected inputs from step three; and (4) an uncertainty analysis was used to determine the uncertainty of the calibration process. Reddy et al. (2007a; 2007b) expanded their method by creating a small set of the most feasible calibrated models instead of choosing only one optimal solution to address the issue of input combinations with underdetermined models.

Heo et al. (2012) developed a simplified method using normative models with a statistical Bayesian which used inputs uncertainty in the energy simulation model, differences between measured and simulated building behaviour, and observational errors.

Gestwick and Love (2014) undertook a trial application of Sun & Reddy's (2006) method. Manual generation of simulation model variations produced 27 models that were considered calibrated in terms of whole-building electricity use. No model was found that met the goodness of fit criteria for both electricity and gas. One likely cause was the steady state lab-based models for condensing gas boilers.

The optimization approach using GenOpt was also integrated into ExCaliBEM (Sansregret et al. 2014) which provided a GUI that was compatible with DOE-2 and EnergyPlus.

### *2.2 Statistical Indices Comparing Simulations to Measurements*

The most common measure of the representativeness of a simulation model is the ASHRAE Guideline 14 (2002) goodness-of-fit criteria mean bias error (MBE) (eq. 2.3) and the coefficient of variation of root-mean-squared error (CV(RMSE)) (eq. 2.4 and eq. 2.5). MBE indicates the degree of spread between measured and estimated values, for the period of interest. The CV(RMSE) quantifies the match while accounting for offsetting positive and negative errors. Guideline 14's maximum MBE and CV(RMSE) for hourly data are 10 and 30%, respectively. If monthly data were used the MBE and CV(RMSE) criterion change to 5 and 15%, respectively.

$$MBE = \frac{\sum_{i=1}^{n}(\hat{x}_i - x_i)}{\sum_{i=1}^{n} x_i} \quad \text{eq. 2.3}$$

$$RMSE = \sqrt{\frac{\sum_{i=1}^{n}(\hat{x}_i - x_i)^2}{n}} \quad \text{eq. 2.4}$$

$$CV(RMSE) = \frac{RMSE}{\bar{x}} \quad \text{eq. 2.5}$$

*where:*
$x$ = sampled data
$\hat{x}$ = simulated data
$\bar{x}$ = mean of the sampled data
$n$ = sample size

Guideline 14 fails to provide an analytical basis for the numerical values in these tolerances (Reddy et al. 2007). Kaplan et al. (1990) suggested that it may be impossible to justify a specific tolerance to determine when a model was considered calibrated. Reddy et al. (2007) discussed how the CV(RSME) may not be an appropriate measure for the tolerance because, as more measurements are used, the CV(RMSE) will be reduced to a level below the uncertainty of the measurement devices.

Reddy et al. (2007) proposed an aggregated index using the MBE and CV(RMSE) in terms of heating energy use and whole-building electricity use and demand. It should be noted that model fit with peak demand in the calibration process was typically omitted in the literature with Soebarto (1997) and Zmeureanu et al. (1995) as the only papers found that addressed this.

Another approach (Mihai and Zmeureanu 2013) used paired difference hypothesis testing. The test determined if the absolute difference between measurements and simulations were statistically significant, in which case the model was determined calibrated. The benefit of using this approach was the inclusion of measurement uncertainty when evaluating whether a model was calibrated or not.

## *2.3 Use of Trend Data in Ongoing Commissioning*

Trend data in ongoing-commissioning was researched and developed over the past 15 years with a large focus on fault detection and diagnosis (FDD) (Brambley et al. 1998; Katipamula et al. 1999; Norford et al. 2002; Sellers 2003; Wang and Xiao 2004; Brown et al. 2006; Tremblay and Zmeureanu 2014). The authors found that BASs were practical and cost-effective to providing the necessary data to conduct these studies.

Friedman and Piette (2001) compared manual and automated FDD tools using HVAC trend data. They noted that one of the advantages of these tools was their capacity to reduce data management and analysis time to obtain information from trend data. Piette et al. (2001) developed a prototype system using dedicated sensors, data acquisition software and hardware, and data visualization software including a web-based remote system. Their system included sensors that were not available in common BASs. They used their system to identify control problems and faults specific to HVAC systems. Seidl (2006) documented his experience troubleshooting control systems using trend data. He calculated how much a trend point deviated from its set point or from a benchmark to determine which trend points might have experienced a fault.

NRCan developed the Diagnostic Agent for Building Operation (DABO) that integrates with existing BEMS to aid in automating ongoing commissioning (Choiniere 2008). DABO automatically analyses trend data to identify faults using a rule-based reasoning module. It also provides suggestions to improve performance (semi-automatically) and generates energy and comfort profiles.

Katipamula and Brambley (2005) stated that trend data are not widely used in industry because FDD is rarely built into BASs and there is a lack of infrastructure to gather data from existing BASs for add-on applications. This may be the case with older BASs but new BASs often have the capacity for storing data. Increasing the automation of FDD methods with BASs was strongly advocated (Norford et al. 2002; Roth 2005; Xiao and Wang 2009).

### *2.3.1 Use of trend data in calibrated simulation*

This section summarizes studies that used trend data and how the trend data benefited the calibration. Use of trend data in calibration was first reported by Carling et al. (2003).

The trend data they used included BAS set points and control signals, submetered electricity, air temperatures in the AHU and zones, and slab temperatures. They identified multiple faults that might have been missed without trend data. Trend data has been used more frequently in calibrated simulation in recent years.

Monfet et al. (2009) used trend data to calibrate AHU supply air flow rates and supply and return air temperatures before calibrating the estimated cooling load of the building. They also used supply and return temperatures for hot and chilled glycol to generate inputs for the model. They noted that trend data revealed operational faults and improved their initial input file.

Pang et al. (2012) used trend data to create inputs for use in modelling an already calibrated model in real-time. Their model was calibrated in a previous study (Eisenhower et al. 2012) using trend data from lighting and AHU operation schedules. The study did not detail how the trend data were used in the calibration.

Gestwick & Love (2014) used trend data to estimate lighting, equipment, and fan schedules and compared hourly plant heating load trend data to simulation outputs. They noted that offsetting errors would likely have occurred if hourly plant heating load trend data were unavailable due to limitations with a boiler model in DOE-2. These errors may have led to erroneous tuning between boiler efficiency and heat recovery effectiveness. They also stated that high resolution data were crucial for understanding the performance of energy systems.

Kandil & Love (2014) used trend data to generate inputs to simulate fan and pump schedules; domestic hot water schedule and capacity; boiler efficiency; AHU air flow rate and demand; dry cooler power; electrical demand for fans, pumps, and combined lighting and equipment. They noted that hourly data were essential to reliably calibrate the model.

Mihai (2014) calibrated zones using zone supply air flow rates and indoor air temperature trend data. She modified internal gain schedules based on the estimated zone cooling loads. She then used supply air flow rates, supply and return air temperatures during the calibration of the AHUs. Trend data provided the study with sufficient information to focus the calibration on zone and system level models.

Mustafaraj et al. (2014) reported that set points, on/off values, schedules, and electrical consumption of heat pumps, coilers, pumps, underfloor heating flow rate, hot water temperatures, and room indoor air temperatures were used in their model calibration. They calibrated the indoor zone temperature, heat pump electrical demand and heat flow, total electrical, and natural gas consumption. They noted that the use of trend data improved the results of their calibration.

### *2.4 Discussion*

There was agreement (Reddy 2006; Coakley et al. 2014) that there are no general methods to calibrate building energy models. It was clear that the initial steps of calibration methods share similarities by using as much information about the building as possible from evidence (e.g., as-built drawings, site inspections, on-site weather data, short-term measurements, trend data etc.).

Overall, the iterative, pragmatic, and manual calibration methods were highly dependent on user experience and knowledge and are non-transparent due to the tuning of inputs. Raftery et al. (2011) addressed the non-transparency issues by advocating more explicit documentation of the tuning process. It was also clear that this was the most frequent method used; perhaps because it was relatively easy to implement compared to the other techniques. For example, the optimization methods require a batch program to become feasible. ExCaliBEM (Sansregret et al. 2014) had the capacity to tune inputs in order to optimize a variable's residual in DOE-2 and EnergyPlus models. However, identifying influential inputs to optimize was time consuming due to the larger parameter space and no batch programs exist, to the author's knowledge, which automatically explore this space. The signature analysis calibration method required a large set of characteristic signatures which must be either created or found in a database for similar buildings in similar climates. No batch programs are available to create characteristic signatures; to the author's knowledge, the only set of published characteristic signatures was in Liu et al. (2003).

The analytical methods approached calibration as an optimization problem. They had the capacity to produce a set of calibrated models using various combinations of tuned parameters. This addressed the underdetermination problem associated with

calibrated models but there have been no examples of use of multiple calibrated models (e.g., stochastically) in ongoing commissioning. Identifying influential inputs and the optimization process can be time consuming depending on computing power and model complexity.

The main advantage of the signature analysis method is that it can guide the analyst to determine the input generating a certain weather-dependant residual. While the signatures can identify an input causing a residual, this does not guarantee that the parameter will be tuned to the correct value. Another issue with this technique is that the analyst may be unsure which inputs to tune if two or more characteristic signatures appear similar to the calibration signature. Certain characteristic signatures may be caused by a combination of characteristic signatures that offset or complement each other.

ASHRAE Guideline 14 (2002) was used to determine when a model is calibrated in terms of energy use. There are currently no recommended criteria for other variables such as temperature and air flow rates.

There is currently discussion regarding simplified versus detailed models for calibration. Heo et al. (2012) showed that simplified models could be as accurate as detailed models at the whole-building level. However, Raftery et al. (2011) argued that simplified models could not represent energy efficiency measures at the zone, system, and plant levels. Raftery et al. (2011) and Kandil & Love (2013) showed that sub-monthly sub-utility measurements revealed substantial calibration errors would have occurred if only monthly utility data had been used. Gestwick & Love (2013) found substantial discrepancies between measured and simulated heating plant performance which could have led to erroneous tuning (e.g., heat recovery effectiveness) if plant level measurements were unavailable.

It is clear that trend data can provide many more measurements than is used in the majority of studies in the past three decades; however, trend data quality has often been questioned in terms of accuracy. The use of dedicated and calibrated sensors is expected to provide higher quality data than those installed in BASs. Haves et al. (1996) listed the main issues with sensors: improper positioning, inadequate calibration during commissioning, and drift during operation. In addition to this, Torcellini et al. (2006, p.

102) noted "with current EMS [energy management systems] and building automation systems there appears to be a low probability of obtaining contiguous error-free, measured data sets over a very long period." Torcellini et al. (2006) recommended dedicated systems for sub-utility monitoring but this presents challenges in terms of additional cost and complexity.

Raftery (2011, p. 128) notes, "Even if the measured end-use data … were available, it would still be difficult to calibrate a model in a cost-effective and timely manner." Coakley et al. (2014) reported a lack of integrated tools to assist in calibration. It is expected that the time using trend data in calibration would be much larger compared with existing methods. Automatic tools integrating trend data with building simulation software may reduce the time but do not exist.

The trend data used in the literature (Section 2.3.1) was most often collected for the HVAC systems with only some studies using zone level trend data (Carling et al. 2003; Kandil and Love 2014; Mihai 2014; Mustafaraj et al. 2014; Zibin et al. 2014). In many studies it was not clear how the trend data were used during the calibration process. It was often unclear how inputs were generated from trend data and entered into the model. For example, trend data has bias and random errors which often create a cloud of points. It was often never explicitly stated whether the input values were approximated based on inspection or quantified using mathematical/statistical techniques. It was also uncertain if the trend data for use in calibrated simulation was being used to its full potential. There is clear disconnect between building simulation software and BASs.

Overall, the majority of calibration methods use a top-down approach with deductive reasoning, assuming that if the whole-building level model is calibrated, then the sub-utility components are likely to be calibrated. These methods are highly susceptible to offsetting errors occurring in the thermal zones, HVAC systems, and plant models. It is also clear that trend data is not currently used to its full potential in calibrated simulation. Section 1.5 summarizes two issues with calibrated simulation identified in this literature review.

# 3 Method

This chapter proposes a new method to calibrate building energy models. The chapter starts with a general description of the new method. This is followed by the description of a case-study building that the method is applied to. Next, the application of the method to the case study building is described in detail. The chapter ends with a discussion of the bottom-up method, compares it to previous methods, and describes its limitations.

## *3.1 Bottom-up Calibration*

This thesis proposes a bottom-up calibration method, which sequentially calibrates the zone, system, plant, and whole-building level models (Figure 3.1). The bottom-up method relies on inductive reasoning based on evidence from measurements to show that if these models are calibrated, then the model is likely to be a good representation of the building. Another reason for using a bottom-up method is that buildings are designed, operated, and modelled in an upward nature. For example, a building's loads are used to size HVAC equipment and determine the HVAC system response in modelling and physical operation. The approach can be applied to the majority of all detailed building simulation software such as DOE-2, EnergyPlus, etc.

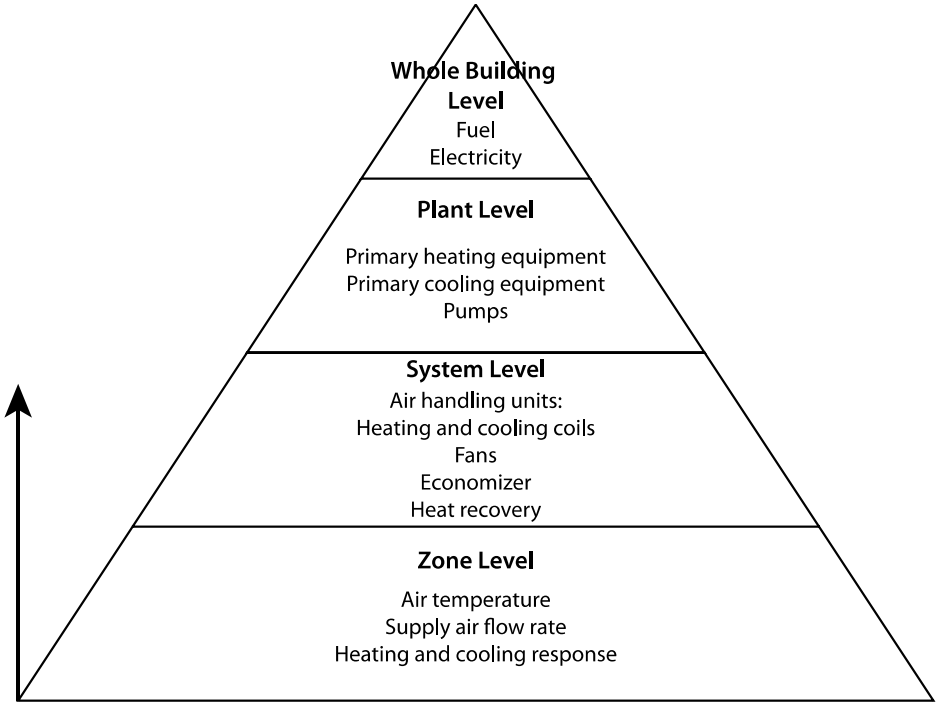


Figure 3.1. Building energy model thermal and spatial hierarchy

A detailed building simulation model can be calibrated at various stages of detail: zone, system, plant, and whole-building levels (Figure 3.1). A similar classification system was proposed by Maile et al. (2012). The zone level consists of thermal zones, which are user-defined control volumes of spaces grouped together based on space function, proximity to the exterior, orientation, and space conditioning method. Zones experience loads from equipment, lights, occupants, infiltration, envelope heat transfer, solar gains, and thermal capacity.

A flow chart describing the general bottom-up calibration procedure is shown in Figure 3.2. The first step in the method develops the initial model using as much information as warranted and removing model errors, similar to many calibration methods. The tuning procedure in bottom-up calibration includes four main steps, depending on available measurements once the initial model is created:

(1) Zone level model calibration is addressed first, including indoor air temperatures, supply air flow rates, and zone heating and cooling system response;
(2) System level model (e.g., AHU) such as air side systems (e.g., supply, mixed, return, exhaust air temperatures and flow rates; electric fan power; economizer position; heat recovery heat flow rates and effectiveness, heating and cooling coil heat flow rates) and water-side systems (e.g., thermofluid temperatures and flow rates);
(3) Plant level model includes primary equipment (e.g., boilers, chillers, cooling towers, pumps, etc.) heat flow rates, part-load ratios, and electric input;
(4) Whole-building level model including electricity and fuel utility data.

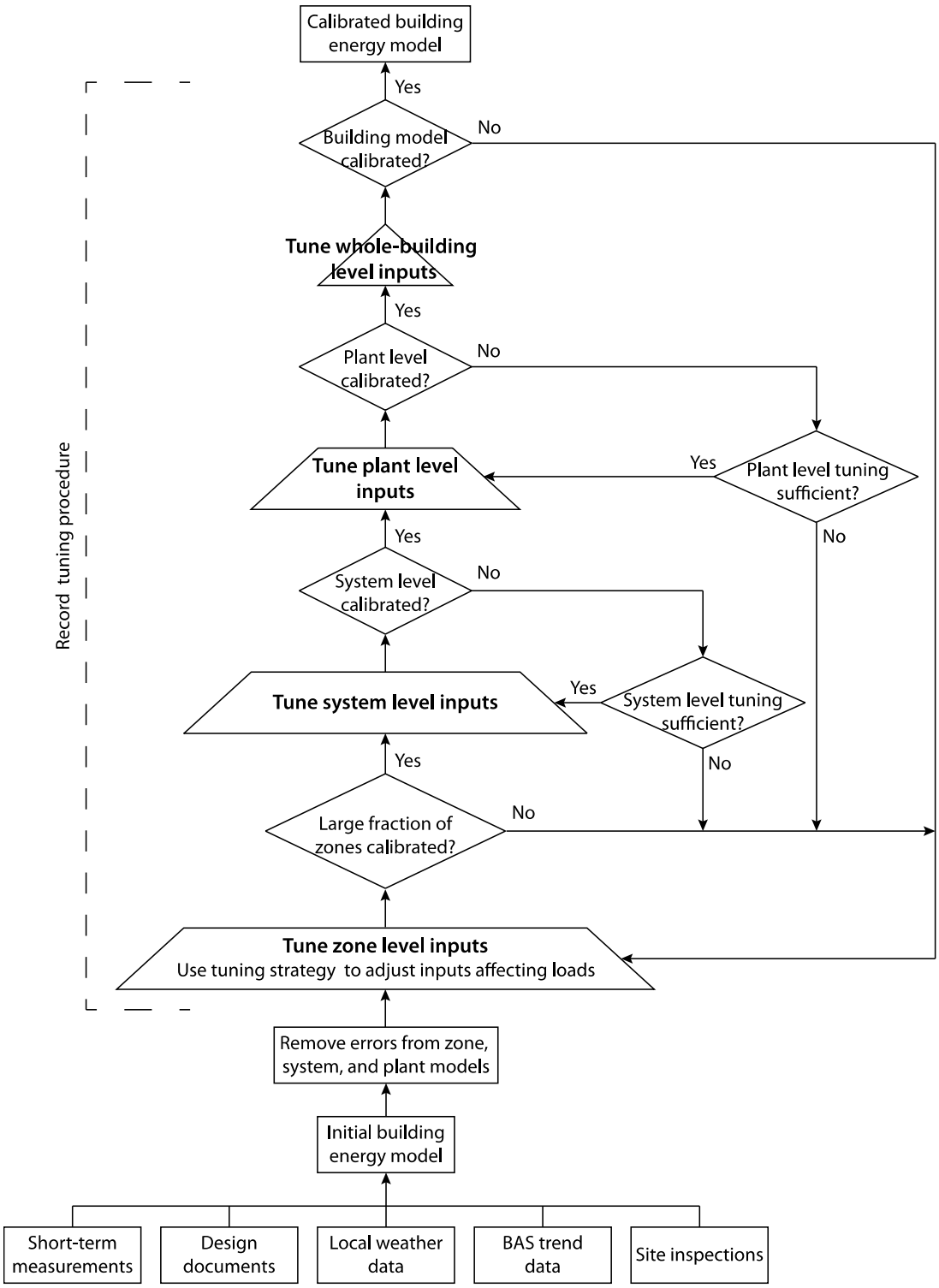


Figure 3.2 Bottom-up calibration flow chart

The number of candidate measurement points required to execute bottom-up calibration is very large. Trend data are essential to enabling bottom-up calibration

because they have the capacity to contain information pertaining to each model level. Short-term measurements can also be implemented in the approach to supplement any missing influential information.

### *3.1.1 Development of the initial model*

As shown in Figure 3.2, the development of the initial model begins by collecting as much information about the building as possible. Sources of information included design documents, local weather data, trend data, site inspections, and short-term measurements. Raftery et al. recommended the following hierarchy of data quality reported:

(1) Data-logged measurements;
(2) Spot or short-term measurements;
(3) Direct observation (site surveys);
(4) Operator and personnel interviews;
(5) Operation documents (e.g., operations and maintenance manuals);
(6) Commissioning documents (e.g., as-built drawings);
(7) Benchmark studies and best practice guides;
(8) Standards, specifications and guidelines;
(9) Design stage information.

#### 3.1.1.1 Weather data

Actual meteorological year (AMY) weather data collected nearby should be used when possible. Services exist such as SIMEB (2013), which provides free AMY weather data for over 80 locations in Quebec and Weather Analytics (2014), who charge for AMY weather data available around the world. Outdoor weather trend data recorded on-site or nearby should be used to replace the values in the weather file when possible to provide site-specific conditions which may be slightly different than where recorded (e.g., due to the urban heat island effect and shading from nearby trees and buildings).

#### 3.1.1.2 Use of trend data

Using trend data in calibration greatly increases the number of inputs and data available for comparison with simulation outputs. Trend data can provide only some of the

required inputs. There are still many phenomena that may be highly influential in energy use, such as occupant heat gains, air infiltration, and envelope and foundation heat loss/gain, but are particularly difficult to measure on an ongoing basis. Lighting and equipment loads are rarely sub-metered (Haves et al. 2001), and occupant loads are very difficult to measure even if time clock or security card records are available, especially at the zone level. Using trend data enables one to focus the tuning on uncertain and difficult to measure inputs related to zone loads.

#### 3.1.1.3 Design documents and site inspection

Design documents often contain information related to HVAC system design performance, duct placement, envelope constructions, and BAS sensor type and placement, all of which can be used to create the initial model. When projects are owner occupied, they may also contain floor layouts and geometry which should be used for zone-typing.

Site inspection is necessary to compare the information in design documents to the completed building. The site inspection should include a walkthrough for visual inspection of the HVAC systems and interviews with the building energy manager. It also provides an opportunity to compare sensor locations in design documents and the BAS GUI to the physical sensor locations in the building.

#### 3.1.1.4 Short-term measurements

Short-term measurements should be used to supplement any uncertain variables that are influential to energy use. These may also be used to verify the quality of questionable trend data. Examples include submetering thermofluid flow rates, electrical power panels, and fan and pump power.

#### 3.1.1.5 Tuning vs. removing model errors

In this thesis, tuning refers to adjusting inputs that are uncertain or when differences between model and field performance exist due to modelling assumptions and limitations. There may also be cases where the building simulation software responds differently than expected. These must be identified at all building levels before calibration begins. For

example, the system level may not be producing a reasonable supply air temperature which will directly affect tuning the internal loads at the zone level. Thus, it is especially important that system level air and thermofluid temperatures be reasonable values before model calibration begins. Zone level calibration begins once key model errors are fixed and removed.

### *3.1.2 Zone level Calibration*

A simplified energy balance at the zone level (eq. 3.1) describes a zone's loads and system response (i.e., VAV reheat) ignoring baseboard heaters. Zone loads consist of gains and losses (Section 1.3) in combination with the thermal lag caused by the thermal capacity of the room (e.g., floor, walls, ceiling, and furniture). A zone's HVAC response (eq. 3.2) provides the heating or cooling required to keep the zone at its thermostat temperature.

$$\dot{Q}_{zsys} + \dot{Q}_{zload} = C_{air} \frac{\partial T_z}{\partial t} \qquad \text{eq. 3.1}$$

$$\dot{Q}_{zsys} = V_{zs} \rho_{air} c_{p_{air}} (T_{zs} - T_z) \qquad \text{eq. 3.2}$$

*where:*

| | | |
|---|---|---|
| $\dot{Q}_{zsys}$ | = | zone heating/cooling system response |
| $\dot{Q}_{zload}$ | = | sum of zone loads at a time |
| $V_{zs}$ | = | zone supply air flow rate |
| $T_{zs}$ | = | zone supply air temperature |
| $T_z$ | = | zone indoor air temperature |
| $C_{air}$ | = | Zone air thermal capacity |
| $t$ | = | time |

BASs provide the trend data to characterize $\dot{Q}_{zsys}$ (e.g., $T_z$, $V_{zs}$, and $T_{zs}$). Once $\dot{Q}_{zsys}$ is calculated the lumped behaviour of the zone's loads and thermal lag are certain. What remains uncertain are the contribution of the many individual loads and the associated thermal lag. The calibration begins at the zone level where inputs affecting zone loads (e.g., U-value, air infiltration, and internal gains) are tuned until $T_z$, $V_{zs}$, $T_{zs}$, and $\dot{Q}_{zsys}$ simulations and trend data are calibrated.

Different combinations of tuning inputs affecting loads may produce multiple calibrated zone level models. However, only a small set of these calibrated zone level models may lead to calibrated system, plant, and whole-building level models. For example, tuning occupant loads will mainly affect the plant and system level models whereas, lighting and equipment gains will affect the system and plant response and whole-building electricity use as well. This is why re-tuning zone loads may be necessary if the system, plant, and/or whole-building level models are not calibrated. If this occurs, one must sequentially re-check that all model levels remain calibrated after the zones are re-tunes, as shown in the flow chart (Figure 3.2).

A building may have a large number of zones and it is therefore unrealistic to calibrate every zone before moving to calibrate the system level. Instead, a large fraction of zones should be calibrated. One of the goals for calibrating $V_{zs}$ is to ensure that the simulated AHU $V_s$ meets the calibration criteria. A large fraction is not quantified in this thesis because it is impossible to select a value that would produce satisfactory results at the system level.

### *3.1.3 System level calibration*

If the system level $V_s$ discrepancy is too great the zone loads may have to be re-tuned to improve the model fit of $V_{zs}$ until $V_s$ meets the calibration criteria. A calibrated AHU $V_s$ is crucial to calibrating the heat recovery heat flow rate, heating coil heat flow rate, and fan power. It is also necessary to ensure that a large fraction of $T_z$ are calibrated to ensure that the return air temperature ($T_r$) in the AHUs are simulated near their trend data values.

The quantity of system level trend data available is very large. Trend data has the capacity to provide the required information to model the system level; tuning may not always be necessary. System level inputs may require tuning if differences in key equipment performance models exist or some trend data are not available. For example, heat recovery effectiveness may be poorly characterized in the simulation software and require tuning to approximate field performance.

The system level variables should be calibrated in a logical method. For example, the heating coil heat flow rate ($\dot{Q}_{hc}$) (eq. 3.3), depends on $V_s$, the temperature exiting the

heating coils ($T_{hd}$), and the mixed air temperature ($T_m$) before the heating coils. The $V_s$, $T_{hd}$, and $T_m$ should be calibrated before adjusting other inputs that may affect $\dot{Q}_{hc}$.

$$\dot{Q}_{hc} = V_s \rho_{air} c_{p_{air}} (T_{hd} - T_m) = V_{hc} \rho_{glc} c_{p_{glc}} (T_{hca} - T_{hcr}) \quad \text{eq. 3.3}$$

*where:*

$V_{hc}$ = Heating coil thermofluid flow rate
$T_{hca}$ = Heating coil supply thermofluid temperature
$T_{hca}$ = Heating coil return thermofluid temperature
$_{glc}$ = Glycol subscript

In general, the air-side components should be calibrated before the water-side components at the system level because building simulation programs often calculate air-side performance before the water-side. The water-side refers to glycol heat flow rate on the right-hand side of eq. 3.3. Plant level calibration begins once the system level model is calibrated.

### *3.1.4 Plant level calibration*

The plant level heating response is described in eq. 3.4 for an *n* number of zones. If $\dot{Q}_{hc}$ is calibrated at the system level, discrepancies may exist in the plant level heating load if $\dot{Q}_{zheat}$ was not calibrated correctly at the zone level. This could occur if the combinations of zone reheat and internal loads were initially tuned incorrectly. Another combination of zone level inputs must be re-tuned if the plant level heating load is not calibrated.

$$\dot{Q}_{plant} = \dot{Q}_{hc} + \sum_{i}^{n} \dot{Q}_{zheat_i} \quad \text{eq. 3.4}$$

$$\dot{Q}_{zheat} = V_{zs} \rho_{air} c_{p_{air}} (T_{zs} - T_s) \quad \text{eq. 3.5}$$

*where:*

$\dot{Q}_{plant}$ = plant level heating load
$\dot{Q}_{zheat}$ = zone reheat heat flow rate
$T_s$ = supply air temperature assuming negligible air temperature change in the ducts

### *3.1.5 Whole-building level calibration*

The whole-building electricity use may or may not match measurements depending on the calibration of the zone electrical loads and other equipment such as fans, chillers, and pumps etc. Therefore, the calibration at the zone, system, and plant levels may have to be revisited if discrepancies exist. The efficiency or part-load conditions of the plant may also have to be calibrated.

$$\dot{Q}_{fuel} = f(\dot{Q}_{plant}, \eta_{plant}) \qquad \text{eq. 3.6}$$

*where:* $\dot{Q}_{fuel}$ = total fuel consumption in the building
$\eta_{plant}$ = plant efficiency/part-load curve

The whole-building level fuel use should be calibrated if the plant level primary equipment are calibrated, after the zone and system performance are calibrated, and if the efficiency or part-load conditions are measured. Measuring the input-output efficiency or coefficient of performance of the primary equipment can be used to derive the part-load ratio; otherwise it may have to be tuned. Correctly characterizing plant equipment performance will directly affect the whole-building level model's fuel and electricity use.

### *3.1.6 Statistical indices for calibration*

This section addresses the calibration criteria to consider when calibrated non-energy related variables such as temperatures and flow rates. ASHRAE Guideline 14 (2002) was used in this thesis to determine when energy use and *all* other variables were considered calibrated. However, it is very likely that temperatures and flow rates must be calibrated well below the criteria. For example, $V_s$, $T_{hd}$, and $T_m$ should each be calibrated with a CV(RMSE) well below the ASHRAE Guideline 14 calibration criteria to ensure $\dot{Q}_{hc}$ has a CV(RMSE) less than 30%. It is possible that some $V_s$, $T_{hd}$, and $T_m$ values may fail to meet the calibration criteria yet offsetting errors in those variables could result in $\dot{Q}_{hc}$ considered calibrated. Therefore, it is rigorous to show that $V_s$, $T_{hd}$, $T_m$, and $\dot{Q}_{hc}$ simulation values each meet the calibration criteria.

Each variable's contribution to model residuals must be balanced. For example, the $T_{hd}$ may have a large residual relative to $V_s$ and $T_m$. Therefore, the $V_s$ and $T_m$ must have a relative small residual to compensate

### *3.2 Case Study Building Description*

The test study building for the thesis research was the Research Centre for Structural and Functional Genomics, referred to herein as the Genome Building (Figure 3.3 to Figure 3.5), located on Concordia University Loyola campus in Montreal, Quebec, Canada. This section presents an overview of the building's enclosure and the heating, ventilation and air-conditioning (HVAC) systems.

The Genome Building has a floor area of 5,400 $m^2$, consisting of 5 levels, including a basement and a mechanical penthouse, an orientation of 60° west of north, and a window-to-wall ratio of 33%. The construction budget was $20 million. The building houses laboratories, offices, conference rooms, and a data centre (located in the basement). The laboratory equipment includes environmental chambers, ventilation hoods, and other equipment required for biological experiments.

The Genome Building was completed in 2011 and was certified LEED Gold in 2013. All of the information in this section was sourced from the available design and construction documents, unless otherwise stated. The available design documents only included information relevant to the HVAC systems.

Figure 3.3 East facing surfaces

Figure 3.4 South facing surfaces

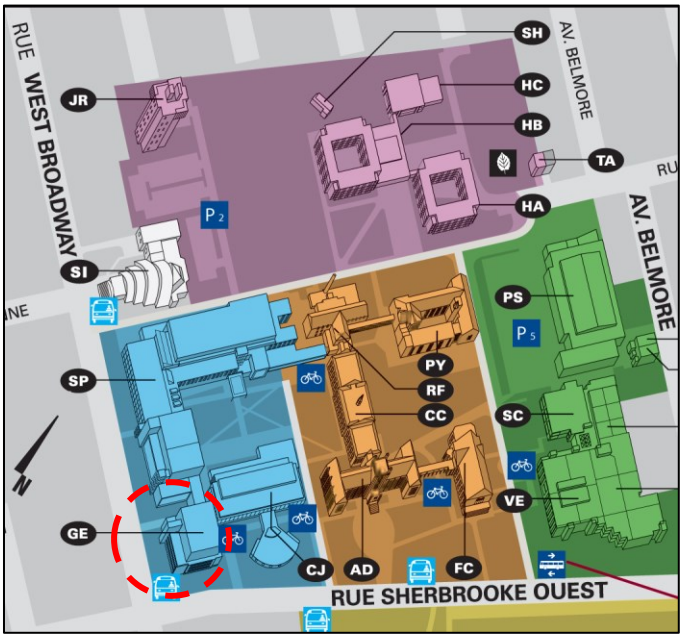


Figure 3.5 Location on Loyola Campus labelled as GE (Concordia University 2014a)

### *3.2.1 Envelope description*

The building envelope consists of a brick façade (Table 3.1), an aluminium panel façade (Table 3.2), a membrane roof (Figure 3.3), and a curtain wall described in Section 3.2.1.1. The U-Values specified in construction documents neglect thermal bridging. Section 5.4.1 describes how U-values were increased to account for thermal bridging. The types of insulation used in the brick and aluminium facades were not mentioned in

the design documents but are estimated from their specified thickness and U-value in Section 5.4.1.

Table 3.1 Brick façade construction

| Brick façade | Thickness (m) | U-Value ($W/m^2 \cdot K$) |
|---|---|---|
| Outside air film | -- | 33.3 |
| Brick façade | 0.090 | 5.56 |
| Air space | 0.040 | 5.88 |
| Insulation | 0.10 | 0.33 |
| Vapor barrier | -- | -- |
| Structural concrete block | 0.19 | 4.76 |
| Inside air film | -- | 8.33 |
| Total | 0.42 | 0.27 |

Table 3.2. Aluminium façade construction

| Aluminum façade | Thickness (m) | U-Value ($W/m^2 \cdot K$) |
|---|---|---|
| Outside air film | -- | 33.3 |
| Aluminum plate façade | 0.040 | -- |
| Aluminum panels connected to 64x25x3 mm "U" aluminum angles connected to vertical steel "Z" bars with a 25mm air space. Dielectric separator tape between steel and aluminum bars | 0.033 | 5.85 |
| Insulation | 0.050 | 0.67 |
| Vertical 50x50x50 mm "Z" bar @ 600 mm c/c | 0.050 | -- |
| Insulation | 0.050 | 0.67 |
| Horizontal 50x50x50 mm "Z" bar @ 600 mm c/c | 0.050 | -- |
| Exterior gypsum board | 0.013 | 12.5 |
| Metal columns 152 mm @ 300 c/c | 0.15 | 5.85 |
| Gypsum board | 0.016 | 10.1 |
| Inside air film | -- | 8.33 |
| Total | 0.45 | 0.27 |

3.2.1.1 Curtain wall

No thermal or optical properties of the curtain walls were available in the design documents. The vision panels of the curtain wall appeared, from site inspection, as double glazed with 6 mm green tinted glass with a 12.7 mm air gap. Apart from dimensions, the only information provided on the spandrel panels are shown in Table 3.4.

Table 3.3. Membrane roof construction

| Roof construction | Thickness (m) | U-Value ($W/m^2K$) |
|---|---|---|
| Air film | -- | 33.3 |
| Elastomeric membrane | -- | -- |
| Insulation panel | 0.25 | 1.89 |
| Polyisocyanurate | 0.75 | 0.33 |
| Vapor barrier | -- | 38.5 |
| Primer | -- | -- |
| Structural concrete | 0.36 | 0.6 |
| Air film | -- | 9.52 |
| Total | 0.46 | 0.19 |

Table 3.4. Curtain wall construction

| Spandrel panels | Thickness (m) | U-Value ($W/m^2K$) |
|---|---|---|
| Opaque glazing | -- | -- |
| Air space | 0.032 | -- |
| Insulation | 0.10 | -- |
| Gypsum board | 0.016 | -- |

Vertical semi-transparent shading fins connect to the south facing windows on the first floor and south, southeast, and north faces on the second and third floors (Figure 3.3, Figure 3.4, and Figure 3.6). The fins extend 560 mm from the wall surface and consist of two 6 mm thick layers of tempered clear glass with a 1.5 mm thick layer of ceramic fritted SentryGlas® with opaque circles (estimated 30% total transparency).

The majority of windows have a manual interior roller shade. No information is available on the thermal or optical properties of the shade.

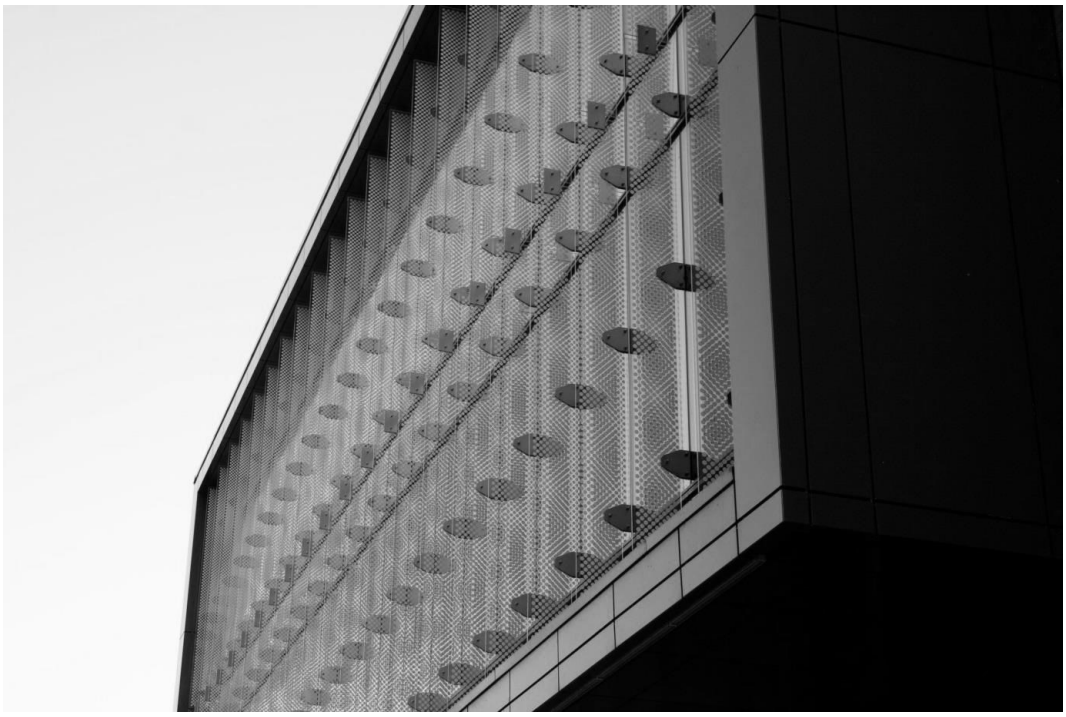

Figure 3.6 Fritted vertical fins on the northeast surface

### *3.2.2 HVAC system description*

This section describes the air handling units (AHUs) and hot water systems in detail and briefly describes the chilled water systems. The basement is heated, if required, mainly with reheat terminals located in the ceiling and a small number of electrical heaters. The supply, return, and exhaust fans run continuously.

#### 3.2.2.1 AHU descriptions

The Genome Building has a variable-air-volume (VAV) system with zone reheat terminals. Two identical AHUs, connected in parallel (Figure 3.7) are located in the mechanical penthouse. Characteristics of the AHU fans are summarized in Table 3.5. The supply fan is referred to as a plenum (Table 3.5) according to the manufacturer because it is a hybrid of a vaneaxial and centrifugal (Twin City Fan and Blower 2014). Return air flows via plenums to ducts in two risers. Exhaust air is extracted from fume hoods, laboratories, and restrooms through two parallel centrifugal exhaust fans (Figure 3.8). The air within the AHUs is conditioned using run-around sensible heat recovery coils (referred to herein as heat recovery coils), heating coils, cooling coils, and steam

humidification grids (Figure 3.7). The AHUs supply to both overhead and perimeter underfloor zone reheat terminals.

Table 3.5 AHU fan characteristics

| Fans | Type | Symbol | Flow (L/s) | Design power (kW) |
|---|---|---|---|---|
| Supply | Plenum | VA1-1 | 10,618 | 30 |
| | | VA2-1 | 10,618 | 30 |
| | | VA1-2 | 10,618 | 30 |
| | | VA2-2 | 10,618 | 30 |
| | | Total | 42,500 | 120 |
| Return | Vaneaxial | VR1-1 | 7,079 | 15 |
| | | VR1-2 | 7,079 | 15 |
| | | Total | 14,200 | 30 |
| Exhaust | Centrifugal | VE1-3 | 16,517 | 30 |
| | | VE2-3 | 16,517 | 30 |
| | | Total | 33,034 | 60 |

The outdoor air dampers are always 100% open and close completely *only* during periods of maintenance or emergency shutdown. The amount of return air mixed with the outdoor air is controlled by the mixing air dampers shown in Figure 3.7.

The heat recovery coils can preheat or precool the outdoor air (Figure 3.8). The exhaust air passes through sensible heat recovery coils (SR1-103) before exiting through an exhaust stack. A three-way valve (PV-3) opens in cold weather causing some of the glycol to bypass the outdoor air for frost control. The heat recovery coils (SC2-1, SC2-2, and SR1-3) and pump (P03-GLC) characteristics are shown in Table 3.6 and Table 3.7, respectively. A static air mixer mixes the return and air exiting the heat recovery coils to prevent stratification in the air stream.

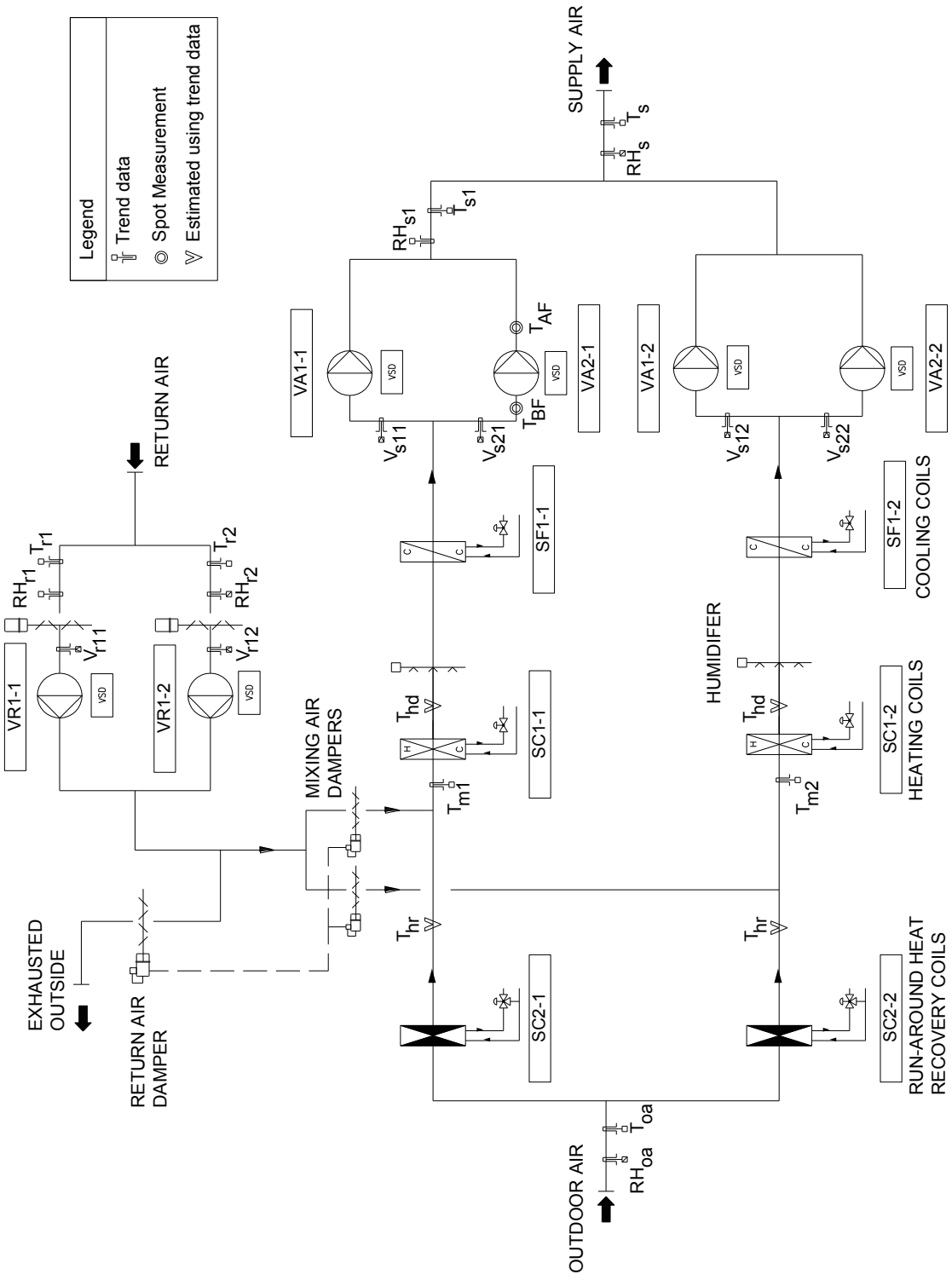


Figure 3.7. AHUs schematic

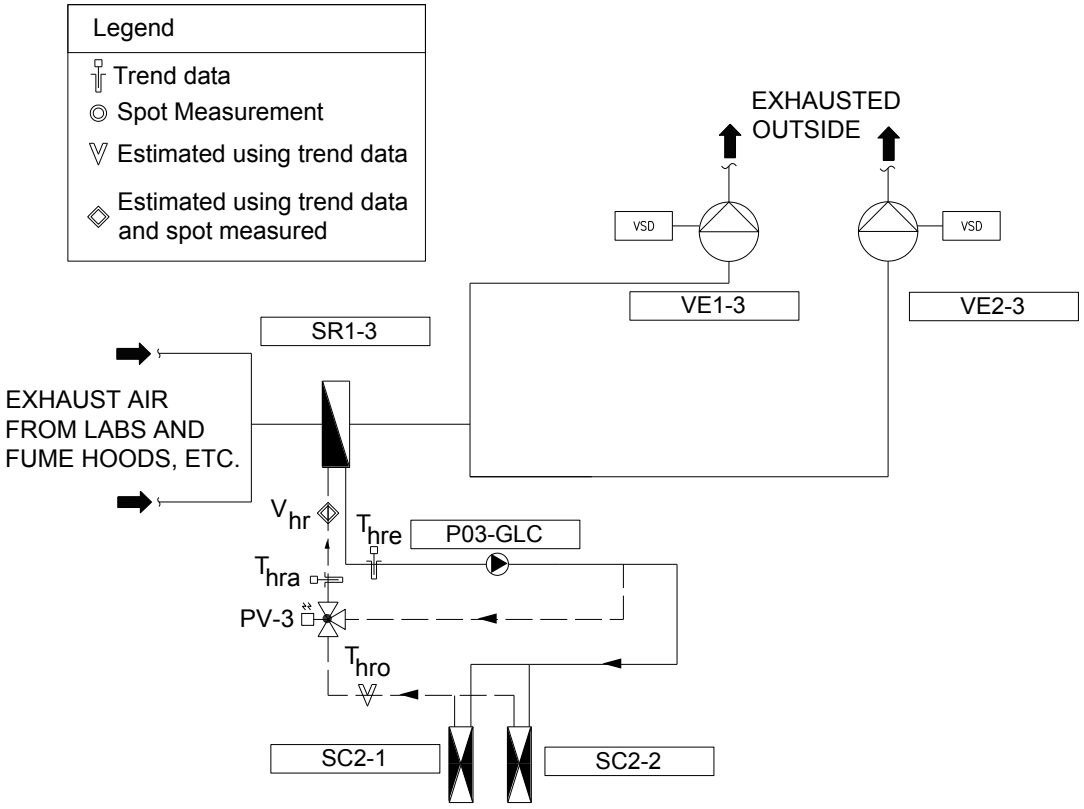


Figure 3.8. Heat recovery and exhaust schematic

Table 3.6 AHU coil characteristics

| Coil | Fluid | Symbol | Coil capacity (kW) |
|---|---|---|---|
| Heat recovery: outdoor air stream | Glycol (50% ethylene) | SC2-1 | 313 |
| | | SC2-2 | 313 |
| | | Total | 626 |
| Heat recovery: Exhaust air steam | Glycol (50% ethylene) | SR1-3 | 626 |
| Heating coil | Glycol (50% ethylene) | SC1-1 | 693 |
| | | SC1-2 | 693 |
| | | Total | 1390 |

Table 3.7 AHU pump characteristics

| Pump | Fluid | Symbol | Design flow rate (L/s) | Design power (kW) |
|---|---|---|---|---|
| Heat recovery | Glycol (50% ethylene) | SR1-1 | 11 | 3.7 |
| Heating coil | Glycol (50% ethylene) | SC1-1 | 5.8 | 2.2 |
| | | SC1-2 | 5.8 | 2.2 |
| | | Total | 11.6 | 4.4 |

3.2.2.2 Heating system description

A campus central plant provides hot water and steam to heat and humidify the supply air, respectively. The supplied hot water enters: (1) VAV reheat coils and (2) two parallel heat exchangers that supply heating coils in the AHUs via a glycol loop (Figure 3.9). The heating coils (SC1-1 & -2) and pumps (P05- & P06-GLC) characteristics are shown in Table 3.6 and Table 3.7, respectively.

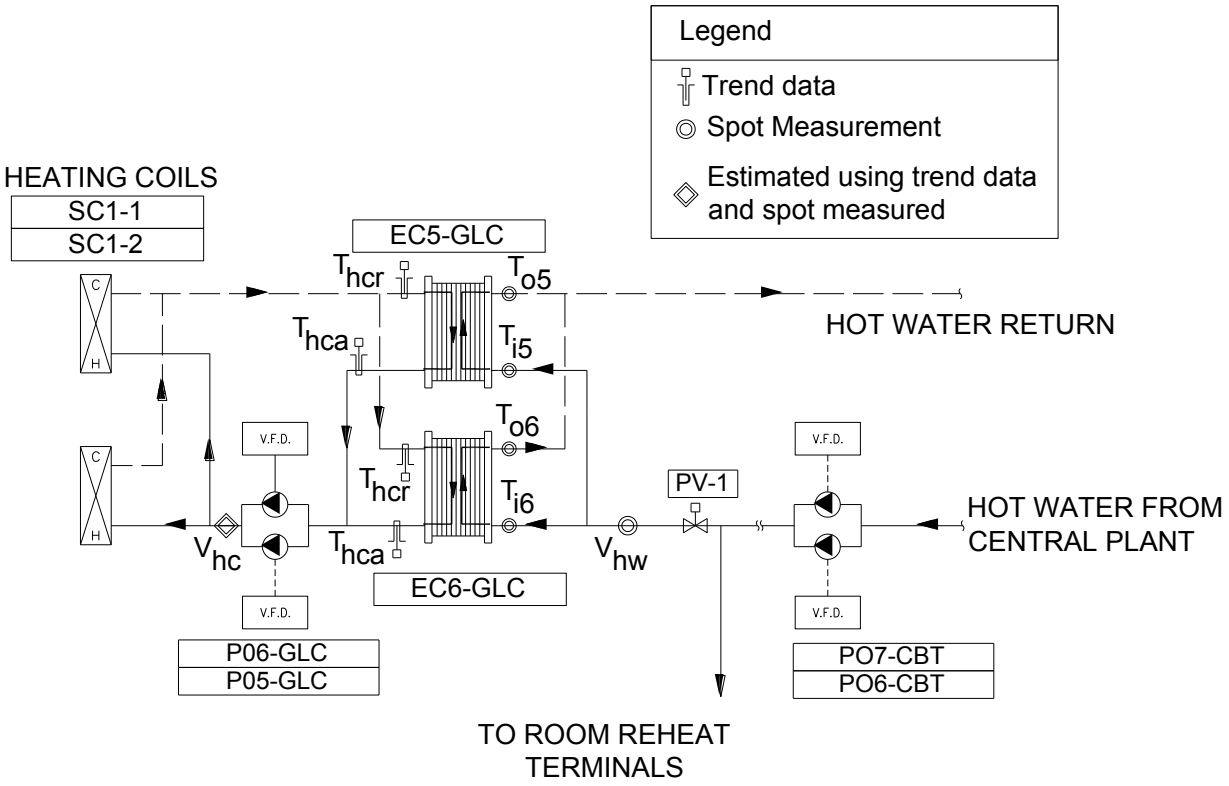


Figure 3.9. Hot water and heating coils schematic

#### 3.2.2.3 Chilled water system descriptions

This section provides a brief description of the cooling systems because this thesis focused on the analysis when the cooling coils were inactive. A detailed description of the campus cooling system was described by Mihai (2014). The chilled water for the cooling coils in the AHUs and environmental chambers is supplied by a campus loop. The data center on the basement floor contains dedicated AHUs, chillers, and cooling towers.

### *3.2.3 HVAC control system description*

Set points for temperatures, damper positions, and valve positions are controlled using proportional-integral control feedback loops programmed into the BAS. This section discusses the control of the AHUs, heating, and cooling systems. All information in this section was extracted from BAS code, unless otherwise specified. BAS code refers to custom programs written in a programming language similar to FORTRAN that controls AHU components.

### *3.2.4 AHU control sequences*

The $T_s$, dependant on the outdoor air temperature ($T_{oa}$) (Figure 3.10)., drives most of the sequence of operation for the mixing air dampers, heat recovery coils, and heating and cooling coils in the AHUs. The $T_s$ reset feedback loop actuator control signal ($XT_s$) varies from 0 to 100%, which controls the position of the mixing air dampers, heat recovery coil bypass valve (PV-3), and the heating and cooling coil two-way valves in the AHUs (Figure 3.11). The $XT_s$ signal maintains energy efficient AHU operation through a control sequence, which is summarized next.

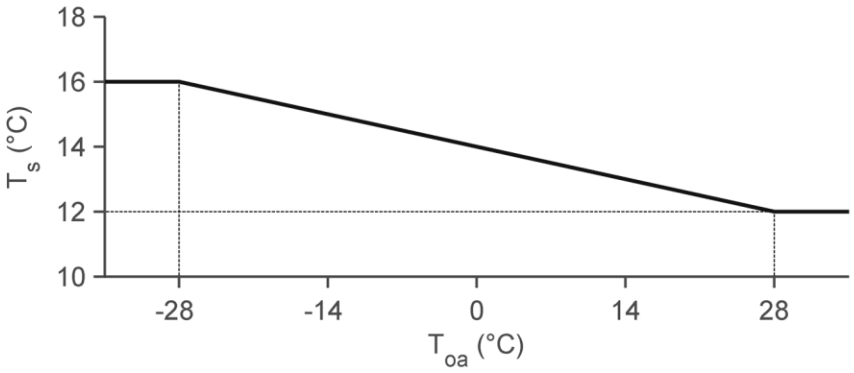


Figure 3.10. BAS supply air temperature reset

When heating is required in the AHUs, the mixing air dampers start opening. When more heating is required than can be obtained with recirculated air, the heat recovery loop is activated. Once the mixing air dampers are open 100% the heat recovery bypass valve starts to open for frost control. Once the bypass valve is 100% open the heating coil valves in the AHUs open. If cooling is required the heating coil valves, heat recovery bypass valve, and the mixing air dampers close and the cooling coil valves open. This avoids simultaneous heating and cooling. Figure 3.11 summarizes how the mixing air dampers, heat recovery coils, and heating and cooling coils in the AHUs are controlled using $XT_s$. More detail on each sequence of control follows.

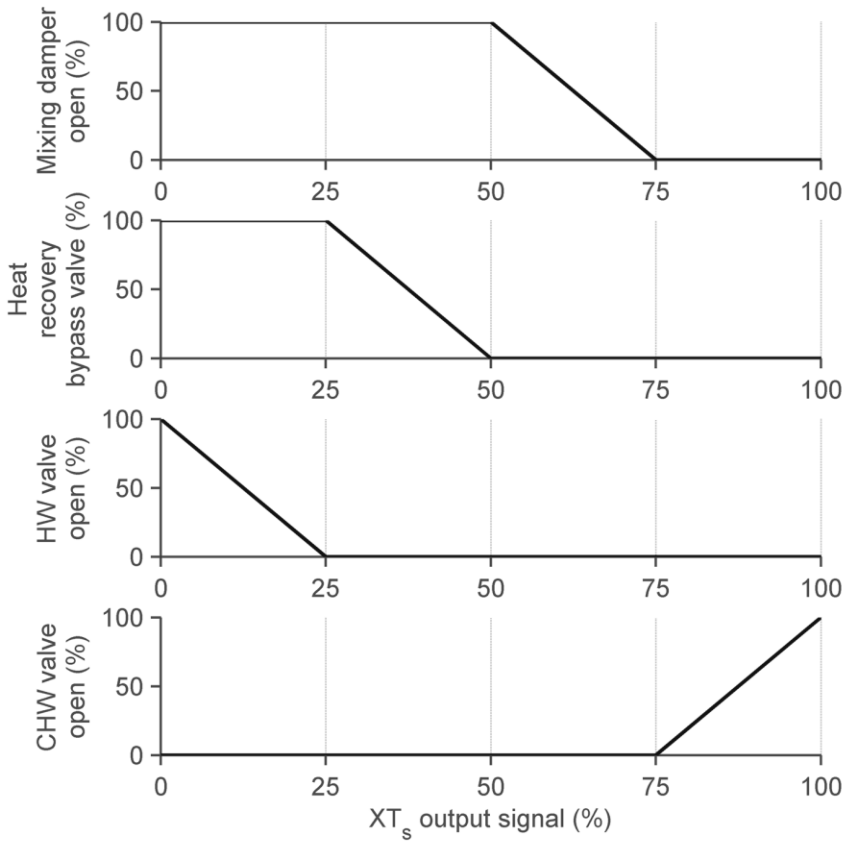


Figure 3.11. Supply air temperature feedback loop actuator signal

3.2.4.1 Economizer damper operation

The BAS activates the mixing air dampers before the other supply air heating equipment. The position of the mixing air dampers is controlled by $XT_s$ and another actuator signal from a feedback loop controlling the mixed air temperature ($XT_m$) to a set point of 14°C. When the outdoor air enthalpy ($h_{oa}$) is less than the return air enthalpy ($h_r$) the mixed air damper position is controlled by the minimum of $XT_s$ and $XT_m$ (i.e., the smaller the actuator signal, the more the mixing air dampers open). When $h_{oa}$ is greater than $h_r$ the mixing air dampers are set 100% open. To summarize: (1) during the shoulder season the mixing air dampers modulate to maintain the $T_s$ and $T_m$ set points, (2) during the heating season when $h_{oa}$ is less than $h_r$ the mixing air dampers are 100% open to provide heating,

and (3) during the cooling season when $h_{oa}$ is often greater than $h_r$ the mixing air dampers are 100% open to provide cooling.

3.2.4.2 Heat recovery coil operation

The heat recovery coils are activated second in the BAS code. When $T_{oa}$ is less than 8 °C or greater than 28 °C pump P03-GLC runs continuously and heat recovery is initiated. The position of the bypass valve is controlled by $XT_s$ and another actuator signal ($XT_{hra}$) maintaining the temperature of glycol arriving at the recovery coils in contact with the exhaust air steam ($T_{hra}$) to a set point of 4 °C or greater to prevent frost from occurring in the AHUs. The bypass valve is controlled by the minimum of the $XT_s$ and $XT_{hra}$ set points (i.e., the smaller the actuator signal the more the bypass valve opens).

3.2.4.3 Heating coil operation

The heating coils in the AHUs are activated third by $XT_s$. The heating coil valves open when $XT_s$ is less than 25%, the mixing air dampers are 100% open, and heat recovery has frost control active. The glycol temperature arriving at the heating coils ($T_{hca}$) is controlled by a reset profile shown in Figure 3.12.

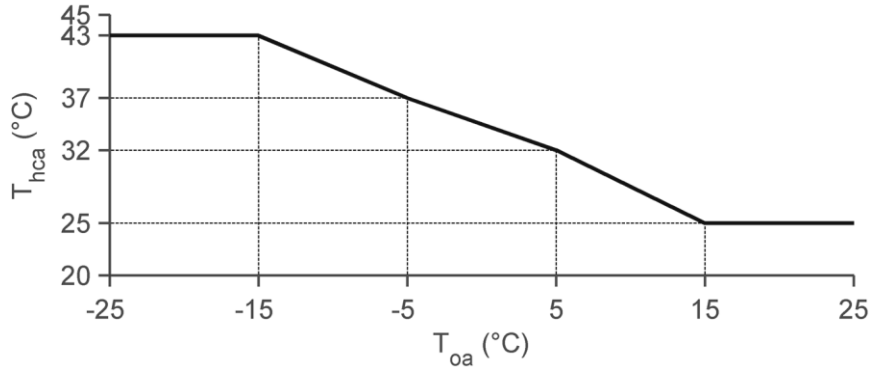


Figure 3.12. BAS supply glycol reset profile in the heating coils

3.2.4.4 Humidification

Humidification is controlled by a feedback loop to keep the return air relative humidity (RH) at 30%. The supply air RH limit is 70%. The humidifier valve closes as required to keep supply air RH under 70%.

3.2.4.5 Cooling coil operation

The cooling coils in the AHUs (SF1-101 & -102) are activated last. The cooling coil valves are controlled by the $XT_s$ actuator control signal. When $XT_s$ is greater than 75% and starts increasing, more cooling is required, so the cooling coil valves open further.

### *3.2.5 Zone control*

The VAV terminals control $V_{zs}$ and $T_{zs}$ entering a space. The $V_{zs}$ is controlled using three modes of operation based on occupants, detected by sensors, described in Table 3.8. If the space requires heating, $T_{zs}$ is controlled with a two-way valve adjusting the hot water flow rate entering the reheat terminal. If a space is unoccupied the supply air flow rate may increase to maintain $T_z$. If a VAV terminal controls multiple spaces, all spaces have to be unoccupied before $V_{zs}$ decreases further. Neither the BAS code nor design documents state what time separates day and night modes. Analysis of the $V_{zs}$ trend data revealed that day mode is approximately 0700 to 2300.

Laboratories are controlled to maintain negative pressure by adjusting the exhaust air (e.g., fume hoods) and supply air dampers. The negative pressure avoids contaminating the adjacent spaces with air that may be of low quality.

Table 3.8 Zone air flow rate modes based on occupants

| Mode | Description |
|---|---|
| Occupied | $V_{zs}$ is controlled to 10 air changes per hour (ACH) when a space's occupant sensor detects movement |
| Unoccupied day | $V_{zs}$ is controlled to 6 ACH when a space's occupant sensor detects no movement during the day |
| Unoccupied night | $V_{zs}$ is controlled to 3 ACH when a space's occupant sensor detects no movement during the night |

### *3.2.6 BAS and available trend data description*

The BAS runs Siemens APOGEE® software to control the building's HVAC systems. A summary of the trend data used in this study is shown in Table 3.9. It should be noted that Table 3.9 is not a comprehensive list of all the available trend data. Cooling system trend

data were not shown because they were not relevant to this thesis. Trend data were recorded every 15 min, with the majority of logs starting in June 2012, and the total size of database, at the time of writing, is approximately 270 Mb.

Table 3.9 List of recorded trend data

| Trend Data | Start date | Abv. | No. | Bias error | Unit |
|---|---|---|---|---|---|
| Ambient | | | | | |
| Outside air temperature | Jun 2012 | $T_{oa}$ | 1 | ± 0.3 + 0.005\|$T$\| | °C |
| Zone Level | | | | | |
| Room air temperature | Jun 2012 | $T_z$ | 95 | ± 0.3 + 0.005\|$T$\| | °C |
| Room supply air temperature | Jun 2012 | $T_{zs}$ | 3 | ± 0.3 + 0.005\|$T$\| | °C |
| Room air supply flow rate | Jun 2012 | $V_{zs}$ | 105 | ± 5% | L/s |
| Zone return air flow rate | Jun 2012 | $V_{zr}$ | 10 | ± 5% | L/s |
| System Level | | | | | |
| AHUs | | | | | |
| Supply air temperature | Jun 2012 | $T_s$ | 2 | ± 0.3 + 0.005\|$T$\| | °C |
| Mixed air temperature | Jun 2012 | $T_m$ | 2 | ± 0.6 | °C |
| Return air temperature | Jun 2012 | $T_r$ | 2 | ± 0.3 + 0.005\|$T$\| | °C |
| Supply air flow rate | Jun 2012 | $V_s$ | 4 | ± 5% | L/s |
| Return air flow rate | Jun 2012 | $V_r$ | 2 | ± 5% | L/s |
| Mixing air damper position | Jul 2013 | - | 2 | - | % |
| Humidification valve position | Sep 2013 | - | 2 | - | % |
| Supply air humidity | Jul 2012 | $RH_s$ | 2 | ± 5 | % |
| Return air humidity | Jul 2012 | $RH_r$ | 2 | ± 5 | % |
| Heat Recovery | | | | | |
| Glycol supply temperature | Jun 2012 | $T_{hre}$ | 1 | ± 0.3 + 0.005\|$T$\| | °C |
| Glycol return temperature | Jun 2012 | $T_{hra}$ | 1 | ± 0.3 + 0.005\|$T$\| | °C |
| Heating coils | | | | | |
| Glycol supply temperature | Jun 2012 | $T_{hca}$ | 2 | ± 0.3 + 0.005\|$T$\| | °C |
| Glycol return temperature | Jun 2012 | $T_{hcr}$ | 2 | ± 0.3 + 0.005\|$T$\| | °C |
| Whole-Building Level | | | | | |
| Hot water flow rate | Sep 2013 | $V_{GE}$ | 1 | ± 5% | L/s |
| Supply hot water temperature | Feb 2014 | $T_{GES}$ | 1 | ± 0.3 + 0.005\|$T$\| | °C |
| Return hot water temperature | Feb 2014 | $T_{GER}$ | 1 | ± 0.3 + 0.005\|$T$\| | °C |
| Total | | | 239 | | |

Many differences between the BAS GUI and physical sensor locations existed in the case-study building. A small number of differences existed between the design documents and physical sensor locations.

### *3.3 Proposed Calibration*

This thesis broke away from traditional calibration at the whole-building level and instead focused on calibrating the zone and system level models of the case study building. The main reasons for this were to explore the use of trend data in calibrated simulation and to focus on the calibration of sub-utility components which are often ignored due to lack of data, as mentioned in the literature review. The Genome building lacks a plant with heating capacity because it is served by hot water and steam from the campus loop. Therefore, no plant level model could be calibrated.

Mihai (2014) applied a similar method to focus on the cooling season defined when the cooling coils are active in the AHUs. This thesis focuses on the calibration of the shoulder and heating seasons. The shoulder season is defined as the period when the heating and cooling coils in the AHUs are inactive.

The procedures described in Sections 3.1.2 to 3.1.5 require many measurement points. It is unlikely that a building will contain all the required measurement points suggested and this thesis was no exception. For example, whole-building electricity use was unavailable for the building and the whole-building hot water heat flow rate ($\dot{Q}_{GE}$) (eq. 3.7) was only available after February 2014. Fan, pump, and other plant equipment using electricity was not submetered. In addition, zone level trend data for the basement floor was not recorded. This section discusses the proposed calibration of the zone and system level models and qualitative calibration of $\dot{Q}_{GE}$.

$$\dot{Q}_{GE} = V_{GE}\rho_{hw}c_{p_{hw}}(T_{GES} - T_{GER}) \qquad \text{eq. 3.7}$$

*where:*

$V_{GE}$ = Whole-building hot water flow rate
$T_{GES}$ = Whole-building hot water flow supply temperature
$T_{GER}$ = Whole-building hot water flow return temperature

#### *3.3.1 Proposed zone level calibration*

As shown in the list of available trend data (Table 3.9), $T_{zs}$ is available in only 3 rooms. Therefore zone $\dot{Q}_{zheat}$ were uncertain. The zone level was considered calibrated once $T_z$ and $V_{zs}$ met the calibration criteria. Knowing $T_z$ and $V_{zs}$ still helped characterize the lumped behaviour of the zone loads; however, the effect on the uncertain $\dot{Q}_{zheat}$ did not

become apparent until the whole-building heating energy was analysed. A strategy for tuning inputs affecting zone loads is recommended when using inputs generated from $T_z$ and $V_{zs}$ trend data to calibrate the simulated $T_z$ and $V_{zs}$:

- Simulated zone air temperatures less than trend data suggests tuning inputs to increase loads;
- Simulated zone air temperatures greater than trend data suggests tuning inputs to decrease loads;
- Simulated zone supply air flow rate greater than the trend data suggests tuning inputs to increase or decrease loads whether the zone model is in a heating or cooling mode, respectively;
- Zone supply air flow rate trend data less than the simulations suggests the applied minimum flow ratio schedule was not representative for the given hour/day (discussed further in Section 4.6).

Separately tuning air infiltration, U-values, lighting, equipment, and occupant loads is incredibly time consuming and highly susceptible to different combinations of inputs (i.e., underdetermination) considering their uncertainty. Air infiltration and U-values were estimated using values in the literature and construction documents, respectively. Since whole-building electricity was unavailable and the server room was not modelled, the lighting, equipment, and occupant gains (referred to herein as internal gains) were aggregated into a single representative gain. This gain also represents any additional offsetting differences caused by the overall lumped behaviour of all other uncertain variables affecting loads. For example, if U-values and air infiltration are underspecified the representative gain would be increased to compensate. This allows for easier tuning of the variables affecting loads to maintain focus on calibrating the system level components that were measured. This technique limits the types of ongoing commissioning techniques when applied to the model. For example, identifying EEMs based on changing the lighting power density or U-values would not provide accurate results. If the goal was to calibrate the whole-building electricity use this technique should be altered to separately tune variables affecting electrical and non-electrical loads.

3.3.1.1 Zone assumptions

Since trend data for only 3 out of 4 floors were recorded, only 3 out of 4 floors were modelled and calibrated. This also meant that the AHUs were calibrated using the sum of $V_{zs}$ instead of $V_s$ measured. This did not require any large assumptions in the model unless the $V_{zs}$ trend data contained errors. In reality, with the high quantity of sensors it was taken with good faith that the sum of $V_{zs}$ was representative (i.e., some $V_{zs}$ sensors over-measure and some under-measure due to error limits and sensor position). Modelling 3 out of 4 floors also simplified the model to avoid modelling the data center with dedicated AHUs and the complex heat transfer in below grade walls and floors. The proposed approach also assumed a zone's average temperature was represented by $T_z$.

This method used trend data as it was recorded. This thesis proposes that re-commissioning agents use trend data instead of sub-metering the entire building with dedicated sensors such as in Piette et al. (2001). It was uncertain whether the sensors had drifted, were positioned correctly (i.e., zone level sensors position were not easily accessible to view), or were calibrated correctly; the analyst must use their engineering judgement and/or redundancy in the sensors to identify obvious erroneous measurements. Trend data quality is further discussed in Section 4.7.1.

### *3.3.2 Proposed system level calibration*

The quantity of system level trend data available was large, as shown in Table 3.9. Therefore the system level inputs were not tuned unless differences between model and field performance was found. The air-side of the heating coils was calibrated before the glycol-side.

### *3.3.3 Proposed whole-building calibration*

This step qualitatively compared the simulated and trend data $\dot{Q}_{GE}$ because it was only available at the later stage of the research (Table 3.9) and 3 out 4 floors were measured and modelled (i.e., $\dot{Q}_{GE}$ pertains to all 4 floors). It was expected that only a small percentage of $\dot{Q}_{GE}$ was used in the basement compared to the above grade floors. The qualitative comparison indicated whether the simulation followed the pattern in the trend

data with reasonable values. Discrepancies are likely to exist at this level because $\dot{Q}_{zheat}$ is uncertain and therefore zone loads may have to be tuned.

### *3.3.4 Calibration stages*

The calibration in this thesis was performed in three stages:

(1) *Shoulder season calibration (April 7th to 21st, 2013):* This served to simplify the model when first attempting the calibration and estimate internal gains;

(2) *2013 Heating season calibration (January 7th to March 31st, 2013);*

(3) *2014 Heating season calibration (November 25th, 2013 to March 31st, 2014):* This calibration focused on calibrating a longer portion of the heating season.

## ***3.4 Discussion***

### *3.4.1 Comparison with other approaches*

The bottom-up method combines elements from the characterisation techniques and procedural extensions classification proposed by Coakley et al. (2014). The method also built upon the use of high resolution data recommended by numerous studies (Norford et al. 1990; Clarke et al. 1993; Raftery et al. 2011; Gestwick and Love 2014; Kandil and Love 2014). It also extended the bottom-up method used by Mihai (2014).

The issue of model underdetermination in calibration occurs with phenomena other than building energy use. The fields of hydrology and hydraulics also experience similar issues. Hydrology faces unclear, interconnected, and uncertain boundary conditions whereas hydraulics describes the flow of water within well-defined boundaries. When modelling hydrological processes, Savenije (2009) recommended using top-down modelling to create site-specific models based on physical laws identified at large scales from observing emerging patterns and organising principles. He argued that a bottom-up method be used when creating hydraulic models because physical laws

apply to its well-defined boundaries. Calibrating building energy models using a bottom-up method is appropriate because buildings have well-defined energy boundaries.

This thesis produced calibrated HVAC components instead of a calibrated whole-building level model. Usually a model calibrated top-down with whole-building data was used to assess EEMs on components that were unlikely to have been calibrated. The level of uncertainty with energy savings when commissioning HVAC components using a model calibrated with utility data was much higher because offsetting errors were likely to exist. Thus, there is large value in calibrating the HVAC components to confidently identify specific strategies to improve energy performance.

### *3.4.2 Method limitations*

If the quality of trend data were poor the calibrated model may have been at risk of consequent calibration error. Trend data quality and availability (i.e., are trend data continuously stored?) remain uncertain. If the trend data were not continuously stored (i.e., the storage function was never activated), a consultant may need to wait for weeks or months until enough data were stored to be used in calibration.

The bottom-up approach is susceptible to offsetting errors. For example, zone electrical loads are rarely sub-metered so it is highly likely that offsetting errors will occur when estimating zone occupant, lighting, and equipment gains. In this case study, offsetting errors were likely with $\dot{Q}_{zheat}$ because some zones were likely modelled with under-/over- heating/cooling.

Loads can be static or time variant. Examples of static loads include equipment gains and occupant gains. Examples of time variant loads include solar energy absorbed into the façade and interior elements of a room. Choosing to tune one aggregated internal gain as an equipment load ignores the time lag effects which may cause offsetting errors in the zone loads. The aggregated gain also inhibits any EEMs related to envelope, occupants, lighting, or equipment.

If zone level trend data were unavailable zone inputs would be tuned until the AHU $V_s$ was calibrated as similarly done by Monfet et al. (2009).

The main limitation of the bottom-up method is the larger amount of time required to calibrate a large fraction of zones. Calibrating more than a dozen zones may be overwhelming to many. The additional time spent on the calibration at sub-utility levels might be offset by revealing errors in trend data, errors in key equipment performance models, and faults. These can be viewed both positively and negatively. It may be difficult to produce a calibrated model if the simulation software has errors in key equipment performance models. BAS sensor or equipment faults during the period of calibration may also lead to difficulty in reaching the calibration criteria. However, finding faults may lead to improved performance and identifying errors in key equipment performance models gives the analyst a greater understanding of their model.

The next chapter discusses a tool that automatically couples trend data and with building energy simulation software to reduce the time required to perform bottom-up simulation calibration.

# 4 An Automatic Assisted Tool to Couple Trend Data with Calibrated Simulation and Ongoing Commissioning

The chapter describes a proof-of-concept prototype tool developed to automate the analysis of trend data for use in calibrated simulation and ongoing commissioning. First, the organizational structure of a trend database is described. This is followed by an explanation of the calculations involved in processing trend data at zone and system levels. The chapter ends with a summary and discusses the tool's limitations and issues with using trend data. The chapter analyses trend data recorded under real operating conditions during the 2013 heating season, unless otherwise stated. All trend data are presented as hourly average values, unless otherwise stated. Short-term measurements were used to supplement the analysis.

## *4.1 Automating the Interaction between Trend Data and Building Simulation Software*

A proof-of-concept prototype software tool called the Automatic Assisted Calibration Tool (AACT) was developed in MATLAB (Figure 4.1). Its primary function was to reduce the time required to extract values from trend data for use in calibrated simulation. The secondary objective was to create performance reports quantifying building operation for comparison with design specifications, BAS set points, and future measured performance. As many inputs in building simulation software are dependent on design information, the relevant design information should also be entered as well.

MATLAB was selected, as opposed to spreadsheet software because it had the capacity to easily deal with large amounts of data and provided a wide variety of pre-defined functions and toolkits. Seidl (2006) also argued that spreadsheet software was not powerful enough to analyse trend data.

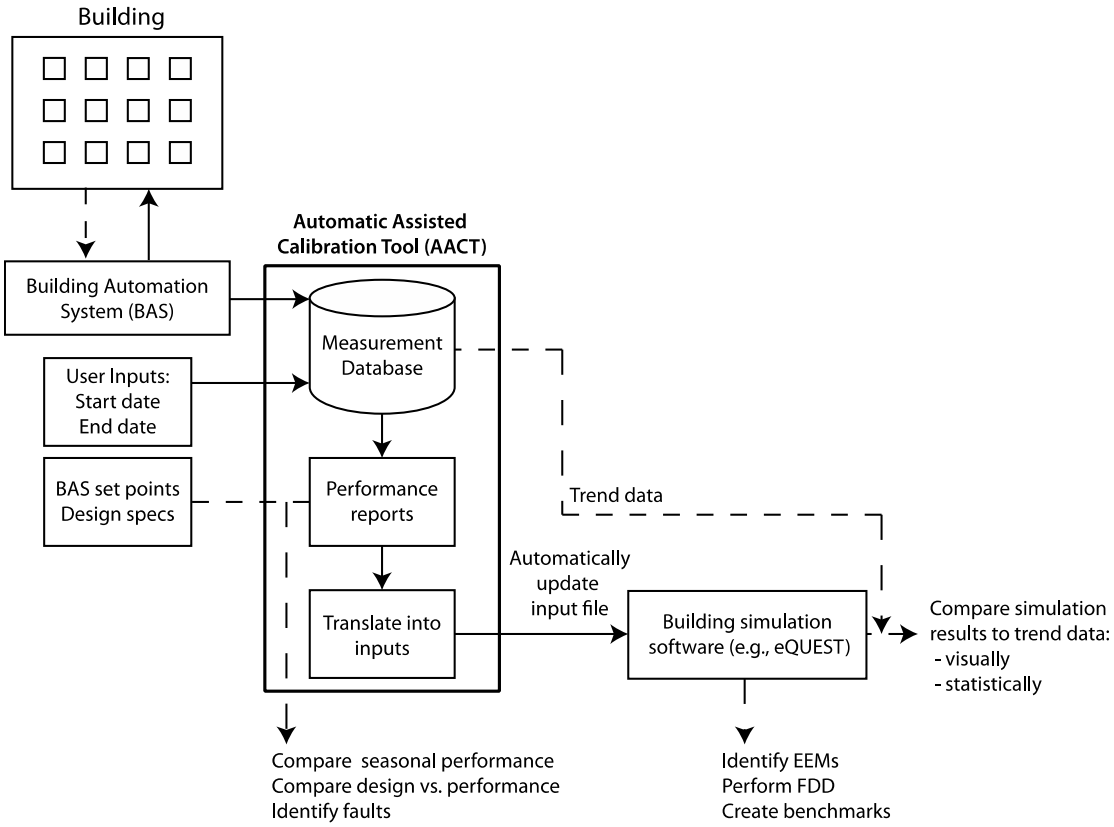


Figure 4.1 Assisted Automatic Calibration Tool schematic

AACT provided a user-selectable start and end dates for the desired period of analysis. This offered flexibility because inputs and performance reports could be generated over a period of one week, a few months, or a whole year. First, the AACT generated performance reports, which consisted of statistical data and performance indices extracted directly and indirectly from values in the trend database. Indirectly refers to estimating HVAC component performance that was not measured using available trend data. Comparing equipment performance under real operating conditions to design specifications could provide feedback on HVAC equipment sizing to building designers for future projects. Comparing the values in these reports to BAS set points could reveal faults when set points are not followed. Ideally a performance report generated after initial commissioning could serve as a benchmark and the ongoing

comparison of measured performance to this benchmark could reveal trends in performance degradation or faults if performance changed unexpectedly.

Only some values in performance reports could be entered directly into building simulation software due to the software's code structure. The AACT then processed these values to automatically update an eQUEST input (.inp) file. This step is referred to herein as inputs generation. The .inp file was composed of lines of text containing all the required information to run a simulation. More information about eQUEST is provided in Section 5.1. The AACT also had the capacity to compare outputs from eQUEST to the trend data using visual and statistical techniques. The AACT automatically generated performance reports and inputs, unless otherwise stated below.

Unlike programs that automatically create a calibrated model by tuning inputs based on an optimization approach (Liu & Henze 2005; Sun & Reddy 2006; Reddy et al. 2007) and ExCaliBEM (Sansregret et al. 2014), the AACT was limited to providing calibration assistance through the generation of inputs.

This chapter focuses on generating inputs and creating performance reports for the 2013 heating season. These performance reports were compared to reports generated for the 2014 heating season to demonstrate how these reports were used to compare changes in operation over time.

### *4.2 Description of Trend Database*

A trend database was created from comma separated value (CSV) files exported weekly from the BAS. All data within this section were hourly averaged values, unless otherwise stated, because eQUEST uses a time step of 1 h.

The trend data were organized in a spatial and thermal hierarchy in the AACT, similar to the one proposed by Maile et al. (2012). The organizational structure of trend data at the zone level is shown in Figure 4.2. The trend data were hierarchically organized by floor number, zone, available trend data types, and room. This structure allowed for easy calculation of average zone air temperatures and total zone and floor supply air flow rates.

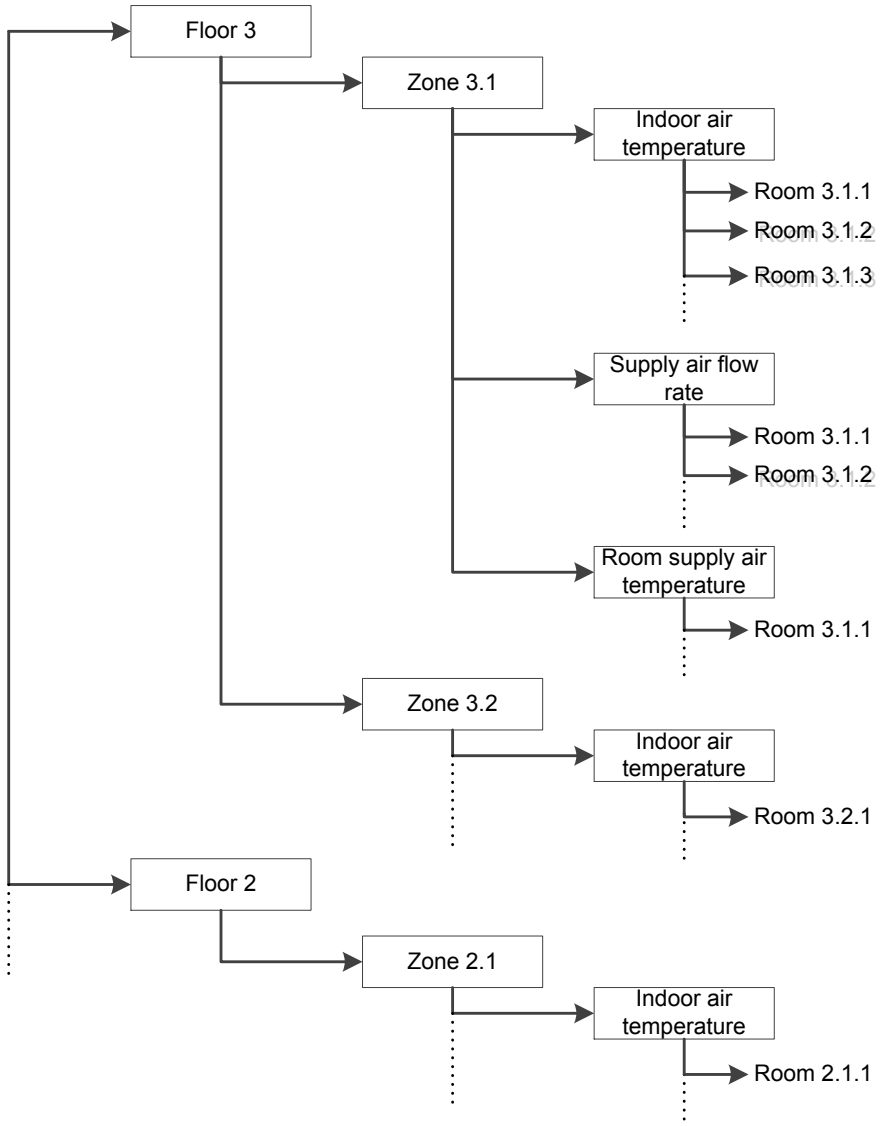


Figure 4.2 AACT zone spatial and thermal organization

The organizational structure of the system level is shown in Figure 4.3. The system level was organized into the AHUs, available trend data types, and parallel AHUs. eQUEST cannot model parallel AHUs so this organizational structure allowed temperature trend data to be averaged and air flow rate trend data to be summed to model a single AHU.

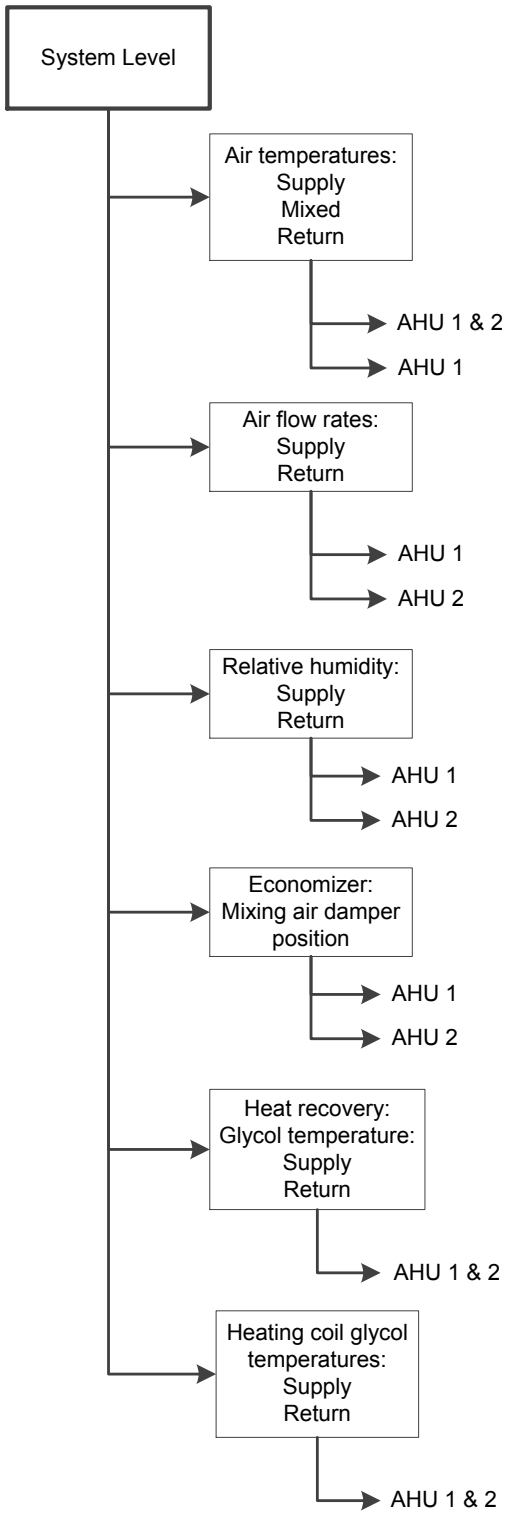


Figure 4.3 AACT system level thermal and spatial organization

### *4.2.1 Removing erroneous trend data*

Trend data are expected to contain erroneous measurements, which can be time consuming to identify and remove. This section discusses the statistical distribution of trend data and how erroneous trend data were removed.

Some trend data were approximately normally distributed, while other data, such as the supply air temperature ($T_s$) and the return air flow rate ($V_r$) in Figure 4.4, respectively, were not. In the following sections the median was used primarily when analysing trend data; however, the mean was also occasionally used. The mean was used occasionally when performing linear regression and uncertainty analysis. It was interesting and important to highlight the uncertainty due to error propagations when using trend data. Data normalization were neglected due to time constraints, but should be considered for future use.

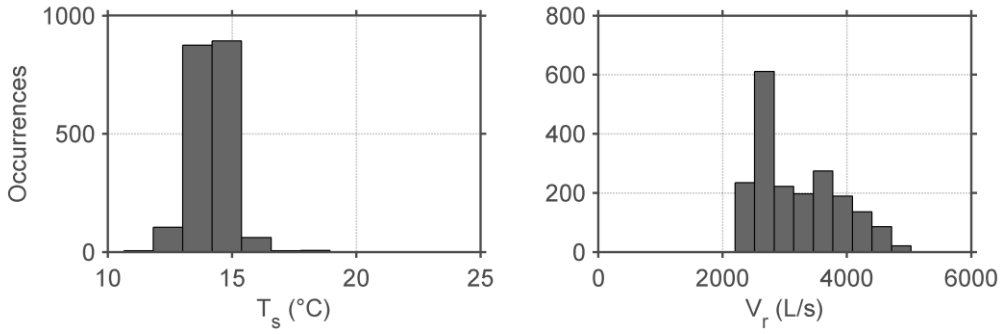


Figure 4.4 Distribution of trend data

Herein *uncertainty of data* refers to its overall uncertainty, which accounts for bias and random errors. Errors from turbulence or stratification due to poor sensor placement were difficult to quantify and were not used when calculating the overall uncertainty. Robust regression techniques such as quantile regression or least trimmed square were neglected in the analysis due to time constraints, but could be considered for future use.

The median was used, instead of the mean, to calculate the hourly average trend data because it is independent of data distribution (e.g., normality) and is less influenced by outliers. It also helped with some automatic data filtering.

Using the median to average hourly data could not remove all outliers such as when the fan AHUs were deactivated for short maintenance periods. Chauvenet's criterion, described by Reddy (2011), was first considered for screening supply air flow rate trend data. The criterion rejected a data point if its magnitude of deviation from the mean of a series was outside a probability band centred around that mean, assuming a normal distribution. The common diurnal variation of trend data (i.e., large standard deviations) caused problems applying Chauvenet's criterion. For example, the criterion admitted zero zone supply air flow rate ($V_{zs}$) when zone VAV terminals experienced short periods of zero air flow because zero was too close to the mean. This was an issue because it was important to automatically calculate the zone minimum air flow ratio as most zones continuously received an air flow rate from the AHUs. Only a small number of zones would have zero $V_{zs}$ during unoccupied periods as discussed further in the next section. The occasional non-normal distribution of trend data also caused difficulties applying the criterion. Therefore, this criterion was rejected; instead all trend data that appeared erroneous, based on inspection and judgement, were removed manually. Implementing automatic data rejection could reduce the time spent removing erroneous data.

From January 28$^{th}$ to February 4$^{th}$, 2013 the supply air flow rates in the AHUs were 1.4 times larger than normal and were excluded from this study because this was considered unrepresentative.

### *4.3 Zone Level Performance*

Zone level inputs and performance reports were generated for a total of 17 zones on the floors above grade. Chapter 5 explains zone definitions in detail. All tables in this section were considered performance reports.

Hourly median zone indoor air temperatures ($T_z$) were calculated from all room air temperatures recorded in a zone. The maximum, minimum, median ($\mu_{½}$), and median absolute deviation (*MAD*) $T_z$ during the 2013 were compared to 2014 heating season performance and design specifications (Table 4.1). Zones Z1-S, Z1-NE, Z1-CONF, Z2-W, Z2-S, and Z3-S median $T_z$ varied by 0.6-1.7 °C but were still within the ranges for

thermal comfort. The design values may not reflect the operating thermostat set point because some thermostats were manually controlled by occupants. The maximum and minimum reported values in perimeter zones showed large temperature swings.

Table 4.1. Indoor air temperatures comparison

| Zone | $T_z$ trend data (°C) | | | | | | | | Design |
|---|---|---|---|---|---|---|---|---|---|
| | 2013 | | | | 2014 | | | | |
| | Max | Min | $\mu_{½} \pm MAD$ | | Max | Min | $\mu_{½} \pm MAD$ | | |
| Z1-S | 29.5 | 15.9 | 20.1 | ± 1.1 | 28.9 | 14.9 | 19.5 | ± 1.2 | 21 |
| Z1-NE | 24.3 | 20.2 | 22.8 | ± 0.5 | 24.3 | 19.3 | 21.8 | ± 1.0 | 22 |
| Z1-NW | 21.7 | 16.6 | 21.0 | ± 0.2 | 22.7 | 18.2 | 21.2 | ± 0.5 | 21 |
| Z1-CORR | 22.6 | 21.0 | 21.6 | ± 0.1 | 22.6 | 21.1 | 21.6 | ± 0.1 | 21 |
| Z1-CONF | 24.9 | 22.1 | 24.1 | ± 0.2 | 23.1 | 20.9 | 22.3 | ± 0.1 | 21 |
| Z2-SW | 28.1 | 20.8 | 22.5 | ± 0.6 | 27.7 | 20.0 | 22.4 | ± 0.8 | 21 |
| Z2-E | 23.3 | 21.7 | 22.2 | ± 0.1 | 24.3 | 22.2 | 22.7 | ± 0.2 | 22 |
| Z2-INT | 23.6 | 22.4 | 23.0 | ± 0.1 | 23.6 | 22.0 | 22.6 | ± 0.2 | 22 |
| Z2-NE | 23.9 | 20.0 | 21.5 | ± 0.8 | 23.7 | 19.4 | 21.5 | ± 0.8 | 22 |
| Z2-S | 23.6 | 21.2 | 22.4 | ± 0.1 | 25.5 | 20.2 | 24.0 | ± 0.4 | 21 |
| Z2-W | 23.9 | 19.8 | 22.3 | ± 0.8 | 25.4 | 19.6 | 23.6 | ± 0.7 | 21 |
| Z3-SW | 29.8 | 19.8 | 21.8 | ± 0.8 | 28.9 | 18.8 | 21.7 | ± 0.8 | 21 |
| Z3-E | 24.1 | 20.7 | 22.7 | ± 0.3 | 24.7 | 21.3 | 22.8 | ± 0.3 | 22 |
| Z3-INT | 24.5 | 22.2 | 23.4 | ± 0.2 | 24.5 | 22.6 | 23.5 | ± 0.2 | 22 |
| Z3-NE | 23.1 | 17.6 | 21.2 | ± 0.8 | 23.0 | 16.8 | 20.2 | ± 1.1 | 22 |
| Z3-S | 24.3 | 20.5 | 22.3 | ± 0.1 | 23.3 | 19.8 | 20.9 | ± 0.2 | 21 |
| Z3-W | 25.0 | 16.7 | 21.4 | ± 1.3 | 24.4 | 14.8 | 21.4 | ± 1.8 | 21 |

The $V_{zs}$ were calculated from the summation of the VAV terminal supply air flow rate trend data from all rooms in a zone. The zone minimum air flow ratio was calculated as the minimum to maximum $V_{zs}$. The maximum $V_{zs}$ and the minimum air flow ratios for the 2013 and 2014 heating seasons were compared to their design values (Table 4.2 and Table 4.3). A few differences were noticed such as the large reduction in the 2014 maximum $V_{zs}$ in zone Z2-E (interior laboratory) caused by an error occurring when the trend data were saved (i.e., not an indication of a change in performance). The cause was an issue internal to the BAS's data saving function. Zone Z1-CONF's maximum $V_{zs}$ increased during the 2014 heating season which caused its minimum flow ratio to decrease. The decrease in minimum flow ratio in zone Z3-E (perimeter/interior

laboratory) was because the zone's $V_{zs}$ decreased in 2014. Changes in occupant numbers, equipment loads, and/or lighting loads may explain the changes in Z1-CONF's and Z3-E's supply air flow rates. One reason some zone air changes per hour (ACH) (Table 4.3) were less than their design values was because $V_{zs}$ were partially based on occupant sensors and perhaps these zones were never fully occupied.

Table 4.2 Zone supply air flow rate comparison

| Zone | Maximum zone $V_{zs}$ (L/s) | | | Min air flow ratio | | |
|---|---|---|---|---|---|---|
| | Trend data | | Design | Trend data | | Design |
| | 2013 | 2014 | | 2013 | 2014 | |
| Z1-S | 1469 | 1344 | 2450 | 0.00 | 0.00 | 0.00 |
| Z1-NE | 708 | 717 | 700 | 0.31 | 0.31 | 0.33 |
| Z1-NW | 473 | 469 | 827 | 0.96 | 0.96 | 0.40 |
| Z1-CORR | 578 | 572 | 347 | 0.71 | 0.72 | 0.77 |
| Z1-CONF | 544 | 807 | 1486 | 0.54 | 0.35 | 0.11 |
| Z2-SW | 1384 | 1397 | 1400 | 0.30 | 0.33 | 0.32 |
| Z2-E | 2494 | 1530 | 2460 | 0.38 | 0.52 | 0.34 |
| Z2-INT | 506 | 445 | 581 | 0.50 | 0.57 | 0.31 |
| Z2-NE | 1841 | 1981 | 2040 | 0.37 | 0.42 | 0.26 |
| Z2-S | 490 | 492 | 687 | 0.97 | 0.90 | 0.57 |
| Z2-W | 263 | 248 | 364 | 0.00 | 0.00 | 0.00 |
| Z3-SW | 1562 | 1436 | 1400 | 0.27 | 0.28 | 0.32 |
| Z3-E | 2475 | 2463 | 2460 | 0.72 | 0.44 | 0.34 |
| Z3-INT | 463 | 463 | 581 | 0.36 | 0.35 | 0.31 |
| Z3-NE | 1544 | 1726 | 2040 | 0.40 | 0.37 | 0.26 |
| Z3-S | 732 | 740 | 687 | 0.11 | 0.10 | 0.57 |
| Z3-W | 294 | 271 | 364 | 0.25 | 0.37 | 0.00 |

Table 4.3 Zone air flow rate comparison continued

| Zone | Area ($m^2$) | Volume ($m^3$) | Max $V_{zs}$ (L/s·$m^2$) | | | Max ACH | | |
|---|---|---|---|---|---|---|---|---|
| | | | Trend data | | Design | Trend data | | Design |
| | | | 2013 | 2014 | | 2013 | 2014 | |
| Z1-S | 158 | 552 | 9.3 | 8.5 | 16 | 9.6 | 8.8 | 16 |
| Z1-NE | 239 | 836 | 3.0 | 3.0 | 2.9 | 3.0 | 3.1 | 3.0 |
| Z1-NW | 130 | 454 | 3.6 | 3.6 | 6.4 | 3.8 | 3.7 | 6.6 |
| Z1-CORR | 254 | 889 | 2.3 | 2.3 | 1.4 | 2.3 | 2.3 | 1.4 |
| Z1-CONF | 155 | 541 | 3.5 | 5.2 | 9.6 | 3.6 | 5.4 | 9.9 |
| Z2-SW | 100. | 287 | 14 | 14 | 14 | 17.4 | 17.5 | 18 |
| Z2-E | 360. | 1030 | 6.9 | 4.2 | 6.8 | 8.7 | 5.3 | 8.6 |
| Z2-INT | 208 | 388 | 2.4 | 2.1 | 2.8 | 4.7 | 4.1 | 5.4 |
| Z2-NE | 162 | 596 | 11 | 12 | 13 | 11 | 12 | 12 |
| Z2-S | 130. | 464 | 3.8 | 3.8 | 5.3 | 3.8 | 3.8 | 5.3 |
| Z2-W | 135 | 373 | 2.0 | 1.8 | 2.7 | 2.5 | 2.4 | 3.5 |
| Z3-SW | 100. | 287 | 16 | 14 | 14 | 20 | 18 | 18 |
| Z3-E | 360. | 1030 | 6.9 | 6.8 | 6.8 | 8.6 | 8.6 | 8.6 |
| Z3-INT | 208 | 388 | 2.2 | 2.2 | 2.8 | 4.3 | 4.3 | 5.4 |
| Z3-NE | 162 | 596 | 9.5 | 11 | 13 | 9.3 | 10.4 | 12 |
| Z3-S | 130. | 464 | 5.6 | 5.7 | 5.3 | 5.7 | 5.7 | 5.3 |
| Z3-W | 135 | 373 | 2.2 | 2.0 | 2.7 | 2.8 | 2.6 | 3.5 |

The zone supply air temperature ($T_{zs}$) from the perimeter heating terminals were recorded in only three rooms. The $T_{zs}$ for these thermal zones were compared to the corresponding BAS set point (Figure 4.5), which showed they followed the reset profile; however, some overheating occasionally occurred in all rooms and room 120-03 (Z1-S) rarely followed the reset profile when $T_{oa}$ was less than -5 °C, indicating a possible fault. The maximum zone reheat was calculated as 18.2 °C by finding the maximum difference between $T_s$ and $T_{zs}$. It was assumed that the maximum $T_{zs}$ found based on these three rooms was representative of all zones. Air temperature change within the ducts was assumed negligible.

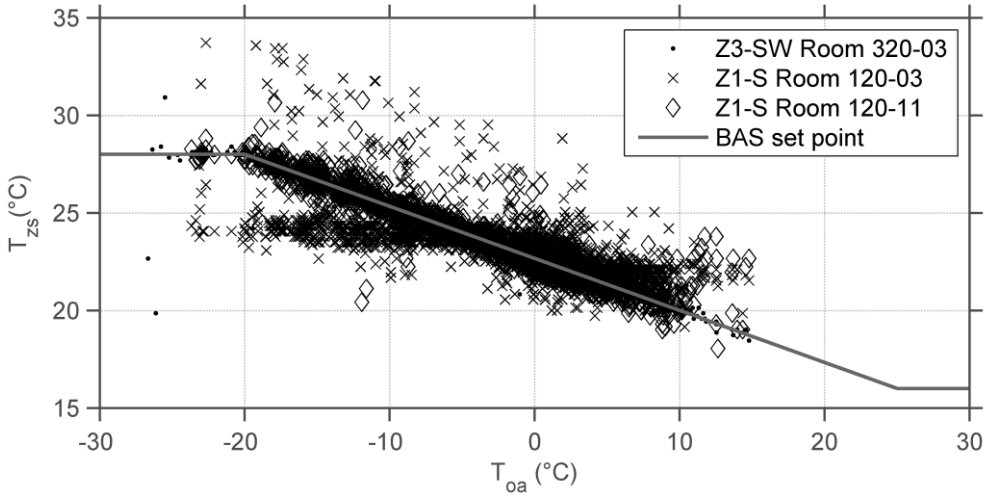


Figure 4.5 Perimeter zone supply air temperature

### *4.3.1 Summary of zone level trend data analyses*

Analysis of heating season performance showed large and small $T_z$ variations in perimeter and interior zones, respectively. Comparing $V_{zs}$ trend data to design specifications revealed that occupant numbers in some zones may be smaller than designed for. No zone ACH greatly exceeded the design value, which demonstrated that all maximum $V_{zs}$ requirements were met. A fault may have occurred in room 120-03 (Z1-S) because $T_{zs}$ did not follow the reset profile. Overall, there were no substantial changes in $T_z$ and $V_{zs}$ between the 2013 and 2014 heating seasons.

## *4.4 System Level Trend Data Analysis*

System level trend data were analysed to generate inputs, create performance reports, and identify faults. System level performance was compared to design values in Section 4.5. All tables in this section were considered performance reports.

### *4.4.1 AHUs*

Analysis of system level trends provided insight into the field performance of HVAC components. The $T_s$ (Figure 3.7) was compared to the BAS reset set point as a function of $T_{oa}$ (Figure 4.6). Linear regression (Table 4.4) showed that $T_s$ followed the reset profile.

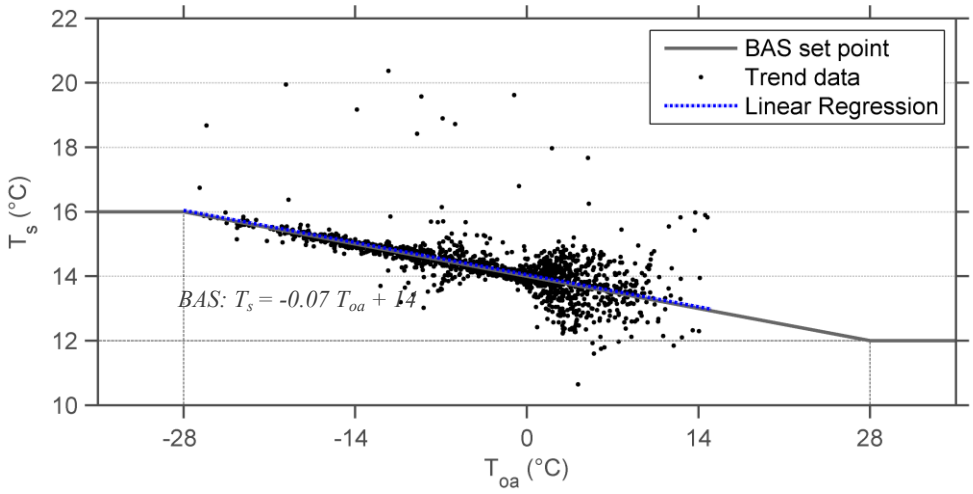


Figure 4.6 Supply air temperature trend data and reset profile comparison

Table 4.4 Supply air temperature generated from trend data

| | Supply air reset (°C) | | | |
|---|---|---|---|---|
| | Trend data | | BAS set point | |
| | 2013 | 2014 | | |
| Supply-high | 16.0 | 16.0 | 16 | |
| Outside-low | -28 | -28 | -28 | |
| Supply-low | 12.1 | 12.1 | 12 | |
| Outside-high | 28 | 28 | 28 | |
| | Linear equation: $c_2 \cdot T_{oa} + c_1$ | | | |
| | 2013 | | 2014 | |
| | $c_2$ | $c_1$ | $c_2$ | $c_1$ |
| Trend data | -0.07 | 14 | -0.06 | 14 |

The measured reset profile was estimated semi-automatically from the $T_s$ trend data (Table 4.4) because the AACT could not automatically calculate change points when reset profiles were followed. All change points were estimated manually in the AACT. Two methods called inward and outward were used to generate reset profiles. In each method the user entered the approximate change points for the outside-low and outside-high air temperatures. The inward method is discussed next and the outward method is discussed in Section 4.4.5.

The inward method used the least squares method to create a line from linear regression. The supply-high and supply-low temperatures were generated as the values

when the outside-low and outside-high were evaluated using the linear equation from regression. It was clear that $T_s$ followed the BAS reset profile so the outside-low and outside-high temperatures were entered as the values in the BAS set point (Table 4.4).

A performance report was created (Table 4.5) in terms of maximum, minimum, median, and median absolute deviations of (1) outside ($T_{oa}$), $T_s$, mixed ($T_m$), and return ($T_r$) air temperatures, (2) supply ($V_s$) and return ($V_r$) air flow rates, and (3) supply ($RH_s$), and return ($RH_r$) air relative humidity trend data. The $T_m$, $T_r$, $RH_s$, and $RH_r$ were averaged across the AHUs and $V_s$ and $V_r$ were summed from the trend data for each fan. The $T_s$ was not averaged because it recorded the overall temperature from both AHUs (Figure 3.7). Comparison between the 2013 and 2014 heating season showed that no substantial changes in performance occurred.

Table 4.5 AHUs performance report obtained directly from trend data

| | 2013 | | | | | 2014 | | | | |
|---|---|---|---|---|---|---|---|---|---|---|
| | Max | Min | ($\mu_{½}$ ± *MAD*) | | | Max | Min | ($\mu_{½}$ ± *MAD*) | | |
| $T_{oa}$ (°C) | 14.8 | -26.7 | -1.1 | ± | 4.6 | 10.7 | -25.3 | -6.9 | ± | 5.3 |
| $T_s$ (°C) | 22.5 | 10.7 | 14.2 | ± | 0.4 | 20.4 | 9.1 | 14.5 | ± | 0.4 |
| $T_m$ (°C) | 23.2 | -3.9 | 10.8 | ± | 0.8 | 20.8 | -3.0 | 10.6 | ± | 1.0 |
| $T_r$ (°C) | 25.0 | 23.3 | 24.2 | ± | 0.2 | 24.6 | 21.7 | 23.6 | ± | 0.2 |
| $V_s$ (L/s) | 25,500 | 16,400 | 20,800 | ± | 1,400 | 26,000 | 17,000 | 19,100 | ± | 1,200 |
| $V_r$ (L/s) | 5,000 | 1,890 | 3,000 | ± | 472 | 5,360 | 2,000 | 3,000 | ± | 380 |
| $RH_s$ (%) | 72.3 | 10.0 | 55.0 | ± | 1.4 | 72.2 | 7.9 | 51.6 | ± | 1.8 |
| $RH_r$ (%) | 31.0 | 17.0 | 25.5 | ± | 0.05 | 39.7 | 11.7 | 30.0 | ± | 0.1 |

The large variation of $V_s$ at all outdoor air temperatures (Figure 4.7) suggested that $V_s$ was primarily dependent on occupant sensor status and building loads. However, $V_s$ increased slightly when $T_{oa}$ was less than -10 °C suggesting that low outdoor air temperatures did influence $V_s$.

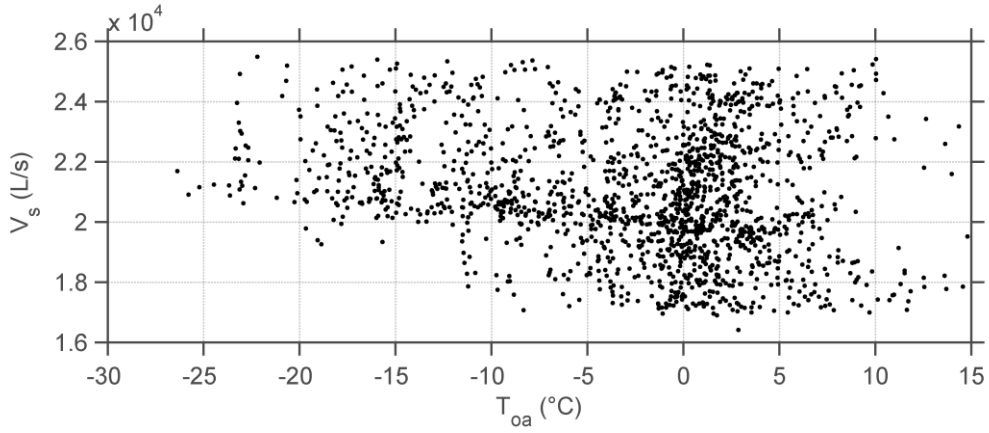


Figure 4.7 Supply air flow rate vs. outdoor air temperature

### *4.4.2 Mixing air damper analysis*

Simultaneous analysis of the heat recovery coils and estimated mixing air damper position was required to approximate their performance. The outdoor air flow rate ($V_{oa}$) was not measured and mixing air damper positions were not recorded, during the 2013 heating season, so the ratio of outdoor to supply air flow rate ($\alpha$) (eq. 4.1) was uncertain. The $\alpha$ could also be estimated using temperatures (eq. 4.1) derived from the thermodynamic equations for adiabatic mixing of two air streams. The air temperature exiting the heat recovery coils ($T_{hr}$) (Figure 3.8), required to calculate the heat recovery heat flow rate and effectiveness, was also not measured. In fact, measuring $T_{hr}$ would be difficult because the air exiting the heat recovery coils was immediately mixed with the return air.

$$\alpha = \frac{V_{oa}}{V_s} = \frac{T_m - T_r}{T_{oa} - T_r} \qquad \text{eq. 4.1}$$

There were three distinct heat recovery and mixing air damper operating conditions that were summarized in Table 4.6 and shown as regions I, II, and III in Figure 4.8. Each region was defined manually by estimating the approximate corresponding change point ($T_{oa} - T_r$).

Table 4.6 Heat recovery operation summary

| Region | Date | Description |
|---|---|---|
| I | Oct 1st to Dec 22nd, 2012 | When $T_{oa}$ was less than 8 °C ($T_{oa} - T_r$ < -15 °C) heat recovery should operate to heat the outdoor air. However, heat recovery never activated because pump P03 did not function due to an electrical system related fault. |
| II | Jan 7th to Mar 31st, 2013 | Pump P03 operated at a constant flow rate and heat recovery heated the outdoor air to a constant temperature as $T_{oa}$ became colder (-30 °C < $T_{oa} - T_r$ < -15 °C). |
| III | Jan 7th to Mar 31st, 2013 | Pump P03 continued to operate and valve PV-3 opened to maintain the glycol temperature entering the heat recovery coils in contact with the exhaust air (SR1) ($T_{hra}$) to 4 °C. The heat recovery heat flow rate to the outdoor air was limited because of frost control causing $T_m$ to decrease as $T_{oa}$ became colder ($T_{oa}$ < -6 °C) ($T_{oa} - T_r$ < -30 °C). |

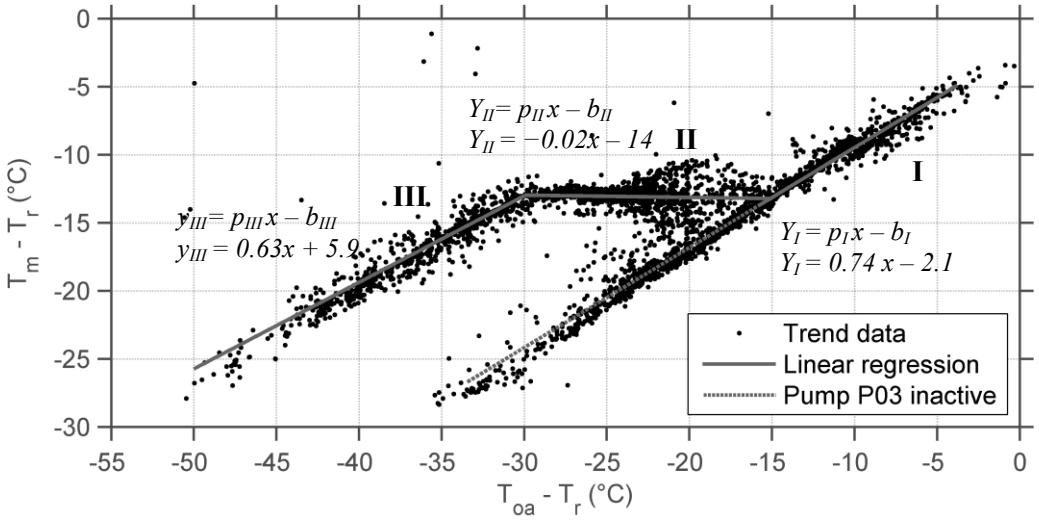


Figure 4.8 Temperatures of heat recovery and mixing air dampers operation

Based on the BAS control sequence (Chapter 3) the mixing air dampers should have been open 100% in all regions. The data in region I had a relatively constant slope, which may confirm that the mixing air damper positions were approximately fixed; however, it was uncertain if they were 100% open. This section used two methods to calculate $\alpha$ called the linear regression and time series methods. Each method used either temperatures or air flow rates.

4.4.2.1 Linear regression method

The linear regression method was first used to estimate $\alpha_I$ (i.e., $\alpha$ in region I) and the mixing air damper position using two steps. First, $\alpha_I$ was estimated as the slope of the line from regression (Figure 4.8) (Sellers 2003; Moser 2013) when heat recovery was inactive (i.e., region I) using temperatures (eq. 4.2). The slope of the lines in regions II and III did not represent $\alpha_{II}$ (i.e., $\alpha$ in region II) or $\alpha_{III}$ because heat recovery was active.

$$\alpha_I = \frac{T_{m_I} - T_{r_I}}{T_{oa_I} - T_{r_I}} \qquad \text{eq. 4.2}$$

Note, $T_r$, which influenced the estimation of $\alpha$, was measured upstream of the return air fan at a relatively constant temperature for all regions. The $T_r$ passing through the mixing air dampers was estimated (Figure 4.9) by adding the estimated air temperature rise across the fan, explained in Section 4.4.4. The $T_r$ downstream of the fan had estimated mean values of 23.4, 24.0, and 24.3 °C for regions I-III, respectively with an uncertainty of ± 0.8 °C.

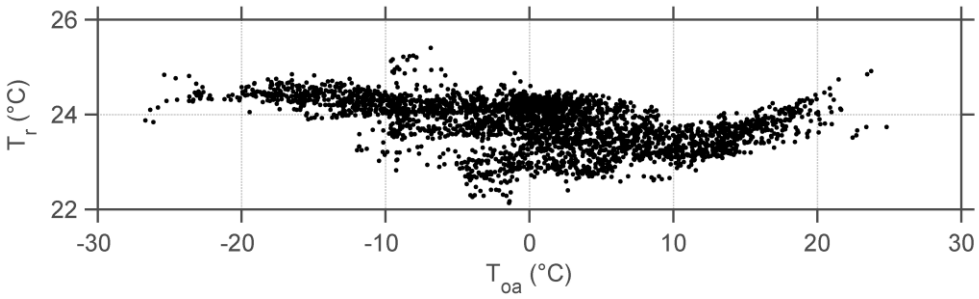


Figure 4.9 Return air temperature for regions I-III

Second, assume that the mixing air dampers were 100% open (i.e., expected from BAS code) and calculate $\alpha_I$ using air flow rates (eq. 4.3) with linear regression (Figure 4.10). Assuming the mixing air dampers 100% open indicates that $V_{oa}$ is the difference between $V_s$ and $V_r$. If $\alpha_I$ calculated using temperatures and air flow rates were equal or within the bounds of their uncertainty it would be reasonable to assume that the mixing air dampers were 100% open in region I.

$$\alpha_I = \frac{V_{oa_1}}{V_{s_1}} = \frac{V_{s_1} - V_{r_1}}{V_{s_1}} \qquad \text{eq. 4.3}$$

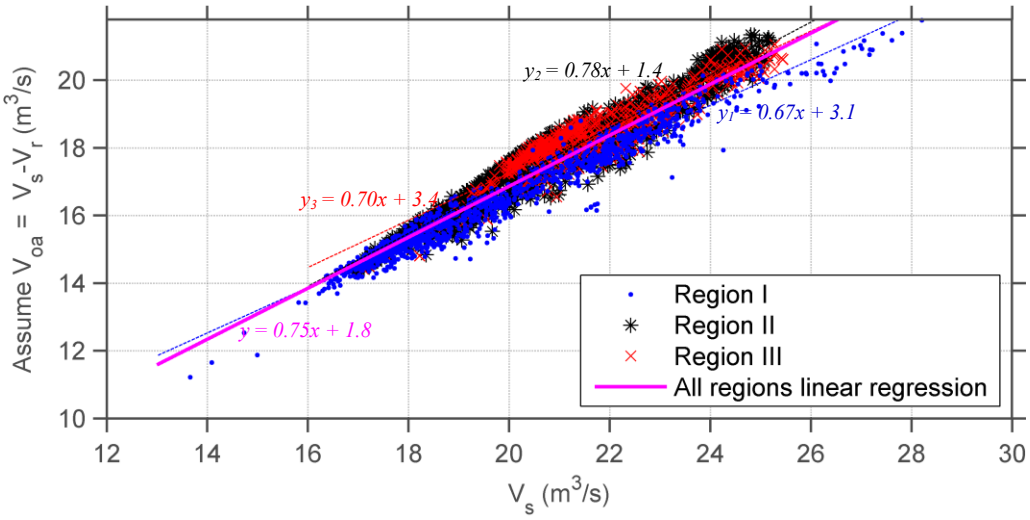


Figure 4.10 Outdoor air flow ratio using linear regression method with air flow rates

Comparisons between the estimated $\alpha$, uncertainty, and coefficients of determination ($R^2$) calculated using air temperatures and flow rates are shown in Table 4.7. The $\alpha_I$ values calculated as a function of air flow rates and temperatures were near their uncertainty bounds in Region I. The values of $\alpha$ in regions II and III were also similar to the $\alpha_I$ values. Therefore, it was estimated that the mixing air dampers were 100% open in all regions. This assumption was strengthened using mixing air damper position trend data, recorded from July 1st, 2013 onward (Figure 4.11), which showed the mixing air dampers 100% open when $T_{oa}$ was less than 10 °C and occasionally 100% open between 10 and 15 °C.

Table 4.7 Estimated outdoor air flow ratio using the linear regression method

| | Region | | | | | |
|---|---|---|---|---|---|---|
| | I | | II | | III | |
| | $\alpha$ | $R^2$ | $\alpha$ | $R^2$ | $\alpha$ | $R^2$ |
| $\alpha = f(T_m, T_r, T_{oa})$ | 0.74 ± 0.04 | 0.97 | - | - | - | - |
| $\alpha = f(V_s, V_r)$ | 0.67 ± 0.03 | 0.96 | 0.78 ± 0.03 | 0.94 | 0.70 ± 0.03 | 0.88 |

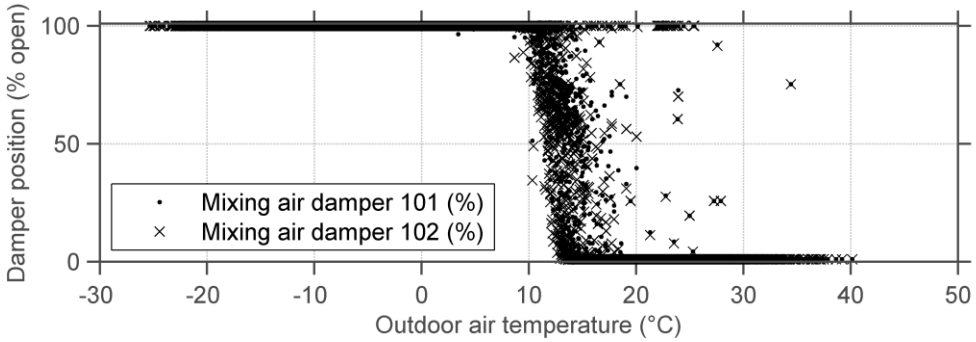


Figure 4.11 Mixing air damper position from July 1st, 2013 onward

4.4.2.2 Time series method

This section estimates $\alpha$ using the time series method and provides comparison (Table 4.8) to the linear regression method. The time series method estimates $\alpha$, using temperatures or air flow rates, as the mean value over a period of time. The $\alpha$ was calculated using the time series method in region I (Figure 4.12) and as a function of air flow rate in regions I-III (Figure 4.13). Each figure also compares the value found using the linear regression method. Comparing the results from both methods revealed that their difference was greater than their uncertainties (Table 4.8). In fact, when comparing both methods using air flow rates (Figure 4.13) the AHUs lacked the capacity to produce an $\alpha$ using the linear regression method based on the trend data.

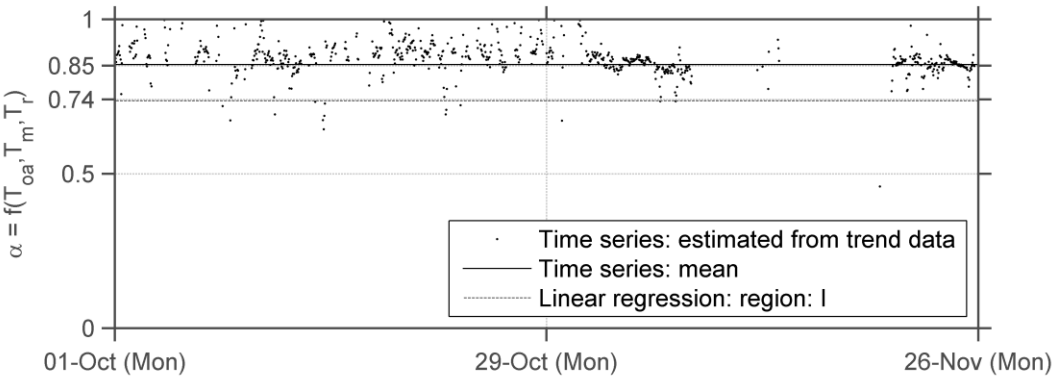


Figure 4.12 Outdoor air flow ratio using time series method with temperatures for region I

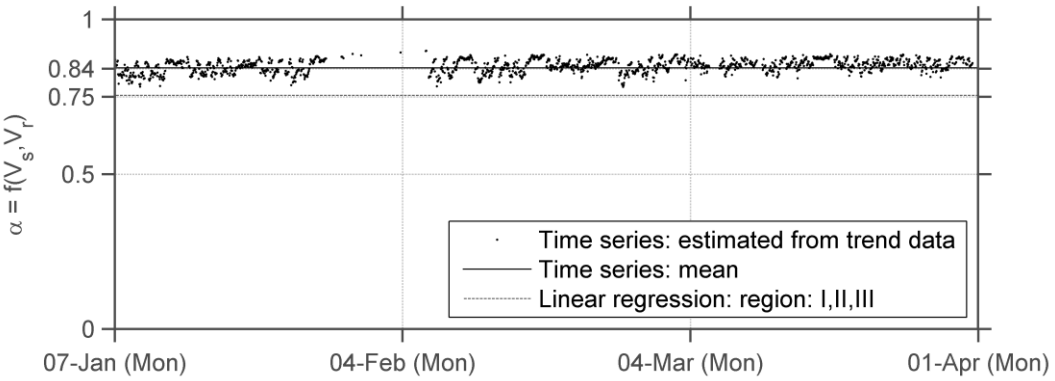


Figure 4.13 Outdoor air flow ratio using time series method with air flow rates for regions I, II, and III

It should be noted that $\alpha$ varied slightly throughout each day from approximately 0.81 to 0.88 using the time series method as a function of air flow rates (Figure 4.13). This occurred because the rate of change of $V_s$ was greater than $V_r$ throughout a day.

Table 4.8 Outdoor air flow ratio using linear regression and time series methods

| Method | Function | Region(s) | Max | Min | Mean |
|---|---|---|---|---|---|
| Time series | $\alpha = f(T_m, T_r, T_{oa})$ | I,II,III | 1.0 | 0.61 | 0.85 ± 0.05 |
| | $\alpha = f(V_s, V_r)$ | I,II,III | 0.90 | 0.73 | 0.84 ± 0.03 |
| Linear regression | $\alpha = f(T_m, T_r, T_{oa})$ | I | - | - | 0.74 ± 0.04 |
| | $\alpha = f(V_s, V_r)$ | I,II,III | - | - | 0.75 ± 0.03 |

The values of $\alpha$ used in the following analysis were calculated as a function of air flow rates using both methods to determine whether the differences affected the estimated heat recovery heat flow rate. They were calculated as a function of air flow rate instead of temperature because their uncertainty was slightly smaller. Theoretically, the y-intercept in the lines from linear regressions (Figure 4.8 and Figure 4.10) should be zero. Bias and random errors in the trend data probably contributed to a non-zero y-intercept (Figure 4.8 and Figure 4.10), which was one reason for the differing values for $\alpha$ when comparing the time series and linear regression methods.

### *4.4.3 Heat recovery analysis*

This section continues the use of the mixing damper and heat recovery analysis plot (Figure 4.8) by first estimating $T_{hr}$. The $T_{hr}$ was estimated by comparing $T_m - T_r$ when heat recovery (Figure 4.8) was active and inactive (i.e., comparing regions II and III to region I). Subtracting the linear equations from regression in region I from region II (Figure 4.8) resulted in eq. 4.4 using $T_{oa}$ as the variable, an average $T_r$, and constant $\alpha$ across each region (eq. 4.5). Assuming average $T_r$ was necessary because the number of data points in each region varied.

$$\left(T_{m_{II}} - \bar{T}_{r_{II}}\right) - \left(T_{m_I} - \bar{T}_{r_I}\right) = \left(p_{II}\left(T_{oa} - \bar{T}_{r_{II}}\right) + b_{II}\right) - \left(p_I\left(T_{oa} - \bar{T}_{r_I}\right) + b_I\right) \qquad \text{eq. 4.4}$$

*where:* $\bar{T}_{r_I}$ and $\bar{T}_{r_{II}}$ = average return air temperatures after the return fans in regions I and II, respectively

$p_{II}$ = slope of the linear regression in region I

$p_{II}$ = slope of the linear regression in region II

$b_I$ = y-intercept of the linear regression in region I

$b_{II}$ = y-intercept of the linear regression in region II

$$\alpha = \alpha_I = \frac{T_{m_I} - T_{r_I}}{T_{oa_I} - T_{r_I}} = \alpha_{II} = \frac{T_{m_{II}} - T_{r_{II}}}{T_{hr_{II}} - T_{r_{II}}} = \alpha_{III} = \frac{T_{m_{III}} - T_{r_{III}}}{T_{hr_{III}} - T_{r_{III}}} \qquad \text{eq. 4.5}$$

Next, $(T_{m_I} - T_{r_I})$ and $(T_{m_{II}} - T_{r_{II}})$ from eq. 4.5 were substituted into the left-hand side of eq. 4.4 resulting in eq. 4.6. Rearranging eq. 4.6 and solving for $T_{hr_{II}}$ resulted in eq. 4.7

$$\alpha\left(T_{hr_{II}} - \bar{T}_{r_{II}}\right) - \alpha\left(T_{oa_I} - \bar{T}_{r_{II}}\right) = \left(p_{II}\left(T_{oa} - \bar{T}_{r_{II}}\right) + b_{II}\right) - \left(p_I\left(T_{oa} - \bar{T}_{r_I}\right) + b_I\right) \qquad \text{eq. 4.6}$$

$$T_{hr_{II}} = \frac{1}{\alpha}\left[(p_{II} - p_I + \alpha)T_{oa} + (p_I - \alpha)\bar{T}_{r_I} + (\alpha - p_{II})\bar{T}_{r_I} + (b_{II} - b_I)\right] \qquad \text{eq. 4.7}$$

The $T_{hrIII}$ was estimated (eq. 4.8) using the same procedure as above with region III instead of II. The linear equation from regression in region I was extrapolated into region III to estimate $T_{hrIII}$. Assuming $T_r$ remained constant would cause $T_{oa} - T_r$ to decrease linearly. This was reasonable if the heating coils, zone reheat, and internal loads would maintain a constant $T_r$ if heat recovery was unavailable. Each of these components operated well below design capacity, as discussed in Section 4.5.

$$T_{hr_{III}} = \frac{1}{\alpha}\left[(p_{III} - p_I + \alpha)T_{oa} + (p_I - \alpha)\bar{T}_{r_I} + (\alpha - p_{III})\bar{T}_{r_{III}} + (b_{III} - b_I)\right] \qquad \text{eq. 4.8}$$

The estimated $T_{hr}$ in regions II and III were calculated using α determined from the linear regression and time series methods (Figure 4.14). The coefficients of the linear equations used to estimate $T_{hr}$ as a function of $T_{oa}$ (eq. 4.7 and eq. 4.8) in the form $c_2 \cdot T_{oa} + c_1$ are summarized in Table 4.9. The $T_{hr}$ estimates are quite close considering the previous assumptions and the fact that the average $T_m$ had an uncertainty of ± 0.6 °C. The other reason for this good agreement was because the amount of return air mixing with the outdoor air in the Genome Building was small relative to the supply air. Thus the estimated $T_{hr}$ was insensitive to $\alpha$. The change points ($CP$) of $T_{oa}$ in Table 4.9 were calculated from the intersection of the $T_{hr}$ equations in regions II (eq. 4.7) and III (eq. 4.8) (Figure 4.14) and the maximum $T_{oa}$ when heat recovery was activated.

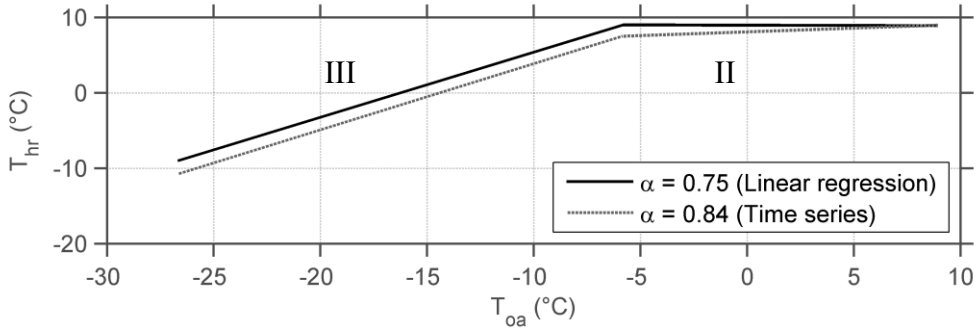


Figure 4.14 Estimated air temperature exiting the heat recovery coils

The heat recovery heat flow rate ($\dot{Q}_{hr}$) was estimated (Figure 4.15) by taking an energy balance across the outdoor air side of the coils (eq. 4.9). The linear equation found from regression for each region is shown in Table 4.9. The CV(RMSE) of $\dot{Q}_{hr}$ when comparing $\alpha$ calculated using the linear regression and time series methods was 0.6%. This demonstrated that the method used to estimate $\alpha$ had a small influence on $\dot{Q}_{hr}$. The change points of $T_{oa}$ in Table 4.9 were calculated when the linear equation of $\dot{Q}_{hr}$ (Figure 4.15) crossed the x-axis and when regions II and III intersected.

Table 4.9 Summary of estimated heat recovery performance

| | Linear equation: $c_2 \cdot T_{oa} + c_1$ | | | | | | | |
|---|---|---|---|---|---|---|---|---|
| | 2013 | | | | 2014 | | | |
| | $\alpha$ | $c_2$ | $c_1$ | Change point | $\alpha$ | $c_2$ | $c_1$ | Change point |
| $T_{hrII}$ (°C) | 0.75 | 0.0 | 9.0 | -5.8<$T_{oa}$<8.9 | 0.71 | 0.0 | 8.5 | -7.7<$T_{oa}$<8.3 |
| | 0.84 | 0.09 | 8.1 | -5.8<$T_{oa}$<8.9 | 0.84 | 0.2 | 7.4 | -7.7<$T_{oa}$<8.3 |
| $T_{hrIII}$ (°C) | 0.75 | 0.86 | 14 | $T_{oa}$<-5.8°C | 0.71 | 1.0 | 16 | $T_{oa}$<-7.7 °C |
| | 0.84 | 0.88 | 13 | $T_{oa}$<-5.8°C | 0.84 | 1.0 | 14 | $T_{oa}$<-7.7 °C |
| $\dot{Q}_{hrII}$ (kW) | 0.75 | -19 | 174 | -6.2<$T_{oa}$<8.9 | 0.71 | -17 | 151 | -8.3<$T_{oa}$<8.3 |
| | 0.84 | -19 | 176 | -6.2<$T_{oa}$<8.9 | 0.84 | -17 | 151 | -8.3<$T_{oa}$<8.3 |
| $\dot{Q}_{hrIII}$ (kW) | 0.75 | -4.0 | 270 | $T_{oa}$<-6.2 | 0.71 | -0.6 | 290 | $T_{oa}$<-8.3 |
| | 0.84 | -4.0 | 270 | $T_{oa}$<-6.2 | 0.84 | -0.6 | 290 | $T_{oa}$<-8.3 |
| | ($\mu_{½} \pm MAD$) | | | | ($\mu_{½} \pm MAD$) | | | |
| $V_{hr}$ (L/s) | 0.75 | 11 ± 1 | | | 0.71 | 11 ± 1 | | |
| | 0.84 | 11 ± 1 | | | 0.84 | 11 ± 1 | | |

$$\dot{Q}_{hr} = \alpha V_s \rho_{air} c_{p_{air}} (T_{hr} - T_{oa}) \quad \text{eq. 4.9}$$

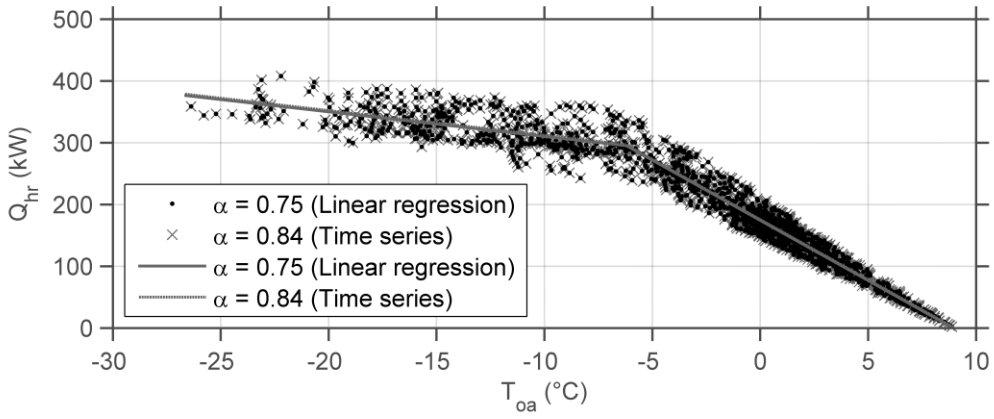


Figure 4.15 Heat recovery heat flow rate

The heat recovery effectiveness ($\varepsilon_{hr}$) was estimated (eq. 4.10) assuming the exhaust air temperature ($T_e$) was equal to $T_r$ without $\Delta T_{fan}$ and the exhaust air flow rate ($V_e$) (eq. 4.11) was equal to the difference between $V_s$ and $V_r$. The $V_e$ was not measured but could be estimated when the mixing air dampers were 100% open (i.e., the return air damper are closed). This $\varepsilon_{hr}$ represented the overall effectiveness of heat transfer between the exhaust and outdoor air (Figure 4.16). The minimum and maximum $\varepsilon_{hr}$ during frost

control varied from 0.3 to 0.5, respectively. If $V_{oa}$, $V_e$, and $T_e$ were measured they could provide a more accurate estimate of $\varepsilon_{hr}$. In this case $V_e$ was always slightly less than $\alpha \cdot V_s$.

$$\varepsilon_{hr} = \frac{\rho_{air} c_{p_{air}} \alpha \cdot V_s (T_{hr} - T_{oa})}{\rho_{air} c_{p_{air}} \min(\alpha \cdot V_s, V_e) \cdot (T_e - T_{oa})} = \frac{(T_{hr} - T_{oa})}{(T_e - T_{oa})} \qquad \text{eq. 4.10}$$

$$V_e = V_s - V_r \qquad \text{eq. 4.11}$$

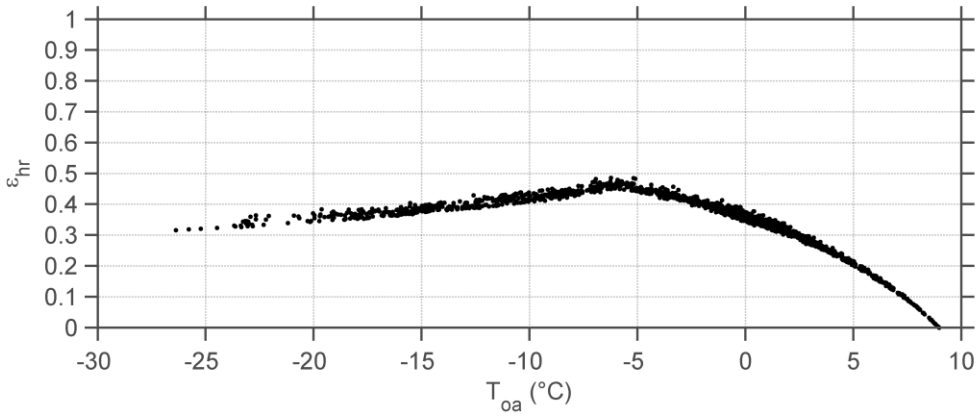


Figure 4.16 Estimated heat recovery effectiveness vs. outdoor air temperature

4.4.3.1 Verification of assumptions in heat recovery analysis

The glycol flow rate in the heat recovery coils ($V_{hr}$) (Figure 3.8) was estimated using trend data and was compared to the constant speed pump P03 design specifications and spot measurements to verify the earlier assumptions. On the glycol-side, the BAS recorded the glycol temperature arriving ($T_{hra}$) and exiting ($T_{hre}$) the exhaust air heat recovery coils (SR1-103) (Figure 3.8).

In region II, valve PV-3 was closed based on the BAS control sequence and $T_{hra}$ was assumed to equal the temperature of glycol exiting the outdoor air heat recovery coils (SC1-101 & -102) ($T_{hro}$) (Figure 3.8). The $V_{hr}$ was calculated using an energy balance across the outdoor air heat recovery coils (SC1-101 & -102) (eq. 4.12). The heat losses from pipes and temperature rise across the pump were assumed negligible.

$$\dot{Q}_{hr} = \alpha \cdot \mathrm{V}_s \rho_{air} c_{p_{air}} (T_{hr} - T_{oa}) = \alpha_{hr} \cdot \mathrm{V}_{hr} \rho_{glc} c_{p_{glc}} (T_{hre} - T_{hro}) \qquad \text{eq. 4.12}$$

$$\alpha_{hr} = \frac{T_{hre} - T_{hra}}{T_{hre} - T_{hro}} \qquad \text{eq. 4.13}$$

*where:* $\alpha_{hr}$ = ratio of heat recovery glycol flow rate passing through the outdoor-side to the exhaust-side . In region II, $\alpha_{hr}$ equals 1. In region III, $\alpha_{hr}$ varies with $T_{oa}$.

Valve PV-3 opened in region III rendering $V_{hr}$ and $T_{hro}$ uncertain. There were two unknowns and one equation; however, $T_{hra}$ was programmed in the BAS to a constant set point of 4.1 °C (Figure 4.17) in region III, which was controlled by changing PV-3's degree of opening. This information was used to estimate $T_{hro}$ by extrapolating the linear regression of region II into region III as shown in Figure 4.17. This was reasonable assuming $T_r$ always remained constant, which would cause $T_{hro}$ to decrease linearly.

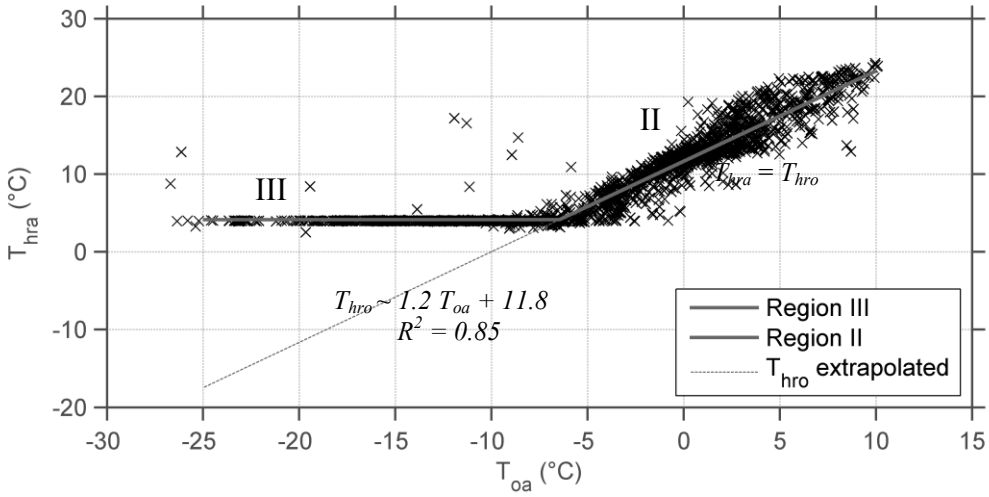


Figure 4.17 Glycol temperature entering coils in exhaust air stream vs. outdoor air temperature

The $V_{hr}$ is estimated (Table 4.9) using eq. 4.12 and is shown in Figure 4.18. The previous assumptions in these calculations made it difficult to estimate $V_{hr}$ near the heat recovery activation temperature (3 °C < $T_{oa}$ < 8 °C). The overall uncertainty of $V_{hr}$ was

not stated because there was no way to propagate the sensor bias error through the previous assumptions; the median and median absolute deviation were used instead.

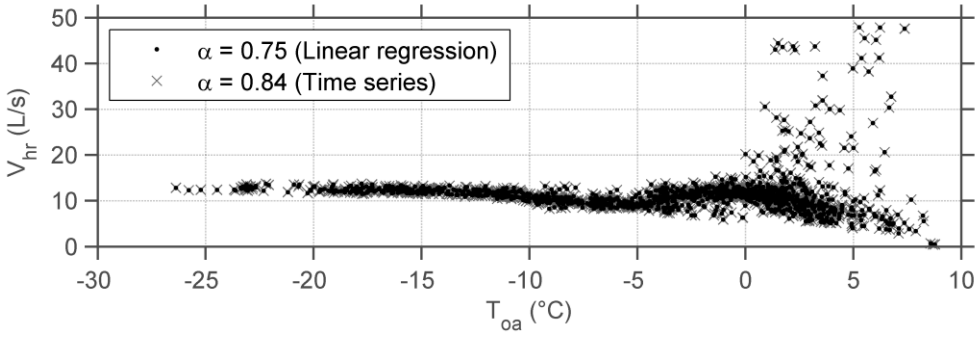


Figure 4.18 Estimated total heat recovery glycol flow rate

Nine spot measurements of $V_{hr}$ were recorded in 5 min intervals on February 26th, 2014 (Table 4.10) using a Model PT400 Portaflow portable ultrasonic flow meter manufactured by Greyline Instruments Inc. (2013). The flow meter had a bias error of ± 2%. The measurements provided a mean flow rate estimate of 10.0 ± 0.5 L/s. The estimated $V_{hr}$ (Table 4.9) for the 2013 and 2014 heating seasons were 10% greater than the spot measured value and 7% smaller than the design specification of 11.8 L/s. Overall, the prior assumptions with the mixing air dampers 100% open, using linear regressions to estimate $T_{hr}$, and using linear regression to extrapolate $T_{hro}$ resulted in a reasonable estimate of $V_{hr}$ compared to its spot measured value and design specification.

Table 4.10 Spot measurements of heat recovery glycol flow rate

| Time | 14:50 | 14:55 | 15:00 | 15:05 | 15:10 | 15:15 | 15:20 | 15:25 | 15:30 | 15:35 |
|---|---|---|---|---|---|---|---|---|---|---|
| $V_{hr}$ (L/s) | 10.1 | - | 9.8 | 9.9 | 10.1 | 10.0 | 9.9 | 10.0 | 10.0 | 9.9 |

### *4.4.4 Temperature rise across the supply air fan*

This section presents the estimation of $\Delta T_{fan}$. This variable was important to measure because it was used to calculate $\dot{Q}_{hc}$ in the AHUs and it was an input in building simulation software. To the author's knowledge, there have been no studies providing

field measurements of $\Delta T_{fan}$. There was one discussion from Haves et al. (1996) that stated the rise was "relatively small (~1 K)".

The temperature difference between $T_s$, measured after all fans (Figure 3.7), and $T_m$, averaged between both AHUs, are shown in Figure 4.19a. The supply ($T_{hca}$) and return ($T_{hcr}$) glycol temperatures in the heating coils (Figure 3.9) are shown in Figure 4.19b. When the glycol temperature differential ($\Delta T_{hc}$) was approximately zero, the difference between $T_s$ and $T_m$ should theoretically equal $\Delta T_{fan}$, assuming isothermal humidification. This was calculated as 3.1 ± 0.7 °C from the mean temperature difference between $T_s$ and $T_m$ ($\Delta T_{sm}$) when the absolute value of $\Delta T_{hc}$ was less than its bias error (± 0.5 °C). This value was large when compared to the default value in eQUEST, which was 1.8 °C. Assuming isothermal humidification was probably incorrect.

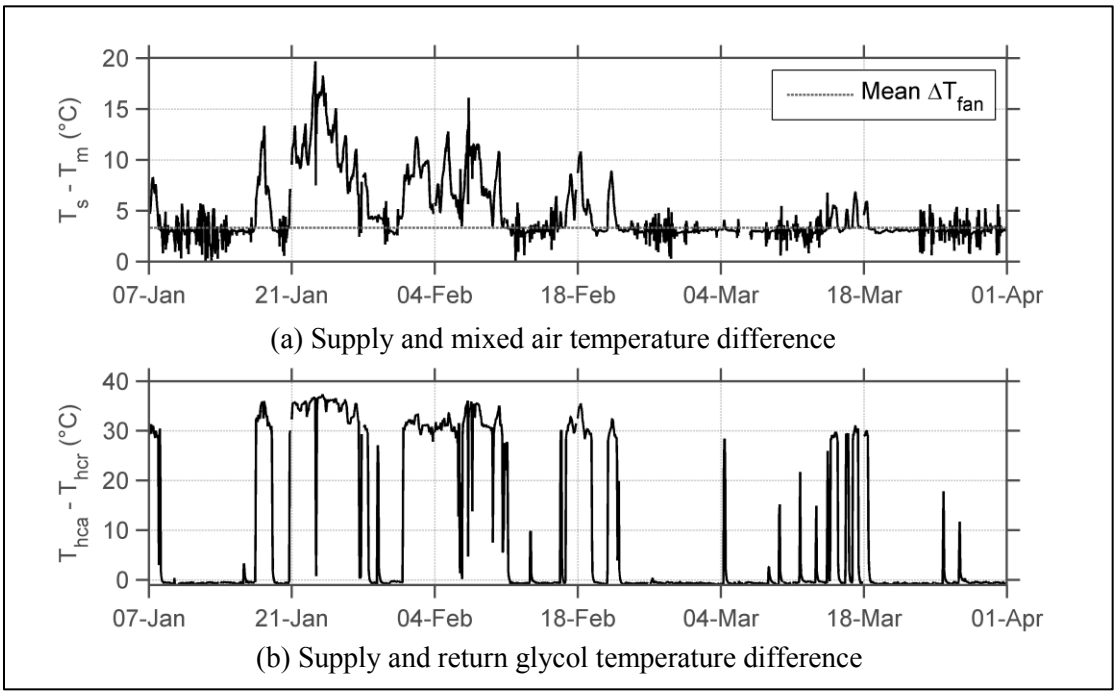

(a) Supply and mixed air temperature difference

(b) Supply and return glycol temperature difference

Figure 4.19 Air and glycol temperature difference comparison for the 2013 heating season

Humidification valve position ($HV$) was not recorded during the 2013 heating season but was recorded from September 1st, 2013 onward. The average $\Delta T_{fan}$ could be estimated when $\Delta T_{hc}$ was less than its associated bias error and when both humidification valve positions ($HV$) were closed as the difference between $T_s$ and $T_m$ (eq. 4.14). A period

plotted from September 1st, 2013 to March 31st, 2014 (Figure 4.20) provided insight to estimating $\Delta T_{fan}$ using trend data. From September 1st, 2013 to October 27th, 2013 $\Delta T_{hc}$ and $HV$ indicated the heating coils and humidification were inactive, respectively. The $\Delta T_{fan}$ estimated during this period is shown in Table 4.11. Only occasionally were these criteria satisfied outside this period. Outside that period humidification and heating coils were regularly active and $\Delta T_{fan}$ could not be calculated. The period from November 25th, 2013 to March 31st, 2014 was used to find the difference between $T_s$ and $T_m$ when the heating coils were inactive but humidification was active ($\Delta T_{sm\_H}$) (eq. 4.15). The $\Delta T_{sm\_H}$ was calculated as 3.2 ± 0.7 °C. The humidification air temperature rise ($\Delta T_H$) was estimated by subtracting $\Delta T_{fan}$ from the mean $\Delta T_{sm\_H}$ (eq. 4.16) which was 1.4 ± 1.0 °C.

$$\Delta T_{fan} = \overline{T_s - T_m},\ \ |T_{hca} - T_{hcr}| \leq bias\ error\ \&\ HV = 0 \qquad \text{eq. 4.14}$$

$$\Delta T_{sm\_H} = \overline{T_s - T_m},\ \ |T_{hca} - T_{hcr}| \leq bias\ error\ \&\ HV > 0 \qquad \text{eq. 4.15}$$

$$\Delta T_H = \Delta T_{sm\_heat} - \Delta T_{fan} \qquad \text{eq. 4.16}$$

Table 4.11 Estimated supply air fan temperature rise summary

| Method | Date | Fan | $\Delta T_{fan}$ (°C) |
|---|---|---|---|
| Trend data | Sep 1st, 2013-Oct 27st, 2013 | Avg. | 1.8 ± 0.7 |
| Short-term | Feb 27th to Mar 20th, 2014 | VA2-1 | 1.3 ± 0.3 |
| Fan electric power | Feb 27th to Mar 20th, 2014 | VA1-1 | 2.2 ± 0.7 |
| | | VA1-2 | 2.0 ± 0.6 |

Overall, eq. 4.14 to eq. 4.16 could be used to estimate $\Delta T_{fan}$ and $\Delta T_H$ over a period with inactive and active heating coils and humidification (e.g., shoulder and heating season).

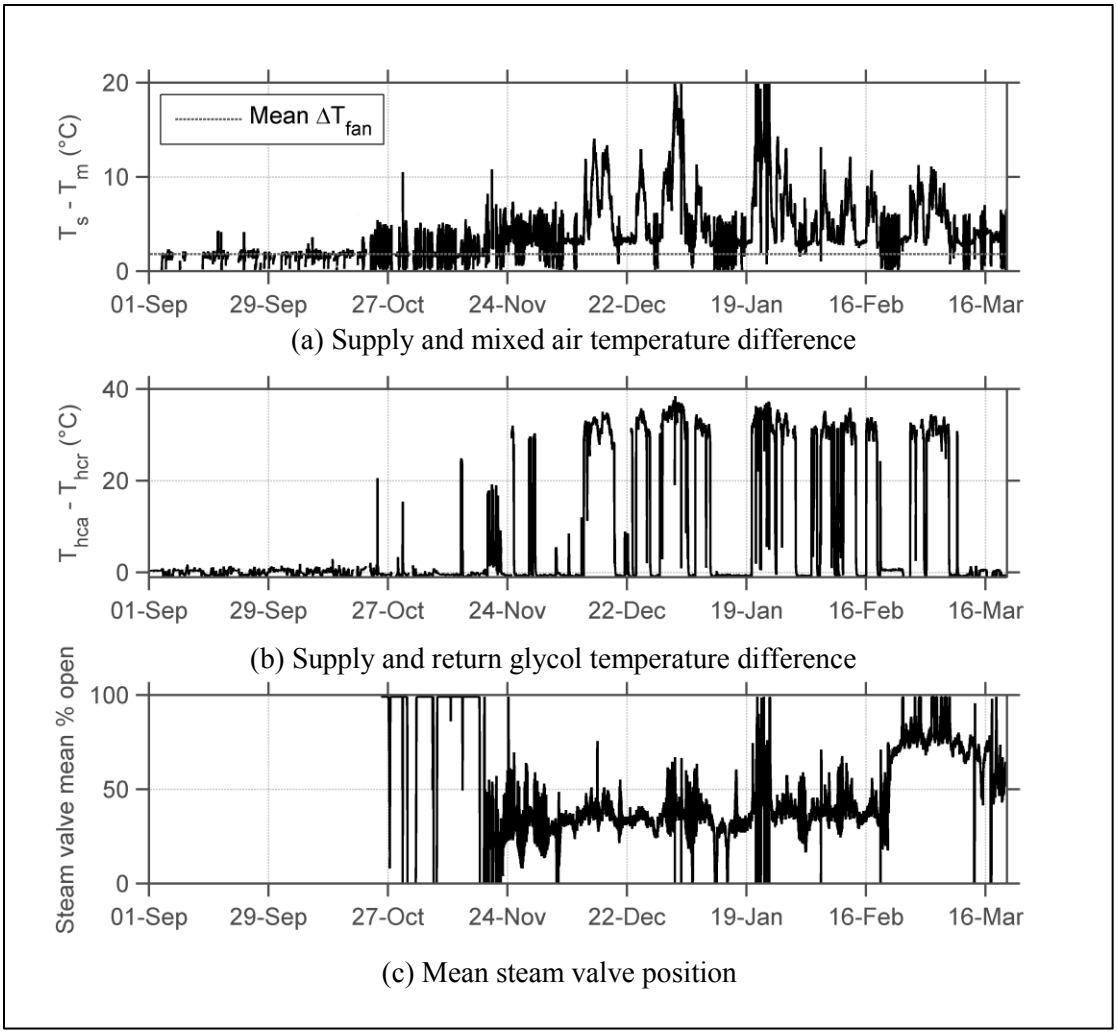


Figure 4.20 Air and glycol temperature differentials and steam valve position

4.4.4.1 Temperature across the supply air fan: short-term

Temperature sensors were placed in the supply air stream before ($T_{BF}$) and after ($T_{AF}$) fan VA2-1 in the AHUs (Figure 3.7) from November 13$^{th}$ to December 5$^{th}$, 2013 with a 2 min sample rate. The temperature sensors consisted of thermistors inside SmartReader 3 data loggers manufactured by ACR Systems Inc. (2013). The sensors had a bias error of ± 0.2 °C, were recently calibrated by the manufacturer, and recorded temperatures, relative to other SmartReader 3 data loggers, within their uncertainty bounds when left at room temperature (i.e., the sensor readings did not drift). The measurements were averaged into 15 min data (i.e., the mean of seven 2 min measurements per 15 min interval) for

synchronization with the trend data. The heating coils were occasionally active in the AHUs which can be seen in Figure 4.21 when $T_{BF}$ was larger than $T_{m101}$. The $\Delta T_{fan}$ estimated from short-term measurements is shown in Table 4.11. The main reason for the difference between the $\Delta T_{fan}$ estimated using trend data and short-term measurements was that $T_{AF}$ had a consistently lower value than the $T_{s101}$ trend data. This demonstrated that the $T_{s101}$ BAS sensor may have drifted or had other issues. It should be noted that the $T_{s101}$ trend data were not used anywhere else in this thesis because the $T_s$ sensor (Figure 3.7) measured the air temperature downstream from both AHUs.

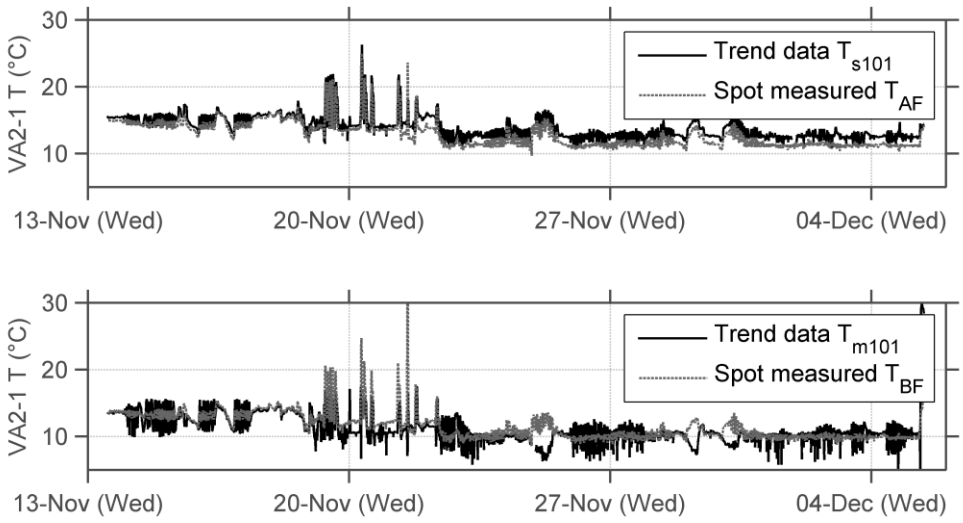


Figure 4.21 Short-term supply and mixed air temperature comparison

4.4.4.2 Estimating $\Delta T_{fan}$ using fan electric power

The $\Delta T_{fan}$ was estimated using supply air flow rate trend data and short-term fan electric power measurements (eq. 4.17) from February 27th to March 20th, 2014.The fan power measurements are described in Appendix A. The $\Delta T_{fan}$ calculated for fans VA1-1 and VA1-2 are summarized in Table 4.11.

$$\Delta T_{fan} = \frac{\dot{W}_{sfan}}{\rho_{air} c_{p_{air}} V_s} \qquad \text{eq. 4.17}$$

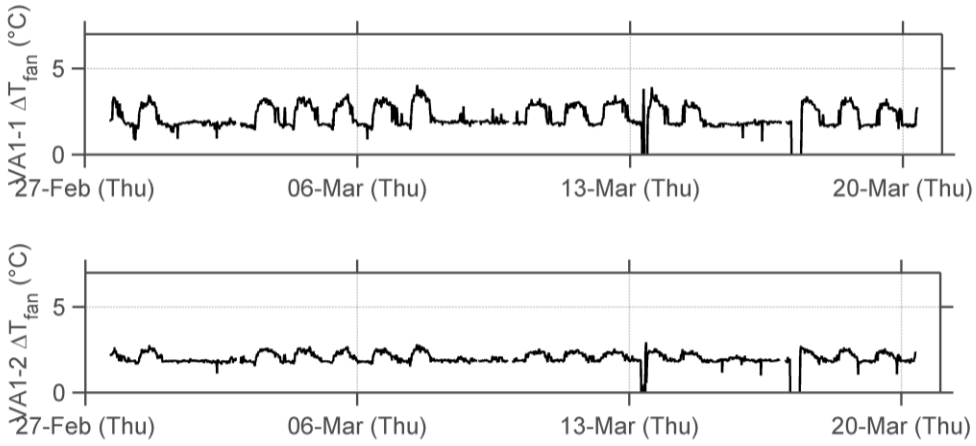


Figure 4.22 Supply air fan temperature rise estimated using fan electric current measurements from February 27th to March 20th, 2014

4.4.4.3 Fan air temperature rise proportional to supply air flow rate

It was important to understand how $\Delta T_{fan}$ varied with $V_s$ because eQUEST modelled $\Delta T_{fan}$ proportional to the ratio of *EIR* to *PLR* (further discussed in Section 4.6.2). Theoretically $\Delta T_{fan}$ increases exponentially proportional to $V_s$ based on the affinity laws for fans in VAV systems. The $\Delta T_{fan}$ estimated from short-term measurements and fan power increased at similar rates proportional to $V_s$ as shown in Figure 4.23 and Figure 4.24. The $\Delta T_{fan}$ found from trend data (Figure 4.25) increased proportionally with $V_s$ but at a slightly smaller rate. The $\Delta T_{fan}$ proportionality to $V_s$ over the range of measured $V_s$ was nearly negligible in each case.

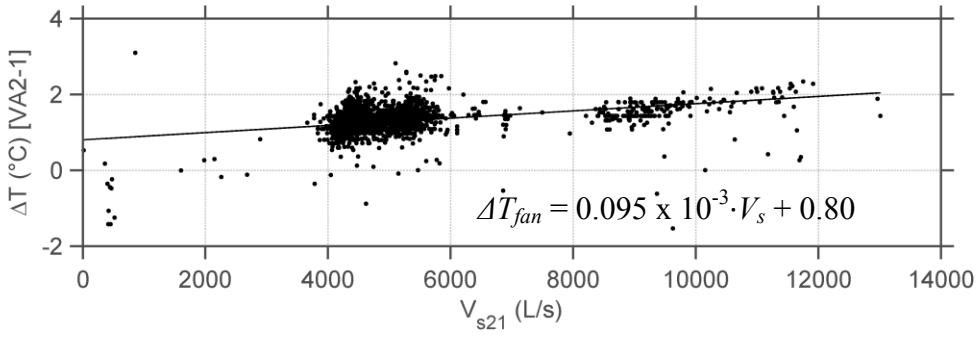


Figure 4.23 Fan air temperature rise from short-term measurements against supply air flow rate

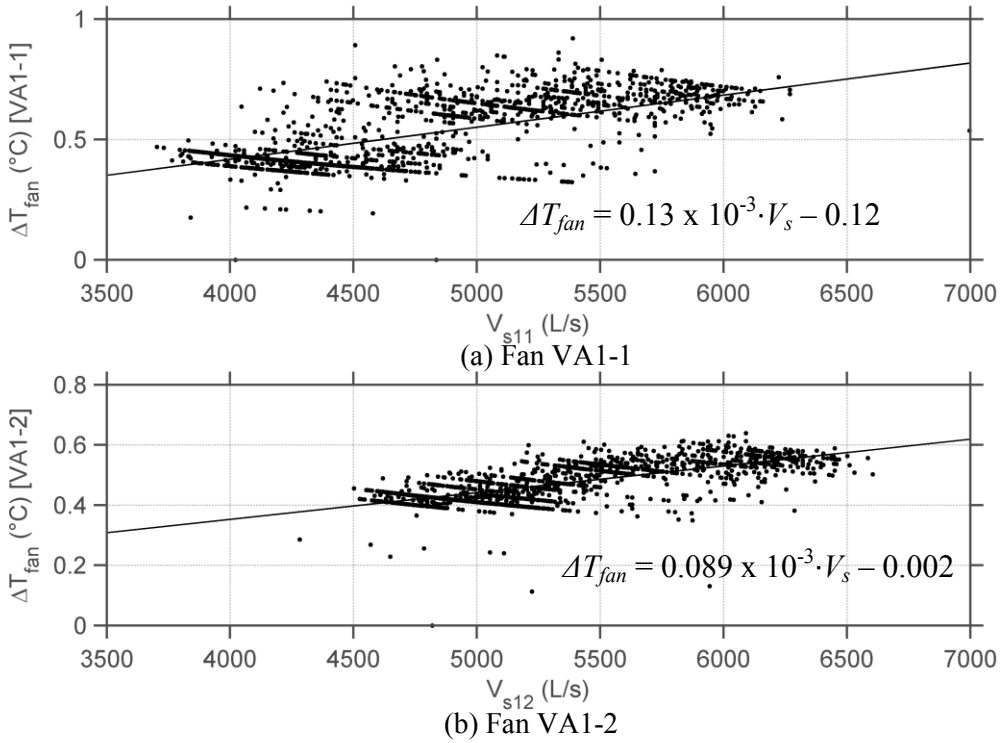


(a) Fan VA1-1

(b) Fan VA1-2

Figure 4.24 Fan air temperature rise from fan power against supply air flow rate

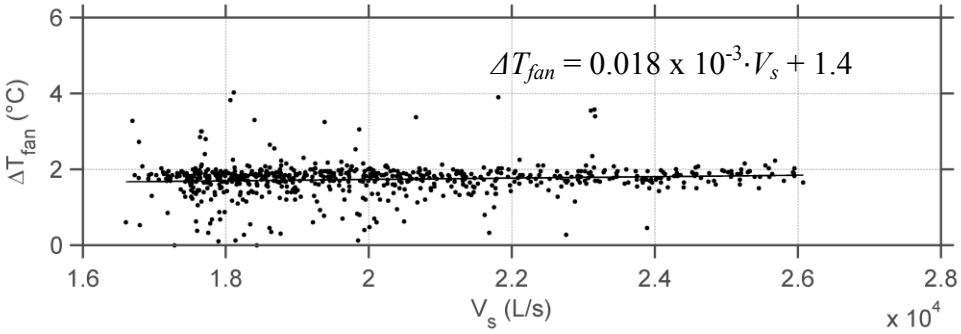


Figure 4.25 Fan air temperature rise from trend data against supply air flow rate

Overall, the $\Delta T_{fan}$ estimated using trend data was near and within the bounds of uncertainty for the values from (1) short-term and (2) calculated from fan power measurements, respectively. The $\Delta T_{fan}$ calculated from trend data was the value used in the following sections of this thesis. If the other values were used it would appear as if the heating coils were activated when, based on $\Delta T_{hc}$, they were not.

### *4.4.5 Heating coil analysis*

The heating coil heat flow rate ($\dot{Q}_{hc}$) (eq. 3.3) was estimated (Figure 4.26) where $T_{hd}$ was calculated using eq. 4.18. The $T_{oa}$ activating the heating coils was calculated as the intersection the of $\dot{Q}_{hc}$ linear equation from linear regression (Figure 4.26) with the x-axis (i.e., range in Table 4.13). A fault with humidification may be responsible for abnormal operation between 0 °C and 8 °C.

$$T_{hd} = T_s - \left(\Delta T_{fan} + \Delta T_H\right) \qquad \text{eq. 4.18}$$

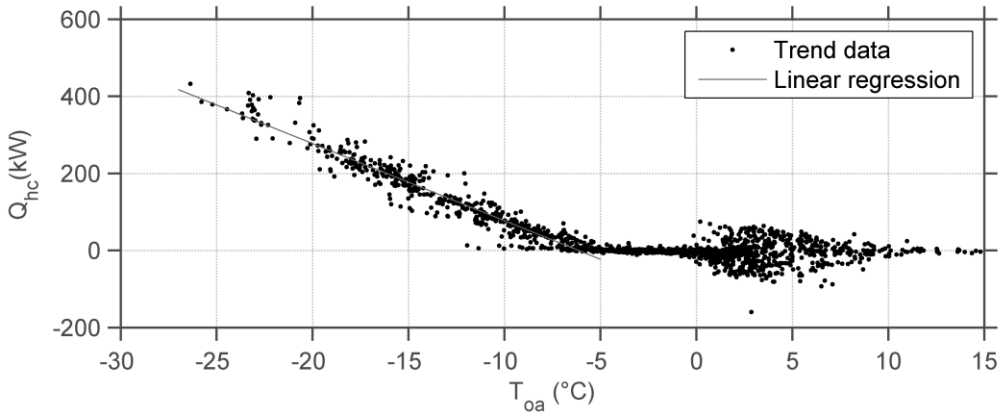


Figure 4.26 Heating coils heat flow rate

Table 4.12 Heating coil performance summary

| | Linear equation: $c_2 \cdot T_{oa} + c_1$ | | | | | | | | | |
|---|---|---|---|---|---|---|---|---|---|---|
| | 2013 | | | | | 2014 | | | | |
| | Max | $c_2$ | $c_1$ | $R^2$ | Range | Max | $c_2$ | $c_1$ | $R^2$ | Range |
| $\dot{Q}_{hc}$ (kW) | 430 | -20 | -120 | 0.93 | $T_{oa}$< -6.1 | 370 | -18 | -120 | 0.86 | $T_{oa}$ < -7.0 |
| $V_{hc}$ (L/s) | 3.5 | -0.14 | -0.69 | 0.90 | $T_{oa}$< -4.9 | 3.2 | -0.12 | -0.61 | 0.77 | $T_{oa}$< -5.0 |
| $T_{hcr}$ (°C) | - | 0.10 | 15 | 0.24 | $T_{oa}$< -5.0 | - | 0.06 | 15 | 0.11 | $T_{oa}$< -5.0 |
| $\Delta T_{hc}$ (°C) | 37.1 | - | - | - | - | 37.5 | - | - | - | |

The $T_{hca}$ was programmed in the BAS to follow a reset profile as a function of $T_{oa}$ (Figure 4.27). The trend data showed that this was followed, however, at a consistently

higher value of temperature. The measured reset profile was estimated semi-automatically (Table 4.13) using the outward method. Once the user entered the outside-low and outside-high change points, the supply-high temperature was calculated as the median $T_s$ when $T_{oa}$ was less than the outside-low temperature. The supply-low temperature was calculated as the median $T_s$ when $T_{oa}$ was greater than the outside-high temperature.

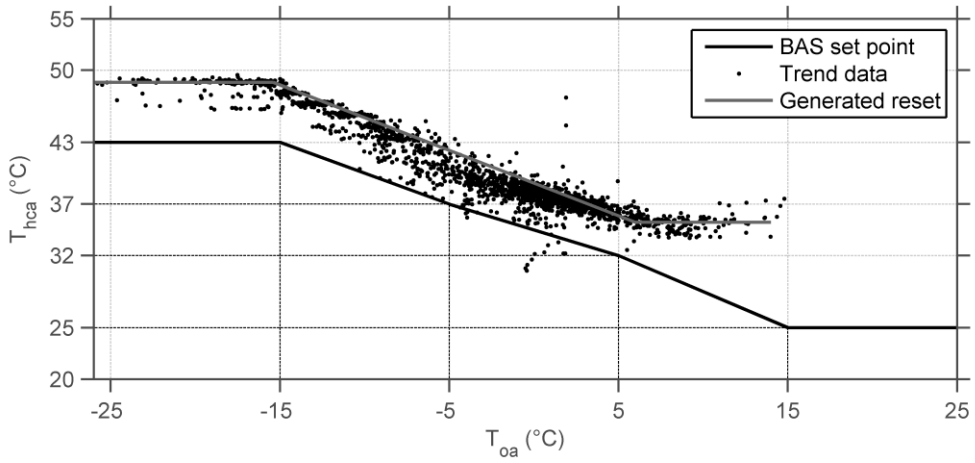


Figure 4.27 Heating coils supply glycol temperature and reset profile comparison

From February 2014 onward the temperature of hot water entering the Genome Building ($T_{gea}$) was added to the BAS. Its measured reset profile was also compared to its BAS set point (Table 4.13), which showed that it followed the profile closely. This also explained $T_{hca}$ measured values being consistently higher than the set point because the hot water temperature arriving at the heat exchangers was higher than the $T_{hca}$ reset profile.

Table 4.13 Heating coil supply glycol temperature reset profile from trend data

| | Hot glycol reset (°C) | | | | Hot water reset (°C) | | |
|---|---|---|---|---|---|---|---|
| | Trend data | | BAS set point | Design | Trend data | | BAS set point |
| | 2013 | 2014 | | | 2013 | 2014 | |
| Supply-high | 48.8 | 48.1 | 43 | 48.9 | - | 46.5 | 46 |
| Outside-low | -15.4 | -14.9 | -15 | - | - | -15.7 | -15 |
| Supply-low | 35.2 | 34.6 | 25 | 15.6 | - | 35.3 | 35 |
| Outside-high | 6 | 6 | 15 | - | - | 5.5 | 5 |

The glycol flow rate ($V_{hc}$) in the heating coils was estimated (Figure 4.28) using eq. 3.7 and is presented in Table 4.12. The $T_{oa}$ in Table 4.12 that activated the heating coils for $V_{hc}$ and $\dot{Q}_{hc}$ differed by 20% from each other during the 2013 heating season, when they should be the same. Uncertainty in the measurements may have caused this.

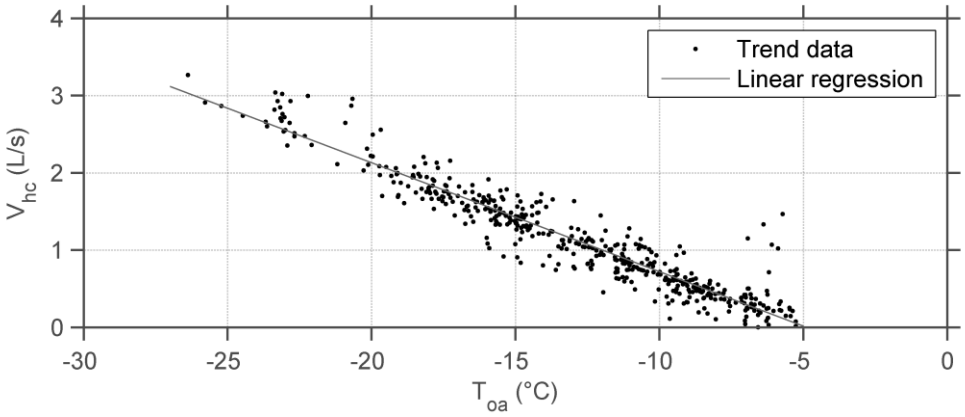


Figure 4.28. Estimated heating coil glycol flow rate

### *4.5 Performance Indices and Comparison to Design Specifications*

System level performance is compared to design specifications in Table 4.14. The maximum air flow rates, heating coil glycol flow rate, and heating coil heat flow rates were operating at 27-93% of design capacities. Overall, there were no substantial changes in performance between the 2013 and 2014 heating seasons.

Other performance indicators were normalized (Table 4.15) by the floor area served by the AHUs (4540 $m^2$) to allow for performance comparisons with similar buildings. It made sense that more heating coil and heat recovery energy was used in the 2014 heating season because the median $T_{oa}$ was colder than in the 2013 heating season (Table 4.5). The trend data required to calculate the whole-building hot water heat flow rate ($\dot{Q}_{GE}$) (eq. 3.7) was recorded from February 3rd, 2014 onward (Table 3.9). The maximum normalized $\dot{Q}_{GE}$ was not shown in Table 4.15 because $\dot{Q}_{GE}$ was not recorded when $T_{oa}$ was coldest. The overall average annual energy used in 2010 by educational services buildings in Canada was 400 kWh/$m^2$/year with approximately 45% of that

energy used for space heating (NRCan 2014). If heating was estimated to be active for 6 months of the year, this would equate to approximately 1 kWh/m$^2$ day which is approximately 60% greater than the mean measured value and is close to the upper limit of the overall uncertainty of the calculation.

Table 4.14 System level performance compared to design values

| Description | Unit | Maximum trend data | | Design | Percent of design (%) | |
|---|---|---|---|---|---|---|
| | | 2013 | 2014 | | 2013 | 2014 |
| Supply air flow rate | L/s | 25,500 | 26,000 | 42,500 | 60 | 61 |
| Return flow rate | L/s | 5,030 | 5,360 | 14,200 | 35 | 38 |
| Heat recovery heat flow rate | kW | 410 | 370 | 626 | 65 | 59 |
| Heat recovery glycol flow rate | L/s | 11 | 11. | 11.8 | 93 | 93 |
| Heating coil heat flow rate | kW | 430 | 370 | 1,390 | 31 | 27 |
| Heating coil glycol ΔT | °C | 37.1 | 37.5 | 33.3 | - | - |
| Heating coil glycol flow rate | L/s | 3.5 | 3.2 | 10.2 | 34 | 31 |
| Zone reheat | °C | 18.3 | 18.7 | 25 | - | - |

Table 4.15 Normalized system level performance comparison

| | Maximum | | | Average and overall uncertainty | | |
|---|---|---|---|---|---|---|
| | 2013 | 2014 | Unit | 2013 | 2014 | Unit |
| $V_s$ | 5.6 | 5.7 | L/s/m$^2$ | 4.6 ± 0.1 | 4.4 ± 0.1 | L/s/m$^2$ |
| $V_r$ | 1.1 | 1.2 | L/s/m$^2$ | 0.70 ± 0.03 | 0.72 ± 0.03 | L/s/m$^2$ |
| $\dot{Q}_{hc}$ | 95 | 81 | W/m$^2$ | 0.18 ± 0.06 | 0.23 ± 0.07 | kWh/m$^2$/day |
| $\dot{Q}_{hr}$ | 90 | 85 | W/m$^2$ | 1.0 | 1.2 | kWh/m$^2$/day |
| $\dot{Q}_{GE}$ | - | - | - | - | 0.61 ± 0.28 | kWh/m$^2$/day |

### *4.6 Inputs Generation*

Some values generated in performance reports could not be entered directly into eQUEST due to software design assumptions and limitations. Some values were processed into inputs through mathematical procedures to obtain outputs from the model that represented physical operation as recorded from trend data. Many system level inputs in eQUEST are based on the design values entered into the program. All system level design information, rather than the maximum measured values, were entered into eQUEST to remain consistent. In a situation where design information was unavailable

the methods below could be used with the maximum measured values instead. This section summarizes how the values extracted from performance reports were processed into inputs used to automatically update an eQUEST .inp file.

### *4.6.1 Zone level inputs generated*

Existing building simulation software lacks the capacity to easily handle some inputs of hourly trend data (e.g., $T_z$ and $V_{zs}$) in a manner similar to hourly weather data. The simulated $T_z$ and $V_{zs}$ are calculated in eQUEST based on loads and HVAC controls and capacity. Changes to the code structure would be required to allow for direct input of trend data. For this reason, the hourly median $T_z$ trend data for each thermal zone, over the period of analysis, were entered into the hourly thermostat set point schedules in eQUEST, instead of their design values; one hourly schedule for weekdays (WD) and a second for weekends and holidays (WEH). Zone hourly median air temperatures were calculated by averaging $T_z$ trend data for all rooms located in a zone. An example of an hourly thermostat set point schedule for zone Z2-NE (office/laboratory) and design indoor air temperature is shown in Figure 4.29.

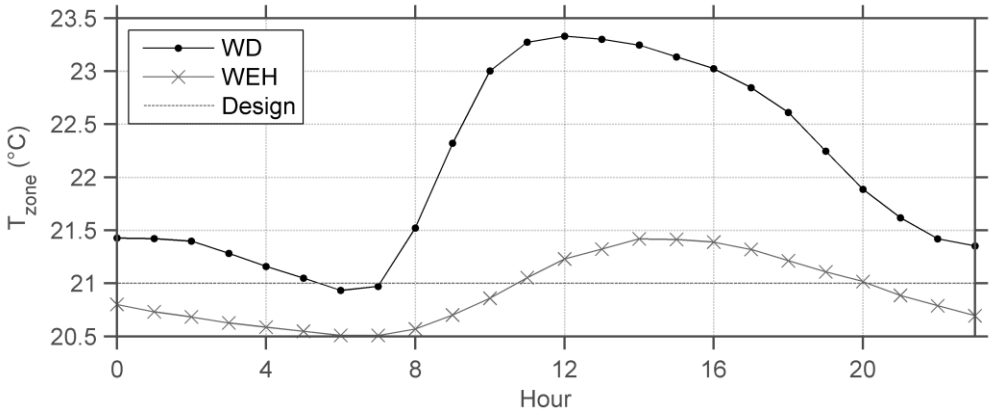


Figure 4.29 Hourly thermostat set point schedule for zone Z2-NE

A $V_{zs}$ schedule cannot be directly entered into eQUEST; however, hourly zone minimum air flow ratio schedules can. Entering a minimum air flow ratio schedule forced the model's $V_{zs}$ to *at least* the air flow rate calculated from multiplying the maximum $V_{zs}$

by the specified minimum air flow ratio. This approach was used to emulate the input of hourly supply air flow rates in eQUEST for each thermal zone. Hourly supply air flow ratios for every zone were calculated by dividing the zone median hourly $V_{zs}$ from the maximum $V_{zs}$ (Table 4.2). A schedule for each zone was created for weekdays and weekends/holidays. An example of a minimum air flow ratio schedule for zone Z2-NE is shown in Figure 4.30. The zone design air flow rate used for eQUEST input was calculated as the maximum measured zone supply air flow rate (Table 4.2). This was the one exception when the design information was not used. The goal of this procedure was to emulate direct input of the measured $V_{zs}$ into the model. The same method could be applied using design values instead of the maximum measured values; however, it was not applied in this study.

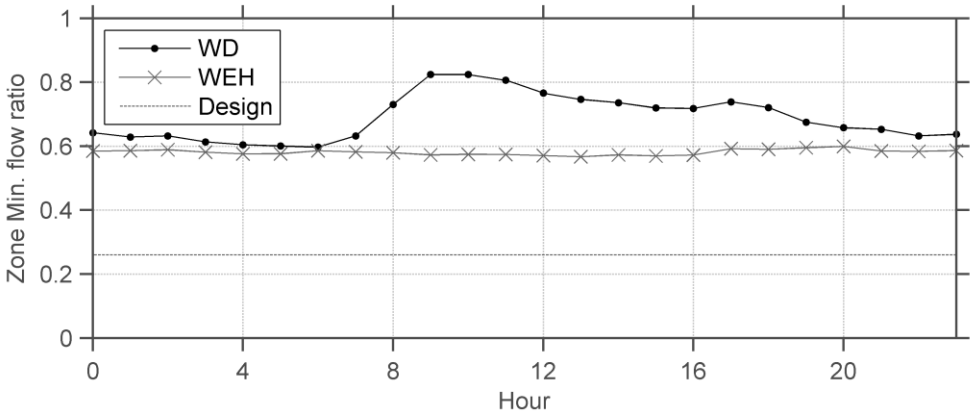


Figure 4.30 Hourly minimum air flow ratio schedule for zone Z2-NE

### *4.6.2 System level inputs generation*

The section describes how the values in performance reports were automatically processed into inputs to update an eQUEST .inp file. The section discusses the procedure to generate air- and water-side inputs. All system level inputs generated are summarized at the end of this section in Table 4.16. Table 4.17 provides the equation used to generate the inputs. The eQUEST keywords of generated inputs are summarized in Appendix B.

4.6.2.1 Air-side inputs

The system level $V_s$, $V_r$, and $V_e$ to be simulated in the AHUs, were calculated from the sum of zone level $V_{zs}$, $V_{zr}$, and $V_{ze}$ trend data, respectively, for the 3 out of 4 floors modelled. All of the calculations that follow using the sum of zone air flow rates would be replaced with system level air flow rates in a building that was fully modelled. It was assumed that $T_r$ in the AHUs was not affected by only using these floors. In reality, approximately 38% of the return air came from the basement (as opposed to 25% per floor), which may change $T_r$, if each floor's $T_r$ was different. The $T_r$ on each floor was not recorded.

The minimum supply air flow ratio was calculated by dividing the minimum sum of $V_{zs}$ to the design supply air flow rate. The maximum supply air flow ratio during heating was calculated by dividing the maximum sum of $V_{zs}$ to the design rate. The maximum heating supply air flow rate limits the supply air flow rate when the AHUs are in heating mode in eQUEST.

The minimum $\alpha$ as a function of hourly flow was calculated as the median $\alpha$ using air flow rates with the time series method. The median value was chosen instead of the minimum value because $\alpha$ varied slightly throughout the day while the mixing air dampers were fixed 100% open. The time series method was used because the AHUs lacked the capacity to physically produce an $\alpha$ calculated using the linear regression method (Section 4.4.2.2). The minimum $\alpha$ was not generated as a function of the design air flow rate, but rather the hourly flow rate.

eQUEST modelled $\Delta T_{fan}$ (eq. 4.19) based on the design conditions when *EIR* and *PLR* equaled 1.0. The design supply $\Delta T_{fan}$ was generated by dividing $\Delta T_{fan} + \Delta T_H$, from trend data, by the median ratio of modelled supply fan electric input ratio (*EIR*) to air flow part-load-ratio (*PLR*) (eq. 4.19). The design supply $\Delta T_{fan}$ generated included the humidification air temperature rise because eQUEST assumed isothermal humidification. The median ratio of EIR to PLR was used to approximate the average conditions of the air flow rate because the fans never operated at design conditions. The fan curve from ASHRAE 90.1 (2010) was used to estimate EIR in this study.

$$\Delta T_{fan} = \Delta T_{fan_{design}} \frac{EIR}{PLR} \quad \text{eq. 4.19}$$

One limitation in eQUEST was that exhaust ducts could not be modelled separately from the return air ducts (i.e., all supply air was returned through the return fan unless directly exhausted outside from a zone). Therefore, the simulated $V_s$ would equal the simulated $V_r$ when there is no duct air loss or any zone exhaust air. The design return air $\Delta T_{fan}$ was generated by dividing $\Delta T_{fan}$ (Table 4.11) by the median ratio of modelled supply fan *EIR* to *PLR*. Overall, these generated inputs were much larger than expected because the fan never operated near the design conditions and only 3 out of 4 floors were modelled.

The $T_s$ reset profile estimated from trend data was generated, using the inward method, for input into eQUEST because it controlled the $T_s$ set point simulated downstream of the fans when the heating coils were inactive.

eQUEST could not model heating coils controlled by an air temperature reset profile for VAV systems (further explained in Section 6.1.2). Instead, preheat coils, located downstream from the economizer and upstream of the cooling coils in eQUEST, were defined to heat the air exiting the coils to a constant temperature. The $T_{hd}$ set point was generated as $T_s - (\Delta T_{fan} + \Delta T_H)$ where $T_s$ was calculated using the $T_s$ linear equation from regression (Table 4.4) at the $T_{oa}$ when the heating coils were activated (Table 4.12). Subtracting $(\Delta T_{fan} + \Delta T_H)$ was necessary because the set point in eQUEST is simulated directly after the preheat coils. This created a smooth transition between the reset profile and constant set point.

Normally the cooling supply air set point in eQUEST pertains to the value of the $T_s$ set point when the AHU is in cooling mode with constant control. Since the $T_s$ set point is controlled with a reset profile with inactive heating coils, as explained in the previous paragraph, the cooling supply air set point does not control the $T_s$ set point. However, the cooling supply air set point is a required input to simulate the heat recovery coils. The cooling supply air set point provided the information to calculate the mixed air controller set point, which was used to simulate the heat recovery coils to ensure they output a reasonable air temperature when controlled with a mixing air reset in

combination with the operation of the economizer. If the cooling supply air set point was not entered into the model, the mixed air controller set point was calculated using the default zone entering minimum temperature (12.8 °C) less the simulated $\Delta T_{fan}$ instead. This value was lower than the $T_m$ trend data and would cause the heat recovery coils to simulate a lower $T_{hr}$ than estimated from trend data. The cooling supply air set point input value should equal the $T_s$ reset profile value when heat recovery was at peak effectiveness (i.e., when region II transitions to III). The cooling supply air set point was generated as the $T_s$ value calculated using the linear equation from regression of $T_s$ (Table 4.4) at the $T_{oa}$ when heat recovery changed from region II to III (Table 4.9). This also represented the maximum $T_s$ that could be maintained with inactive heating coils.

The information from the mixing air dampers and heat recovery performance in Figure 4.8 provides insight regarding the temperature difference between the return and outdoor air temperature that activated heat recovery. This value was calculated as the intersection between the linear equations from regression of regions I and II.

eQUEST accepted only one input to simulate $\varepsilon_{hr}$ at the design heat recovery $V_{oa}$. The design heat recovery $V_{oa}$ was 33,000 L/s; much greater than the maximum $V_{oa}$ estimated from trend data. DOE-2 used the design $\varepsilon_{hr}$ to calculate the design heat transfer value between the exhaust and outdoor air inlet temperatures ($UA_{design}$) which remained constant throughout the simulation as follows. The design effectiveness was unknown so it was estimated using trend data and the simulation algorithm in DOE-2 to ensure the output effectiveness matched the trend data. The DOE-2 code was reverse engineered to generate the design $\varepsilon_{hr}$ that simulated the maximum $\varepsilon_{hr}$ value from trend data (0.48) at the median $V_{oa}$ trend data. The maximum $\varepsilon_{hr}$ was chosen because this represented the estimated maximum performance. The median $V_{oa}$ was selected because the simulated $\varepsilon_{hr}$ varies inversely proportional to the minimum of $V_{oa}$ and $V_e$ in eQUEST. Generating the design $\varepsilon_{hr}$ was a non-linear process. The DOE-2 heat recovery algorithm, numerical method, and code used to solve for the design $\varepsilon_{hr}$ are shown in Appendix C.

The VAV reheat temperature difference was generated as the maximum difference between $T_s$ and $T_{zs}$ trend data available from each room where the data were available.

eQUEST controlled the simulated return air humidity set point to the minimum humidity input. Therefore, the minimum humidity was generated as the median $RH_r$. The maximum humidity set point was generated equal to the maximum $RH_r$. The value entered into eQUEST must be less than 100% to activate humidity control and greater than 30%. If the maximum $RH_r$ was less than 30% the maximum humidity set point was set equal to 30%.

#### 4.6.2.2 Water-side inputs

As shown in Figure 4.26, the $T_{oa}$ at which $\dot{Q}_{hc}$ activated formed a cloud of values. The $T_{oa}$ at which the heating coils activated for input into eQUEST was calculated in the AACT when the linear equation of $\dot{Q}_{hc}$ from regression intersected with the x-axis. The simulated heating coils activated when $T_{oa}$ was *less than* this set point (i.e., not *less than or equal to*). eQUEST simulated $T_{oa}$ to the nearest integer in degrees Fahrenheit. Therefore, the point of intersection was rounded down to the nearest integer in degrees centigrade before being subtracting 5/9 °C (i.e., 1 °F) to activate the heating coils at the $T_{oa}$ from trend data. If this operation was not performed the simulated heating coils would activate at lower $T_{oa}$ than indicated by trend data.

The design $\Delta T_{hc}$ was generated as the maximum heating coil temperature difference from trend data. The design value was not used because the maximum measured value was greater. The heating coil supply fluid temperature reset profile was generated using the outward method (Table 4.13). The zone reheat coil supply fluid temperature was generated using the outward method from the reset profile (Table 4.13) from whole building hot water supply temperature trend data.

Table 4.16 System level inputs generated from trend data for heating season

| System | Input | | AACT 2013 | AACT 2014 | Unit |
|---|---|---|---|---|---|
| Air-side | Cooling supply air set point | | 14.4 | 14.5 | °C |
| | Maximum heating supply air flow ratio | | 0.35 | 0.34 | - |
| | Minimum supply air flow ratio | | 0.19 | 0.19 | - |
| | Design supply $\Delta T_{fan}$ | | 7.9 | 8.9 | °C |
| | Design return $\Delta T_{fan}$ | | 4.6 | 5.0 | °C |
| | Temperature exiting heating coils | | 11.1 | 11.2 | °C |
| | Supply air reset temperature | Supply-high | 16 | 16 | °C |
| | | Outside-low | -28 | -28 | °C |
| | | Supply-low | 12 | 12 | °C |
| | | Outside-high | 28 | 28 | °C |
| | Minimum outside air ratio | | 84 | 79 | % |
| | Heat recovery activation $\Delta T$ | | 15.1 | 14.7 | °C |
| | Heat recovery effectiveness | | 0.24 | 0.21 | - |
| | Minimum humidity | | 26 | 30 | % |
| | Maximum humidity | | 31 | 40 | % |
| | Zone reheat | | 18.3 | 18.7 | °C |
| Water-side | Design heating coil temperature difference | | 37.1 | 37.5 | °C |
| | Heating coil activation temperature | | -5.6 | -6.7 | °C |
| | Heating coil reset temperature | Supply-high | 48.8 | 48.1 | °C |
| | | Outside-low | -15.4 | -14.9 | °C |
| | | Supply-low | 35.2 | 34.6 | °C |
| | | Outside-high | 6 | 6 | °C |
| | Zone reheat hot water reset temperature | Supply-high | 46.5 | 46.5 | °C |
| | | Outside-low | -15.7 | -15.7 | °C |
| | | Supply-low | 35.2 | 35.2 | °C |
| | | Outside-high | 5.5 | 5.5 | °C |

Table 4.17 System level inputs generated from trend data for heating season

| System | Input | Method |
|---|---|---|
| Air-side | Cooling supply air set point | $c_2(CP_{T_{hr}}) + c_1$<br>See Table 4.4 for $c_1$ and $c_2$ of $T_s$ and Table 4.9 for the $T_{oa}$ when $T_{hr}$ changed from region II to III ($CP_{T_{hr}}$). |
| | Maximum heating supply air flow ratio | $\frac{\min(\sum V_{zs})}{\max(\sum V_{zs})}$ |
| | Minimum supply air flow ratio | $\frac{\min(\sum V_{zs})}{V_{s_{design}}}$ |
| | Design supply $\Delta T_{fan}$ | $\frac{\Delta T_{fan} + \Delta T_H}{\text{median}\left(\frac{EIR}{PLR}\right)}$ |
| | Design return $\Delta T_{fan}$ | $\frac{\Delta T_{fan}}{\text{median}\left(\frac{EIR}{PLR}\right)}$ |
| | Temperature exiting heating coils | $c_2\left(CP_{T_{Qhc}}\right) + c_1 - \left(\Delta T_{fan} + \Delta T_H\right)$<br>See Table 4.4 for $c_1$ and $c_2$ of $T_s$ and Table 4.12 for the $T_{oa}$ activating the heating coils ($CP_{T_{Qhc}}$). |
| | Supply air reset temperature | See inward method to calculate reset profiles in Section 4.4.1 |
| | Minimum outside air ratio | $\text{median}\left(\frac{\sum V_{zs} - \sum V_{zr}}{\sum V_{zs}}\right)$ |
| | Heat recovery activation $\Delta T$ | $\frac{b_{II} - b_I}{p_I - p_{II}}$<br>See Figure 4.8 |
| | Heat recovery effectiveness | See Appendix B for sample code |
| | Minimum humidity | $\text{median}(RH_r)$ |
| | Maximum humidity | $\begin{cases}\max(RH_r), & RH_r \geq 30 \\ 30, & RH_r < 30\end{cases}$ |
| | Zone reheat | $\max(T_{zs} - T_s)$ |
| Water-side | Design heating coil temperature difference | $\max(T_{hca} - T_{hcr})$ |
| | Heating coil activation temperature | $\text{floor}\left(\frac{-c_2}{c_1}\right) - \frac{5}{9}$<br>See $\dot{Q}_{hc}$ in Table 4.12 for $c_1$ and $c_2$ |
| | Heating coil reset temperature | See outward method to calculate reset profiles in Section 4.4.5 |
| | Zone reheat hot water reset temperature | See outward method to calculate reset profiles in Section 4.4.5 |

### *4.7 Discussion and Limitations of the AACT*

Further development of the AACT for widespread use would be challenging and tedious due to the complexity of building simulation software and processing trend data. Building simulation software has the capacity to model multiple different HVAC configurations resulting in hundreds of inputs that could potentially be generated. Use of this tool would require the user to not only understand inherent model limitations but also the assumptions when generating inputs. For example, when equipment were oversized the inputs did not necessarily reflect the trend data but were processed so eQUEST simulated the output representing measured performance. This was clear when estimating the design $\Delta T_{fan}$ and $\varepsilon_{hr}$. It is likely that it may take years of experience using trend data from multiple systems and buildings to develop a robust automatic tool requiring minimal manual user input.

The current version of the AACT was called proof-of-concept prototype because it was used to demonstrate the concept for one building. It was not robust enough for any analyst to use because it lacked a GUI. A GUI was not implemented because the AACT was used for research purposes and required high flexibility. The time required to create a flexible GUI exceeded the time available for this research.

The AACT had the capacity to deal with short time frames (i.e., days or weeks) as long as trend data from a full heating and shoulder season were available. For example, heat recovery performance was characterized only when regions I-III (Figure 4.8) were measured. Calculating $\Delta T_{fan}$ was another example that required trend data with inactive humidification and heating and cooling coils.

In this study, the trend data were easily accessible but this may not be the case with all BASs. The Building Automation and Control Networks (BACnet) communications protocol could be integrated to ensure compatibility among BASs and the AACT. The AACT did not automatically acquire the trend data as it relied on the BAS for weekly exports. Integration of the BAS with the AACT could create a more robust tool in case the weekly export was disrupted or experienced an error. Building managers may be reluctant to release zone level trend data due to occupant privacy

concerns. Zone airflow rates are often controlled partially with occupant sensors, which could potentially reveal occupant schedules.

The performance reports acted as a first step using trend data in commissioning, whether it be benchmarking, fault detection, etc. or comparing performance to other buildings, design values, or seasonal performance. In terms of identifying faults, the performance reports offered a reactive, as opposed to a proactive, approach where faults were investigated manually based on measured performance. The performance reports were only useful to someone very familiar to the Genome Building. Future commissioning techniques development would benefit from an approach similar to the performance reports. For example, the value of the reports could be improved using user-specified limits and other automated techniques employed by Siedl (2006) for FDD.

Another main area for improvement of the AACT would be automating the identification of temperature change points. This would reduce the number of values manually identified to approximate the change points associated with the economizer, heat recovery, and heating coils in addition to identifying reset profiles for $T_s$, $T_{hca}$, and $T_{ges}$. Identifying change points has been researched (Kissock et al. 2003) and could be applied. When data for the full reset profile is available, the outward method should be used instead of the inward method because the linear equation created from linear regression between outside-low and outside-high temperatures may not pass through the point where the supply-high or outside-low temperature (or supply-low and outside-high temperatures) data are located due to variation in the data.

The trend data collection was continuous in this study, experiencing only very short disruptions. Other studies may be less fortunate. A method to deal with trend data disruptions is currently beyond the AACT capacity; the AACT converted all trend data disruptions to the data type Not-a-Number (NaN), which represents an undefined value.

This study did not have any influence on BAS design and sensor placement. It was clear that some sensors could have been added or changed to reduce the number of estimated variables. Measuring the glycol temperature exiting the heat recovery coils in contact with outdoor air (SC2-1 and -2) would have removed the extrapolation shown in

Figure 4.17. More consideration of ongoing commissioning requirements and planning accordingly in sensor placement could increase the information extracted from trend data.

### *4.7.1 Trend data quality*

Trend data quality has often been questioned as mentioned in the literature review. Xiao et al. (2006) provided examples of errors that may occur:

> "*For example, improper sensor location, such as stratification within air ducts after devices like mixing dampers or heat exchangers, may result in a sensor not giving values representative of the conditions as required. Incorrect electrical installation, such as the use of unshielded cables, may result in increased amounts of noise in measurements. Another fault source may be related to the sensor itself, such as a broken sensor that gives no signal or a completely wrong signal as well as a drifting and biased sensor due to abnormal physical changes or aging. Sensor faults may hide in the large scale and distributed HVAC systems, and consequently, it is very difficult to find them manually.*"

In this study, it was unrealistic to verify the calibration of all the sensors (Table 3.9). It may be more realistic to focus on verifying the calibration of sensors that have a large impact when estimating energy use such as the system level sensors.

Short-term measurements could be used to verify the trend data quality. Fortunately, sensors in BASs exist which allow other sensors to be validated indirectly; ideally using automatic tools. An example of this was the estimation of the mixing air damper position (Section 4.4.2). In this case positions were estimated directly from the mixing air damper position and indirectly using air temperature and flow rates. Similar research was conducted by Wang and Xiao (2004) who identified sensor faults in AHUs. Additional commentary on trend data quality is provided in Appendix D.

### *4.8 Summary*

This chapter demonstrated how values extracted from trend data could be automatically coupled with ongoing commissioning and calibrated simulation. A description of the AACT, a proof-of-concept prototype tool used to generate performance reports and translate these reports into inputs for use in calibrated simulation, was provided. No reports of such a tool were found in the literature. The AACT was developed for use with eQUEST but could be adapted for other building energy simulation programs such as EnergyPlus.

Performance reports allowed comparison with design specifications and ongoing measured performance. The maximum air flow rates, heating coil heat flow rate and glycol flow rate, and heating recovery heat and glycol flow rates operated between 27 to 93% of their design capacities. No substantial performance changes were observed between the 2013 and 2014 heating seasons. The comparison between measured performance and BAS set points revealed faults that occurred with the zone reheat, the inactive heat recovery glycol pump, and the high supply glycol temperature.

Generating the inputs once all the data were processed and updating an eQUEST .inp file was relatively easy. The main challenge was automatically processing the data and understanding how eQUEST used these inputs relative to the design capacities. Since most HVAC equipment is oversized it is important to understand how these inputs are used in eQUEST to represent physical operation.

Generating the maximum zone supply air flow rates and hourly median air temperatures and minimum air flow ratios for weekdays and weekends for 17 zones resulted in 1649 inputs at the zone level inputs. There were 26 system level inputs, resulting in a total 1675 inputs. Automatically updating the eQUEST .inp file reduced time and errors associated with manual data entry.

The primary purpose of this chapter was to verify the proof-of-concept to automate the integration of trend data into building simulation software. Tools similar to the AACT are necessary to make dealing with large sets of trend data for feasible use with commissioning.

# 5 Initial Building Energy Model and Shoulder Season Calibration

This chapter describes the development of the initial building energy model. To make the bottom-up calibration more manageable the initial model was developed for the 2013 shoulder season, defined by inactive AHU heating and cooling coils. The outputs from eQUEST were extracted from the .SIM file.

## *5.1 eQUEST Description*

eQUEST (the quick energy simulation tool) was used as the simulation software in this study. It provided a building creation wizard (i.e., GUI) for the DOE-2 building energy simulation program. DOE-2 simulates hourly energy use of a building given hourly weather data, building form, envelope characteristics, internal loads and schedules, and HVAC information. There are 5 main subprograms within DOE-2: Building Description Language (BDL) Processor, LOADS, SYSTEMS, PLANT, and ECON (i.e., economics). These subprograms are described next using the information found in the DOE-2 Basics Manual (LBNL and JJH 2004).

The BDL processor reads the .inp file created by eQUEST and translates it so the computer can process the information and run simulations. The BDL processor also calculates response and weighting factors for transient heat flow in walls and thermal response of building spaces, respectively. The simulation starts with the LOADS subprogram.

The LOADS subprogram calculates the sensible and latent heating or cooling load for each thermal zone assuming a fixed user-specified temperature. Outdoor weather files are read into eQUEST; these contain hourly values of outdoor dry-bulb and wet-bulb temperature, atmospheric pressure, cloud type and coverage, wind speed and direction, humidity ratio, air density and enthalpy, and sometimes total horizontal and direct normal solar radiation. Solar radiation is estimated using cloud type and cover if it is missing from the weather file. The results from LOADS are passed to SYSTEMS.

The SYSTEMS subprogram calculates the supply flow rate and air-side performance of fans, heating and cooling coils, heat recovery, economizer, zone reheat terminals, and other equipment located in the AHUs. SYSTEMS also adjusts the fixed

user-specified temperature calculated in LOADS by taking into account outside air requirements, availability status of equipment, HVAC control strategies, supply air flow rate, and zone reheat to calculate the hourly indoor air temperature in each zone. The results from SYSTEMS are passed to PLANT.

The PLANT subprogram simulates the performance of primary equipment such as boilers, chillers, and cooling towers to satisfy the heating and cooling loads of HVAC components calculated by SYSTEMS. PLANT accounts for equipment part-load conditions to calculate the fuel and electrical demand.

The ECONOMICS subprogram calculates the hourly, monthly, and yearly whole-building energy and fuel cost. ECONOMICS uses the results from LOADS (e.g., lighting and equipment electricity), SYSTEMS (e.g., fan electricity), and PLANT (e.g., primary equipment gas and electricity use).

eQUEST was chosen as the building simulation software because it is one of the most widely used building simulation tools in North America; it uses the DOE-2 simulation engine, which has been extensively documented and validated. eQUEST and the DOE-2 source code can be downloaded for free from http://doe2.com/. NRCan is currently developing a version for use in Canada called CAN-QUEST. At the time of writing, the beta version is available for download at:
ftp://ftp.nrcan.gc.ca/pub/outgoing/canquest/CAN-QUEST_NECB2011

### *5.2 Weather Data*

Weather data were obtained from SIMEB (2013) using data collected at the Montreal-Pierre Elliot Trudeau International Airport, located approximately 9 km west of the Genome Building. The file contained the measured total horizontal and direct normal solar radiation. The difference between the outdoor air temperature ($T_{oa}$) trend data recorded at an adjacent building and at the airport (Figure 5.1) had an MBE of -16%, RMSE of 1.8 °C, and CV-RMSE of 25%.

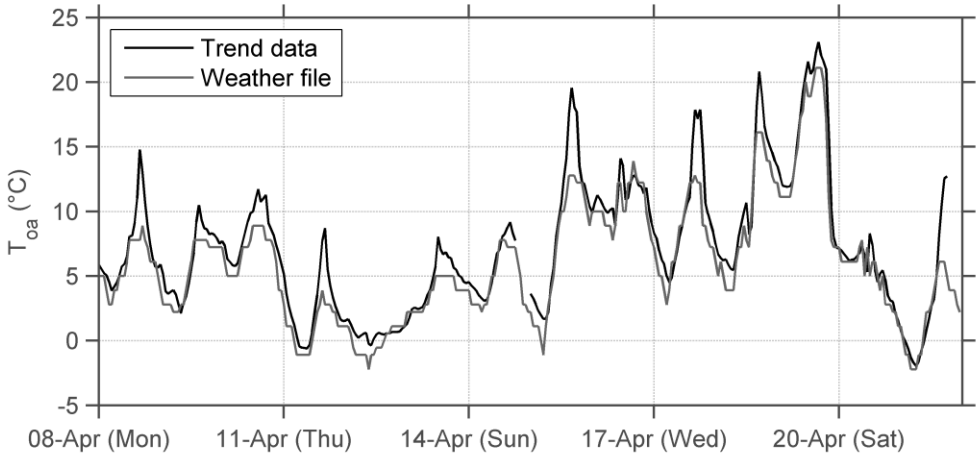


Figure 5.1 Initial trend data and weather file outdoor air temperature comparison

It would be convenient to replace the $T_{oa}$ trend data in the eQUEST weather file format; however, no easy method was available to modify the weather file because it was of type .BIN and could not be opened with any standard programs. This was also demonstrated through multiple online threads in public mailing lists expressing a need to edit these weather files using local data (Bhatia 2008; Choi 2008; Chew 2011; Gerometta 2012). Therefore, a program was written in MATLAB to facilitate easy editing of eQUEST weather files. This program was used to replace the original weather file's $T_{oa}$ with trend data. The program required: (1) the start and end dates for the desired period of replacement, (2) the type of weather data being replaced (e.g., $T_{oa}$), (3) the data used for replacement, and (4) a binary input determining if the year was a leap year or not. The program incorporated the BIN2TXT.EXE and TXT2BIN.EXE programs found in DOE-2.2 Weather Utilities (JJH n.d.) to convert the weather file to a formatted text file (.fmt). The $T_{oa}$ data found in the weather file were used when trend data experienced a disruption. Issues with discontinuity were not addressed but should be in future version. The $T_{oa}$ the trend data replaced the weather file data and resulted with an MBE of 0.3%, RMSE of 0.2 °C, and CV(RMSE) was 2.8%. Differences were caused by rounding to the nearest degree Fahrenheit in eQUEST's conversion process.

### *5.3 Geometry and Thermal Zones*

The building geometry (Figure 5.2) was imported into eQUEST using AutoCAD construction drawings. The basement floor was not modelled because it housed a large data center with dedicated chillers and cooling towers that would greatly increase model complexity. The mechanical penthouse and emergency staircase located on the SW face of the building were excluded to further simplify the model. The excluded features were replaced with adiabatic surfaces. Shading from nearby buildings to the north and northwest and the vertical fenestration fins were included (Figure 5.2).

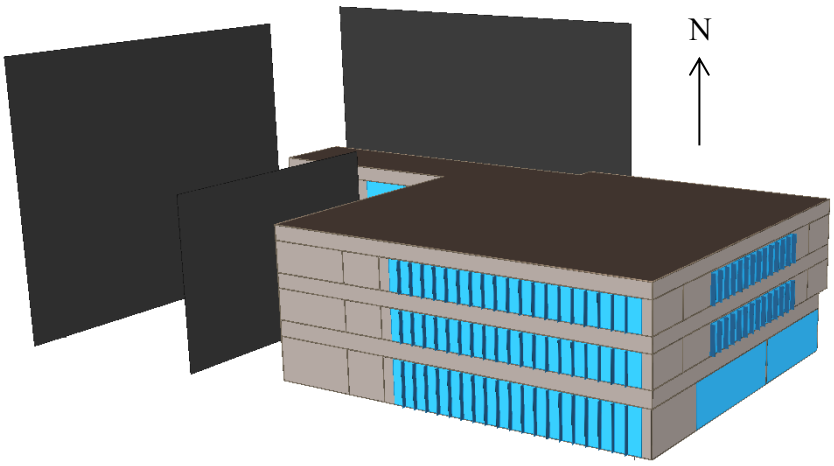


Figure 5.2 Genome building energy geometry in eQUEST

A total of 20 thermal zones (including 3 plenum zones) were defined based on space function, proximity to the exterior, orientation, and ventilation. Figure 5.3 and Figure 5.4 show the first and second floor thermal zone placement with their internal space functions. The third floor thermal zone placement was identical to the second floor. The total areas and percentages of space functions modelled are shown in Table 5.1.

Table 5.1 Genome building modelled space function

| Space Function | Area ($m^2$) | Percentage |
|---|---|---|
| Office | 695 | 22% |
| Corridor | 826 | 26% |
| Lounge | 77 | 2% |
| Washroom | 114 | 4% |
| Inactive Storage | 131 | 4% |
| Laboratory | 1138 | 36% |
| Conference | 139 | 4% |
| Total | 3122 | 100% |

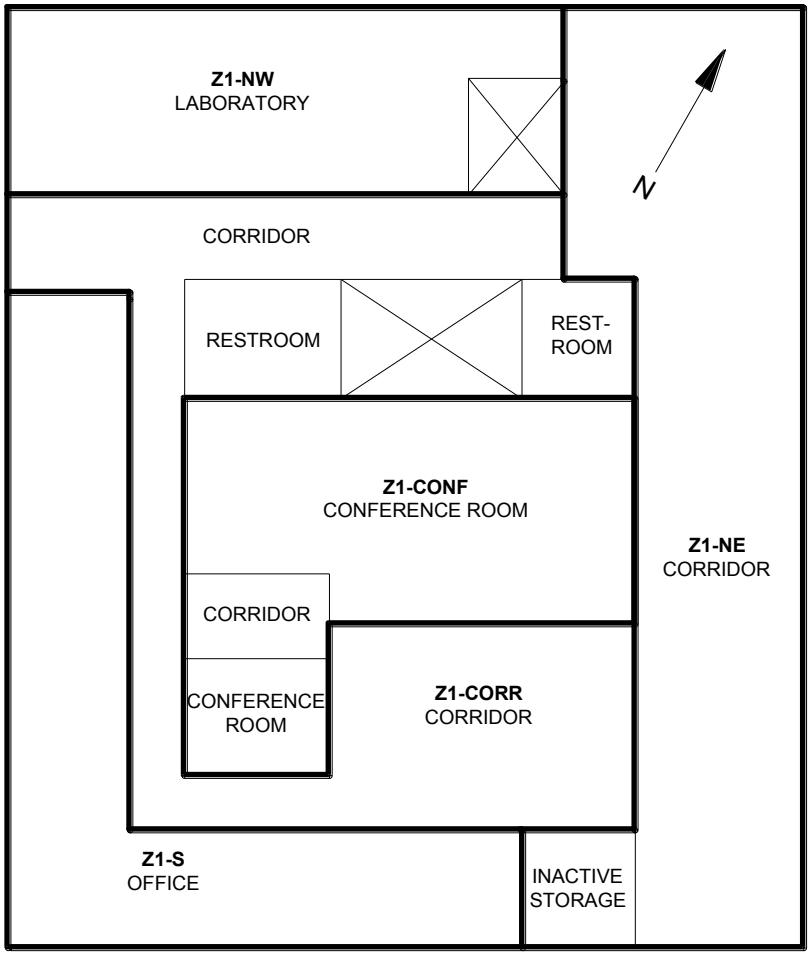


Figure 5.3. Ground floor thermal zone placement and space functions

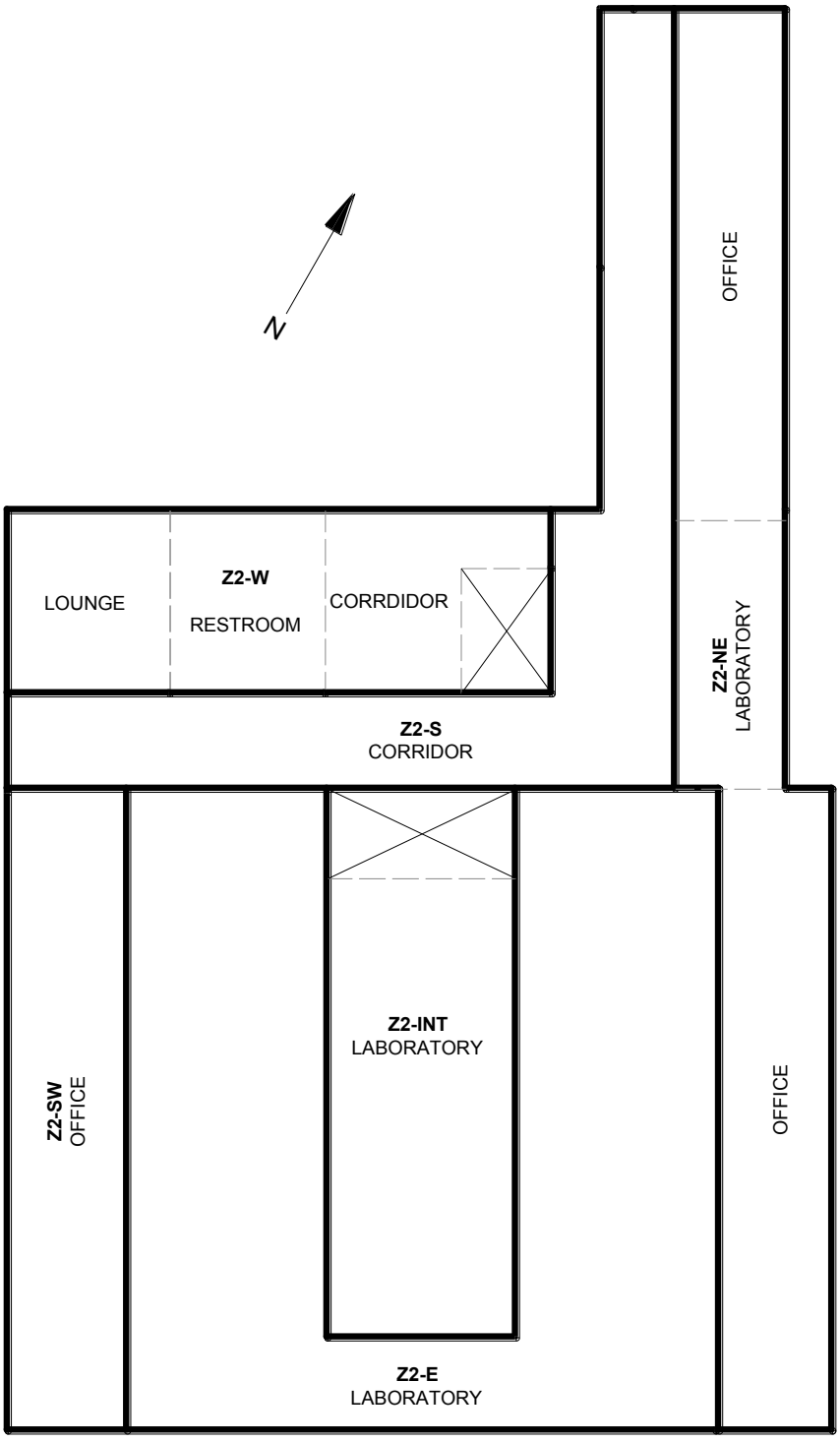


Figure 5.4. Second and third floor thermal zone placement and space functions

The room air flow rates within a zone must be summed in order to calculate $V_{zs}$. This may cause zoning issues for large open spaces with perimeter and interior features. In general, dividing the air flows into perimeter and interior zones presented a challenge that was not easily solvable in this analysis. For example, zones Z2- & Z3-E and Z2- & Z3-S were likely to experience a cooling load in the interior and heating load near the exterior which may cancel each other out. It was unlikely that this would have a large impact in this study because the ratio of exterior to interior area in these zones was small but could be an issue when applied to another building.

## *5.4 Building Envelope*

### *5.4.1 Definition of wall construction assemblies*

#### 5.4.1.1 Brick and aluminium facades

Custom envelope constructions were created for the brick and aluminium panel façades (Table 5.3 and Table 5.2). Not all the materials in wall constructions were specified in Section 3.2.1. For example, the types of insulation used were not specified; thus, they were deduced by comparing their thickness and reported U-value to the materials library in ASHRAE (2009; Table 26.4). The density and specific heat for all materials were estimated using ASHRAE (2009; Table 26.4). The outside air film coefficient of heat transfer was calculated by eQUEST depending on wind speed and surface roughness and is omitted in the tables below.

Thermal bridging was accounted for in each wall construction to estimate effective U-values. It is difficult to approximate effective U-values because thermal bridging is a three dimensional heat transfer problem with temperature differences occurring between surfaces in contact with each other. Two-dimensional approximations such as the zone method, as described in ASHRAE (2009), are also available but are difficult to apply to the vertical and horizontal z-bar construction in the aluminium façade. The effective U-value of the aluminium façade was approximately 33% higher than the nominal value reported in the construction documents using a method similar to

the zone method in Appendix C of NRC (1997). this estimate was smaller than the results from three-dimensional finite difference heat transfer models used to model a similar assembly, which showed a 51% increase in U-value (Morrison Hershfield 2011). Therefore, the nominal aluminium façade's U-value was increased by 51% by increasing the thermal conductivity of the expanded polystyrene (Table 5.2) in the model.

Table 5.2 Modelled aluminium façade thermal properties

| Material Layer | Thickness (m) | Thermal conductivity (W/m·K) | Density (kg/m$^3$) | Thermal Capacity (J/kg·K) | U-Value (W/m$^2$·K) |
|---|---|---|---|---|---|
| Aluminum Siding | 0.005 | - | 2800 | 1220 | - |
| Air space | 0.04 | - | - | - | 5.9 |
| Expanded polystyrene (Adjusted) | 0.05 | 0.055 | 20 | 1470 | 1.1 |
| Expanded polystyrene (Adjusted) | 0.05 | 0.055 | 20 | 1470 | 1.1 |
| Gypsum Board | 0.013 | 0.16 | 640 | 1150 | 12.5 |
| Air space | 0.152 | - | - | - | 8.3 |
| Gypsum Board | 0.016 | 0.16 | 640 | 1150 | 10 |
| Inside air film | - | - | - | - | 8.3 |
| | | | | Effective U-Value: | 0.41 |

Thermal bridging in the brick façade caused by ties and shelf angles used to support was also accounted for. Morrison Hershfield (2011) showed that these effects increased the U-value of a similar wall construction by approximately 53%. The nominal brick façade's U-value was increased by 53% by increasing the thermal conductivity of the expanded polystyrene (Table 5.2) in the model.

The interior floors and ceilings were modelled as 150 mm of concrete and 6.3 mm acoustical panels, respectively. The interior walls were modelled with a U-value of 1.5 W/m$^2$·K assuming two layers of gypsum board with a 90 mm air gap. The thermal capacitive effects from interior wall are ignored in eQUEST. The floor weight and

weighting factors accounting for zone internal mass remained unchanged using eQUEST default values.

Table 5.3 Modelled brick façade thermal properties

| Material Layer | Thickness (m) | Thermal conductivity (W/m·K) | Density (kg/m$^3$) | Thermal Capacity (J/kg·K) | U-Value (W/m$^2$·K) |
|---|---|---|---|---|---|
| Face brick | 0.09 | 0.5 | 1280 | 800 | 5.6 |
| Air space | 0.04 | - | - | - | 5.9 |
| Expanded polystyrene (Adjusted) | 0.1 | 0.056 | 20 | 1470 | 0.56 |
| Normal-weight aggregate concrete block | 0.19 | 0.9 | 2100 | 920 | 4.76 |
| Inside air film | - | - | - | - | 8.3 |
| | | | | Effective U-Value: | 0.41 |

5.4.1.2 Curtain walls

The visible curtain wall sections and exterior entrances were modelled as green-tinted double-glazed with a 12.7 mm air gap. The solar and optical window properties for the center-of-glass were obtained from the eQUEST library for glazing type 2210. The vision panel overall U-value accounting for the edge-of-glass and frame coefficients was taken to be 3.5 W/m$^2$·K for a standard size window (ASHRAE 2009; Table 15.4). The vision panel U-value was adjusted in eQUEST by modifying the frame thickness around the window and setting the thermal conductivity of the aluminium to the maximum allowable value until the equivalent U-value was reported in eQUEST's output file.

The curtain wall's thermal break was identified in the construction documents and was compared to the curtain walls manufactured by Kawneer. The curtain wall had a thermal break similar to the 1600 Wall System 2 (Kawneer 2013). The effective U-value value obtained from Kawneer (2013) product information using the spandrel panel and mullion dimensions from construction documents was 1.7 W/m$^2$·K. An effective value of 1.7 W/m$^2$·K for a similar curtain wall was obtained using FRAME™plus Online (Enermodal Engineering and NRCan 2010); a tool that estimated effective U-values in

curtain wall vision and spandrel panels based on Canadian Standards Association (CSA) standard A440.2. The thermal conductivity of the fiberglass insulation and U-value of the spandrel panels was increased (Table 5.4) in the model to account for thermal bridging.

Table 5.4 Modelled curtain wall thermal properties

| Material Layer | Thickness (m) | Thermal conductivity (W/m·K) | Density ($kg/m^3$) | Thermal Capacity (J/kg·K) | U-value ($W/m^2 \cdot K$) |
|---|---|---|---|---|---|
| Opaque Glazing (Adjusted) | -- | -- | -- | -- | 5 |
| Air space | 0.025 | -- | -- | -- | 5.9 |
| Fiberglass (Adjusted) | 0.1 | 0.8 | 120 | 840 | 8 |
| Gypsum board | 0.016 | 0.16 | 640 | 1150 | 10 |
| Inside air film | -- | -- | -- | -- | 8.3 |
| Total | | | | | 1.7 |

Vertical fenestration fins were added into the eQUEST model (Figure 5.2). The installed vertical fins have a transparency of approximately 30%. eQUEST modelled only opaque fins so the protrusion length of the fins were input as 30% of the installed outward protrusion to approximate the fin's transparency.

### *5.5 Definition of Internal Loads*

Lighting and plug loads were not sub-metered and occupants were not tracked. The lighting and equipment power could have been surveyed, but lack of sub-metering demand patterns still resulted in uncertain hourly magnitudes. Lighting, equipment, and occupant peak values and schedules were estimated using values found in the literature for use as a starting point in the initial model. These values could be tuned later during calibration if necessary.

The maximum occupant density by space type was estimated based on values in ASHRAE 62.1 (2001), while corresponding sensible heat gains were obtained from ASHRAE (2009; Table 18.1). Average zone internal load peak values were calculated based on the area weighted percentage of space function area within a zone shown in Table 5.5.

Equipment power densities (EPD) were estimated using ASHRAE (2009; Table 18.11). The office and laboratory space functions were assumed to have light and heavy office EPDs, respectively. All other space functions were assumed to have zero EPD. Lighting power densities (LPD) were estimated using ASHRAE 90.1 (2010; Table 9.6.1). The inactive storage spaces were assumed to have zero LPD. The equipment and lighting power densities are shown in Table 5.5.

Table 5.5 Internal gains by zone

| Zone | EPD ($W/m^2$) | LPD ($W/m^2$) | Area/person ($m^2$) | People | Sensible (W/person) | Latent (W/person) |
|---|---|---|---|---|---|---|
| Z1-S | 8.1 | 12.0 | 18.6 | 8.5 | 70 | 45 |
| Z1-NE | 0 | 4.7 | - | 0 | 0 | 0 |
| Z1-NW | 9.6 | 10.0 | 4.2 | 31.1 | 75 | 70 |
| Z1-CORR | 0 | 5.0 | - | 0 | 0 | 0 |
| Z1-CONF | 1.0 | 13.1 | 2.1 | 74.9 | 75 | 55 |
| Z2-SW | 8.1 | 12.0 | 18.6 | 5.4 | 70 | 45 |
| Z2-E | 10.8 | 15.0 | 3.7 | 96.7 | 75 | 70 |
| Z2-INT | 9.0 | 13.0 | 4.4 | 30.4 | 75 | 70 |
| Z2-NE | 8.6 | 12.6 | 10.6 | 19.5 | 73 | 58 |
| Z2-S | 0 | 5.0 | - | 0 | 0 | 0 |
| Z2-W | 0.6 | 8.6 | 6.2 | 20.8 | 70 | 45 |
| Z3-SW | 8.1 | 12.0 | 18.6 | 5.4 | 70 | 45 |
| Z3-E | 10.8 | 15.0 | 3.7 | 96.7 | 75 | 70 |
| Z3-INT | 9.0 | 13.0 | 4.4 | 0.0 | 75 | 70 |
| Z3-NE | 8.6 | 12.6 | 10.6 | 19.5 | 73 | 58 |
| Z3-S | 0 | 5.0 | 0 | 0 | 0 | 0 |
| Z3-W | 0.6 | 8.6 | 6.2 | 30.4 | 70 | 45 |

Occupant schedules were estimated using the diversity factors developed by Davis and Nutter (2010) from measurements in a university building (Figure 5.5) applied to the maximum occupancy given by occupant densities defined in ASHRAE 62.1 (2004). ASHRAE 62.1 (2001) was used instead of the 2004 version based on convenience and was unlikely to have substantial differences. This should have had little impact on the results because these gains for most zones had to be tuned.

Diversity factors are numbers between zero and one that were used to multiply a peak value to define a schedule over a period of 24 hours for use in building simulation. To the authors' knowledge no lighting and equipment diversity factors have been

published for university research buildings similar to the Genome Building. Therefore, these were estimated using the factors created by Claridge et al. (2004) for office buildings. These profiles (Figure 5.5) were developed based on the measured peak equipment and lighting loads in offices. Since the peak lighting and equipment load density values were uncertain, the peak values were assumed to be those presented in Table 5.5.

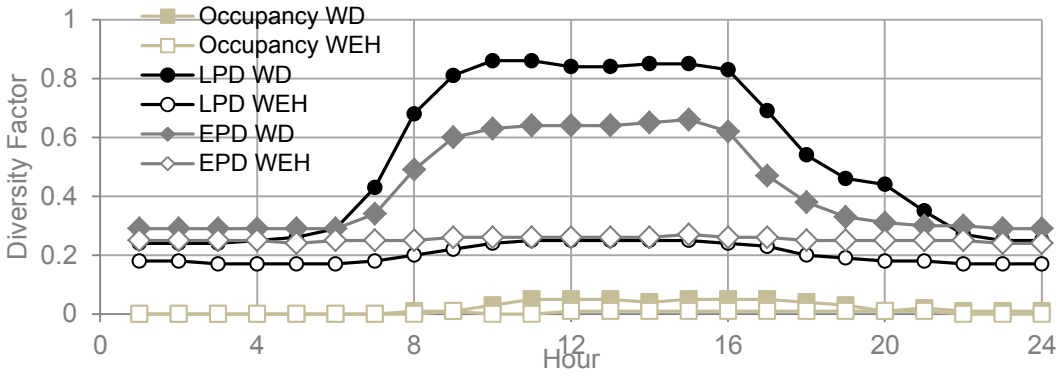


Figure 5.5 Lighting, equipment, and occupant diversity factors in the literature

To simplify the calibration of internal loads because of their large uncertainty, the effect of several internal loads were replaced with one single equivalent internal load, as described in Section 3.3.1. All the aforementioned loads were aggregated into one single load (sum of all internal loads) for each zone (Table 5.6). All schedules were aggregated into two schedules for the entire building for (1) weekdays and (2) weekends/holidays. The aggregated average diversity factors were calculated from the hourly whole-building average lighting, occupant, and equipment loads multiplied by their respective hourly diversity profile value, all divided by the average hourly whole-building internal load.

Table 5.6 Lumped internal gain and infiltration by zone

| Zone | Aggregated peak value ($W/m^2$) | Air infiltration ($L/s/m^2$) |
|---|---|---|
| Z1-S | 23.6 | 0.33 |
| Z1-NE | 4.7 | 0.27 |
| Z1-NW | 64.0 | 0.25 |
| Z1-CORR | 5.0 | 0.0 |
| Z1-CONF | 81.0 | 0.00 |
| Z2-SW | 23.6 | 0.20 |
| Z2-E | 75.5 | 0.04 |
| Z2-INT | 63.7 | 0.00 |
| Z2-NE | 29.3 | 0.21 |
| Z2-S | 5.0 | 0.12 |
| Z2-W | 28.6 | 0.15 |
| Z3-SW | 23.6 | 0.20 |
| Z3-E | 75.5 | 0.04 |
| Z3-INT | 63.7 | 0.00 |
| Z3-NE | 29.3 | 0.21 |
| Z3-S | 5.0 | 0.12 |
| Z3-W | 28.6 | 0.15 |

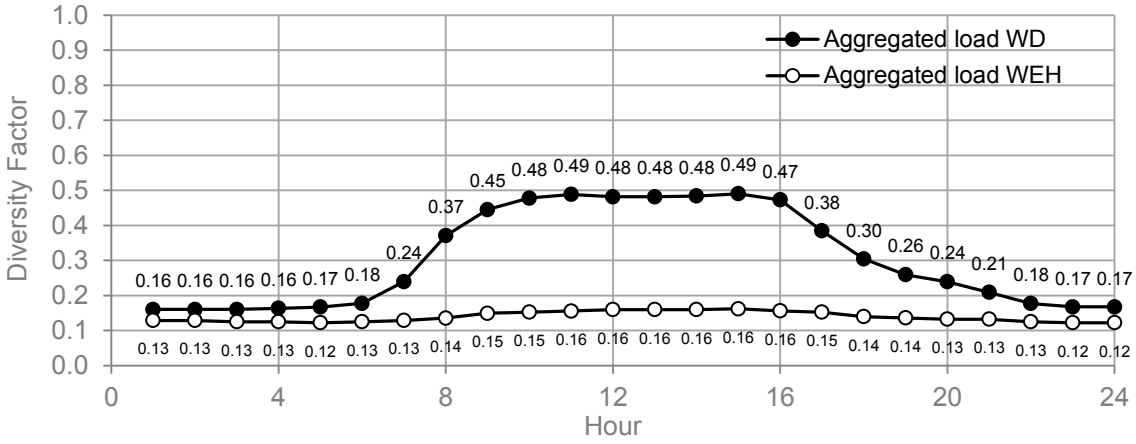


Figure 5.6 Aggregated diversity factors

Air infiltration in commercial and institutional buildings is another input required for building simulation, which is very difficult to measure and therefore highly uncertain. Air infiltration was assumed to equal 0.25 $L/s \cdot m^2$ of exterior wall area as specified in Model National Energy Code for Buildings (NRC 1997) as a reference value. eQUEST

accepts infiltration per unit floor area so the values were converted to this format in the model (Table 5.6).

## *5.6 Zone Level Model Description*

For the period of analysis, the AACT generated the maximum zone supply air flow rate ($V_{zs}$) and hourly median zone indoor air temperature and zone minimum supply air flow ratio schedules for weekdays and weekends using the method in Section 4.6.

Each zone was set to *adjust loads* to allow for adjustment of the peak heating load and to account for (1) the difference between the thermal zone's hourly temperature and the thermal zone's design temperature, (2) a steady state adjustment of thermal conduction through the interior and exterior walls of the thermal zone, and (3) an adjustment to air infiltration. Each thermostat was set as *reverse acting* that caused the thermostat's signal to reverse when a thermal zone experienced a heating load. The throttling range for all zones was left at the eQUEST default of 1.1 °C.

## *5.7 System Level Model Description*

### *5.7.1 System level model description*

The system was modelled as VAV with zone hot water reheat. There was no option available to model two parallel AHUs each with two parallel fans in eQUEST so they were modelled as one AHU equal to the capacity of the sum of the four fans. The return air path was specified as plenum. The system level model schematic is shown in Figure 5.7 and the system level inputs generated are summarized at the end of this section in Table 5.7. During the shoulder season the heating and cooling coils were inactive in the model. The hot water pump attached to the zone heating loop was specified as variable speed based on trend data. The design supply air flow rate was entered in as 42,500 L/s. The design exhaust and outdoor air flow rates were entered as 33,000 L/s. eQUEST calculated design fan power using a variable that defines the design fan power per design supply air flow rate. This value was entered as 0.0028 kW/(L/s) calculated from the design information.

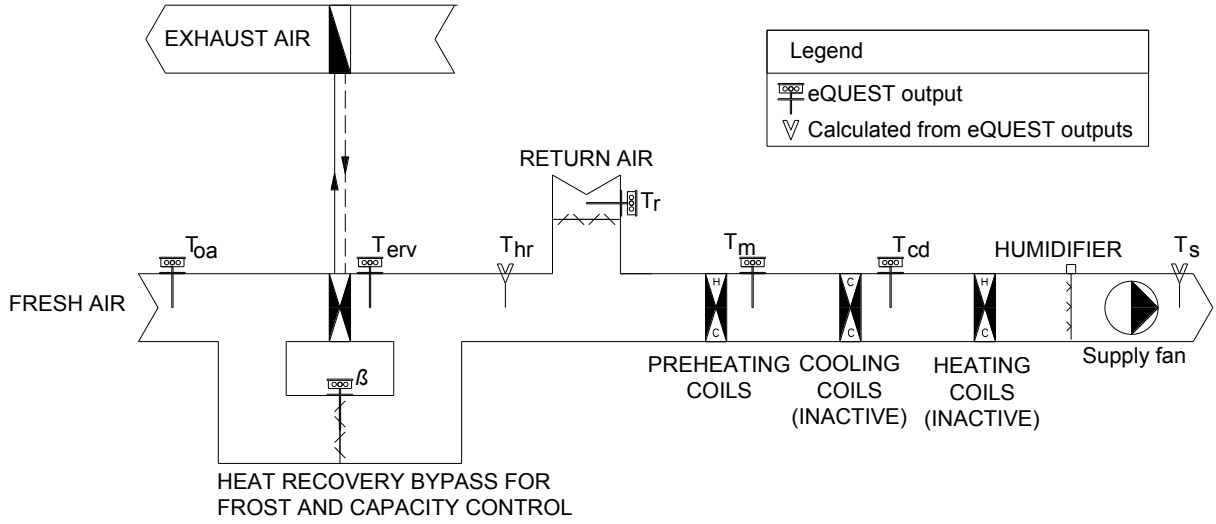


Figure 5.7 eQUEST AHU model schematic

eQUEST had the capacity to output many variables which allowed direct comparison with trend data but some differences existed. For example, the simulated supply air temperature ($T_s$) could not be directly output so it was calculated based on other outputs. The output $T_s$ was calculated by adding the simulated air temperature rise from the fan ($\Delta T_{fan}$) to the simulated air temperature exiting the preheating coils (i.e., $T_m$ in Figure 5.7). Other issues with the location of the mixed air temperature ($T_m$) are addressed in the discussion of heating season calibration (Chapter 6).

The simulated temperature exiting the heat recovery coils ($T_{hr}$) was calculated outside eQUEST because it could not be directly output. The run-around heat recovery coils were modelled as a sensible heat exchanger. eQUEST could not model the physical configuration (Figure 3.8) of the heat recovery coils. Instead a thermodynamically equivalent system was modelled using an outdoor air bypass for capacity and frost control. The simulated $T_{hr}$ was calculated (eq. 5.1) from the ratio of air bypassed to total outside air flow rate ($\beta$) and the air temperature exiting heating coils before mixing with the bypassed air ($T_{erv}$). Heat recovery was controlled using a mixed air reset, which specified the outlet temperature, based on the economizer position, necessary for $T_m$ to be at a set point satisfying the simulated $T_s$ set point. Frost control was inactive during the shoulder season and was analysed during the heating season calibration (Chapter 6).

$$T_{hr} = (1 - \beta)T_{erv} + \beta \cdot T_{oa} \quad \text{eq. 5.1}$$

The output heat recovery effectiveness ($\varepsilon_{hr}$) was based on $T_{erv}$ and the air flow rate passing through the heat recovery coils only (i.e., did not include the air bypassed around the heat recovery coils). Thus, the output $\varepsilon_{hr}$ did not represent the physical configuration and was instead calculated using eq. 4.10 based on other output variables. The model also assumed that outdoor air ($V_{oa}$) and exhaust ($V_e$) air flow rates were equal. The simulated return air temperature ($T_r$) included $\Delta T_{fan}$ whereas the estimated $\varepsilon_{hr}$ excluded $\Delta T_{fan}$ (further discussed in Section 5.8.2).

$$\varepsilon_{hr} = \frac{V_{oa}(T_{erv} - T_{oa})}{V_e(T_r - T_{oa})} = \frac{(T_{erv} - T_{oa})}{(T_r - T_{oa})} \quad \text{eq. 5.2}$$

The $T_s$ set point, in eQUEST, with inactive heating and cooling coils was modelled as the set point subtracted by half the throttling range. The default throttling range for the $T_s$ set point was 2.2 °C and would cause the simulated $T_s$ to be 1.1 °C below the desire reset profile calculated from trend data. Therefore the throttling range was set to 0 °C in order to maintain the set point indicated by trend data. This operation was deemed reasonable because the cooling season was excluded in this thesis and the physical controllers used PI control, which essentially has a small throttling range.

The economizer model in eQUEST used variable outdoor air dampers whereas the physical configuration did not. Specifying a minimum outdoor air flow ratio schedule as a function of hourly air flow equal to $\alpha$ generated from trend data created a thermodynamically equivalent system. The economizer control was specified as dual enthalpy which opened the mixing air dampers when the enthalpy of the outside air was less than the return air.

The cooling supply air temperature set point, used to simulate heat recovery performance, was generated using the set point from the 2013 heating season (Table 4.16). The shoulder season did not contain information about the maximum $T_s$ that could be achieved without heating coils because they were never activated.

Information about heat recovery when frost control was active was required to generate the design $\varepsilon_{hr}$. During the shoulder season frost control was inactive and therefore the $\varepsilon_{hr}$ input was generated as the value from the 2013 heating season. Generating the temperature exiting the heating coils ($T_{hd}$) set point and design $\varepsilon_{hr}$ demonstrated the need for use of long periods of measurement to generate inputs for shorter time periods.

A summary of the system level inputs generated for the shoulder season are shown in Table 5.7. The majority of inputs were similar to the values generated from the 2013 and 2014 heating seasons; however, a few changes occurred. The design supply $\Delta T_{fan}$ was smaller than the value generated during the heating seasons because there was less steam humidification. The zone reheat generated was also smaller than the heating seasons because $T_{oa}$ was warmer as its set point was controlled by a reset profile.

Table 5.7 Shoulder season inputs generated from trend data

| | Description | | AACT | Unit |
|---|---|---|---|---|
| Air-side | Cooling supply air set point | | 14.4 | °C |
| | Maximum heating supply air flow ratio | | 0.35 | - |
| | Minimum supply air flow ratio | | 0.19 | - |
| | Design supply $\Delta T_{fan}$ | | 6.8 | °C |
| | Design return $\Delta T_{fan}$ | | 4.6 | °C |
| | Supply air reset temperature | Supply-high | 16 | °C |
| | | Outside-low | -28 | °C |
| | | Supply-low | 12 | °C |
| | | Outside-high | 28 | °C |
| | Minimum outdoor air ratio | | 83 | % |
| | Heat recovery activation $\Delta T$ | | 14.5 | °C |
| | Heat recovery effectiveness | | 0.24 | - |
| | Zone reheat | | 13.3 | °C |
| | Minimum humidity | | 26 | % |
| | Maximum humidity | | 30 | % |
| Water-side | Zone reheat hot water reset temperature | Supply-high | 46.5 | °C |
| | | Outside-low | -15.7 | °C |
| | | Supply-low | 35.2 | °C |
| | | Outside-high | 5.5 | °C |

### *5.7.2 Model limitations and errors*

A limitation of the simulated $T_m$ was that the model assumed that a fan heating penalty ($FHP_{hr}$) would increase $T_m$ to account for the additional fan power required to overcome the pressure difference caused by the heat recovery coils. The equations eQUEST used to calculate $FHP_{hr}$ are shown in Appendix E. Physically, $FHP_{hr}$ did not occur because the additional fan power only affected the air at the supply fan. In reality, the pressure drop across the heat recovery coils, filters, or any coils will increase temperature due to friction experienced as the air passes through the coils. It was uncertain why this was included in the model for heat recovery but not for the heating and cooling coils. The trend analysis in Chapter 4 assumed the temperature rise due to friction across coils was negligible. The static pressure drop across the heat recovery coils in contact with the outdoor and exhaust air was modelled with 0 Pa to remove $FHP_{hr}$ from the model.

Another model limitation was the exhaust air temperature entering the heat recovery coils including $\Delta T_{fan}$. In the case of the Genome building the exhaust air ducts were separate from the return air ducts and did not receive a temperature rise caused by a fan when passed through the heat recovery coils. The return air fan temperature rise was not removed because it was important to model $T_r$ with $\Delta T_{fan}$ to ensure the economizer was simulated correctly.

## *5.8 Bottom-up Calibration Iteration 1*

The initial model was created and initial model errors and limitations were removed. Next, the bottom-up calibration started at the zone level. This section sequentially reports calibration of the zone and system level models and qualitatively compares $\dot{Q}_{GE}$ with measurements from the 2014 shoulder season.

### *5.8.1 Zone calibration*

Statistical indices compare the initial zone level model simulation outputs to trend data in Table 5.8. The initial model had 11 out of 17 zones that were calibrated according to the criteria in ASHRAE Guideline 14 (2002), referred to herein as the calibration criteria.

This represented zones containing 62% of the modelled floor area and 72% of the supply air flow. Cells highlighted in grey referred to zone indoor air temperatures ($T_z$) or air flow rate statistical indices that did not meet the calibration criteria. The checkmark or cross beside each zone indicated if a zone met or did not meet the calibration criteria, respectively, based on if any cells in its row were highlighted grey. Visual comparisons of $T_z$ for selected zones are shown in Figure 5.8.

Table 5.8 Statistical indices comparing initial zone level results

| Zone | | Temperature | | | Supply air flow rate | | |
|---|---|---|---|---|---|---|---|
| | | MBE (%) | RMSE (°C) | CV(RMSE) (%) | MBE (%) | RMSE (L/s) | CV(RMSE) (%) |
| Z1-S | x | -3.6 | 1.2 | 5.6 | 127 | 343 | 172 |
| Z1-NE | x | -10 | 2.7 | 12 | 72 | 302 | 89 |
| Z1-NW | ✓ | -1.0 | 0.9 | 4.3 | 0.2 | 3.4 | 0.7 |
| Z1-CORR | ✓ | -1.9 | 0.7 | 3.2 | -0.5 | 16 | 3.4 |
| Z1-CONF | x | 0.5 | 1.0 | 4.8 | 20 | 194 | 56 |
| Z2-SW | ✓ | -3.7 | 1.2 | 5.6 | 1.1 | 117 | 15 |
| Z2-E | x | -1.1 | 0.9 | 4.1 | 12 | 618 | 30 |
| Z2-INT | ✓ | -0.7 | 0.8 | 3.4 | 4.3 | 79 | 22 |
| Z2-NE | ✓ | -2.6 | 0.8 | 3.5 | 0.3 | 114 | 9.3 |
| Z2-S | ✓ | -3.3 | 0.9 | 4.0 | 0.1 | 114 | 0.4 |
| Z2-W | x | -2.0 | 0.7 | 3.1 | 43 | 74 | 85 |
| Z3-SW | ✓ | -1.6 | 1.0 | 4.6 | -0.6 | 101 | 14 |
| Z3-E | ✓ | -1.4 | 0.9 | 3.8 | 5.3 | 336 | 15 |
| Z3-INT | ✓ | -0.8 | 0.7 | 3.1 | 6.9 | 59 | 21 |
| Z3-NE | ✓ | -2.7 | 0.8 | 3.6 | -0.4 | 106 | 10 |
| Z3-S | ✓ | -3.4 | 0.9 | 4.2 | 7.8 | 106 | 28 |
| Z3-W | x | -1.3 | 0.8 | 3.8 | 1.7 | 45 | 33 |

The majority of zones $T_z$ in Figure 5.8 closely followed the pattern in the trend data. However, the $T_z$ in zone Z1-NE was simulated at a consistent lower value.

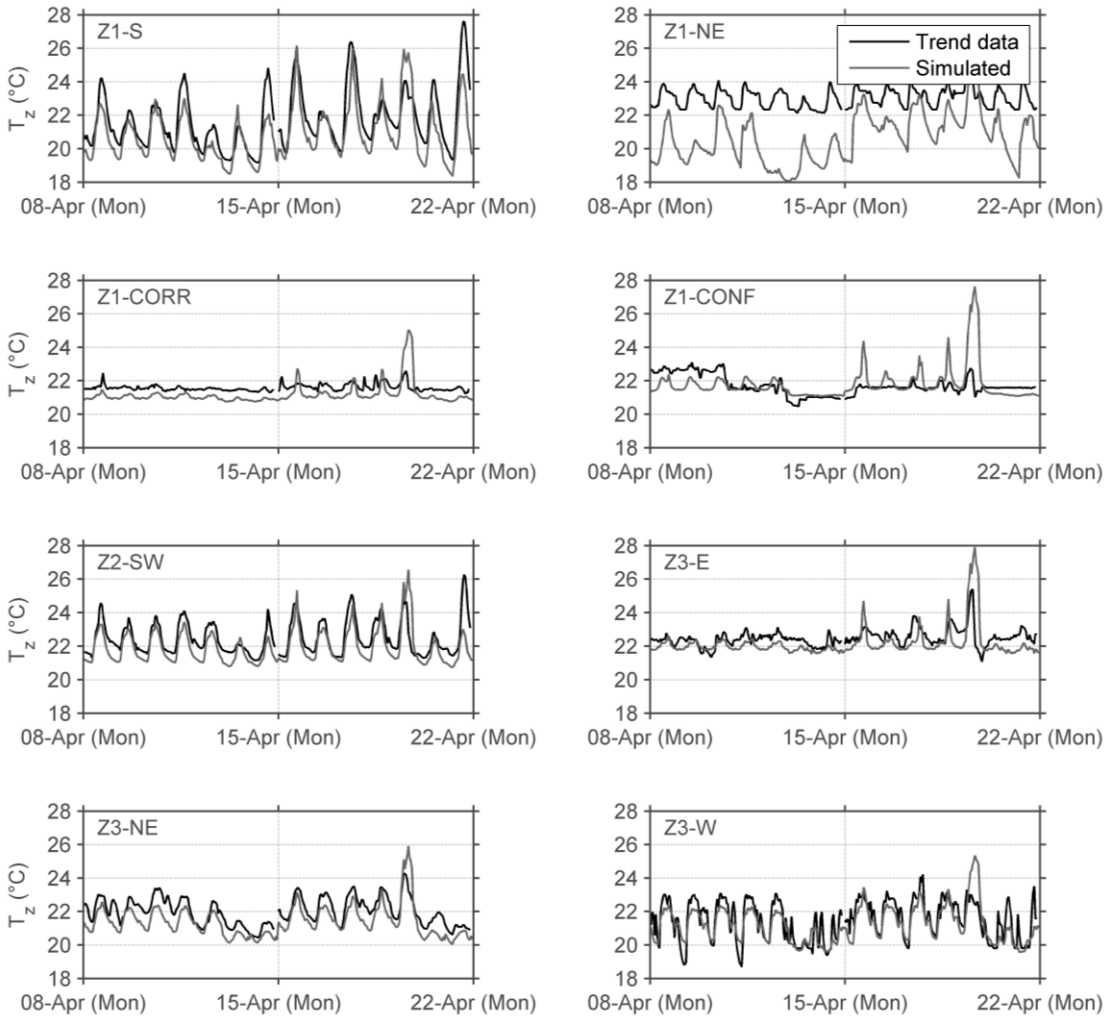


Figure 5.8 Selected zone indoor air temperatures simulation vs. trend data

Visual comparisons of zone supply air flow rates ($V_{zs}$) for selected zones are shown in Figure 5.9. The simulated $V_{zs}$ in zones Z1-CORR, Z2-SW, and Z3-NE fit the trend data very well. Zones Z1-S's and Z1-NE's simulated $V_{zs}$ was consistently larger than the trend data. Hourly median air flow rate schedules worked poorly for zones that had irregular air flow rates such as Z1-CONF and Z2-E. The $V_{zs}$ in Z3-W followed the pattern in the trend data but its mean was small in comparison to its RMSE, which resulted in poor model fit.

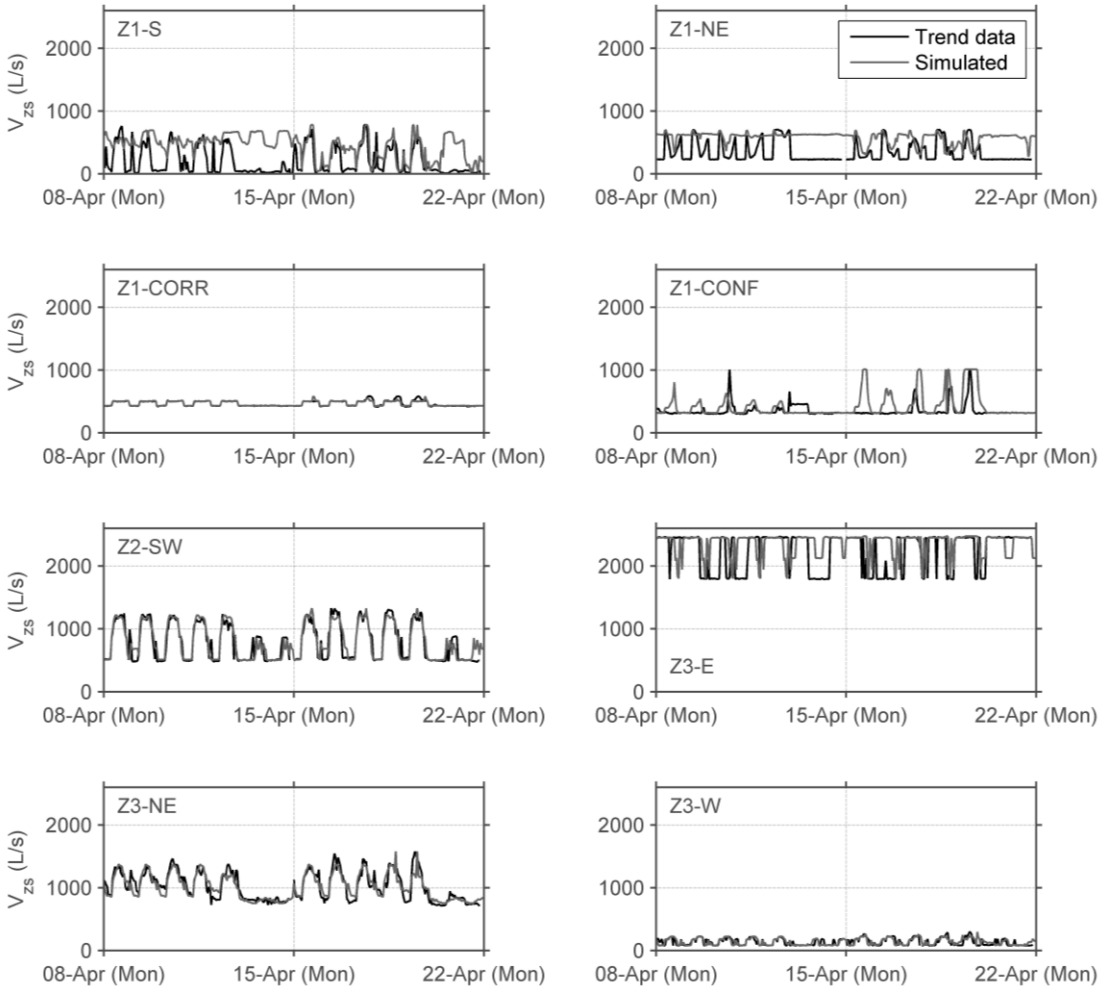


Figure 5.9 Selected zone supply air flow rates simulation vs. trend data

5.8.1.1 Zone level tuning

The first iteration of calibration involved tuning zone internal gains using the tuning strategy described in Section 3.3.1. It is important to emphasize that only the internal gains were tuned to simply the procedure for the reasons described in Section 3.3.1. Two sets of internal gain schedules were used throughout the tuning procedure. The first was the aggregated schedule presented in Figure 5.6, initially applied to all zones. The second was a constant schedule with each diversity factor equal to 1. In the following sections, tuning a *peak value* refers to changing one of the aggregated values in Table 5.6 which used the aggregated schedule. If the schedule was changed to a constant schedule the

*hourly magnitude* was used to describe the power density during each hour. The first iteration of internal gains tuning is summarized in Table 5.9.

Table 5.9 Zone tuning summary: iteration 1

| Zone | Tuning procedure | Reason |
|---|---|---|
| Z1-S | Changed to a constant schedule with an hourly magnitude of 19 W/m$^2$ | Large $V_{zs}$ during unoccupied periods |
| Z1-NE | Changed to a constant schedule with an hourly magnitude of 38 W/m$^2$ to account for electric fan coils | Consistently low $T_z$ and large $V_{zs}$ |
| Z1-CONF | Changed to a constant schedule with an hourly magnitude of 3.2 W/m$^2$ | Constant $V_{zs}$ indicated constant loads |
| Z2-W | Changed to a constant schedule with an hourly magnitude of 11 W/m$^2$ | Large $V_{zs}$ during unoccupied periods |
| Z3-S | Changed to a constant schedule with an hourly magnitude of 11W/m$^2$ to account for a large laboratory freezer | Large $V_{zs}$ during unoccupied periods |
| Z3-W | Changed to a constant schedule with an hourly magnitude of 9.7 W/m$^2$ | Large $V_{zs}$ during unoccupied periods |

Zone Z1-S was a good example to demonstrate how highly uncertain the zone loads were. For the case of Z1-S, no more information from evidence was available to guide the tuning process as it had been exhausted in the model creation. For example. effective curtain wall U-values and air infiltration were uncertain but were estimated using information from design documents and the literature. The model fit was poor in zone Z1-S during the unoccupied periods such as weekends and many evenings. One of the reasons for poor fit during the weekends was because the hourly median $T_z$ for weekend temperature profiles did not correctly represent the lower $T_z$ during the first weekend and the higher $T_z$ during the second weekend. The large simulated $V_{zs}$ during unoccupied periods indicated that the zone's internal loads had to be increased.

From site inspection, the equipment in Z1-S contained computers and monitors. Zone Z1-S also had zero $V_{zs}$ during unoccupied periods (Figure 5.9) and thus relied on its loads to maintain the set point temperature. This was the reason why the internal gains in

zone Z1-S (Table 5.9) were tuned larger than the value originally specified. There were many reasons the internal loads had to be increased; for example, the entered curtain wall vision panel U-value and/or infiltration may have been too large or perhaps the doors were left open in which case interzonal air flow may have contributed to heat gains, which was not measured and DOE-2 lacked the capacity to model. The thermostat may also not be representative of some room which could make some zones appear warmer.

The gains in Z1-NE were increased because it contained electric fan coils with a total capacity of 60 kW which were neglected in the initial model and might have explained its low simulated $T_z$ and large $V_{zs}$.

The $V_{zs}$ trend data in Z1-CONF indicated that this zone was occupied intermittently. Thus its internal gains were reduced and changed to a constant schedule. The constant schedule was used because $V_{zs}$ was often constant.

Zones Z2- and Z3-W both contained a lunch room that housed refrigerators, microwaves, and kettles, etc. The plug and occupant loads might have exceeded initially estimates. The losses may have been smaller than initial estimates. Either way they were uncertain.

Zone Z3-S was changed to a constant schedule because its $V_{zs}$ was constant which indicated constant internal loads. The hourly magnitude was increased because it housed a large laboratory-size freezer.

The first iteration of tuning improved the model fit of the zones tuned but resulted with no additional calibrated zones (Table 5.10). Improving the zone model fit further was not practical for two reasons. First, the use of hourly median $T_z$ and minimum air flow ratio schedules were not appropriate for zones with irregular $V_{zs}$ patterns. Daytyping techniques could be used to improve model fit but would have required further expansion of the AACT. Second, developing custom internal gain schedules for each zone might have also improved model fit but was impractical to implement. These two additional methods were not worth the time to gain a slight improvement. The system level model was calibrated next since a large fraction of zones met the calibration criteria. This large fraction of zones represented 62% of the modelled floor area and 72% of the supply air flow.

Table 5.10 Statistical indices comparing zone level results after iteration 1

| Zone | | Temperature | | | Supply air flow rate | | |
|---|---|---|---|---|---|---|---|
| | | MBE (%) | RMSE (°C) | CV(RMSE) (%) | MBE (%) | RMSE (L/s) | CV(RMSE) (%) |
| Z1-S | x | -1.8 | 1.0 | 4.8 | 83 | 248 | 125 |
| Z1-NE | x | -0.7 | 1.0 | 4.4 | 13 | 125 | 37 |
| Z1-NW | ✓ | -0.9 | 0.9 | 4.3 | 0.2 | 3.4 | 0.7 |
| Z1-CORR | ✓ | -1.7 | 0.7 | 3.1 | -0.4 | 16 | 3.5 |
| Z1-CONF | x | -1.4 | 0.8 | 3.6 | -6.5 | 115 | 33 |
| Z2-SW | ✓ | -3.2 | 1.2 | 5.3 | 1.1 | 117 | 15 |
| Z2-E | x | -1.1 | 0.9 | 4.1 | 12 | 619 | 30 |
| Z2-INT | ✓ | -0.7 | 0.8 | 3.4 | 4.4 | 79 | 22 |
| Z2-NE | ✓ | -2.6 | 0.8 | 3.5 | 0.4 | 112 | 9.1 |
| Z2-S | ✓ | -2.9 | 0.9 | 3.9 | 0.1 | 112 | 0.5 |
| Z2-W | x | -1.1 | 0.6 | 2.8 | 15 | 57 | 65 |
| Z3-SW | ✓ | -0.7 | 1.0 | 4.5 | -0.6 | 101 | 14 |
| Z3-E | ✓ | -1.4 | 0.9 | 3.8 | 5.3 | 337 | 15 |
| Z3-INT | ✓ | -0.8 | 0.7 | 3.1 | 7.0 | 59 | 21 |
| Z3-NE | ✓ | -2.7 | 0.8 | 3.5 | -0.5 | 106 | 10 |
| Z3-S | ✓ | -2.4 | 0.8 | 3.7 | 0.5 | 106 | 22 |
| Z3-W | x | -0.8 | 0.8 | 3.8 | 5.1 | 49 | 37 |

### *5.8.2 System level calibration*

Statistical indices were used to compare the initial system level model outputs to trend data after the first iteration of zone level calibration (Table 5.11). A row with a grey cell determined that the variable did not meet the calibration criteria. Using information from trend data and partially calibrating the zone level first yielded a calibrated system level model. Visual comparisons of system level variables are shown in Figure 5.10 to Figure 5.18.

Table 5.11 Statistical indices comparing system level results after zone iteration 1

| Variable | MBE (%) | RMSE | CV(RMSE) (%) |
|---|---|---|---|
| $T_s$ (°C) | 2.7 | 2.1 | 15 |
| $T_m$ (°C) | 1.8 | 1.6 | 14 |
| $T_r$ (°C) | -0.9 | 0.88 | 3.7 |
| $RH_r$ (%) | 6.1 | 3.6 | 14 |
| $V_s$ (L/s) | 5.1 | 1208 | 11 |
| $\alpha$ (%) ($T_{oa}$ < 10 °C) | -0.3 | 4.3 | 5.1 |
| $\dot{Q}_{hr}$ (kW) | 3.3 | 8.6 | 18 |
| $\varepsilon_{hr}$ (%) | -6.9 | 2.6 | 17 |
| $T_{hr}$ (°C) | 0.5 | 47 | 4.7 |

Large differences in the peak $T_s$ (Figure 5.10) occurred during the second week when outdoor air temperaturtes were higher. Comparing $T_{oa}$ measured on-site to the weather file (Figure 5.1) revealed large differences between the peak values that occurred in the second week. The high temperature peaks recorded may have been caused by a $T_{oa}$ sensor error because the cooling coils were inactive. Overall, the $T_s$ closely followed the pattern in the trend data. The $T_r$ (Figure 5.12) varied with a larger amplitude and at a lower value than the trend data.

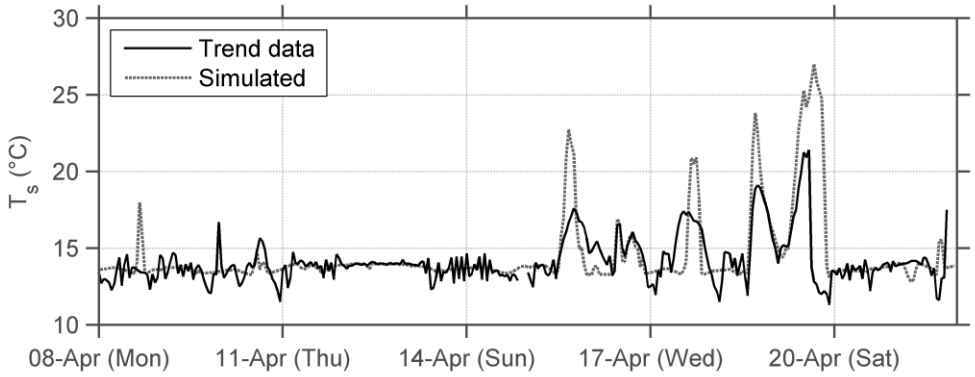


Figure 5.10 Supply air temperature simulation vs. trend data

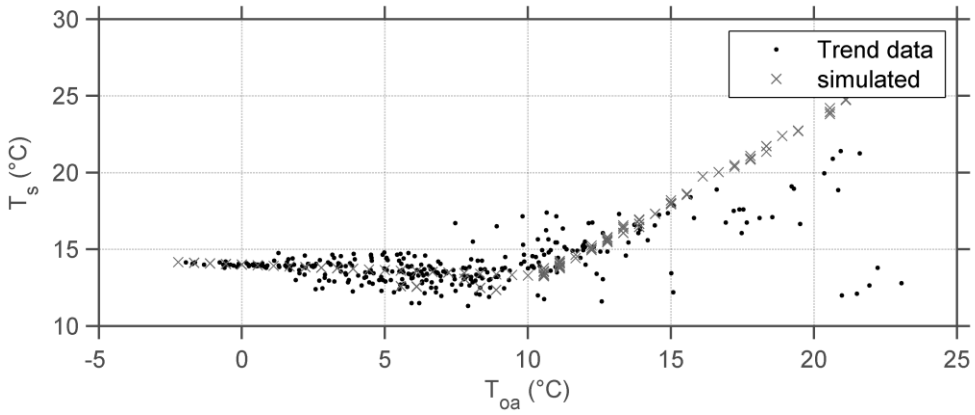


Figure 5.11 Supply air temperature against outdoor air temperature simulation vs. trend data

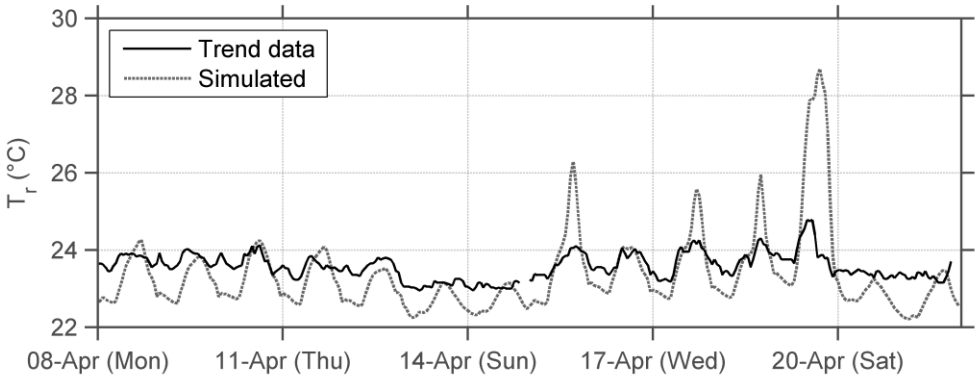


Figure 5.12 Return air temperature comparison

The return air relative humidity ($RH_r$) (Figure 5.13) generally followed the pattern in the trend data but was sometimes larger than measured. The weather file was not updated with the outdoor air relative humidity ($RH_{oa}$) trend data because the sensor generated many anomalous values. A difference between the weather file and measured $RH_{oa}$ may have contributed to differences in $RH_r$.

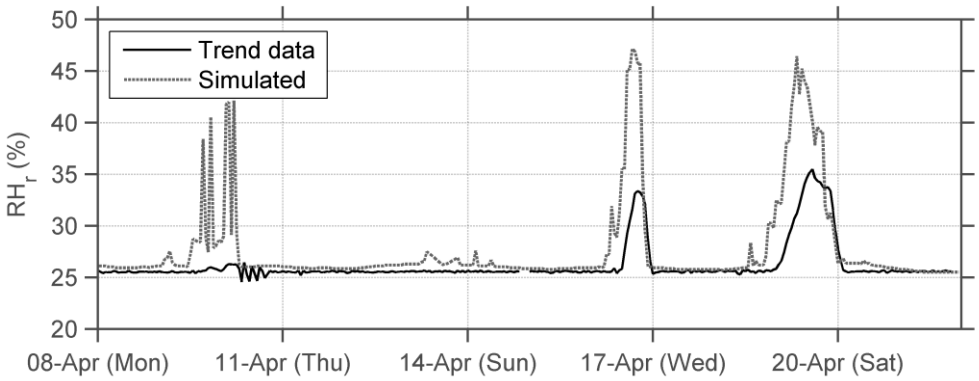


Figure 5.13 Return air relative humidity simulation vs. trend data

The simulated $V_s$ followed the pattern in the trend data well but was often greater during weekends and some evenings. The main reason for this was because the $V_{zs}$ fit was poor during the same evenings and weekends in Z1-S, Z1-NE, Z2-E, and Z3-E.

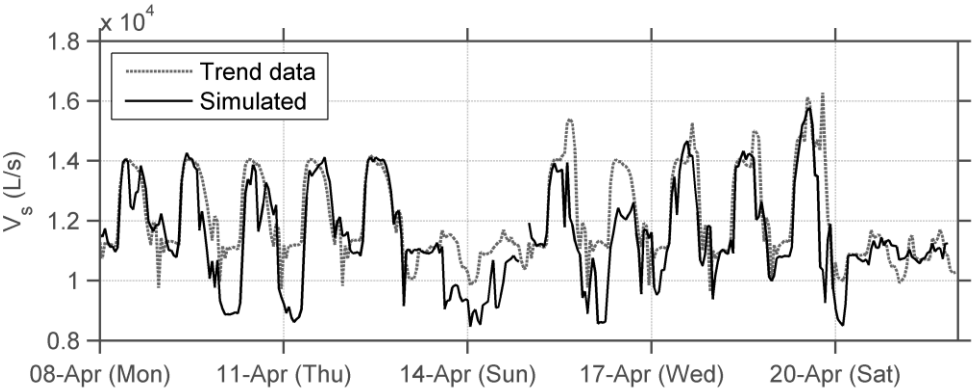


Figure 5.14 Supply air flow rate simulation vs. trend data

The ratio of outdoor to supply air flow rate ($\alpha$) (Figure 5.15) followed a pattern similar to the one estimated based on air flow rates using the time series method. It showed that the mixing air dampers reached their minimum position when $T_{oa}$, recorded with the trend data, was less than approximately 8 °C rather than 10 °C (Figure 4.11). This may have occurred due to differences between the $RH_{oa}$ trend data and the weather file.

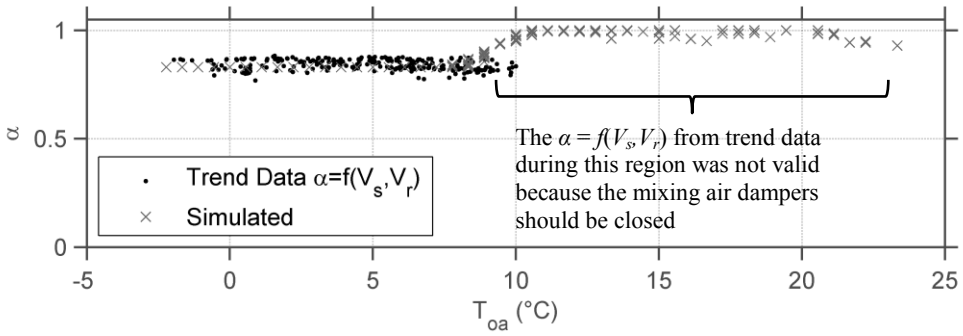


Figure 5.15 Outdoor air flow ratio simulation vs. trend data

The $T_{hr}$ (Figure 5.16) and heat recovery heat flow rate ($\dot{Q}_{hr}$) (Figure 5.17) followed the pattern in the trend data well. The simulated $\varepsilon_{hr}$ (Figure 5.18) used the return air which contained $\Delta T_{fan}$ whereas the value estimated from trend data did not. This caused the simulated $\varepsilon_{hr}$ to be less than estimated from trend data. If the $\Delta T_{fan}$ was removed from the simulated $T_r$, the MBE, RMSE, and CV(RMSE) of $\varepsilon_{hr}$ would be 0.2, 3.1, and 20%, respectively. Therefore, the $\Delta T_{fan}$ included in the output $T_r$ did not greatly affect the results because the difference between $T_r$ and $T_{oa}$ when heat recovery was active was much greater than $\Delta T_{fan}$. The $T_{erv}$, $\beta$, and $\varepsilon_{hr}$ directly output from eQUEST are shown in Appendix G but are discussed in detail during the heating season calibration (Chapter 6).

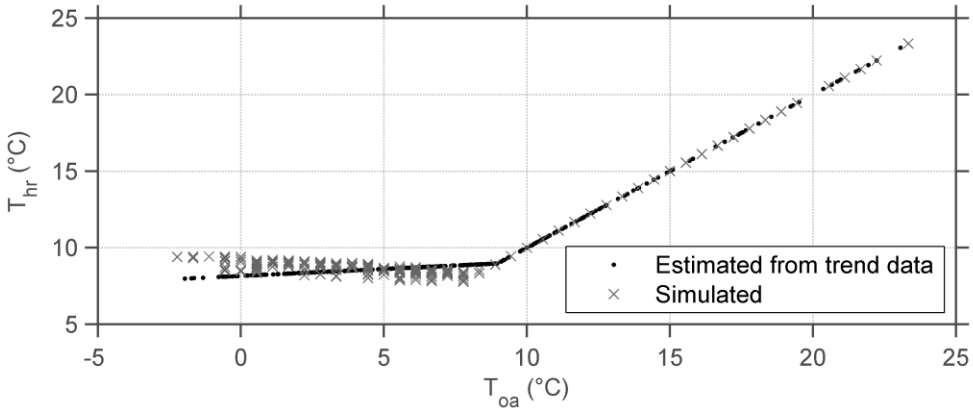


Figure 5.16 Air temperature exiting heat recovery simulation vs. trend data

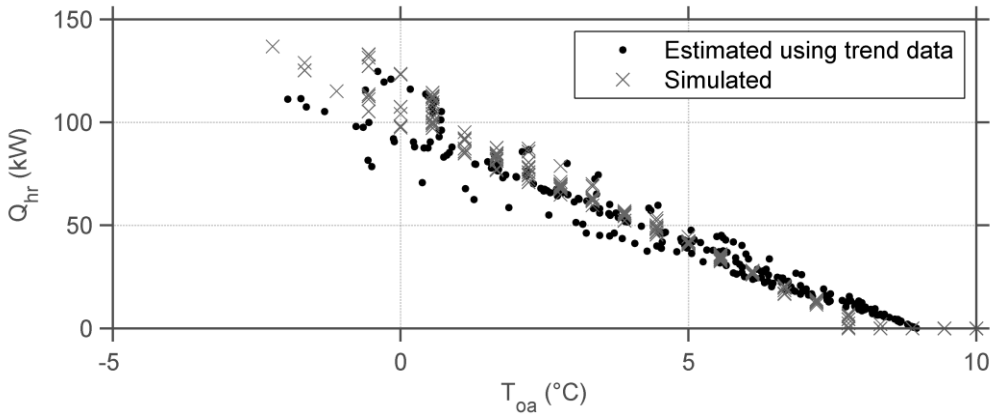


Figure 5.17 Heat recovery heat flow rate simulation vs. trend data

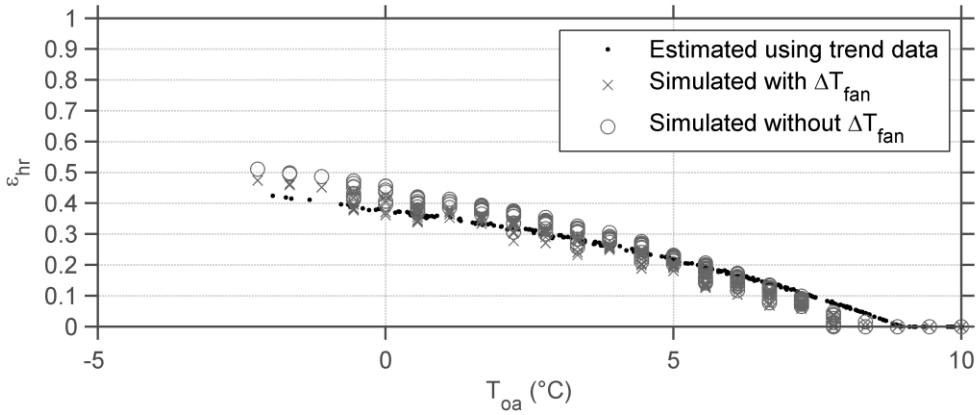


Figure 5.18 Heat recovery effectiveness simulation vs. trend data

The whole-building level was calibrated next since the system level model was calibrated.

### *5.8.3 Initial whole-building hot water heating results*

The whole-building hot water heat flow rate ($\dot{Q}_{GE}$) (eq. 3.7) was only available from February 2014 onward. It was still useful to qualitatively compare the simulated 2013 to 2014 shoulder season $\dot{Q}_{GE}$ trend data to ensure that the results were within a reasonable range and followed the pattern in the trend data. The $\dot{Q}_{GE}$ during the shoulder seasons represented the energy used in zone reheat only because the heating coils were inactive. It should also be mentioned that the overall $\dot{Q}_{GE}$ distribution for 3 out of 4 floors was

uncertain but it was likely that most, if not all, of $\dot{Q}_{GE}$ was used to condition the floors above grade because the basement housed a large quantity of active lab equipment and server room (Concordia University 2014b).

A visual comparison of $\dot{Q}_{GE}$ is shown in Figure 5.19; the simulated $\dot{Q}_{GE}$ followed the pattern in the trend data but at a consistently higher value. This indicated that the internal loads had to be further increased to reduce the simulated $\dot{Q}_{GE}$ which was larger than the trend data. The $\dot{Q}_{GE}$ overall uncertainty was large because the overall uncertainty in temperature sensors was large relative to the temperature difference measured.

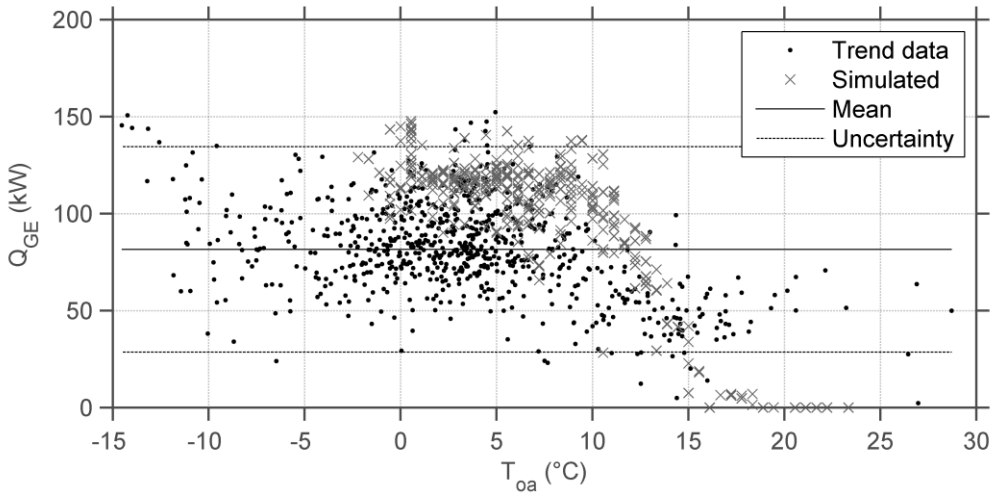


Figure 5.19 Initial whole-building hot water heat flow rate comparison

Even though the zone and system level models were considered calibrated, the simulated $\dot{Q}_{GE}$ was larger than measured due to model underdetermination caused with the uncertain zone reheat energy. This demonstrated the need to re-tune the zone loads.

### *5.9 Bottom-up Calibration: Iteration 2*

Analysing the estimated heat loss from the vision panels only in Z3-SE revealed it was often 3 times greater than $\dot{Q}_{zheat}$ (eq. 3.2) (Figure 5.20) estimated from trend data. The $\dot{Q}_{zheat}$ was calculated assuming that $T_{zs}$ measured in room 320-03 was representative of each room in the zone. Negative and positive $\dot{Q}_{zheat}$ referred to heat loss and gain, respectively. Adding $\dot{Q}_{zheat}$ to the estimated vision panel heat loss and dividing by the

zone area generated the heat flow rate density per $m^2$ of internal loads required to maintain $T_z$ (Figure 5.21). This procedure was most beneficial when the area was unoccupied and the solar gains were zero. Matching the estimated net heat loss required an additional approximate 30 $W/m^2$ difference (Figure 5.21) between gains and losses during the unoccupied periods, which was large for an office space. Each of the rooms in zone Z3-SW had the capacity to house 4 office desks. It was uncertain if the offices in this zone contained lab equipment or were performing intensive computer simulations overnight to explain the estimated missing heat gains. The thermal capacity and lag associated with hot water zone reheat coils, which were not estimated or simulated, may also have contributed additional gains. Without submetered power data, it remained uncertain where the additional gains came from. This was another example of large uncertainties at the zone level. The author also questions the overall quality of the $T_{zs}$ data because it was uncertain why the BAS set points and sensors were available in only 3 rooms (Figure 4.5).

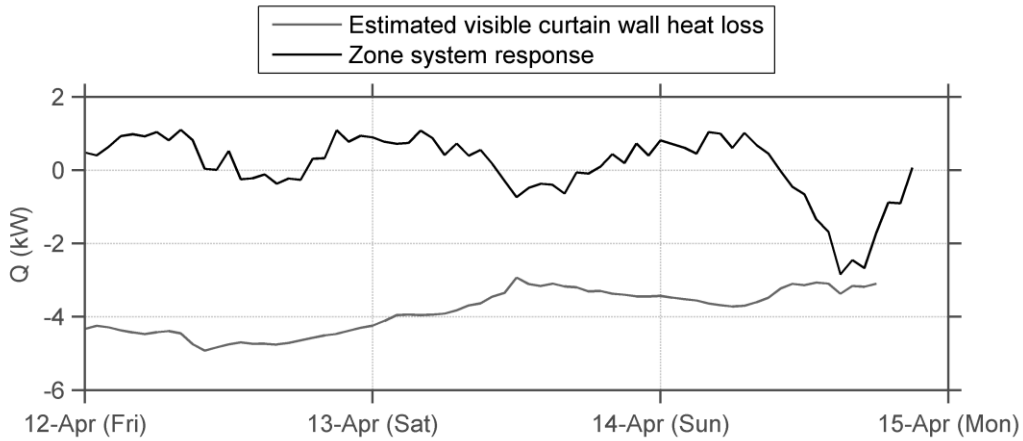


Figure 5.20 Zone heating response and vision panel wall heat loss

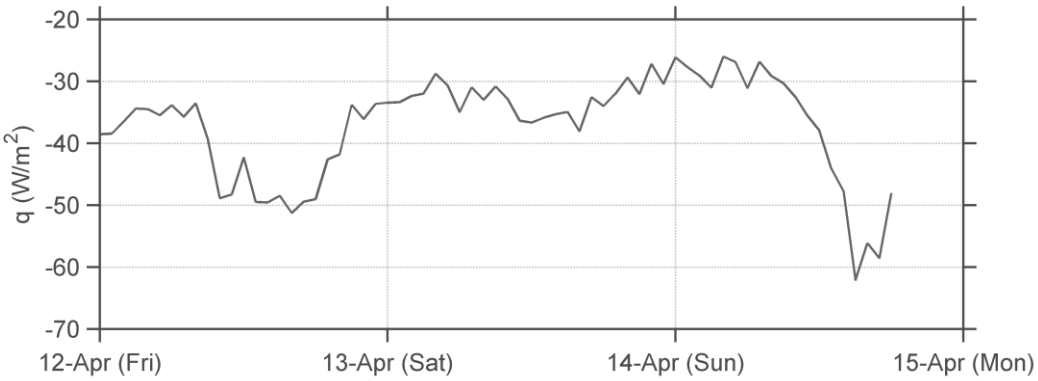


Figure 5.21 Estimated heat flow rate per area to maintain zone indoor air temperature

The zone heating coil heat flow rates ($\dot{Q}_{zheat}$) extracted from eQUEST provided information to understand the simulated $\dot{Q}_{zheat}$ when compared to their maximum design capacity (Figure 5.22). The maximum zone reheat design information is shown in Appendix F. For example, Z2-SW, Z3-W, and Z1-CORR were already operating at their design capacity which was unlikely because it was the shoulder season. Therefore, it was likely that their internal gains were larger than initially modelled. Zone internal gains tuning is summarized in Table 5.12. The values in Table 5.12 may seem large for internal gains but it is important to note that these values represent the tuning required to adjust the lumped behaviour of the all zone loads as described in Section 3.3.1.

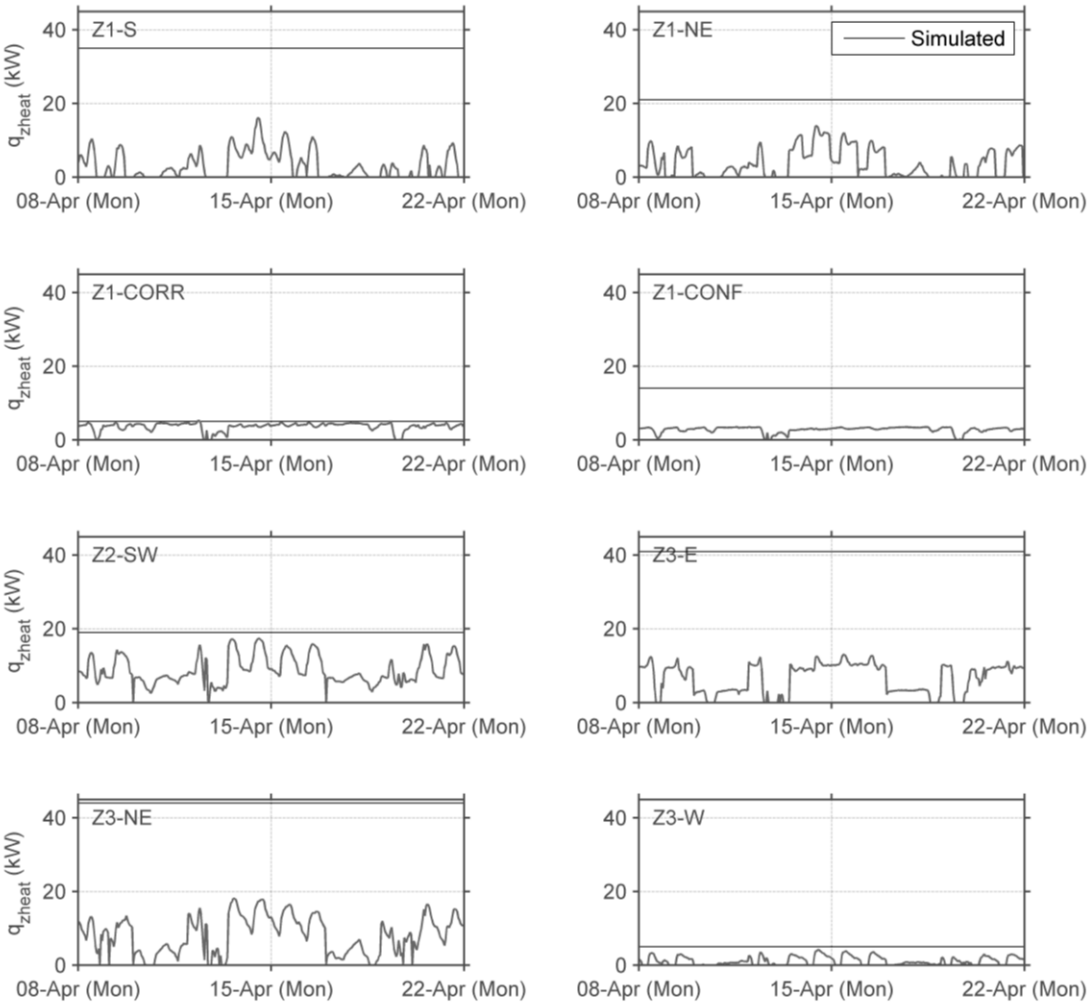


Figure 5.22 Zone reheat flow rate comparison with design values

Table 5.12 Zone tuning summary: iteration 2

| Zone | Tuning procedure | Reason |
|---|---|---|
| Z1-S | Changed hourly magnitude to 21 W/m$^2$ | Large $V_{zs}$ during unoccupied periods |
| Z1-NW | Changed to a constant schedule with an hourly magnitude of 25 W/m$^2$ | Constant $V_{zs}$ indicated constant loads |
| Z1-CORR | Changed peak value to 11 W/m$^2$ | Large simulated $\dot{Q}_{zheat}$ for a corridor |
| Z2-SW | Increased peak value to 47 W/m$^2$ | Large simulated $\dot{Q}_{zheat}$ |
| Z2-E | Changed to a constant schedule with an hourly magnitude of 38W/m$^2$ | Had large simulated $\dot{Q}_{zheat}$ for a laboratory |
| Z2-INT | Changed to a constant schedule with an hourly magnitude of 22 W/m$^2$ | Large simulated $\dot{Q}_{zheat}$ and constant $V_{zs}$ indicated constant loads |
| Z2-NE | Changed peak value to 47 W/m$^2$ | Large simulated $\dot{Q}_{zheat}$ for laboratory/office |
| Z3-SW | Increased peak value to 47 W/m$^2$ | Large simulated $\dot{Q}_{zheat}$ |
| Z3-E | Changed to a constant schedule with an hourly magnitude of 38W/m$^2$ | Had large simulated $\dot{Q}_{zheat}$ for a laboratory |
| Z3-INT | Changed to a constant schedule with an hourly magnitude of 22 W/m$^2$ | Large simulated $\dot{Q}_{zheat}$ and constant $V_{zs}$ indicated constant loads |
| Z3-NE | Changed peak value to 47 W/m$^2$ | Large simulated $\dot{Q}_{zheat}$ for laboratory/office |

The internal gains of the perimeter zones Z1-S, Z2- and Z3-SW, and Z2- and Z3-NE were increased because of the heat loss analysis earlier in this section. Zone Z1-S still had a large $V_{zs}$ during unoccupied periods after the first iteration of tuning. In the case of Z2- and Z3-NE, approximately 50% of this zone was a laboratory which may have had larger internal gains than earlier specified.

Zone Z1-NW housed a laboratory and loading bay. It had a constant $V_{zs}$ which indicated that it had constant internal loads. The loading bay had an electric heater and the laboratory was full of large equipment and computers which indicated its internal gains may have been larger than initially specified.

As shown in Figure 5.22, Z1-CORR had a large $\dot{Q}_{zheat}$ for a corridor. Thus, the peak value of its internal gains was increased to reduce its $\dot{Q}_{zheat}$.

A constant schedule was applied to Z2- and Z3-INT because its constant $V_{zs}$ indicated constant internal loads. It was likely that the internal gains specified earlier were too small because these zones housed laboratories and environmental chambers.

The zone and system level results after the second iteration of zone tuning are shown in Table 5.13 and Table 5.14. The model fits of $T_z$ and $V_{zs}$ changed little; instead, the MBE and CV(RMSE) in some zones slightly increased or reduced. Overall, there were 11 out 17 zones that were considered calibrated with Z1-NE, Z1-CONF, Z2-E, and Z3-W very close to being calibrated. System level results changed little.

A visual comparison of $\dot{Q}_{GE}$ after the second iteration of zone level tuning is shown in Figure 5.23. The simulated $\dot{Q}_{GE}$ had a mean and median of 82 kW and 90 kW and a standard deviation and MAD of 32 kW and 11 kW, respectively. The mean was used here to highlight the large uncertainty when estimating $\dot{Q}_{GE}$ from trend data. The $\dot{Q}_{GE}$ trend data had a mean value of 81 ± 53 kW and a median and *MAD* of 81 kW and 15 kW, respectively. Overall, $\dot{Q}_{GE}$ followed the pattern in the trend data with a reasonable value given its large uncertainty.

Table 5.13 Calibrated zone level model summary after zone iteration 2

| Zone | | Indoor air temperature | | | Supply air flow rate | | |
|---|---|---|---|---|---|---|---|
| | | MBE (%) | RMSE (°C) | CV(RMSE) (%) | MBE (%) | RMSE (L/s) | CV(RMSE) (%) |
| Z1-S | x | -1.4 | 1.0 | 4.7 | 76 | 235 | 118 |
| Z1-NE | x | -0.7 | 1.0 | 4.5 | 13 | 126 | 37 |
| Z1-NW | ✓ | -0.1 | 0.9 | 4.3 | 0.2 | 3.6 | 0.8 |
| Z1-CORR | ✓ | -1.5 | 0.7 | 3.2 | -0.3 | 16 | 3.5 |
| Z1-CONF | x | -1.3 | 0.8 | 3.6 | -5.6 | 123 | 35 |
| Z2-SW | ✓ | -2.5 | 1.1 | 5.1 | 1.4 | 119 | 15 |
| Z2-E | x | 0.0 | 1.0 | 4.5 | 12 | 621 | 30 |
| Z2-INT | ✓ | -0.2 | 0.7 | 3.2 | 4.6 | 80 | 22 |
| Z2-NE | ✓ | -2.3 | 0.8 | 3.5 | 0.9 | 121 | 9.9 |
| Z2-S | ✓ | -2.1 | 0.8 | 3.6 | 0.1 | 121 | 0.5 |
| Z2-W | x | -1.0 | 0.6 | 2.8 | 15 | 58 | 67 |
| Z3-SW | ✓ | -0.6 | 1.0 | 4.5 | -0.3 | 103 | 14 |
| Z3-E | ✓ | -0.4 | 0.9 | 4.1 | 5.6 | 341 | 15 |
| Z3-INT | ✓ | -0.2 | 0.7 | 2.8 | 7.2 | 60 | 21 |
| Z3-NE | ✓ | -2.3 | 0.8 | 3.5 | 0.0 | 110 | 11 |
| Z3-S | ✓ | -2.3 | 0.8 | 3.7 | 0.6 | 110 | 22 |
| Z3-W | x | -0.7 | 0.8 | 3.8 | 6.4 | 50 | 37 |

Table 5.14 Statistical indices comparing system level results after zone iteration 2

| Variable | MBE (%) | RMSE | CV(RMSE) (%) |
|---|---|---|---|
| $T_s$ (°C) | 2.8 | 2.1 | 15 |
| $T_m$ (°C) | 1.8 | 1.6 | 14 |
| $T_r$ (°C) | -0.3 | 0.91 | 3.9 |
| $RH_r$ (%) | 5.8 | 3.6 | 14 |
| $V_s$ (L/s) | 5.3 | 1268 | 11 |
| $\alpha$ (%) ($T_{oa}$ < 10 °C) | -0.3 | 4.3 | 5 |
| $\dot{Q}_{hr}$ (kW) | 2.6 | 8.4 | 18 |
| $\varepsilon_{hr\,(\%)}$ | -7.9 | 2.6 | 17 |
| $T_{hr}$ (°C) | 0.3 | 47 | 4.7 |

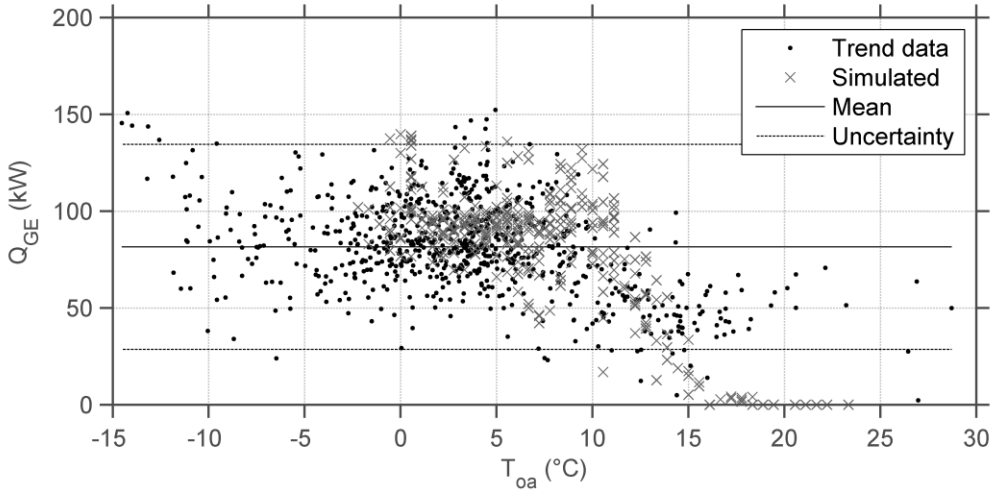


Figure 5.23 Whole-building hot water heating energy comparison after second zone iteration

### *5.10 Summary*

The goal of this chapter was to develop the initial building energy model and to apply the bottom-up method when the heating and cooling coils were inactive. Using information from trend data and by calibrating the zone level model first yielded a calibrated system level model. The $\dot{Q}_{GE}$ followed the pattern in the trend data with a reasonable value after the second iteration of zone tuning.

Problems in the calibration arose for a small number of zones using the hourly median temperature (e.g., Z1-S) and minimum air flow ratio schedules (e.g., Z1-CONF, Z2-E, and Z3-E; these zones had irregular air flow rates). The model fit could be improved if custom internal gain schedules were developed and daytyping methods were used to create hourly median $T_z$ and air flow ratio schedules for each zone. The next chapter explores if the median hourly $T_{zs}$ and minimum air flow ratio schedules will generate better model fit when applied over a period of months rather than a 2 weeks.

It was highly unlikely that someone would calibrate $V_{zs}$ or $V_s$ with sufficient accuracy using only whole-building data. It was likely that the perimeter zones would probably have been simulated with a larger $V_{zs}$ because of their unexpectedly large internal gains.

Offsetting errors occurred when modelling $V_{zs}$ and contributed to a calibrated AHU $V_s$. The zones with offsetting errors were known to be minor rather than unknown (i.e., in cases when zone level trend data was not used).

Calibrating the shoulder season first helped verify that DOE-2 could model the thermodynamically equivalent heat recovery coils before frost control occurred. This was important because, as is further discussed in Section 6.1.2, the $T_m$ output by eQUEST was not available in the heating season models.

# 6 Heating Season Calibration

This chapter describes the 2013 and 2014 heating season model calibrations using the bottom-up method. First, the calibrated 2013 shoulder season model was updated using the inputs generated from the AACT for the 2013 heating season (Table 4.16).

## *6.1 2013 Heating Season Model*

This section discusses changes to the 2013 shoulder season model to ensure that it will simulate the 2013 heating season. The heating coil design heat and glycol flow rates were entered into the model as 1390 kW and 8.9 L/s, respectively. eQUEST is limited to modelling hot water as the plant thermofluid. As the building is supplied by hot water from a campus loop, the hot water source was simulated to be produced by a virtual steam meter. This is a device in eQUEST that simulates the heating required to meet the loads calculated by SYSTEMS. The use of the word steam in the name does imply that the thermofluid is steam; the meter is just a heat transfer quantification tool.

### *6.1.1 Weather data*

The initial difference between the airport outdoor air temperature ($T_{oa}$) and the site trend data had an MBE of 33%, RMSE of 1.7 °C, and CV(RMSE) of -52%. The weather file was edited to use the $T_{oa}$ trend data (Figure 6.1) and resulted in an MBE of 0.6%, RMSE of 0.7 °C, and CV(RMSE) of 5.1% between the $T_{oa}$ trend data and edited weather file. Differences were caused by rounding as mentioned in Section 5.2.

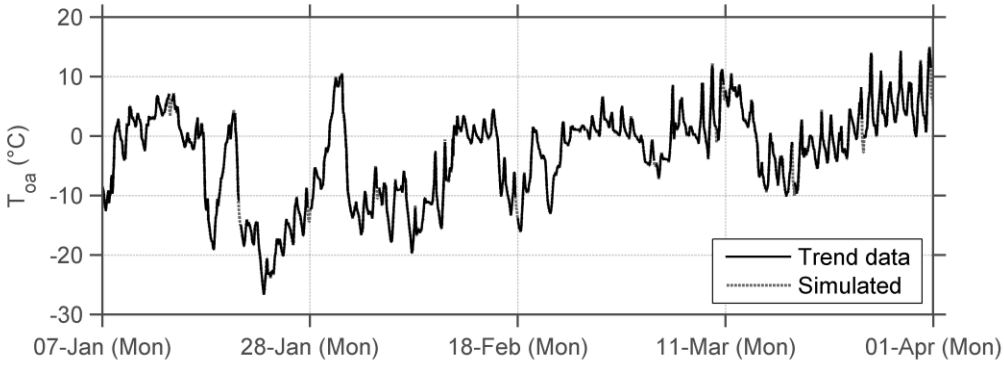


Figure 6.1 Outdoor air temperature 2013 heating season

### *6.1.2 Model limitations and assumptions*

The simulated air temperature exiting the heating coil ($T_{hd}$) set point could not be controlled with a reset profile using the main heating coils with a VAV system. The only $T_{hd}$ set point control available was to provide $T_{hd}$ to adequately heat the zone with the coldest air temperature. This was not the control strategy in the Genome Building therefore the main heating coils were disabled and the preheating coils were enabled instead. The preheating coils could not model a reset profile but could provide heating to maintain a constant $T_{hd}$ set point.

Modelling a preheat coil in eQUEST also created issues when outputting the simulated mixed air temperature ($T_m$). The eQUEST $T_m$ output was located after the preheat coils as shown in Figure 5.7. Therefore, the simulated $T_m$ was calculated outside eQUEST using eq. 6.1 where air temperature exiting the heat recovery coils ($T_{hr}$) was calculated using eq. 5.1 all based on other simulated outputs. This variable is simulated within eQUEST but cannot be output directly.

$$T_m = \alpha \cdot T_{hr} + (1 - \alpha) T_r \qquad \text{eq. 6.1}$$

*where:* $\alpha$ = Ratio of outdoor to supply air flow rate

eQUEST lacked the capacity to define an AHU with both a steam humidification loop and a the hot water. This caused issues outputting $V_{hc}$ because it was calculated based on the sum of $\dot{Q}_{hc}$ and steam humidification heat flow rate. Instead, $V_{hc}$ was calculated (eq. 3.3) with the simulated $\dot{Q}_{hc}$, $T_{hca}$, and $T_{hcr}$.

### *6.1.3 Zone level calibration*

The initial zone level statistical indices are shown in Table 6.1. The initial model had 11 out of 17 zones calibrated with Z2-E, Z3-S, and Z3-W close to being considered calibrated. This represented zones containing 63% of the modelled floor area and 73% of the supply air flow. The zone loads were not tuned because of limitations improving the zone model fit when using hourly median schedules (Section 5.10). Zone Z3-S met the calibration criteria during the shoulder season but not during the heating season because

its $V_{zs}$ was consistently larger during the first 2 weeks before falling to a lower constant level. Zone Z1-CONF was now considered calibrated because the zone was rarely occupied as indicated by the predominantly constant $V_{zs}$. The air-side system level was calibrated next.

Table 6.1 Statistical indices comparing initial zone level results

| Zone | | Temperature | | | Supply air flow rate | | |
|---|---|---|---|---|---|---|---|
| | | MBE (%) | RMSE (°C) | CV(RMSE) (%) | MBE (%) | RMSE (L/s) | CV(RMSE) (%) |
| Z1-S | x | -2.4 | 1.5 | 7.4 | 48 | 242 | 106 |
| Z1-NE | x | -3.4 | 1.0 | 4.3 | 20 | 166 | 46 |
| Z1-NW | ✓ | 0.8 | 1.0 | 4.8 | 0.0 | 2 | 0.4 |
| Z1-CORR | ✓ | -1.5 | 0.4 | 1.7 | -0.6 | 21 | 4.5 |
| Z1-CONF | ✓ | -1.7 | 0.7 | 2.9 | -3.6 | 40 | 12 |
| Z2-SW | ✓ | -4.0 | 1.3 | 5.7 | -5.4 | 166 | 22 |
| Z2-E | x | -0.9 | 0.2 | 1.1 | 10 | 631 | 32 |
| Z2-INT | ✓ | -0.7 | 0.2 | 1.0 | 5.4 | 51 | 15 |
| Z2-NE | ✓ | -2.5 | 0.7 | 3.2 | 2.2 | 164 | 14 |
| Z2-S | ✓ | -2.5 | 0.6 | 2.7 | 0.1 | 164 | 0.4 |
| Z2-W | x | -1.8 | 0.7 | 3.1 | 15 | 65 | 75 |
| Z3-SW | ✓ | -1.6 | 1.4 | 6.4 | -3.1 | 148 | 19 |
| Z3-E | ✓ | -1.1 | 0.5 | 2.3 | 10 | 392 | 18 |
| Z3-INT | ✓ | -0.7 | 0.4 | 1.5 | 2.5 | 55 | 19 |
| Z3-NE | ✓ | -2.2 | 0.8 | 3.9 | -1.3 | 126 | 13 |
| Z3-S | x | -2.2 | 0.7 | 3.1 | -12 | 126 | 35 |
| Z3-W | x | -2.0 | 1.4 | 6.7 | -1.0 | 49 | 35 |

### *6.1.4 Air-side system level calibration*

Statistical indices were used to compare the initial system level model simulation outputs to trend data (Table 6.2). Visual comparisons of system level variables are shown in Figure 6.2 to Figure 6.18. All the variables met calibration criteria. Additional comments are presented below.

Table 6.2 Statistical indices comparing initial air-side system level results

| Variable | MBE (%) | RMSE | CV(RMSE) (%) |
|---|---|---|---|
| $T_s$ (°C) | -1.7 | 0.8 | 5.4 |
| $T_m$ (°C) | -4.8 | 1.4 | 15 |
| $T_r$ (°C) | -4.4 | 1.2 | 5.1 |
| $RH_r$ (%) | 2.9 | 1.5 | 6.0 |
| $V_s$ (L/s) | 4.8 | 1240 | 11 |
| $\alpha$ (%) ($T_{oa}$ < 10 °C) | 0.7 | 3.3 | 4.0 |
| $\dot{Q}_{hr}$ (kW) | 5.7 | 16.9 | 15 |
| $\varepsilon_{hr}$ (%) | -2.5 | 3.5 | 10 |
| $T_{hr}$ (°C) | 1.6 | 0.9 | 14 |
| $\dot{Q}_{hc}$ (kW) | 6.0 | 19 | 27 |

The simulated supply air temperature ($T_s$) (Figure 6.2) fit the trend data well even though the reset profile was not followed when the heating coils were active (Figure 6.3). The simulated $T_s$ decreased slightly when frost control activated before the heating coils activated. The reason $T_s$ slightly varied with active heating coils was because the simulated air temperature exiting the preheating coils was controlled to a constant temperature before being added to the fan air temperature rise ($\Delta T_{fan}$) which varied based on eq. 4.19.

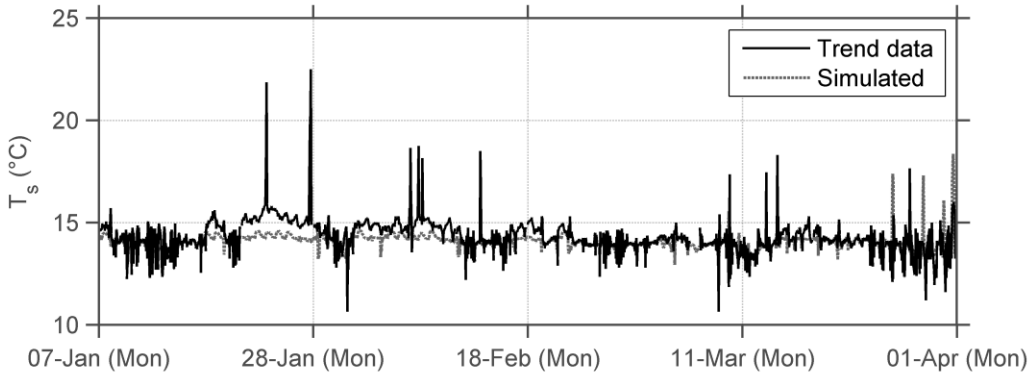


Figure 6.2 Supply air temperature simulation vs. trend data

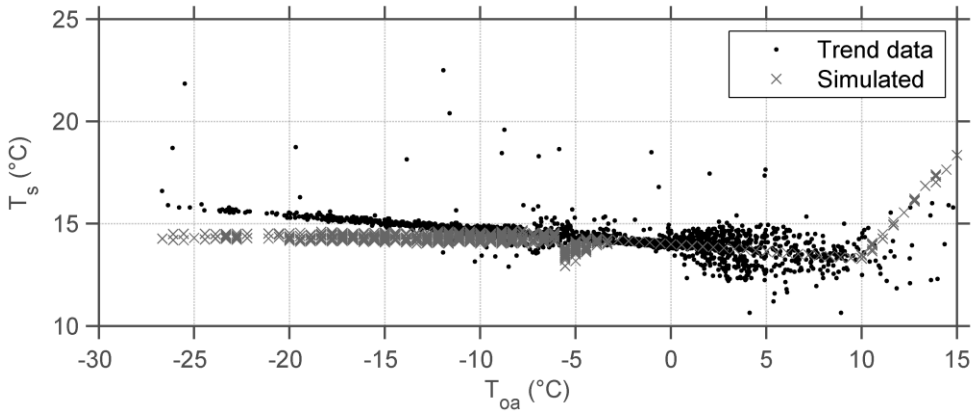


Figure 6.3 Supply air temperature against outdoor air temperature simulation vs. trend data

The simulated $T_m$ (Figure 6.4) decreased at a faster rate than the trend data when $T_{oa}$ was less than -12 °C. The difference between the simulated and measured $T_m$ was caused by differences between estimated and simulated heat recovery performance.

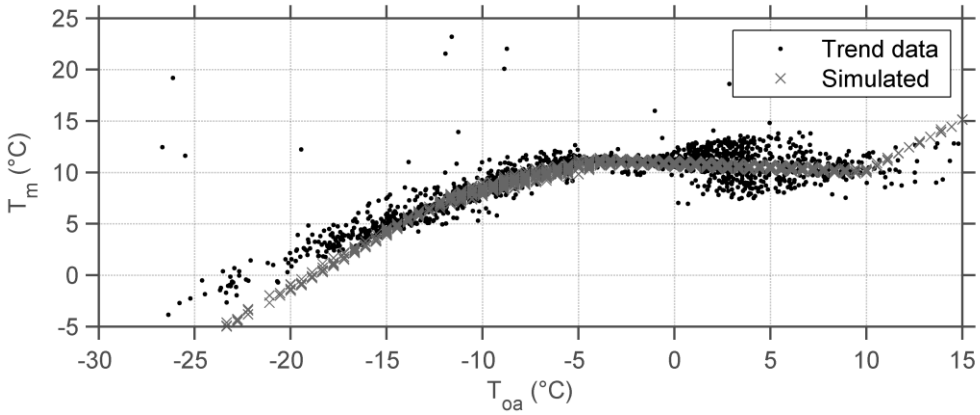


Figure 6.4 Mixed air temperature simulation vs. trend data

The simulated $T_r$ was estimated at a consistently lower value than the trend data and with a larger amplitude of variation. The large temperature variation may have been a result of combining the return and exhaust air steams in the model and not measuring $T_e$ which represented the temperature of most of the air exiting the zones. It remained uncertain how $T_e$ varied over time.

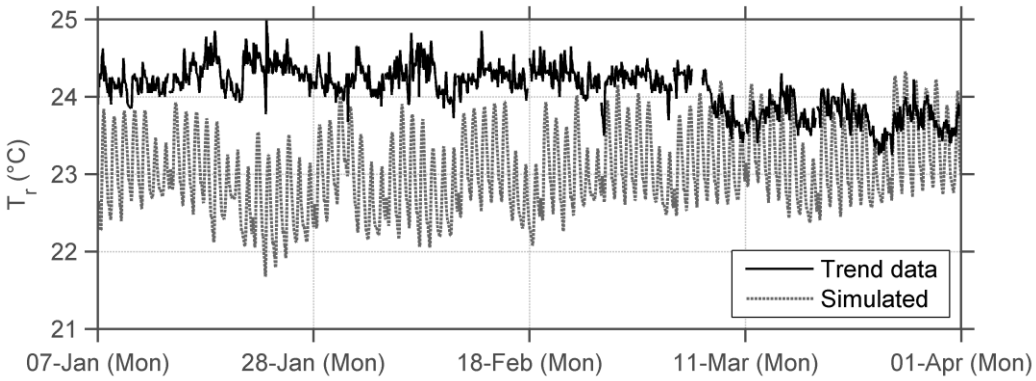


Figure 6.5 Return air temperature comparison

The simulated return air relative humidity ($RH_r$) (Figure 6.6) generally followed the pattern in the trend data but was sometimes larger than measured. It was important to ensure that $RH_r$ was calibrated because it was used in DOE-2 to calculate when condensation and frost occurred with heat recovery.

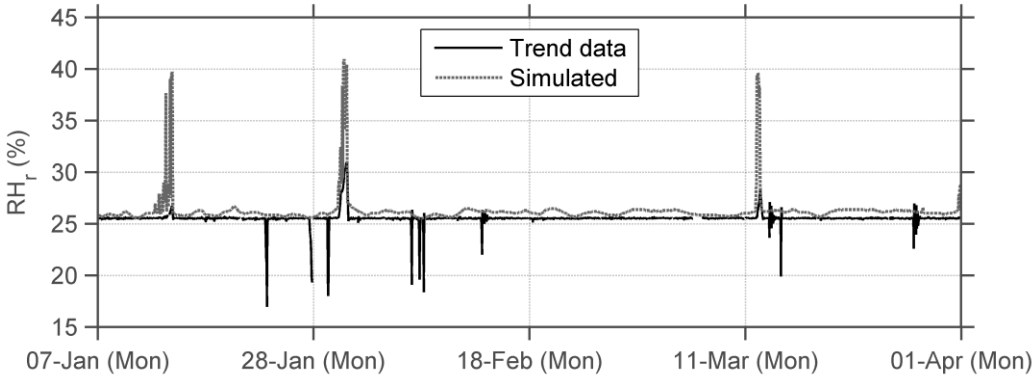


Figure 6.6 Return air relative humidity simulation vs. trend data

The simulated supply air flow rate ($V_s$) (Figure 6.7 and Figure 6.8) followed the pattern in the trend data well with differences often occurring during the unoccupied periods. The differences were mainly caused by the irregular schedules in the laboratory zones Z2- and Z3-E.

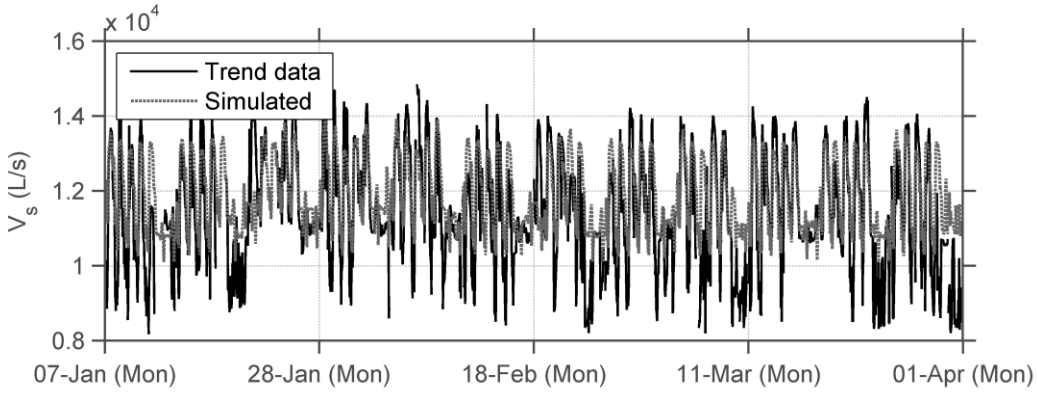


Figure 6.7 Supply air flow rate simulation vs. trend data

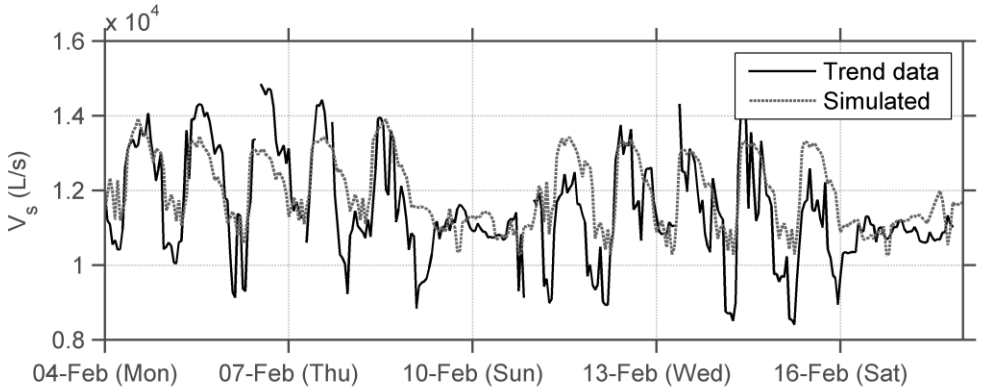


Figure 6.8 Supply air flow rate simulation vs. trend data from February 4$^{th}$ to 16$^{th}$, 2013

The simulated $\alpha$ (Figure 6.9) followed the pattern in the trend data well.

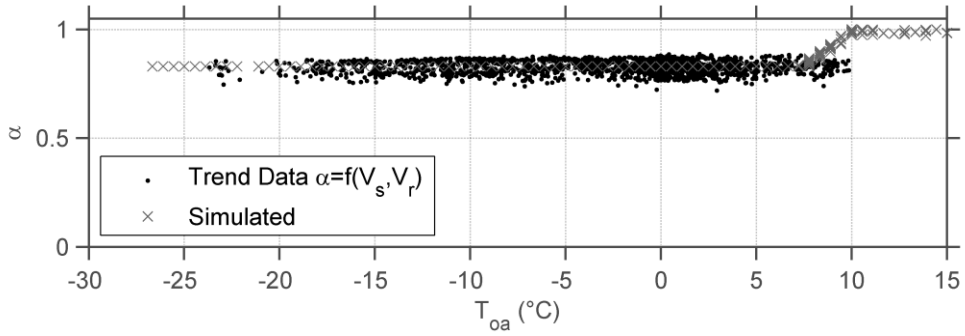


Figure 6.9 Outdoor air flow ratio simulation vs. trend data

The $T_{hr}$ (Figure 6.10), heat recovery heat flow rate ($\dot{Q}_{hr}$) (Figure 6.11), and heat recovery effectiveness ($\varepsilon_{hr}$) (Figure 6.12) generally followed the pattern in the trend data well. The simulated $\varepsilon_{hr}$ had three distinct modes of operation described in Table 6.3.

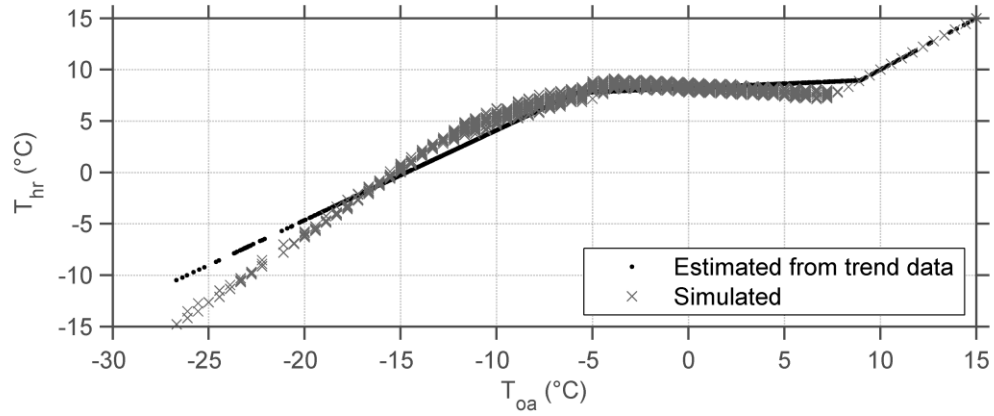


Figure 6.10. Air temperature exiting heat recovery simulation vs. trend data

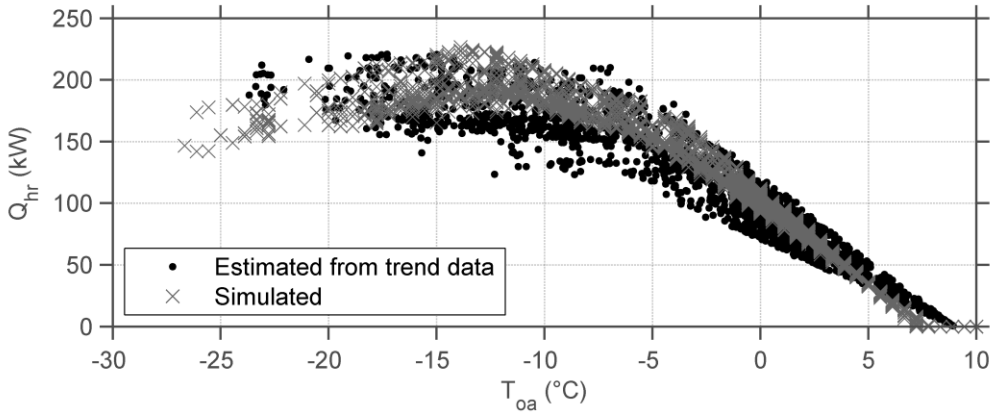


Figure 6.11. Heat recovery heat flow rate simulation vs. trend data

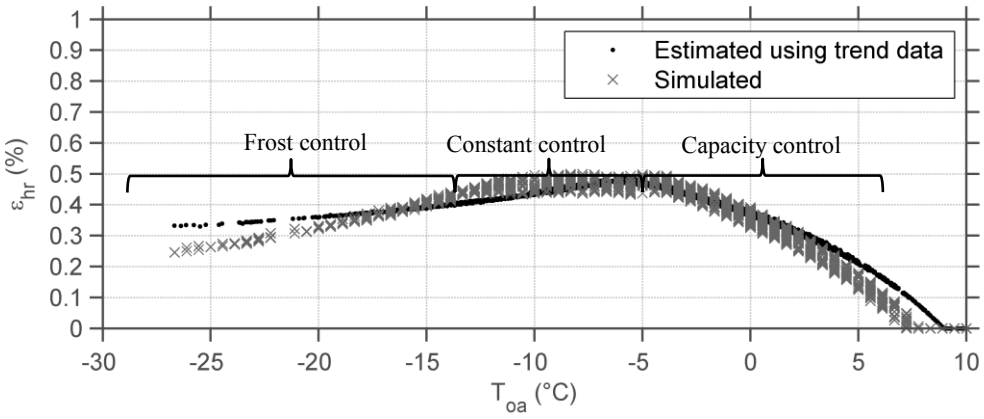


Figure 6.12. Heat recovery effectiveness simulation vs. trend data

Table 6.3 Simulated modes of heat recovery

| Control | Description |
|---|---|
| Capacity | The air bypassing the modelled heat recovery coils ($\beta$) increased to maintain $T_m$ at set point as $T_{oa}$ became colder. The outdoor conditions were not cold enough to cause frost on the exhaust air coils. |
| Constant | Heat recovery operated at the maximum $\varepsilon_{hr}$ from trend data (i.e., the $\varepsilon_{hr}$ from trend data at which the design $\varepsilon_{hr}$ was generated). The $\varepsilon_{hr}$ varied inversely proportional to $V_{oa}$ but did not decrease relative to outdoor conditions because $\beta$ was 100% open. The outdoor conditions were not cold enough to cause frost on the exhaust air coils. |
| Frost | The $\beta$ decreased as $T_{oa}$ became colder because frost could start to occur on the exhaust air coils. |

The simulated air temperature exiting the modelled heat recovery configuration ($T_{erv}$), $\beta$, and $\varepsilon_{hr}$ directly output from eQUEST describe how the heat recovery model operated in Figure 6.13 to Figure 6.15. The $T_{hr}$ decreased at a slower and faster rate during constant control and frost control, respectively. The rate was slower during constant control because the heat recovery design heat transfer value ($UA_{design}$) caused $\varepsilon_{hr}$ to vary inversely proportional to the outdoor air flow rate ($V_{oa}$) rather than decrease with outdoor conditions as estimated. The reason frost control performed differently in the model was that DOE-2 calculated when frost control was required whereas the physical system maintained a constant glycol set point temperature entering the exhaust air coils (Figure 4.17). The physical system and BAS code never measured or estimated (e.g.,

based on $T_{oa}$, $T_r$, outdoor air relative humidity $RH_{oa}$, and $RH_r$ trend data) to confirm if frost was occurring.

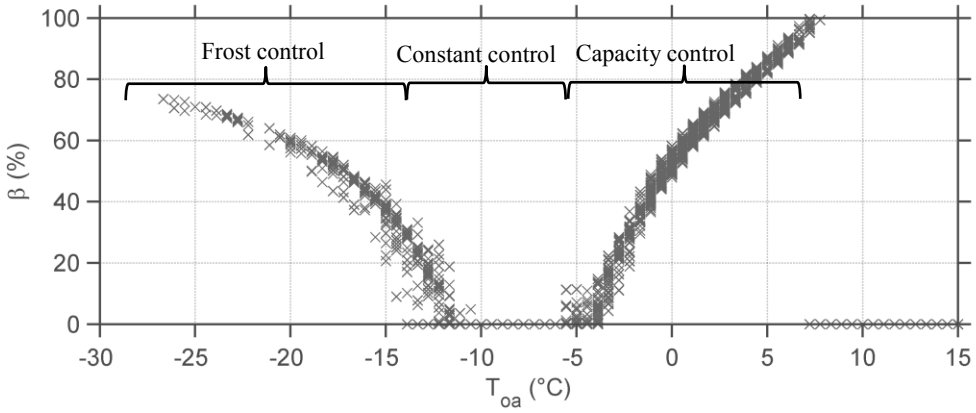


Figure 6.13. Simulated ratio of outdoor air bypassed around heat recovery

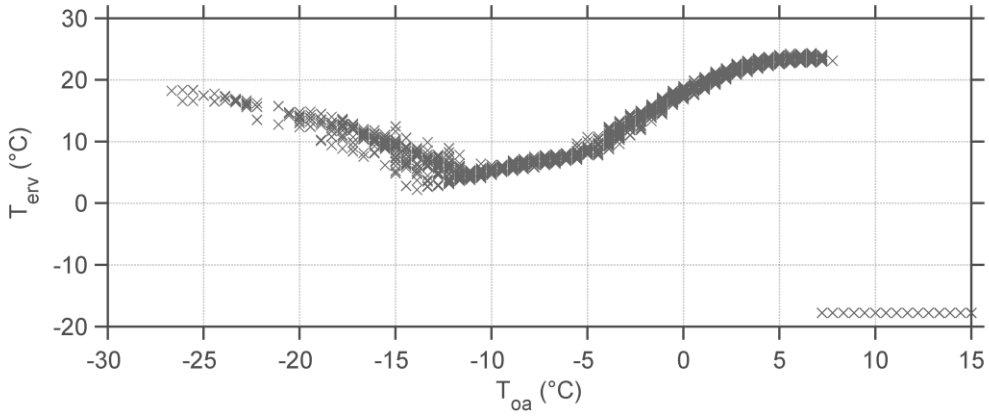


Figure 6.14. Simulated air temperature exiting the heat recovery coils.

Note: The value of $T_{erv}$ was automatically simulated with a value of -17.7 °C when heat recovery was inactive and was not used in any calculations within DOE2 or this thesis.

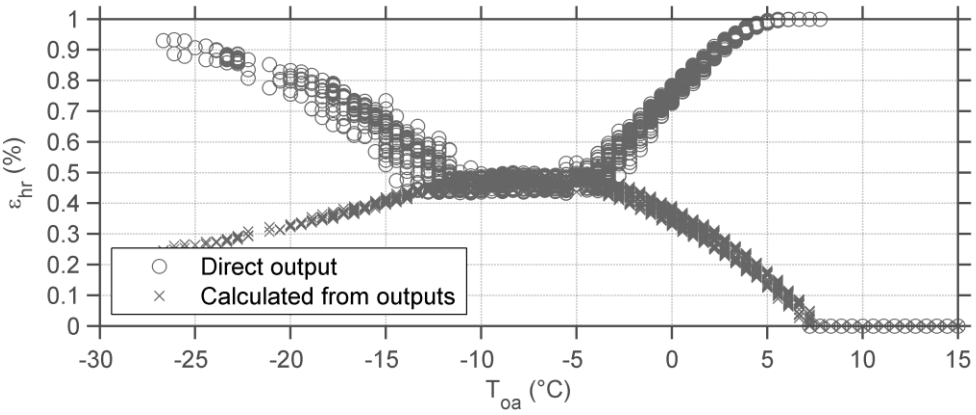


Figure 6.15. Simulated direct and calculated from outputs effectiveness

The simulated temperature rise across the supply and return air fan is shown in Figure 6.16 and Figure 6.17 and is compared to $\Delta T_{sm}$. The simulated variation of $\Delta T_{fan}$ did not seem to greatly vary relative to the value estimated from trend data. The water-side was calibrated next as no further tuning was required.

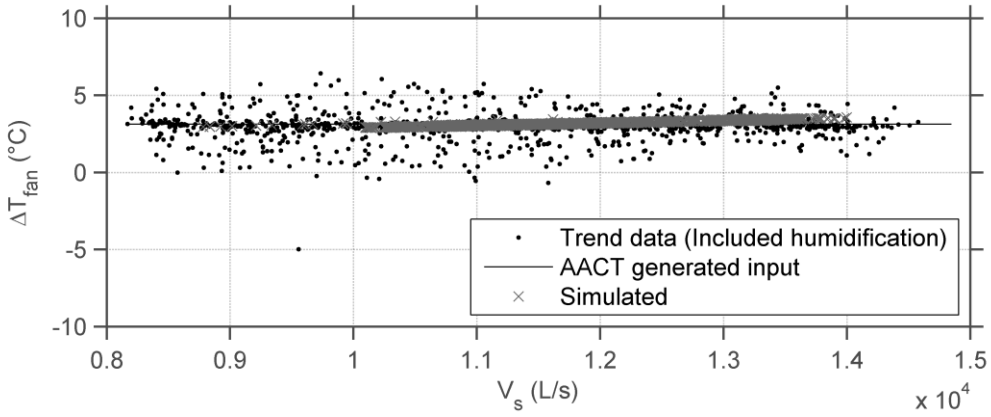


Figure 6.16. Supply air fan temperature rise simulated vs. trend data

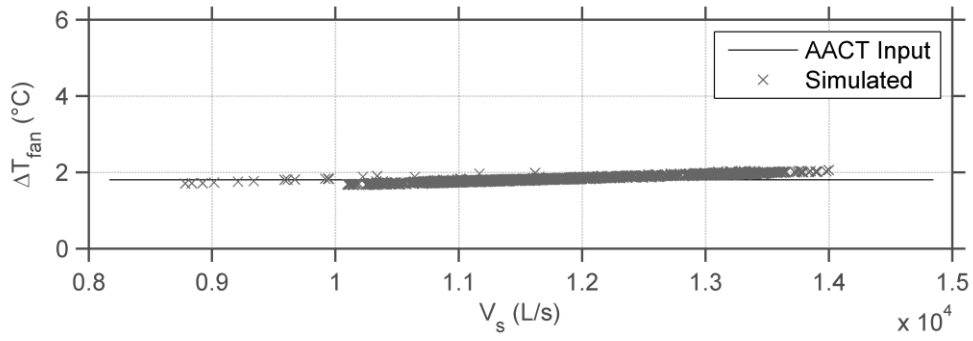


Figure 6.17. Return air fan temperature rise simulated vs. trend data

The heating coil heat flow rate ($\dot{Q}_{hc}$) (Figure 6.18) was calibrated because the model fit with $V_s$, $T_s$ (i.e., $T_{hd} + \Delta T_{fan}$), and $T_m$ were far below the calibration criteria. The simulated $\dot{Q}_{hc}$ overestimated the heat flow rate once frost control was activated because $T_m$ decreased at a faster rate than measured. Once the simulated frost control was activated the $T_{hd}$ was lower than the trend data because a reset profile was not modelled. The difference in frost control performance and reset profile limitations in the simulated $T_{hd}$ and $T_m$ created an offsetting error which unintentionally improved the model fit of $\dot{Q}_{hc}$.

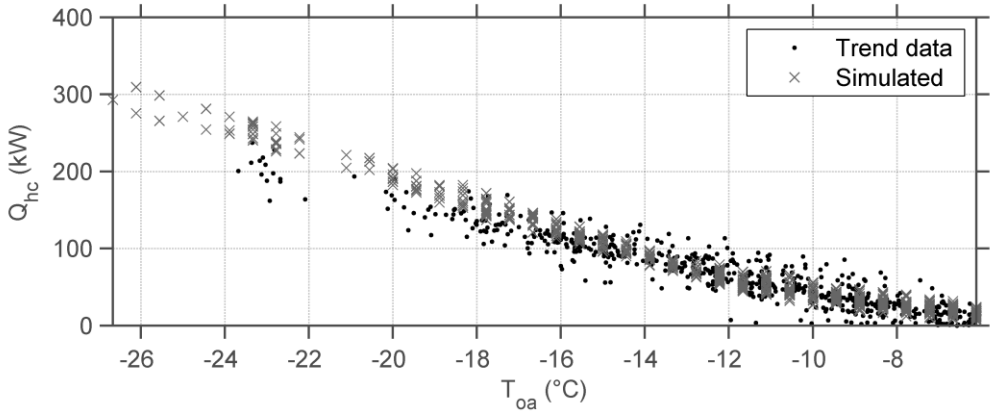


Figure 6.18. Heating coils heat flow rate simulated vs. trend data

### *6.1.5 Water-side system level calibration*

Statistical indices were used to compare the initial water-side model simulation outputs to trend data (Table 6.4). Visual comparisons of water-side level variables are shown in Figure 6.19 to Figure 6.22. The glycol temperature arriving at the heating coils ($T_{hca}$) (Figure 6.19) followed the reset profile generated in the AACT. The glycol temepature returning from the heating coils ($T_{hcr}$) (Figure 6.20) met calibration criteria but was simulated with a pattern that did not match the trend data. This was the reason the glycol temepature difference across the heating coils ($\Delta T_{hc}$) (Figure 6.21) did not follow the pattern in the trend data. The reason $T_{hcr}$ did not fit the simulation output better was uncertain. The simulated $T_{hcr}$ was calculated based on the design $\dot{Q}_{hc}$, design glycol flow rate in the heating coils ($V_{hc}$), input $\Delta T_{hc}$, and the available capacity in eQUEST. Reviewing the DOE-2 source code did not reveal any cause of the unexpected performance of $T_{hcr}$. The main reason $V_{hc}$ was considered calibrated was because $\dot{Q}_{hc}$, $T_{hca}$, and $T_{hcr}$ were calibrated. It should be noted that the $V_{hc}$ estimated from trend data was calculated using the thermal properties of water instead of glycol.

Table 6.4 Statistical indices comparing of initial water-side level results

| Variable | MBE (%) | RMSE | CV(RMSE) (%) |
|---|---|---|---|
| $T_{hca}$ (°C) | 2.2 | 1.7 | 3.6 |
| $T_{hcr}$ (°C) | 2.2 | 1.7 | 3.6 |
| $V_{hc}$ (L/s) | 3.9 | 0.2 | 28 |

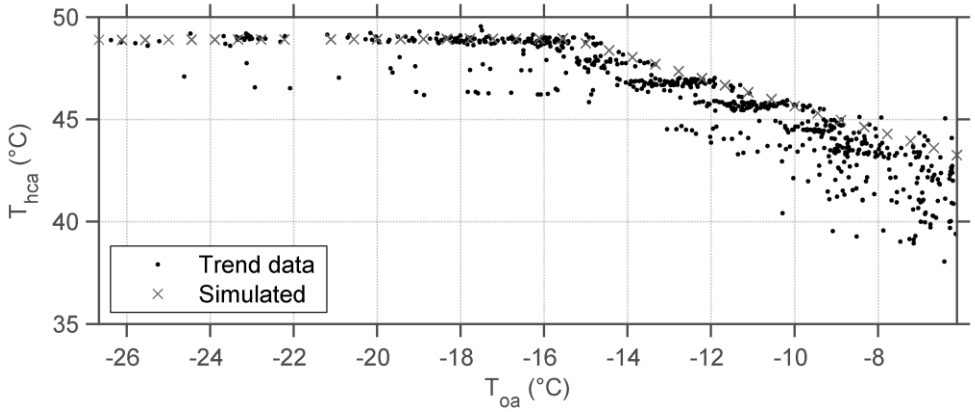


Figure 6.19 Heating coils supply glycol temperature simulated vs. trend data

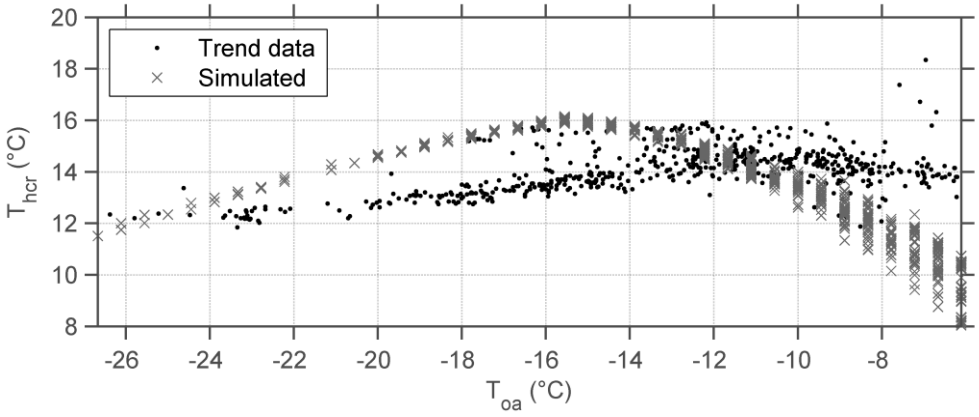


Figure 6.20 Heating coils return glycol temperature simulated vs. trend data

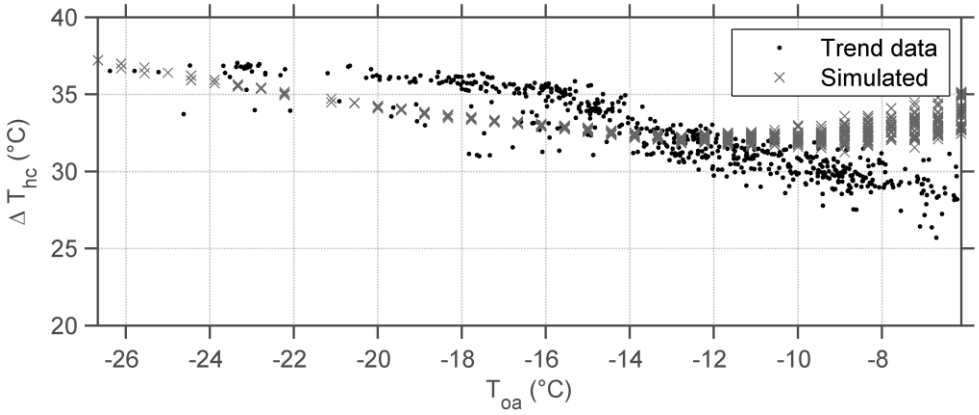


Figure 6.21 Heating coils glycol temperature difference simulated vs. trend data

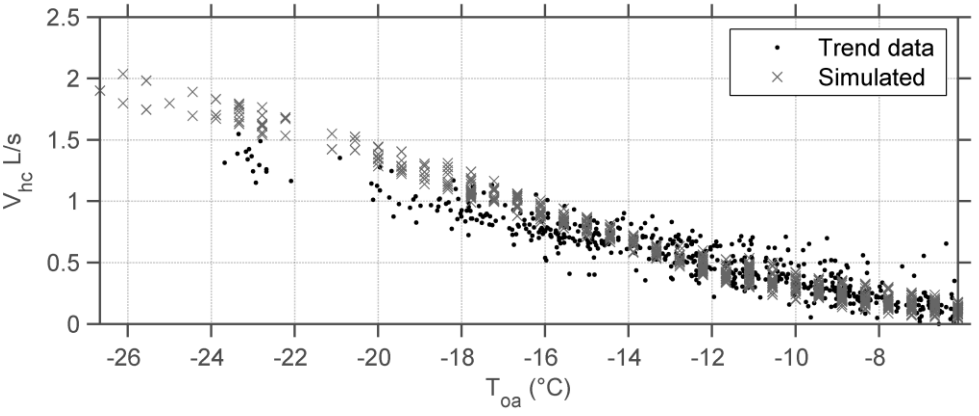


Figure 6.22 Heating coils hot water flow rate simulated vs. trend data

### 6.1.6 *Whole-building hot water heat flow rate calibration*

A visual comparison of $\dot{Q}_{GE}$ is shown in Figure 6.23. The simulated $\dot{Q}_{GE}$ followed the pattern in the trend data at a reasonable value. It should be noted that $\dot{Q}_{GE}$ was not recorded when $T_{oa}$ was at its coldest value. Some statistical comparisons are shown in Table 6.5. The 2013 heating season model met the calibration criteria and the 2014 heating season was calibrated next.

Table 6.5 Qualitative comparison with whole-building hot water heat flow rate

| | Trend data | | | Model | | |
|---|---|---|---|---|---|---|
| $\mu \pm \sigma$ (kW) | 116 | ± | 48 | 146 | ± | 69 |
| $\mu_{½} \pm MAD$ (kW) | 104 | ± | 26 | 123 | ± | 25 |
| $\mu$ and uncertainty (kW) | 116 | ± | 54 | - | - | - |

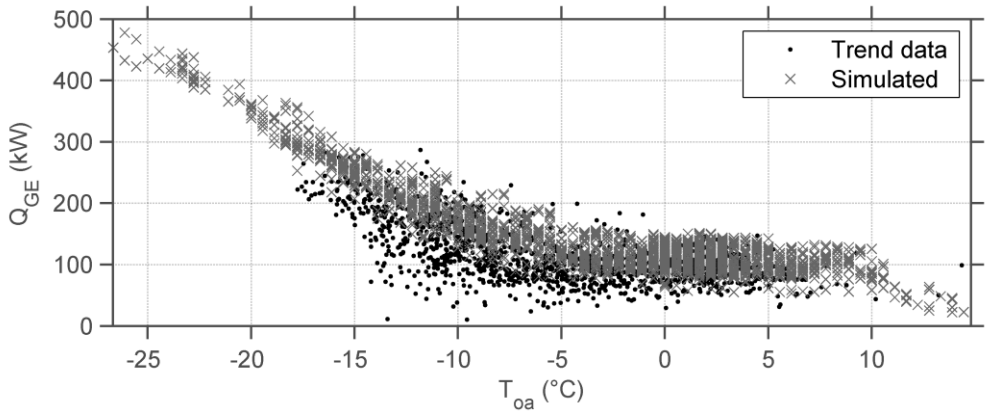


Figure 6.23 Whole-building hot water heat flow rate simulated vs. trend data

## *6.2 2014 Heating Season Calibration*

The calibrated 2013 heating season's model inputs were modified using the inputs generated for the 2014 heating season (Table 4.16) and the 2014 weather file was updated using the $T_{oa}$ trend data.

### 6.2.1 *Initial zone level model*

The initial zone level statistical indices are shown in Table 6.6. The initial model had 14 out of 17 zones that met the calibration criteria. This represented zones containing 83%

of the modelled floor area and 92% of the supply air flow. The number of calibrated zones increased because the heating season period analysed was longer and $V_{zs}$ followed more regular patterns making more effective use of hourly median minimum air flow ratio schedules. No further zone tuning was required.

Table 6.6 Statistical indices comparing initial zone level results

| Zone | | Temperature | | | Supply air flow rate | | |
|---|---|---|---|---|---|---|---|
| | | MBE (%) | RMSE (°C) | CV(RMSE) (%) | MBE (%) | RMSE (L/s) | CV(RMSE) (%) |
| Z1-S | x | -5.6 | 2.2 | 11 | 68 | 251 | 99 |
| Z1-NE | x | -5.4 | 1.4 | 6.5 | 25 | 176 | 45 |
| Z1-NW | ✓ | -2.3 | 0.8 | 3.6 | 0.0 | 2 | 0.4 |
| Z1-CORR | ✓ | -2.0 | 0.5 | 2.1 | -0.5 | 12 | 2.6 |
| Z1-CONF | ✓ | -0.9 | 0.4 | 2.0 | -5.5 | 62 | 19 |
| Z2-SW | ✓ | 2.9 | 1.4 | 6.1 | -6.4 | 148 | 20 |
| Z2-E | ✓ | -0.4 | 0.3 | 1.1 | -3 | 144 | 16 |
| Z2-INT | ✓ | -0.3 | 0.2 | 0.9 | -3.2 | 28 | 10 |
| Z2-NE | ✓ | -3.3 | 0.9 | 4.0 | -3.6 | 188 | 15 |
| Z2-S | ✓ | -0.8 | 1.3 | 5.4 | 1.2 | 188 | 3.0 |
| Z2-W | x | -3.4 | 1.1 | 4.8 | 41 | 81 | 93 |
| Z3-SW | ✓ | -7.1 | 2.1 | 9.7 | -4.3 | 119 | 17 |
| Z3-E | ✓ | -0.8 | 0.5 | 2.3 | -4 | 458 | 29 |
| Z3-INT | ✓ | -0.9 | 0.4 | 1.6 | 3.4 | 56 | 19 |
| Z3-NE | ✓ | -4.4 | 1.3 | 6.2 | -7.8 | 187 | 17 |
| Z3-S | ✓ | -1.7 | 0.7 | 3.2 | -2.5 | 187 | 28 |
| Z3-W | ✓ | -3.7 | 2.0 | 9.3 | 2.3 | 26 | 14 |

### *6.2.2 Air-side calibration*

Statistical indices were used to compare the initial system level model simulation outputs to trend data (Table 6.7). Visual comparisons of system level variables are shown in Figure 6.24 to Figure 6.30. All variables met calibration criteria except for $T_m$, $T_{hr}$, and $\dot{Q}_{hc}$. Additional comments are below.

Table 6.7 Statistical indices comparing system level results after zone iteration 1

| Variable | MBE (%) | RMSE | CV(RMSE) (%) |
|---|---|---|---|
| $T_s$ (°C) | -1.0 | 0.7 | 5.1 |
| $T_m$ (°C) | -13 | 2.3 | 24 |
| $T_r$ (°C) | -4.4 | 1.3 | 5.4 |
| $RH_r$ (%) | 2.2 | 1.7 | 5.6 |
| $V_s$ (L/s) | -0.6 | 713 | 7.1 |
| $\alpha$ (%) ($T_{oa}$ < 10 °C) | 0.1 | 2.6 | 3.3 |
| $\dot{Q}_{hr}$ (kW) | -6.7 | 15 | 14 |
| $\varepsilon_{hr}$ (%) | -6.5 | 4.8 | 12 |
| $T_{hr}$ (°C) | -12 | 1.5 | 30 |
| $\dot{Q}_{hc}$ (kW) | 49 | 32 | 63 |

It appeared that a fault occurred with the $T_s$ trend data (Figure 6.24) because the heating coils were occasionally not activating once frost control activated. It was evident that the heating coils were responsible because the $T_m$ trend data (Figure 6.25) showed no abnormal operation.

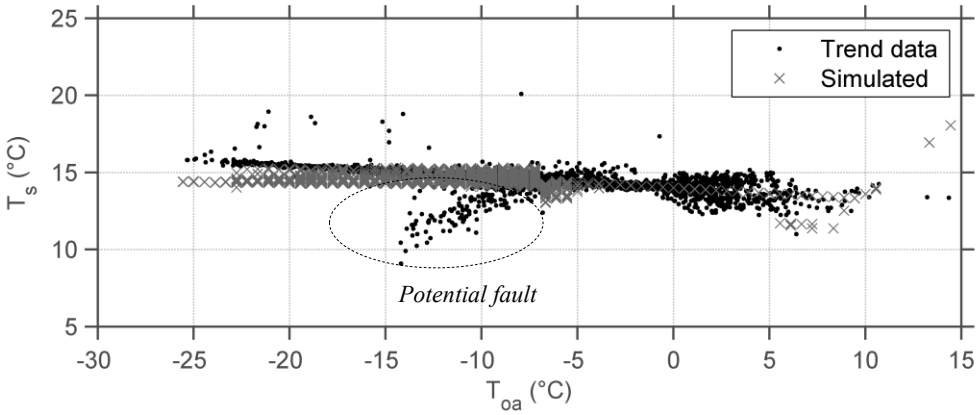


Figure 6.24 Supply air temperature comparison

The $T_{oa}$ at which frost control activated was lower in the 2014 heating season which can be seen in the range of region III (Table 4.9). The simulated $T_m$ decreased earlier and at a rate faster than measured.

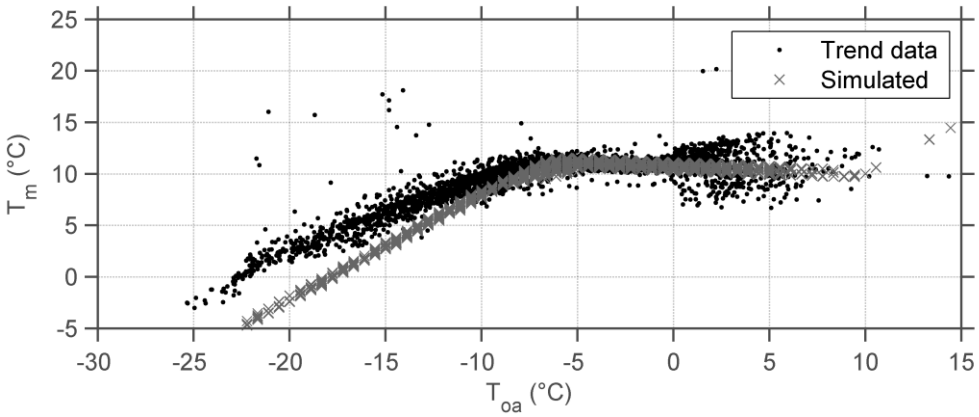


Figure 6.25 Mixed air temperature comparison

The simulated $V_s$ (Figure 6.24) now followed the trend data much more closely during the unoccupied periods because the zone model fit was better in more zones when compared to the 2013 heating season.

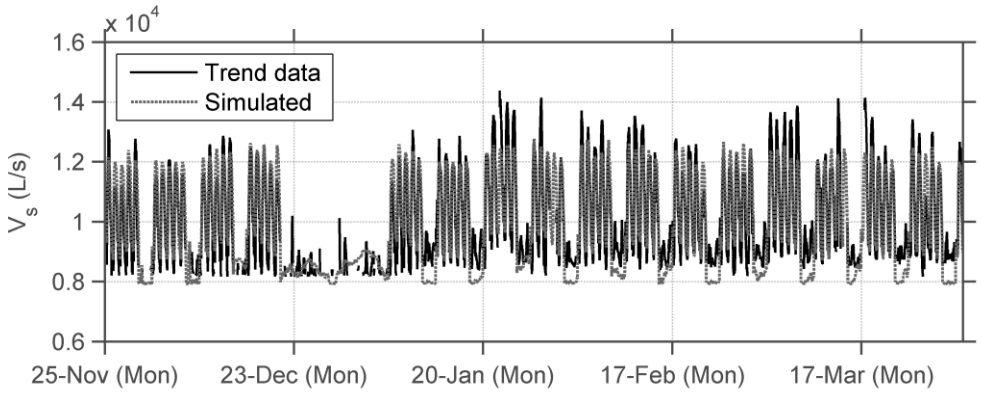


Figure 6.26 Supply air flow rate comparison

The $T_{hr}$ (Figure 6.27) was not calibrated because the simulated frost control was activated earlier than estimated. The main reason the constant control mode of the simulated heat recovery coils was shorter during the 2014 heating season was because $RH_r$ had a median value 4% higher than the 2013 heating season. This caused the frost control mode in DOE-2 to activate at a higher $T_{oa}$. The $\dot{Q}_{hr}$ (Figure 6.28) was considered calibrated because the difference between $T_{hr}$ and $T_{oa}$ was large relative to $T_{hr}$, which was

not calibrated, and the model fit with $\alpha$ and $V_s$ (i.e., $V_{oa}$) were much lower than the calibration criteria. The simulated $\varepsilon_{hr}$ (Figure 6.29) was considered calibrated but decreased at a faster rate during frost control than estimated.

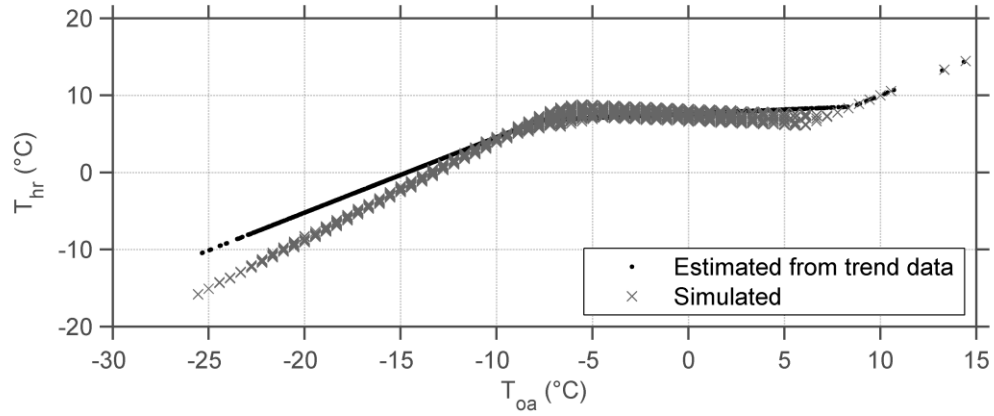


Figure 6.27 Air temperature exiting heat recovery comparison

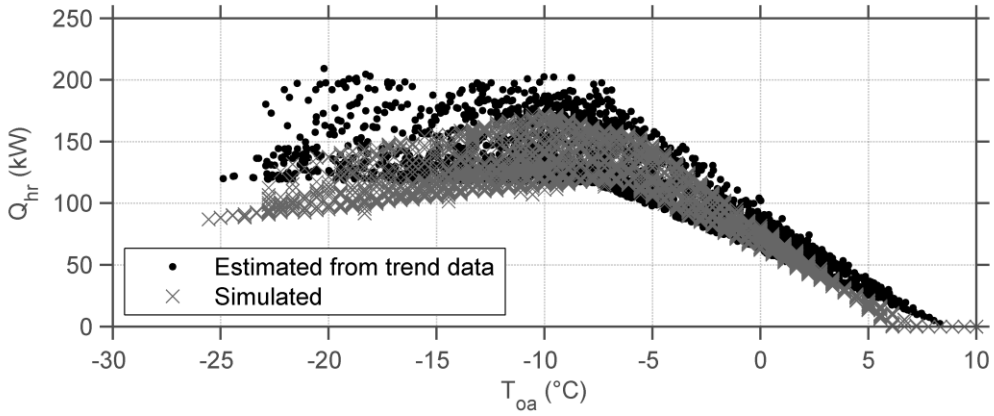


Figure 6.28 Heat recovery heat flow rate comparison

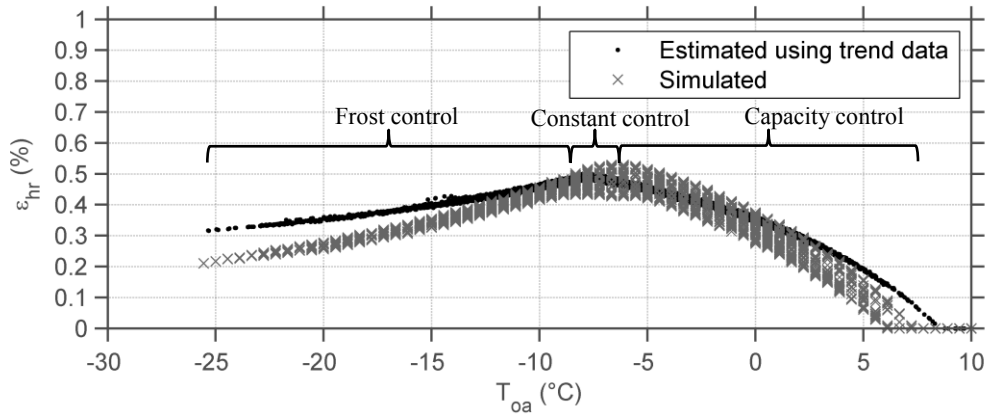


Figure 6.29 Heat recovery effectiveness comparison

The simulated $\dot{Q}_{hc}$ (Figure 6.30) was consistently larger than estimated from trend data because of the issues modelling frost control. No tuning could improve the model fit due to the limitations with heat recovery and the preheating coils constant set point. The water-side was calibrated next because no tuning could further improve the system level model fit.

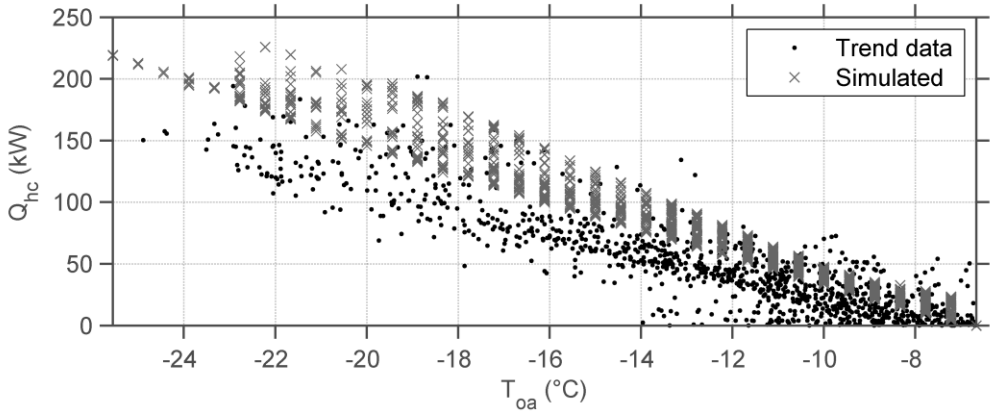


Figure 6.30 Heating coil heat flow rate comparison

### 6.2.3 Water-side calibration

Statistical indices were used to compare the initial water-side model simulation outputs to trend data (Table 6.8). Overall, the water-side level $V_{hc}$ was not calibrated due to the limitations when simulating $\dot{Q}_{hc}$.

Table 6.8 Statistical indices comparing water-side level results after zone iteration 1

| | Initial $\varepsilon_{hr}$ | | |
|---|---|---|---|
| Variable | MBE (%) | RMSE | CV(RMSE) (%) |
| $T_{hca}$ (°C) | 3.4 | 3.0 | 6.6 |
| $T_{hcr}$ (°C) | -10 | 2.1 | 15 |
| $V_{hc}$ (L/s) | 34 | 0.2 | 47 |

### 6.2.4 Whole-building hot water heat flow rate calibration

A visual comparison of $\dot{Q}_{GE}$ is shown in Figure 6.31. Some statistical comparisons are shown in Table 6.9. The results were similar to those in the 2013 heating season (Section 6.1.6). From February 5$^{th}$ to March 31$^{st}$, 2014 the MBE, RMSE, and CV(RMSE) of $\dot{Q}_{GE}$ was 18%, 41 kW, and 36%, respectively. It was important to note that the RMSE was less than the overall uncertainty of the trend data which would indicate that this model fit well considering the large uncertainty in $\dot{Q}_{GE}$. This was still a qualitative assessment that confirmed the simulated $\dot{Q}_{GE}$ was a reasonable value and followed the overall pattern in the trend data.

Table 6.9 Qualitative comparison with whole-building hot water heat flow rate

| | Trend data | | | Initial $\varepsilon_{hr}$ | | |
|---|---|---|---|---|---|---|
| $\mu \pm \sigma$ (kW) | 116 | ± | 48 | 147 | ± | 70 |
| $\mu_{½} \pm MAD$ (kW) | 104 | ± | 26 | 134 | ± | 46 |
| $\mu$ and uncertainty (kW) | 116 | ± | 54 | - | ± | - |

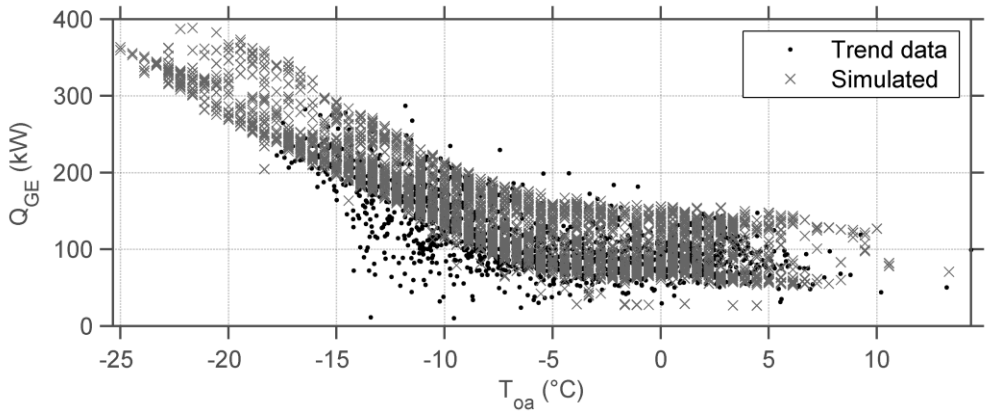


Figure 6.31 Whole-building hot water heat flow rate comparison

## *6.3 Summary*

Updating the calibrated 2013 shoulder season model with inputs generated for the 2013 heating season resulted in the same number of calibrated zones. All system level variables were calibrated during the 2013 heating season without any tuning. The estimated $\dot{Q}_{hc}$ was considered calibrated due to unintended offsetting errors caused by modelling $T_s$ without a reset profile during heating and with frost control causing $T_m$ to decrease at a faster rate than the trend data.

An additional 3 zones were calibrated when the 2013 heating season model was updated with inputs generated for the 2014 heating season. Not all system level variables were calibrated during the 2014 heating season due to limitations with frost control and modelling reset profiles for heating coils. Identifying the model limitations with heat recovery and the heating coils were important because offsetting errors could have occurred if only the whole-building heating energy. These offsetting errors may have involved tuning effectiveness to compensate for the heating coils heat flow rate.

In a sense, the calibrated 2013 heating season model when used with the AACT to create a 2014 heating season model acted as a benchmark. Even though the 2014 heating season model was not fully calibrated a deep understanding of the model and its limitations was achieved. Understanding the model and its limitations was more important than achieving every variable calibrated when applying commissioning techniques.

# 7 Conclusions and Future Work

## *7.1 Conclusions*

A bottom-up method to calibrate building energy models where the zone, system, plant, and whole-building levels are calibrated sequentially was developed and applied to a case study building. The bottom-up method relied on inductive reasoning with evidence from trend data to calibrate the model as opposed to deductive reasoning used when calibrating a building with utility data only. Use of a bottom-up method was also supported by the upward nature of building simulation and operation. Overall, the procedure reduced offsetting errors at sub-utility levels. The bottom-up method relied upon the use of trend data obtained from building automation systems (BASs) common in commercial/institutional buildings.

The use of trend data in calibrated simulation has increased in recent years; however, it remained uncertain if it was being used effectively. In addition, the time required to manually process and analyse a large set of trend data for use in calibrated simulation was expected to be large. A proof-of-concept prototype tool to automatically couple trend data with building simulation software was developed to reduce the time associated with analysing and processing large trend datasets. The tool was the first of its kind and increased the feasibility of applying the bottom-up method with a large set of trend data. Its primary function was to reduce the time required to extract values from trend data for use in calibrating simulation models. The secondary objective for the AACT was to create performance reports quantifying building operation for comparison with design specifications, BAS set points, and future measured performance. These performance reports were the first step in applying FDD or benchmarking. The proof-of-concept was verified in this thesis by automatically generating inputs for the 2013 shoulder season and 2013 and 2014 heating seasons. Future development of the AACT would require a serious effort due to the complexity of commercial building systems and simulation software.

Trend data provided a substantial amount of information that was crucial in using the bottom-up method; however, it could not provide all the information required to model a building. Variables affecting zone loads (e.g., envelope U-values, air infiltration, equipment power demand, and occupant gains) are incredibly difficult to measure in institutional/commercial building, which creates uncertainty in tuning.

The trend data available in this study had the capacity to provide the necessary information to model the system level models without requiring any tuning once the zone level was calibrated. Monfet and Zmeureanu (2013) recently calibrated a central cooling plant using trend data and manufacturers' data; they noted that no tuning was required. It is emerging that trend data can provide sufficient information to model the system and plant level models and utility data (i.e., ideally hourly or sub-hourly) can represent whole-building energy performance. Many previous studies have installed additional sensors or performed short-term measurements to measure missing information relevant to the system, plant, or whole-building level models. It is becoming clear that the most uncertain and difficult to measure variables were the ones affecting zone loads. This inspired a tuning strategy used to calibrate the zone level models when using zone level trend data because air temperature and supply air flow rate trend data characterized the lumped behaviour of the variables affecting zone loads. In this study, an equipment load, representing the lumped behaviour of lighting, equipment, occupant, and additional offsetting differences with remaining uncertain variables, was tuned until a large fraction zones were calibrated. This strategy avoided issues related to model underdetermination at the zone level and reduced the time spent tuning the large number of zone level variables. However, this strategy limited energy efficiency measures applied to the variables affecting zone loads.

### *7.1.1 Results summary*

This thesis performed one of the most detailed zone and system level model calibrations to date. First a shoulder season model was calibrated with inactive heating and cooling coils. The tuning was dominated by adjusting the aggregated internal gain. Using information from trend data and calibrating the zone level first yielded calibrated system

level variables. However, qualitatively comparing the whole-building hot water heat flow rate ($\dot{Q}_{GE}$), used for zone reheat, indicated that the simulated $\dot{Q}_{GE}$ was consistently larger than the trend data. Thus, a second iteration of tuning zone the loads was required to increase the internal gains to reduce the zone reheat. This procedure resulted in the same number of calibrated zones, with all system level variables calibrated. The simulated $\dot{Q}_{GE}$ was reduced to follow the pattern in the trend data with a reasonable value.

Updating the calibrated 2013 shoulder season model with inputs generated for the 2013 heating season resulted in the same number of calibrated zones. All system level variables were also calibrated during the 2013 heating season with no tuning required. The estimated heating coil heat flow rate was considered calibrated due to unintended offsetting errors caused by modelling the supply air temperature without a reset profile during heating and with heat recovery frost control causing $T_m$ to decrease at a faster rate than the trend data. An additional 3 zones were calibrated when the 2013 heating season model was updated with inputs generated for the 2014 heating season. Not all system level variables met calibration criteria for the 2014 heating season due to limitations with heat recovery frost control and modelling reset profiles for heating coils. No tuning could improve the model fit of the variables that failed to meet the calibration criteria. In both 2013 and 2014 model the $\dot{Q}_{GE}$ followed the pattern in the trend data with a reasonable value.

The bottom-up procedure revealed other information about the building as well. The process revealed several faults occurring in the building. Differences between building operation via trend data and BAS set points were revealed. It was also clear that the building was operating well below peak design conditions.

Identifying model limitations with heat recovery and the heating coils provided the analyst with a deeper understanding of the model. These limitations may not be recognized and offsetting errors could occur if only the whole-building heating energy was used.

The bottom-up method substantially reduced the number of offsetting errors occurring at the system level. Building simulation programs are highly complex tools with many important details that may be overlooked unless modelling at a component

level. An analyst may easily miss the substantial effect of certain features, leading to offsetting errors. Buildings are likely to have unique features that cannot be directly modelled in building simulation software. These model limitations are bound to cause offsetting errors that may lead to incorrect tuning when not using sub-utility data. The main offsetting errors occurred at the zone level but were caused by uncertainties in the variables affecting loads that were difficult to measure. It would be very unlikely, if not impossible, to calibrate the zone or system level models using only whole-building data.

## *7.2 Summary of Contributions*

(1) Developed and applied a bottom-up method to calibrate a building energy model of a case study building;
(2) Verified the proof-of-concept that an automated tool can couple trend data with calibrated simulation and ongoing commissioning;
(3) Demonstrated comprehensive use of trend in calibrated simulation;
(4) Analysed and measured air temperature rise caused by supply air fans;

## *7.3 Future Work*

New areas of research are identified and recommendations to improve the limitations and results in this thesis are discussed.

It was challenging and time consuming tuning the internal gains. It is likely that zone tuning would be too time consuming without automated tools if a larger more complicated building was calibrated using the bottom-up method. Using automatic tools with optimization approaches (e.g., ExCaliBEM) could reduce the time when tuning zone inputs. It may also be worthwhile to investigate the benefits of using the signature analysis calibration method to focus on developing signatures specific to uncertain zone loads.

In future studies, it may save time to focus calibrating influential zones in terms floor area, air flow rates, or energy use. For example, comparing the zone performance report in Table 4.2 and Table 4.3 revealed that Z2- and Z3-E/NE were quite influential in terms of percentage of floor area and air flow rates. The zone floor area and air flows

representing calibrated zones in this study ranged from 62-83% and 72-92%, respectively, that resulted with a calibrated AHU supply air flow rate. Techniques to determine influential zones could be investigated further.

A model could be considered calibrated if its RMSE was less than the overall measured uncertainty or, similarly, if the CV(RMSE) was less than the overall uncertainty as a percentage. It is unlikely that this would often occur because the measurement uncertainty is usually much lower than 30%. The overall uncertainty in measurements may be greater than 30% as a result of error propagation common when calculating heat flow rates. For example, the overall uncertainty in $\dot{Q}_{GE}$ was greater than 30% in this thesis. Measurement uncertainty applies to normally distributed data only which may cause issues.

Applying daytyping methods to generate the hourly median temperature and minimum hourly air flow schedules would improve the model fit of zones with irregular patterns.

Testing the bottom-up approach in a building with whole-building electricity measurements is crucial to gain a better understanding of tuning the uncertain zone loads affecting electricity use.

General questions remain in terms of trend data quality and availability. New BASs have the capacity to store and record trend data but it is uncertain if older systems do and if their logging functions are used. A survey investigating trend data quality and availability is recommended. Researching methods to monitor sensor health is recommended to help maintain trend data quality.

Implementing automatic change point identification in the AACT could improve the speed of generating inputs and reduce the requirement for user input of values.

Bannister et al. (2011) compared HVAC control representations of different building simulation programs. They specifically noted that a substantial gap existed when representing control of AHU supply air temperature. This was directly experienced in this thesis among other difficulties representing heat recovery and mixing air damper control and physical configuration. It is recommended that HVAC component field performance be compared to simulations in common building energy program be provide feedback to

building simulationists when improving building energy programs and modelling existing buildings.

Using shorter interval data would be another interesting area to explore. The trend data in this study were recorded every 15 min but the BAS had the capacity to change the recording length. eQUEST is limited to having hour long time steps, but EnergyPlus is not. Using shorter interval trend data with EnergyPlus may give insight into what is an appropriate time step to record and model.

Many abatement opportunities exist in buildings with net economic benefits but are not realized due to lack of incentives, information gaps, and high capital costs with long payback periods (McKinsey and Company 2009). The use of integrated software (e.g., eQUEST and AACT) and hardware tools (e.g., BAS) to evaluate energy performance at a component level can improve the accuracy and speed when identifying cost-effective energy efficiency measures.

# 8 References


AECOM Ltd. 2010. Project Summary Report: Commissioning Tools for Improved Building Energy Performance, Energy Conservation in Buildings and Community Systems Programme, International Energy Association (IEA) Annex 40, United Kingdom. Accessed May 2014. http://www.ecbcs.org/docs/ECBCS_Annex_40_PSR.pdf

ASHRAE, 2001. *ANSI/ASHRAE Standard 62-2001*, *Ventilation for Acceptable Indoor Air Quality*, ASHRAE, Atlanta, Georgia.

ASHRAE, 2002. *ASHRAE Guideline 14-2002, Measurement of Energy and Demand Savings,* ASHRAE, Atlanta, Georgia.

ASHRAE, 2009. *ASHRAE Handbook – Fundamentals,* ASHRAE, Atlanta, Georgia.

ASHRAE. 2010. ANSI/ASHRAE/IES Standard 90.1-2010*, Energy Standard for Buildings Except Low-Rise Residential Buildings*, ASHRAE, Atlanta, Georgia.

ASHRAE. 2013. ANSI/ASHRAE/IES Standard 90.1-2013*, Energy Standard for Buildings Except Low-Rise Residential Buildings*, ASHRAE, Atlanta, Georgia.

ACR Instruments Inc. (2013). http://www.acrsystems.com/

BC Hydro. 2014. Continuous Optimization Program. Accessed July 2014. https://www.bchydro.com/powersmart/business/commercial/continuous_optimization/program_results.html

Bannister, P., P.C. Thomas, and P. Lowndes. 2011. Representation of HVAC control in common simulation packages. *Proceedings of the 12th IBPSA Building Simulation Conference,* Sydney, Australia, 70-77.

Bhatia, A. 2008. To convert CSV to BIN. eQUEST-users mailing list. Accessed January 2014. http://lists.onebuilding.org/pipermail/equest-users-onebuilding.org/2008-August/000297.html

Bou-Saada, T.E., and J.S. Haberl 1995. An improved procedure for developing calibrated hourly simulation models. *Proceedings of the international Building Performance Simulation Association.* Madison, Wisconsin.

Brambley, M., R. Pratt, D. Chassin, S. Katipamula, and D. Hartley. October 1998. Diagnostics for Outdoor Air Ventilation and Economizers. *ASHRAE Jounrnal*, 49-55.

Bronson, D.J., J.S. Haberl, and D.L. O'Neal. 1992. A procedure for calibrating the DOE-2 simulation program to non-weather-dependent measured loads. *ASHRAE Transactions,* 98(1):636-52.

Brown, K., M. Anderson, and J. Harris. 2006. How Monitoring-Based Commissioning Contributes to Energy Efficiency for Commercial Buildings. *2006 ACEEE Summer Study on Energy Efficiency in Buildings*, 3:27-40.

Bynum, J.D., D.E. Claridge, and J.M. Curtin. 2012. Development and testing of an Automatic Building Commissioning Analysis Tool (ABCAT). *Energy and Buildings*, 55:607-617.

Carabott, M. 1989. Building simulation reconciliation using empirical data. *Proceedings* of the *IBPSA Building Simulation Conference,* Vancouver, Canada, 27-30.

Carling, P, P. Isakson, P. Blomberg, and J. Eriksson, 2003. Experiences from evaluation of the HVAC performance in the Katsan building based on calibrated whole building simulation and extensive trending. Accessed February, 2014. <http://www.commissioning-hvac.org/files/doc/A40-D-M6-SWE-%C3%85F_KTH-2.pdf>

Carroll, W.L., and R.J. Hitchcock. 1993. Tuning simulated building descriptions to match actual utility data: methods and implementation. *ASHRAE Transactions* 99(2), 928-934.

Chew, J. 2011. Editing eQUEST Weather Files. eQUEST-users mailing list. Accessed January 2014. http://lists.onebuilding.org/pipermail/equest-users-onebuilding.org/2011-March/008275.html

Choi, J.H. 2008. Convert CSV to BIN weather file. BLDG-SIM mailing list. Accessed January 2014. http://lists.onebuilding.org/pipermail/bldg-sim-onebuilding.org/2008-March/007067.html

Choiniere, D. 2008. DABO$^{TM}$: A BEMS assisted on-going commissioning tool. *Proceedings of the National Conference on Building Commissioning.*

Claridge, D.E., J.S. Haberl, B. Abushakra, and A. Sreshthaputra. 2004. Electric Diversity Profiles for Energy Simulation of Office Buildings, *ASHRAE Transactions,* 110(1): 365-377.

Clarke, J.A., P.A. Strachan, & C. Pernot. 1993. An approach to the calibration of building energy simulation models. *ASHRAE Transactions,* 99(2), 917-27.

Coakley, D., P. Raftery, and M. Keane. 2014. A review of methods to match building energy simulation models to measured data. *Renewable and Sustainable Energy Reviews.* 37:123-141.

Concordia University. 2014a. Loyola Campus Map. *University Communications Services T13-13660: Design.* Accessed June 2014. https://www.concordia.ca/content/dam/common/docs/maps/loyola_campus_map.pdf

Concordia University. 2014b. Centre for Structural and Function Genomics. Accessed July 2014. http://www.concordia.ca/research/genomics.html

Crawley, D.B., J.W. Hand, M. Kummert, and B.T. Griffith. 2008. Contrasting the capabilities of building energy performance simulation programs. *Building and Environment,* 43:661-673.

Davis, J.A., and D.W. Nutter. 2010. Occupancy diversity factors for common university building types. *Energy and Buildings* 42:1543-1551.

Enermodal Engineering and Natural Resources Canada (NRCan). 2010. FRAME™plus Online. Accessed May 2014. http://tools.enermodal.com/webframeplus/

Diamond, S.C., and B.D. Hunn. 1981. Comparison of DOE-2 computer program simulations to metered data for seven commercial buildings. *ASHRAE Transactions,* 87(1), 1222-1231.

Department of Energy (DOE). 2013. EnergyPlus. Accessed August 2014. http://apps1.eere.energy.gov/buildings/energyplus/

Eisenhower, B., Z. O'Neill, V.A. Fonoberov, and I. Mezic. 2012. Uncertainty and sensitivity decomposition of building energy models. *Journal of Building Performance Simulation*, 5(3):171-184.

Friedman, H., and M.A. Piette. 2001. Comparative Guide to Emerging Diagnostic Tools for Large Commercial HVAC Systems. High Performance Commercial Building Systems, LBNL No. 48629, California Energy Commission Public Interest Energy Research Program. Accessed June 2014. http://escholarship.org/uc/item/37b942xx

Gerometta, C. 2012. Weather Data Files. eQUEST-users mailing list. Accessed January 2014. http://lists.onebuilding.org/pipermail/equest-users-onebuilding.org/2012-July/012138.html

Gestwick, M.J., and J.A. Love. 2014. Trial application of ASHRAE 1051-RP: calibration method for building energy simulation, *Journal of Building Performance Simulation*, 7(5):346-359.

Greyline Instruments Inc. (2013). http://www.greyline.com/

Haberl, J.S., & D. Claridge. 1985. Retrofit studies of a recreation center. *ASHRAE Transactions,* 91(1), 1421-1433.

Haves, P., T.I. Salsbury, and J.A. Wright. 1996. Condition Monitoring in HVAC Subsystems Using First Principles Models. *ASHRAE Transactions,* 102(1):519-527.

Heidell, J.A., and Z.T. Taylor. 1985. Comparison of empirically measured end-use metered data with DOE 2.1 simulations. *Proceedings* of the *IBPSA Building Simulation Conference,* Seattle, USA, 290-295.

Heo, Y., R. Choudhary, and G.A. Augenbroe. 2012. Calibration of building energy models for retrofit analysis under uncertainty. *Energy and Buildings*, 47:550-560.

Hubler, D., K. Tupper, and E. Greensfelder. 2010. Pulling the levers on existing buildings: a simple method for calibrating hourly energy models. *ASHRAE Transactions*, 116(2):261-268.

IBPSA-USA. 2014. BEMBook: History of Building Energy Modelling. International Building Performance Simulation Association – USA Affiliate. Accessed October 2014. http://www.bembook.ibpsa.us/index.php?title=History_of_Building_Energy_Modeling

Jamieson, D., and S.B. Harding. 1989. Computer simulation/end-use metering or "can we count on energy savings estimates in designing demand-side programs?". *Proceedings of the 1st IBPSA Building Simulation Conference*, Vancouver, Canada, 207-212.

J.J. Hirsch & Associates (JJH). n.d. DOEWth: Convert NOAA/NCDC and Other Common Format Files into eQUEST and DOE-2 BIN Files, Accessed January, 2013. http://doe2.com/download/weather/DOE22WeatherUtilities.ZIP

Kandil, A.E. and J.A. Love, 2013. Signature analysis calibration of a school energy model using hourly data, *Journal of Building Performance Simulation*, 7(5):326-45.

Kaplan, M.B., J. McFerran, J. Jansen, and R. Pratt. 1990. Reconciliation of a DOE2.1C model with monitored end-use data for a small office building. *ASHRAE Transactions,* 96(1):981-993.

Katipamula, S., and D.E. Claridge. 1993. Use of simplified system models to measure retrofit energy savings. *Journal of Solar Energy Engineering,* 115:57-68.

Katipamula, S., R.G. Pratt, D.P. Chassin, Z.T. Taylor, K. Gowri, and M.R. Brambley. 1999. Automated Fault Detection and Diagnostics for Outdoor-Air Ventilation Systems and Economizers: Methodology and Results from Field Testing. *ASHRAE Transactions*, 105(1):1-13.

Katipamula, S., and M. R. Brambley. 2005. Review Article: Methods for Fault Detection, Diagnostics, and Prognostics for Buildings Systems – A Review, Part I. *HVAC&R Research* 11(1):3–25.

Kawneer. 2013. 1600 Wall System 2. Accessed January 2013. http://www.kawneer.com/kawneer/north_america/en/product.asp?cat_id=1338&prod_id=1802

Kissock, J.K., J.S. Haberl, and D.E. Claridge. 2003. Inverse Modelling Toolkit: Numerical Algorithms. *ASHRAE Transactions*, 109(2):425-434.

Knebel, D. 1983. *Simplified Energy Analysis Procedure.* Atlanta: American Society of Heating, Refrigerating, and Air-Conditioning Engineers.

Lavigne, K., A. Daoud, S. Sansregret, and M.A. Leduc. 2014. Demand Response Strategies in a Small All-Electric Commercial Building in Quebec. *Proceedings from the 8th eSim conference, Ottawa, Ontario, Canada*, 426-439.

Lawrence, T.M., and J.E Braun. 2007. Calibrated simulation for retrofit evaluation of demand-controlled ventilation in small commercial buildings. *ASHRAE Transactions,* 113(2):227-240.

Lawrence Berkeley National Laboratory (LBNL) and J.J. Hirsch & Associates (JJH). 1998. DOE-2.2. Accessed January 2013. http://www.doe2.com/equest/

Lawrence Berkeley National Laboratory (LBNL) and J.J. Hirsch & Associates (JJH). 2004 DOE-2.2 Building Energy Use and Cost Analysis Program Volume 1: Basics. Accessed January, 2013. http://doe2.com/download/DOE-22/DOE22Vol1-Basics.pdf

Liu, G., and M. Liu. 2011. A rapid calibration procedure and case study for simplified simulation models of commonly used HVAC systems. *Building and Environment,* 46:409-420.

Liu, M., and D.E. Claridge. 1998. Use of calibrated HVAC system models to optimize system operation. *Journal of Solar Energy Engineering, 120*, 131-138.

Liu, M., D.E. Claridge, N. Bensouda, K. Heinemeier, and S.U. Lee. 2003. *Manual of procedures for calibrating simulations of buildings.* California Energy Commission, Public Interest Energy Research Program.

Liu, S., and G.P. Henze. 2005. Calibration of building models for supervisory control of commercial buildings. *Building Simulation* (pp. 641-648). Montreal, Canada: International Building Performance Simulation Association Conference.

Lombard, L.P., J. Ortiz, and C. Pout. 2008. A review on buildings energy consumption information. *Energy and Buildings,* 40:394-398.

Morrison Hershfield. 2011. Thermal Performance of Building Envelope Details for Mid- and High-Rise Buildings (1365-RP). Report No. 5085243.01, ASHRAE. Accessed May 2014. http://www.morrisonhershfield.com/ashrae1365research/Documents/MH_1365RP_Final_%20small.pdf

Maile, T. V. Bazjanac, and M. Fischer. 2012. A method to compare simulated and measured data to assess building energy performance. *Building and Environment*, 56:241-251.

McFarlane, D. June 2013. Technical vs. Process Commissioning. *ASHRAE Journal,* 28-34.

McKinsey and Company. 2009. Pathways to a Low-Carbon Economy: Version 2 of the Global Greenhouse Gas Abatement Cost Curve. McKinsey and Company. Accessed June 2014. http://www.mckinsey.com/client_service/sustainability/latest_thinking/greenhouse_gas_abatement_cost_curves

Mihai, A. and R. Zmeureanu. 2013. Calibration of predicted hourly zone-level supply air flows with measurements. *Proceedings of the 13th International Conference for Enhanced Building Operations (ICEBO)*, Montreal, Canada.

Mihai, A. 2014. Calibration of a Building Energy Model Using Measured Data for a Research Center. Master's Thesis, Concordia University, Montreal, Quebec, Canada.

Monfet, D., R. Charneux, R. Zmeureanu, and N. Lemire. 2009. Calibration of a building energy model using measured data. *ASHRAE Transactions,* 115(1):348-359.

Monfet, D., and R. Zmeureanu. 2012. Ongoing commissioning of water-cooled electric chillers using benchmarking models. *Applied Energy* 92:99-108.

Monfet, D., and R. Zmeureanu. 2013. Calibration of a central cooling plant model using manufacturer' data and measured input parameters and comparison with measured performance. *Journal of Building Performance Simulation* 6(2):141-155.

Moser, D.E. 2013. Commissioning Existing Airside Economizer Systems. *ASHRAE Journal* 55(3):34-44.

Mustafaraj, G., D. Marini, A. Costa, and M. Keane. 2014. Model calibration for building energy efficiency simulation. *Applied Energy*, 130:72-85.

Motegi, N., M.A. Piette, S. Kinney, and K. Herter. 2003. Web-based Energy Information Systems for Energy Management and Demand Response in Commercial

Buildings. High Performance Commercial Building Systems, LBNL-52510 California Energy Commission Public Interest Research Program. Accessed June 2014. http://cbs.lbl.gov/publications/web-based-energy-information-system-0

Norford, L.K., R.H. Socolow, E.S. Hsieh, and G.V. Spadaro. 1994. Two-to-one discrepancy between measured and predicted performance of a 'low energy' office building: insights from a reconciliation based on the DOE-2 model. *Energy and Buildings*, 21:121-131.

Norford, L.K., J.A. Wright, R.A. Buswell, D. Luo, C.J. Klassen, and A. Suby. 2002. Demonstration of Fault Detection and Diagnosis Methods for Air-Handling Units (ASHRAE 1020-RP). *HVAC&R Research,* 8(1):41-71.

National Research Council of Canada (NRC), 1997. *Model National Energy Code for Buildings*, NRC, Ottawa, Canada.

NRCan. 2009. Energy Efficiency Trends in Canada 1990 to 2009. Natural Resources Canada, Canada. Accessed June 2014. http://publications.gc.ca/site/eng/440661/publication.html

Oh, S. 2013. *Origins of Analysis Methods in Energy Simulation Programs used for high performance commercial buildings*. Master's Thesis, Texas A&M University, Texas, USA.

O'Neill, Z., X. Pang, M. Shashanka, P. Haves, and T.Bailey, 2014. Model-based real-time whole building energy performance monitoring and diagnostics. *Journal of Building Performance Simulation*, 7(2):83-99.

Pan, Y., Z. Huang, and G. Wu. 2007. Calibrated building energy simulation and its application in a high-rise commercial building in Shanghai. *Energy and Buildings,* 39:651-657.

Pang, X., M. Wetter, P. Bhattacharya, and P. Haves. 2012. A framework for simulation-based real-time whole building performance assessment. *Building and Environment*, *54*:100-108.

Pedrini, A., F.S. Westphal, and R. Lamberts. 2002. A methodology for building energy modelling and calibration in warm climates. *Building and Environment*, 37:903-912.

Piette, M.A., S.K. Kinney, and P. Haves. 2001. Analysis of an information monitoring and diagnostic system to improve building operations. *Energy and Buildings*, 33: 783-791.

Raftery, P. 2011. Calibrated whole-building energy simulation: an evidence-based methodology. PhD Dissertation, NUI Galway, Galway, Ireland.

Raferty, P., M. Keane, and J. O'Donnell. 2011. Calibrating whole building energy models: An evidence-based methodology. *Energy and Buildings, 43*:2356-2364.

Reddy, T. A. 2006. Literature review on calibration of building enegry simulation programs: uses, problems, uncertainty, and tools (RP-1051). *ASHRAE Transactions,* 112(1):226-240.

Reddy, T. A., I. Maor, and C. Panjapornpon. 2007. Calibrating detailed building energy simulation programs with measured data-part I: general methodology (RP-1051). *HVAC&R Research, 13*(2):221-241.

Reddy, T. A., I. Maor, and C. Panjapornpon. 2007. Calibrating detailed building energy simulation programs with measured data-part II: Application to three case study office buildings (RP-1051). *HVAC&R Research, 13*(2):243-265.

Reddy, T.A., 2011. Applied Data Analysis and Modeling for Energy Engineers and Scientists. Springer New York.

Roth, K., P. Llana, D. Westphalen, and J. Brodrick. 2005. Automated Whole Building Diagnostics. *ASHRAE Journal,* 47(5):82-84.

Savenije, H.H.G. 2009. HESS Opinions "The art of hydrology". *Hydrology and Earth System Sciences*, 13:157-161.

SECO. 2014. LoanSTAR Revolving Loan Program, State Energy Conservation Office (SECO). Accessed June 2014. http://www.seco.cpa.state.tx.us/ls/

Sansregret, S., K. Lavigne, A. Daoud, and L.A. Leclaire. 2014. ExCaliBEM: Tool Development to Calibrate Building Energy Models. *Proceedings of the 8th IBPSA Canada eSim Conferece*, Ottawa, Ontario, Canada.

Seidl, R. 2006. Trend analysis for commissioning. *ASHRAE Journal* 48:34-43.

Sellers, D.A. 2003. Data Logger Operation Tips: Working with data: trend analysis and spreadsheeting. *HPAC Engineering,* February, pp. 50-51. Accessed June 2014. http://resources.cacx.org/library/holdings/192.pdf

SIMEB. 2013. Simulation énergétique des bâtiments (SIMEB): Weather data. Accessed October 2013. https://www.simeb.ca:8443/index_en.jsp

Soebarto, V. I. 1997. Calibration of hourly energy simulations using hourly monitored data and monthly utility records for two case study buildings. *Proceedings of IBPSA Building Simulation Conference,* Prague, Czech Republic.

Subbarao, K. 1988. PSTAR – Primary and Secondary Terms Analysis and Renormalization: A Unified Approach to Building and Energy Simulations and Short Term Testing - A Summary. Solar Energy Research Institute, Golden Colorado.

Sun, J., & Reddy, A. T. 2006. Calibration of Building Energy Simulation Programs Using the Analytic Optimization Approach (RP-1051). *HVAC&R Research,* 12(1), 177-196.

Tamburrini, M., D. Palmer, and I.A. Macdonald. 2003. Calibrating models for simulation use in design practices. *Proceedings of IBPSA Building Simulation Conference,* Eindhoven, Netherlands, 1273-1278.

Torcellini, P.A., M. Deru, B. Griffith, N. Long, S. Pless, R. Judkoff, and D.B. Crawley. 2006. Lessons Learned from Field Evaluation of Six High-Performance Buildings. National Renewable Energy Laboratory. Viewed December 2013, http://www.nrel.gov/docs/fy06osti/37542.pdf

Tremblay, V., and R. Zmeureanu. 2014. Benchmarking models for the ongoing commissioning of heat recovery process in a central heating and cooling plant. *Energy* 70: 194-203.

Turner, W.D., D.E. Claridge, D.L. O'Neal, J.S. Haberl, W.M Heffington, T. Harvey, and T. Sifuentes. 1998. Program Overview: The Texas LoneSTAR Program; 1989-1997. *Proceedings of the 11$^{th}$ Symposium on Improving Building Systems in Hot and Humid Climates*, Fort Worth, Texas, USA.

Twin City Fan and Blower. 2012. E-Series Plenum Fans - Catalogue 470. Twin City Fan and Blower. Accessed January 2013. http://tcf.com/products/plenum-and-plug-fans/epfn---plenum-fan-airfoil-wheel-9-blades-arrangement-1-4

Wang, S., and F. Xiao. 2004. Detection and diagnosis of AHU sensor faults using principal component analysis method. *Energy Conservation and Management,* 45:2667-2686.

Wang, S. 2010. *Intelligent Buildings and Building Automation.* Spon Press, New York, USA: Taylor and Francis.

Wang, L., S. Greenberg, J. Fiegel, A. Rubalcava, S. Earni, X. Pang, R. Yin, S. Woodworth, and J. Hernandez-Maldonado. 2013. Monitoring-based HVAC commissioning of an existing office building for energy efficiency. *Applied Energy* 102:1382-1390.

Wei, G., M. Liu, and D.E Claridge. (1998). Signatures of heating and cooling energy consumption for typical AHUs. *Proceedings of the 11th Syposium on Improving Building Systems in Hot and Humid Climates*, Fort Worth, Texas, 387-402.

Westphal, F. S., and R. Lamberts. 2005. Building simulation calibration using sensitivity analysis. *Proceedings of IBPSA Building Simulation Conference,* Montreal, Canada, 1331-1338.

Xiao, F., S. Wang, and J. Zhang. 2006. A diagnostic tool for online sensor health monitoring in air-conditioning systems. *Automation in Construction,* 15:489-503.

Xiao, F., and S. Wang. 2009. Progress and methodologies of lifecycle commissioning of HVAC systems to enhance building sustainability. *Renewable and Sustainable Energy Reviews,* 13:1144-1149.

Yoon, J., E.J. Lee, and D.E. Claridge. 2003. Calibration Procedure for Energy Performance Simulation of a Commercial Building. *Journal of Solar Energy Engineering,* 125:251-257.

Zibin, N.F., Zmeureanu, R.G., & J.A. Love. 2013. Use of Building Automation System Trend Data for Inputs Generation in Bottom-Up Simulation Calibration, Proceedings of the 13th International Conference for Enhanced Building Operations (ICEBO), Montreal, Canada.

Zibin, N.F., Zmeureanu, R.G., & J.A. Love. May 2014. Bottom-up simulation calibration of zone and system level models using building automation system (BAS) trend data, Proceedings of the 8th IBPSA-Canada eSim Conference, Ottawa, Canada.

Zmeureanu, R., L. Pasqualetto, and F. Bilas. 1995. Comparison of cost and energy savings in an existing large building as predicted by three simulation programs. *Proceedings of IBPSA Building Simulation Conference,* Madison, Wisconsin, 485-492.

## Appendix A – Short-term fan power measurements

Fan electric power was calculated using short-term measurements of current passing through each phase of the motors in supply air fans VA1-1, VA2-1, and VA1-2 (Figure 3.7). Fan motor VA2-2's current was not recorded because there were too few current clamps available to simultaneously measure all fans. It was important to measure fan power because they operated continuously. The current clamps used to measure current were model A60FL and were connected to SmartReader 3 data loggers; both manufactured by ACR Systems Inc. (2013). The current clamp bias error was ± 3%. Measurements were recorded from November 15$^{th}$ to December 5$^{th}$, 2013 and February 27$^{th}$ to March 20$^{th}$, 2014 using a 6 min sampling interval. The measurements were averaged into 15 min data (i.e., the mean of two 6 min measurements per 15 min interval) for synchronization with the supply air flow rate trend data.

Fan power ($\dot{W}_{fan}$) was calculated using eq. A.1. Fan line-to-line voltages ($V_{LL}$) were spot measured, using a voltmeter, and averaged 592 V, 590 V, and 594 V for fans VA1-1, VA2-1, and VA1-2, respectively. The power factor (*pf*) for the fan was assumed to be the nameplate value of 0.805.

$$\dot{W}_{fan} = \sqrt{3} \cdot V_{LL} \cdot pf \cdot (I_1 + I_2 + I_3) \qquad \text{eq.A.1}$$

*where:* $I_1, I_2, I_3$ = three phases of current measured, in Amps

### *A.1 Fan Power:* November 15$^{th}$ to December 5$^{th}$, 2013

The supply air flow rate ($V_s$) trend data and measured $\dot{W}_{fan}$ are shown in Figures A.1 and A.2. From November 29$^{th}$ to December 5$^{th}$, 2013 there was a supply air flow rate of approximately 5000 L/s for fans VA1- & VA2-1 yet there was approximately zero measured current causing zero power measured. These erroneous measurements were probably caused by a low resolution setting (0-250 A) on the current clamps. The maximum current measured was approximately 50 A per phase and the median was 10 A per phase. The reason VA1- & VA2-1 operated at a larger $V_s$ than VA1-2 from

November 18th to 22nd, 2013 was because VA1-2 (Figure A.1) and VA2-2 were deactivated for unknown reasons.

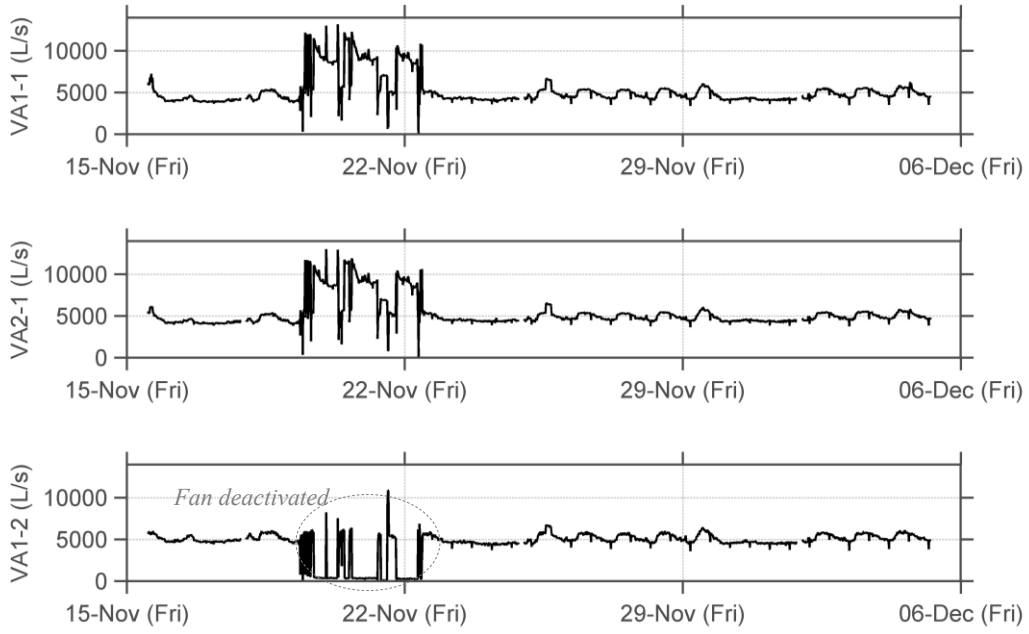


Figure A.1 Supply air flow rate from November 15th to December 5th, 2013

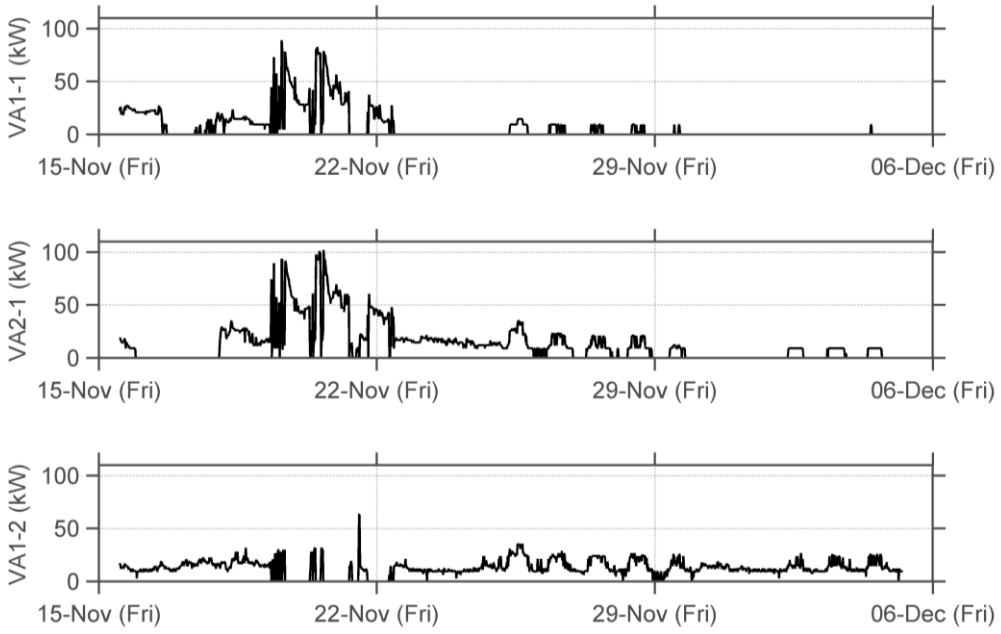


Figure A.2 Fan power from November 15th to December 5th, 2013

### *A.2 Fan Power:* February 27th to March 20th, 2014

The $V_s$ trend data and $\dot{W}_{fan}$ from this period are shown in Figures A.3 and A.4. These measurements were taken at a higher resolution setting (0-100 A) than the previous measurements and the results rarely recorded zero $\dot{W}_{fan}$ (Figure A.4). The $\dot{W}_{fan}$ for VA2-1 was smaller than VA1-1 and VA1-2 because one of the current clamps connected to VA2-1 rarely recorded a value greater than 0 A. It was likely that either the resolution setting was too low and/or the fan power consumption per phase was unbalanced for this fan.

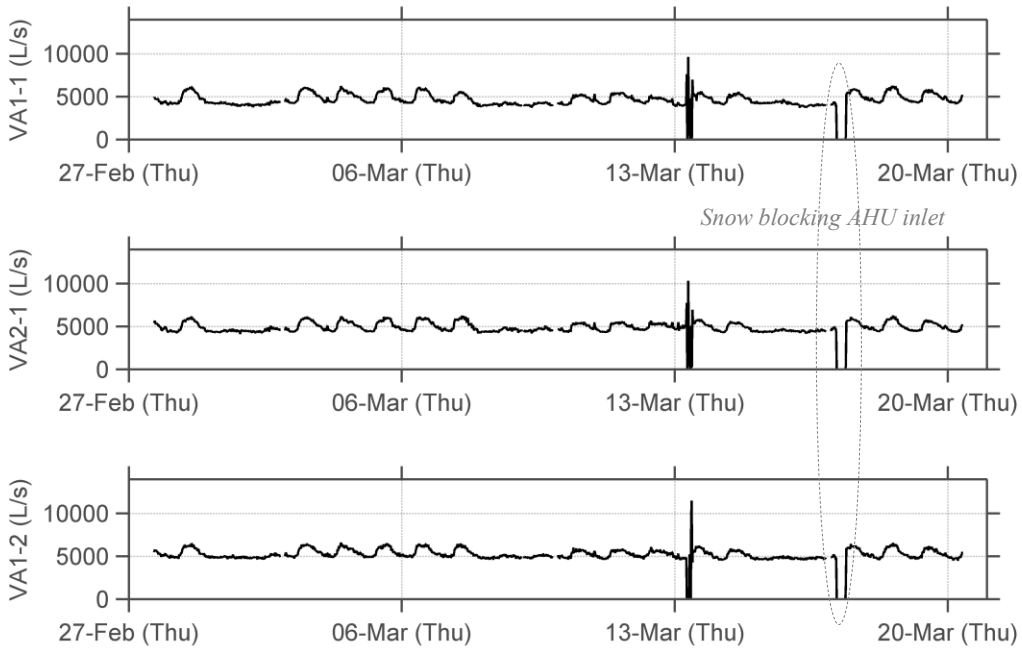


Figure A.3 Supply air flow rate from February 27th to March 20th, 2014

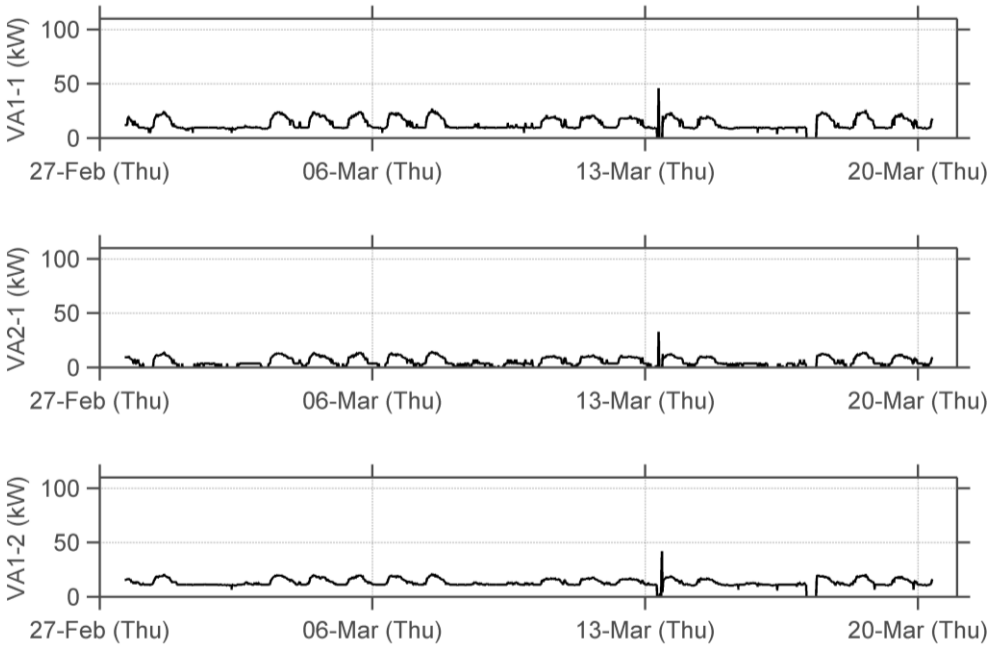


Figure A.4 Fan power from February 27th to March 20th, 2014

The erroneous data measured from November 15th to December 5th, 2013 were removed and the remaining data were combined with the February 27th to March 20th, 2014 measurements to compare $\dot{W}_{fan}$ and $V_s$ for each fan measured in Figure A.5. The results were as expected from the fan affinity laws such that $\dot{W}_{fan}$ increased exponentially to $V_s$.

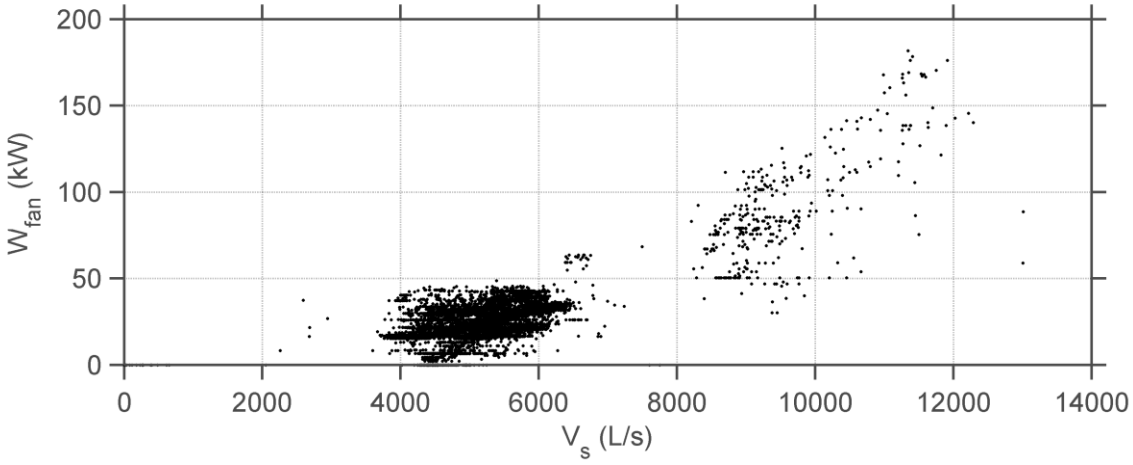


Figure A.5 Fan power vs. supply air flow rate

This section explained difficulties measuring VAV fan electric power using current clamps due to the large range that current varies. A longer measurement period would provide more data to assess fan performance. The VAV motor controllers continuously monitor fan power but these sensors were not set up to connect with the BAS. The current measurements from February 27$^{th}$ to March 20$^{th}$, 2014 were used in Section 4.4.4.2 as opposed to the November 15$^{th}$ to December 5$^{th}$, 2013 data because the more recent set contained higher resolution data and were nearly error free.

The $\Delta T_{fan}$ calculated from fan power (see Section 4.4.4.2) across fan VA2-1's was calculated as 0.8 ± 0.2 °C, which was lower than the previous fans (VA1-1 and VA1-2) (Table 4.11) because problems occurred measuring this fan's current.

## Appendix B – eQUEST input keywords

Table B.1 List of inputs generated and eQUEST input name

| System | Input | eQUEST inputs |
|---|---|---|
| Air-side | Cooling supply air set point | COOL-SET-T |
| | Maximum heating supply air flow ratio | HMAX-FLOW-RATIO |
| | Minimum supply air flow ratio | MIN-FLOW-RATIO |
| | Design supply $\Delta T_{fan}$ | SUPPLY-DELTA-T |
| | Design return $\Delta T_{fan}$ | RETURN-DELTA-T |
| | Temperature exiting heating coils | PREHEAT-T |
| | Supply air reset temperature | COOLING-RESET-SCH |
| | Minimum outside air ratio | MIN-AIR-SCH |
| | Heat recovery activation $\Delta T$ | OA-EXHAUST-DT |
| | Heat recovery effectiveness | ERV-SENSIBLE-EFF |
| | Minimum humidity | MIN-HUMIDITY |
| | Maximum humidity | MAX-HUMIDITY |
| | Zone reheat | REHEAT-DELTA-T |
| Water-side | Design heating coil temperature difference | PHW-COIL-DT |
| | Heating coil activation temperature | SNAP-T |
| | Heating coil reset temperature | HEAT-RESET-SCH |
| | Zone reheat hot water reset temperature | HEAT-RESET-SCH |

## Appendix C – Algorithm and code to estimate the design heat recovery effectiveness

First, the design $V_{oa}$ was specified for both the design outdoor and exhaust air flow rates in eQUEST. Second, the number of heat transfer units (*NTU*) at the design $\varepsilon_{hr}$ was calculated using a numerical method (e.g., interpolating bi-sectional search) to solve the non-linear heat exchanger effectiveness for a cross flow configuration with no mixing (eq C.1). The heat capacity ratio rate (*C*) (eq. C.2) at design conditions was set equal to one because it was standard manufacturer practice to assume equal $V_{oa}$ and $V_e$ at design conditions. Next, the design *UA* was calculated (eq. C.3) at the design *NTU* and design outdoor air heat capacity rate ($C_{oa}$) (eq. C.4). The design *UA* film coefficient ($UA_{film\_coeff}$) was calculated next in eqs. C.5 to C.10. It should be noted the film resistance ($R_{film}$) (eq. C.7) was divided by two to account for both sides of the heat recovery coils. The following equations use imperial units of cubic feet per min (CFM).

$$\varepsilon_{hr} = 1 - e^{\frac{\left(e^{-NTU^{0.78}\cdot C} - 1\right)}{NTU^{-0.22}\cdot C}} \quad \text{eq. C.1}$$

$$C = \frac{C_{min}}{C_{max}} = \frac{\rho_{air} c_{p_{air}} \min(V_{oa}, V_e)}{\rho_{air} c_{p_{air}} \max(V_{oa}, V_e)} = 1 \quad \text{eq. C.2}$$

$$UA_{design} = NTU_{design} \cdot C_{oa_{design}} \quad \text{eq. C.3}$$

$$C_{oa_{design}} = \rho_{air} c_{p_{air}} V_{oa_{design}} \quad \text{eq. C.4}$$

$$R_{total} = {}^{1}/_{UA_{design}} \quad \text{eq. C.5}$$

$$R_{media} = R_{total}\left(1 - F_{sen\_res}\right) \quad \text{eq. C.6}$$

$$R_{film} = \frac{1}{2}\left(R_{total} - R_{media}\right) \quad \text{eq. C.7}$$

$$UA_{film} = {}^{1}/_{R_{film}} \quad \text{eq. C.8}$$

$$UA_{film\_coeff} = \frac{UA_{film}}{V_{oa_{design}}{}^{F_{sen\_exp}}} \quad \text{eq. C.9}$$

$$V_{min} = 0.3 \cdot V_{oa_{design}} \quad \text{eq. C.10}$$

*where:*

| | | |
|---|---|---|
| $R_{total}$ | = | Total design thermal resistance |
| $R_{total}$ | = | Median resistance |
| $F_{sen\_res}$ | = | Sensible film resistance ($0 < F_{sen\_res} \leq 1$). The default value in eQUEST was 0.4 |
| $UA_{film}$ | = | Air film *UA* for one side of heat recovery |
| $F_{sen\_exp}$ | = | Sensible film exponential ($0 \leq F_{sen\_exp} \leq 1$). The default value in eQUEST was 0.2 |
| $V_{min}$ | = | Minimum flow at which the $UA_{film}$ remained constant if $V_{oa} < V_{min}$ |

The simulated effectiveness was calculated based on the hourly $V_{oa}$ and $V_{exh}$ passing through the heat recovery coils once the design $UA_{film\_coeff}$ was known. In the case of this model, $V_{oa}$ and $V_e$ are simulated with equal values as discussed earlier. The following equations (eqs. C.11 to C.16) were used in eQUEST to calculate the hourly *NTU* to estimate the hourly simulated $\varepsilon_{hr}$ (eq. C.1).

$$UA_{oa} = UA_{film\_coeff} \cdot \max(V_{oa}, V_{min})^{F_{sen\_exp}} \quad \text{eq. C.11}$$

$$UA_{exh} = UA_{film\_coeff} \cdot \max(V_{exh}, V_{min})^{F_{sen\_exp}} \quad \text{eq. C.12}$$

$$R_{oa} = {}^{1}/_{UA_{oa}} = R_{exh} = {}^{1}/_{UA_{exh}} \quad \text{eq. C.13}$$

$$R_{hr} = R_{oa} + R_{media} + R_{exh} \quad \text{eq. C.14}$$

$$UA_{hr} = {}^{1}/_{R_{hr}} \quad \text{eq. C.15}$$

$$NTU = \frac{UA_{hr}}{C_{min}} \qquad \text{eq. C.16}$$

The following code essentially reverse engineers the code in DOE2 to estimate the design $\varepsilon_{hr}$ using numerical methods based on: (1) design $V_{oa}$, (2) the maximum $\varepsilon_{hr}$ estimated from trend data, (3) the median $V_{oa}$, and (4) an initial guess for the design $\varepsilon_{hr}$.

```
%%%%%%%%%%%%%%%%%%%%%%%%%%%%%%%%%%%%%%%%%%%%%%%%%%%%%%%%%%%%%%%%%%%%%%%%%%%%%%%
% GENERATE THE EFFECTIVENESS INPUT
%%%%%%%%%%%%%%%%%%%%%%%%%%%%%%%%%%%%%%%%%%%%%%%%%%%%%%%%%%%%%%%%%%%%%%%%%%%%%%%

% 1. Define parameters:
e_need = median(e_hr_III);      % The maximum effectivness (i.e., 0.41)
V_des  = 33.3;                  % Heat recovery design air flow rate [m^3/s]
V_oa   = alpha * median(Vs_III);% Median Voa during frost control [m^3/s]
e_ini  = 0.22;                  % Initial guess for design effectiveness

% 2. Reverse engineer the non-linear DOE2 code for the design effectiveness
% This used MATLAB's 'fzero' function. It essentially solves a nonlinear
% equation for its root(s) using numerical methods. The function uses
% a combination of bi-section, secant, and inverse quadratic
% interpolation methods.
% In this case, 'fzero' was used to find the roots of a the function
% e_hr_design explained below

e_design = fzero(@(e_in) e_hr_design(e_need,e_in,V_oa,V_des), e_ini)

function [e_out] = e_hr_design(e_need,e_in,V_oa,V_des)
%%%%%%%%%%%%%%%%%%%%%%%%%%%%%%%%%%%%%%%%%%%%%%%%%%%%%%%%%%%%%%%%%%%%%%%%%%%%%%%
% MINIMIZES THE DIFFERENCE BETWEEN e_des AND SIMULATED EFFECTIVENESS
%%%%%%%%%%%%%%%%%%%%%%%%%%%%%%%%%%%%%%%%%%%%%%%%%%%%%%%%%%%%%%%%%%%%%%%%%%%%%%%
% 1. Change units and initialize variables
V_oa  = V_oa  * 2.11888;% [L/s] to [CFM]
V_des = V_des * 2.11888;% [L/s] to [CFM]
C_des = V_des * 1.08;   % Design OA heat capacity ratio [Btu/(hrK)]
F_s_r = 0.2;            % Sensible air film resistance
F_s_e = 0.4;            % Sensible air film exponent
C     = 1;              % Design heat capacity ratio

% 2. Find design UA by first solving for the design NTU for e_in
% The initial NTU guess was 1
NTU = fzero(@(NTU) e_in - (1-exp((exp(C * -NTU^0.78)-1)/(C * NTU^-0.22))),1);
UA  = NTU * Cdes;

% 3. Calculate the design UA film coefficient
Rtotal   = 1 / UA;                % Total resistance
Rmedia   = Rtotal * (1 - F_s_r);  % Media resistance
Rfilm    = 0.5 * (Rtotal - Rmedia);% Film resistance for 1 side
UAfilm   = 1 / Rfilm;             % Film UA-value
UAfilm_c = UA / V_des^F_s_e;      % Design UA film coefficient
V_min    = 0.3 * V_des;           % Minimum flow

% 4. Solve for the effectiveness at the median V_oa
```

```
% Output the difference between measured and simulated effectiveness
% because this function is used within 'fzero'
UAoa   = Uafilm_c * min(V_oa,V_min)^Senfilm;% Outdoor air UA-value
Roa    = 1 / UAoa; Rehx = Roa;              % Outdoor air R-value (C=1)
Rhr    = Roa + Rmedia + Rexh;               % Total resistance
UAsim  = 1 / Rhx;                           % Simulated U-value
NTUsim = UAsim / (Voa * p_air * cp_air);    % Simulated NTU
e_sim  = 1-exp((exp(C * -NTUsim^0.78)-1)/(C * NTUsim^-0.22));
e_out = e_need - e_sim;
end
```

## Appendix D - Quality of heat flow rate calculations using trend data

The AACT relied on air and thermofluid temperatures and air flow rates to estimate heat and thermofluid flow rates. The objective of this section was to compare heat flow rates calculated using supply air flow rate trend data and short-term thermofluid flow measurements.

Spot measurements of thermofluid flow rates were collected to check $V_{hc}$ and the hot water flow rate entering heat exchangers EC5- & EC6-GLC ($V_{hw}$) (Figure 3.9). Measurements were recorded at 5 min intervals on February 26, 2014 using the same portable ultrasonic flow meter mentioned earlier (Section 4.4.3.1).

The recorded $V_{hw}$ values are shown in Table D.1 along with the spot measured inlet ($T_{i5}$ & $T_{i6}$) and outlet ($T_{o5}$ & $T_{o6}$) hot water temperatures of the heat exchangers (Figure 3.9) and heat transfer rate calculated using eq. D.1. The hot water thermometers had a bias error of ± 0.5 °C.

$$\dot{Q}_{hw} = \mathrm{V}_{hw}\rho_{hw}c_{p_{hw}}\left(\left(\frac{T_{i5}+T_{i6}}{2}\right)-\left(\frac{T_{o5}+T_{o6}}{2}\right)\right) \qquad \text{eq. D.1}$$

Table D.1 Spot measurements of hot water flow rate entering heat exchangers

| Time | $V_{hw}$ (L/s) | $T_{i5}$ (°C) | $T_{i6}$ (°C) | $T_{o5}$ (°C) | $T_{o6}$ (°C) | $\dot{Q}_{hw}$ (kW) |
|---|---|---|---|---|---|---|
| 15:50 | 9.23 | 44 | 44 | 42 | 42 | 76 ± 19 |
| 15:55 | 9.07 | 44 | 44 | 42 | 42 | 75 ± 19 |
| 16:00 | 9.02 | 44 | 44 | 42 | 42 | 75 ± 19 |
| 16:05 | 9.13 | 44 | 44 | 42 | 42 | 76 ± 19 |
| Mean | 9.11 | 44 | 44 | 42 | 42 | 76 ± 19 |

Figure D.1 compares the heat flow rates calculated using the air-side ($\dot{Q}_{hc}$) (eq. 3.7), glycol-side (i.e., should equal $\dot{Q}_{hc}$), and hot-water-side of the heating coils and heat exchangers. The large uncertainty in the air and hot-water-side calculations were primarily caused by large propagated bias erorrs of temperature sensors and small temperature differences across the heating coils and heat exchanger. The glycol-side heat flow rate followed the pattern of the air-side heat flow rate but at a slightly lower value,

which would violate the first law of thermodynamics if the uncertainty of $\dot{Q}_{hc}$ was smaller. Neglecting heat transfer losses may have also accounted for the low value. The low value of the glycol-side $\dot{Q}_{hc}$ may have occurred because the glycol velocity was measured with an average of 0.06 m/s. The flow meter cannot measure velocities less than 0.01 m/s and the flow meter was calibrated by the manufacturer at velocities between 1-2 m/s. The source of the discrepancy may have been velocities below the flow meter calibration range. The bias error reported by the manufacturer was ± 6% when the velocity was less than 0.2 m/s; however, it was known that the sensor was not calibrated for these low flow conditions so the bias error may have been larger.

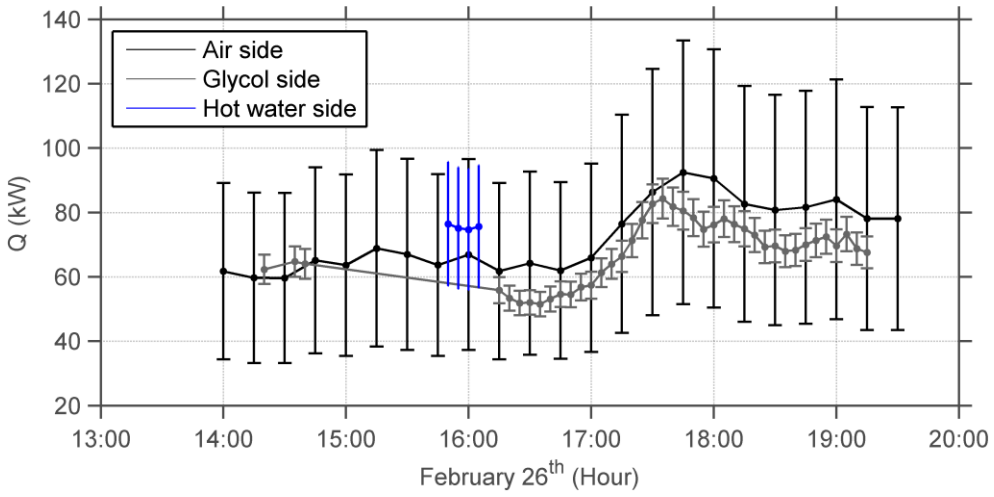


Figure D.1 Heat flow rate calculated using trend data and spot measurements

Comparison of $\dot{Q}_{hc}$ and $\dot{Q}_{hw}$ showed good agreement when considering their large uncertainty bounds. This indicated that calculating heat flow rate of the heating coils using air-side trend data was practical and could be used as an alternative to flow meters. The efficiency of the heat exchanger was calculated using eq. D.2 as 0.85 ± 0.43 during the time the hot water flow rate was measured.

$$\eta_{ss} = \frac{\dot{Q}_{hc}}{\dot{Q}_{hw}} = \frac{64.3\ kW}{75.5\ kW} = 0.85 \qquad \text{eq. D.2}$$

## Appendix E – Fan power heating penalty equations

$$FHP_{hr} = \frac{\dot{W}_{fan_{hr}}}{\rho_{air} c_{p_{air}} V_{oa}} \quad \text{eq. E.1}$$

$$\dot{W}_{fan_{hr}} = V_{oa} \Delta P_{hroa} \left( \dot{W}_{sfan} \Big/ \Delta P_{hroa} \right) \quad \text{eq. E.2}$$

$$\dot{W}_{sfan} \Big/ \Delta P_{hroa} = \frac{0.746}{6356 \eta_{fan} \eta_{motor}} \quad \text{eq. E.3}$$

$$\eta_{motor} = f(hp, motor\ class) \quad \text{eq. E.4}$$

$$\Delta P_{hroa} = \Delta P_{hroa_{static}} \left( \frac{V_{oa}}{V_{oa_{design}}} \right)^{K} \quad \text{eq. E.5}$$

*where:*

| | | |
|---|---|---|
| $FHP_{hr}$ | = | fan heat penalty associated with the temperature rise across the heating recovery coils associated with additional supply air fan energy required to overcome the additional pressure difference |
| $\dot{W}_{fanhr}$ | = | additional fan energy required to overcome the pressure increase from the heat recovery coils |
| $\Delta P_{hroa}$ | = | total pressure loss across the heat recovery coils |
| $\dot{W}_{fanhr}/\Delta P_{hroa}$ | = | fan power per total pressure loss |
| $\eta_{fan}$ | = | mechanical efficiency of the fan |
| $\eta_{motor}$ | = | motor efficiency as a function of horse power (hp) and motor class (e.g., standard, high efficiency, or premium) |
| $\Delta P_{hroastatic}$ | = | static pressure loss across the heat recovery coils |
| $V_{oadesign}$ | = | design air flow rate, in this case |
| $K$ | = | static pressure drop exponent coefficient |

## Appendix F – Zone reheat capacity

The total zone reheat energy was not measured but the capacity of each reheat terminal was listed in the design documents (Table F.1). This was used when calibrating the zone level to ensure that the zone heating energy remained within the capacity of installed terminal units.

Table F.1 Zone reheat capacity

| Zone reheat capacity | Reheat capacity (kW) | Capacity density ($W/m^2$) |
|---|---|---|
| Z1-S | 35 | 220 |
| Z1-NE | 21 | 88 |
| Z1-NW | 12 | 95 |
| Z1-CORR | 5 | 18 |
| Z1-CONF | 14 | 88 |
| Z2-SW | 19 | 187 |
| Z2-E | 41 | 115 |
| Z2-INT | 7 | 53 |
| Z2-NE | 44 | 211 |
| Z2-S | 15 | 91 |
| Z2-W | 5 | 39 |
| Z3-SW | 19 | 187 |
| Z3-E | 41 | 115 |
| Z3-INT | 7 | 53 |
| Z3-NE | 44 | 211 |
| Z3-S | 15 | 91 |
| Z3-W | 5 | 39 |

## Appendix G – Shoulder season heat recovery variables directly output

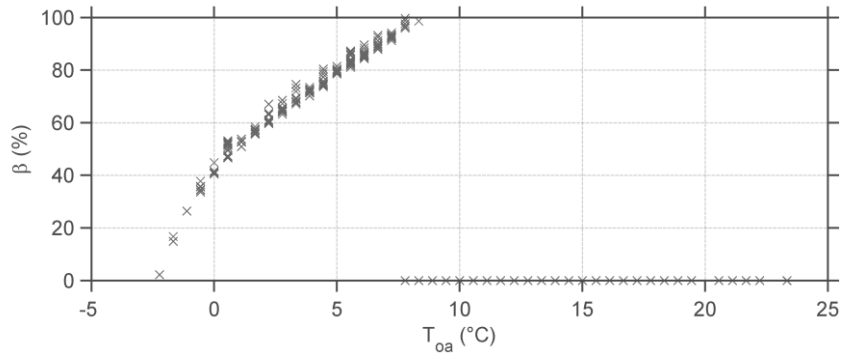


Figure G.2 Simulated ratio of outdoor air bypassed around heat recovery. Frost control was active when $\beta$ equalled one.

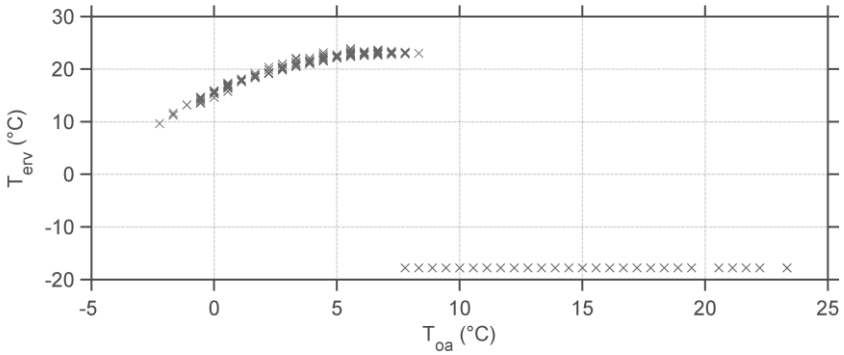


Figure G.3 Simulated air temperature exiting the heat recovery coils. The value of $T_{erv}$ was automatically -17.7 °C when heat recovery was inactive and was not used in any calculations within DOE-2 or this thesis.

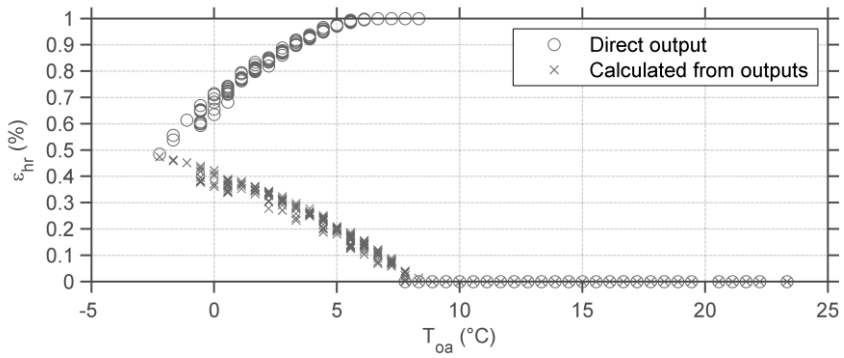


Figure G.1 Simulated effectiveness. The direct out refers to the thermodynamically equivalent heat recovery configuration when heating $T_{erv}$.